Feasibility Studies of an Inverse Compton Scattering Based Gamma Source at MESA

Dissertation
submitted for the award of the title
"Doctor of Natural Sciences"
to the Faculty of Physics, Mathematics, and Computer Science
of the Johannes Gutenberg-University
in Mainz

Christoph Lukas Lorey
born in Frankfurt a.M.

Mainz, 19th December, 2024

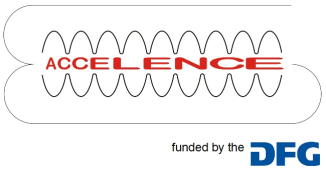

"Darauf dich fasse, alle Kunst hat Länge und Maße"
- Johann Liechtenauer

Abstract

Recent years saw a number of accelerator projects attempt to utilize Inverse Compton Scattering (ICS) as gamma sources and beam diagnostic tools. With it's low cross section, ICS is a prospective pairing with energy recovery linacs (ERL) as they require low impact experiments for energy recovery efficiency to be high.
At the Johannes Gutenberg-University Mainz, the Mainz Energy Recovering Superconducting Linear Accelerator (MESA) is under construction. To investigate the potential of an ICS experiment at MESA, the task was given to conduct a feasibility study for ICS at MESA.
In this thesis, the mathematical foundation of ICS as a relativistic particle collision between fermions and photons is summarized and derived. On this foundation, a semi-analytical numerical ICS simulation code named Comparse was written. It's principles and focus on performance are described in a chapter of it's own. Three positions in the accelerator layout possibly suitable for an ICS experiment were identified in the plans and beam line simulations according to which MESA is currently under construction. Using beam parameters in these locations, a number of ICS performance studies were conducted with Comparse. Through various investigated implementation scenarios, a detailed picture of MESA's potential as the driver for a ICS gamma source is formed.
We have shown that with minimal effort, MESA can drive a $\overline{E}'_{ph} > 200\,\mathrm{keV}$ or $\lambda_\gamma < 6.2\,\mathrm{pm}$ photon source with a flux of at least $\mathfrak{F}_\gamma > 14\,000$ ph/s. At the other end of the scale, assuming moderate modifications to the MESA beamline and an amplified $\lambda = 193\,\mathrm{nm}$ laser, we project the potential for a $\mathfrak{F}_\gamma > 5 \cdot 10^8$ ph/s gamma source above 1 MeV photon energy. Finally, we present various aspects of ICS experiment that impact the performance, including polarization effects.
With this thesis, we have thus provided a rare comprehensive review of the interdependence of the ICS behavior between polarization, scattering and incident angles as well as recoil and momentum distribution.

Zusammenfassung

In den letzten Jahren erfuhr Compton Rückstreuung, Inverse Compton Scattering (ICS) in Englisch, vermehrt Interesse von Forschungszentren mit Teilchenbeschleunigeranlagen. Im Blick ist hierbei das Potential von Compton Rückstreuungsexperimenten als Gammastrahlenquelle oder Strahldiagnostikwerkzeug. Mit ihrem niedrigen Wechselwirkungsquerschnitt liegt die Nutzung von ICS in Energie-Rückgewinnungs-Linearbeschleuniger, Energy Recovery Linacs (ERL) im Englischen, nahe, da ERL Anwendungen mit möglichst geringem Einfluss auf die beschleunigten Teilchen erfordern. Andersweitig sinkt die Energierückgewinnungseffizienz.
An der Johannes Gutenberg-Universität Mainz befindet sich der Mainz Energy Recovering Superconducting Linear Accelerator, genannt MESA, im Bau. Um das Potential von ICS Experimenten an MESA zu erforschen wurde eine Machbarkeitsstudie in Auftrag gegeben.
Die Dissertation beginnt mit der Herleitung und Zusammenfassung der mathematischen Grundlagen von ICS als relativistischer Teilchenstoßprozess. Darauf aufbauend wurde ein semianalytischer Numeriksimulationscode namens Comparse geschrieben, mit dem sich ein eigenes Kapitel befasst. Hier werden die Entwicklungsprinzipien und die Umsetzung mit Priorität auf schneller Performanz erklärt. In der MESA Strahlführung wurden drei Orte ausgemacht an denen wir eine experimentelle Umsetzung von ICS für möglich halten. Die Kriterien hierfür sind zum einen ausreichender Platz in den Experimentierhallen und zum anderen geeignete Elektronenparameter in den bestehenden Strahldynamiksimulationen ohne zusätzliche Fokuselemente. Mit für diese Orte simulierten Elektronenpaketen wurden ICS Simulationensstudien in Comparse durchgeführt. Dabei wurden verschiedene Umsetzungsszenarien in Betracht gezogen und so der Bereich des Machbaren betreffend ICS an MESA ausgeleuchtet.
Wir konnten zeigen, dass mit geringem Aufwand, mit MESA eine $\overline{E}'_{ph} > 200\,\mathrm{keV}$, das entspricht $\lambda_\gamma < 6.2\,\mathrm{pm}$, ICS Photonenquelle betrieben werden kann, bei der mehr als $\mathfrak{F}_\gamma > 14\,000$ Photonen pro Sekunde emittiert werden. Mit moderaten Veränderungen an MESA und einem optisch verstärktem $\lambda = 193\,\mathrm{nm}$ Laser öffnet sich das Potential für eine $\mathfrak{F}_\gamma > 5 \cdot 10^8$ ph/s Gammaquelle mit Photonenenergien über 1 MeV. Zuletzt wird der Einfluss von verschiedenen Aspekten des Experimentaufbaus auf die ICS Leistung anhand weiterer Studien präsentiert. Auch polarizationseffekte verschiedener Art werden hier berücksichtigt. Diese Doktorarbeit vermittelt einen selten detaillierten Überblick über die Wechselwirkungen und Abhängigkeiten von Comptonrückstreuung mit Polarisierung, Kollisions- und Streuwinkel sowie Rückstoß und Impulsverteilung.

Contents

1. Abbreviations, Constants and Notation

States	
x	before scattering
x'	after scattering
x^*	Lorentz transformed

Scalars, Vectors and Matrices	
E_{ph}, k_0, k	photon energy
$\vec{k}$	photon 3D momentum
$\mathbf{k}$	photon four-vector momentum
k_x, k_1	horizontal photon momentum component
k_y, k_2	vertical photon momentum component
k_z, k_3	longitudinal photon momentum component
E_{el}, p_0	electron energy
$\vec{p}$	electron 3D momentum
$\mathbf{p}$	electron four-vector momentum
p_x, p_1	horizontal electron momentum component
p_y, p_2	vertical electron momentum component
p_z, p_3	longitudinal electron momentum component
$\boldsymbol{S}$	Stokes Vector of fermion beam
$\boldsymbol{Q}$	Stokes Vector of detected radiation
$\boldsymbol{P}$	Stokes Vector of incident laser beam
S_0, I	Stokes Vector Intensity
S_1	Stokes Vector $\boldsymbol{S}$ degree of transversal polarization
S_2	Stokes Vector $\boldsymbol{S}$ degree of transversal polarization at an angle $\frac{\pi}{4}$
S_3	Stokes Vector $\boldsymbol{S}$ degree of circular polarization
$\vec{S}$	polarization components (S_1, S_2, S_3) of Stokes Vector $\boldsymbol{S}$
$\mathbf{T}$	Stokes Transformation Matrix for ICS
$\mathbf{M}_{rot}$	Euler rotation matrix

Statistics	
N_{par}	number of particles in distribution
M_{par}	macro factor of particle distribution

$\mathfrak{F}_\gamma$	scattered photon flux [ph/s]
$\mathfrak{N}_{ph}$	expected average number of scattering photons
$\mathfrak{L}_\gamma$	ICS luminosity [1/(cm^2 s)]
$\overline{E}$	average energy
σ_{KN}	Klein-Nishina Cross Section
σ_{ics}	Inverse Compton Scattering Cross Section
W	polarization dependent Compton Scattering probability

Other Physical Variables

r_{par}	$(x_{par}, y_{par}, z_{par})$ fermion position in laboratory frame
s	longitudinal position in electron beam path
$\sigma_{el,z}$	longitudinal bunch size / bunch length [µm] or [ps]
$\sigma_{el,x/y}$	transversal bunch size / bunch length [µm] or [ps]
$\sigma_{ph,x}$&$\sigma_{ph,y}$	Gaussian laser beam spot size
w_0	laser focal beam waist $w_0 = \sqrt{\sigma_{ph,r}^2 + \sigma_{ph,y}^2}$
$\sigma_{ph,z}$	longitudinal laser pulse size / pulse length [µm] or [ps]
E_0	particle rest energy $E_0 = mc^2$
$E_{el,ref}$	kinetic energy of the reference electron
σE	energy spread
λ	wavelength
$\Delta\lambda$	spectral bandwidth
$\epsilon_{x/y,n}$	normalized transversal emittance in x or y coordinates
ν_{RF}	electron bunch repetition rate
$\nu_{ph,rep}$	laser pulse repetition rate
I_{el}	electron beam current
E_{pulse}	laser pulse energy
Q_{el}	electron bunch charge

Simulation Parameters

ρ_ϕ	density of azimuthal angles ϕ in a spherical coordinate direction grid
ρ_θ	density of orbital angles θ in a spherical coordinate direction grid
$N_{t,input}$	number of time steps used in temporally dynamic simulation
$\Delta\overline{N}_c$	Comparse condition for what change in mean scattering particles $\overline{N}_{par}$ is still considered static
$n_{sim,c}$	Comparse condition for how many iterative simulations need to be considered static
T_{ics}	real time equivalent of number of simulated ICS collisions
$\boldsymbol{i}$	array of particle indices in simulated distribution
n_{sim}	number of fermion bunch - photon pulse collisions simulated
T_{obs}	period of observation

Meaning of Indices	
el	electron
pr	proton
par	fermion with undefined type (el, pr)
ph	photon
inc	incident or initial state of the experiment
sc	scattering
lab	Laboratory Frame
erf	Electron Rest Frame or Fermion Rest Frame
cmf	Center of Mass System or Center Mass Frame
ref	reference
$norm$	normalized
col	collimated or collimator
los	lost (due to collimation or ICS impact)
rep	repetition
ff	far field
obs	observation
max	maximum
ts	time static
tv	time variable

Physical Constants [1], [2]	
c	Speed of Light in Vacuum: $299\,792\,452\,\mathrm{m\,s^{-1}}$
h	Planck's Constant: $6.626\,070\,15 \times 10^{-34}\,\mathrm{J\,s}$
$\hbar$	Reduced Planck's Constant: $1.054\,571\,817 \times 10^{-34}\,\mathrm{J\,s}$
e	Elementary Charge: $1.602\,176\,46 \times 10^{-19}\,\mathrm{A\,s}$
m_e	Rest Mass of the Electron: $0.510\,998\,90\,\mathrm{MeV\,c^{-2}}$

2. Introduction to Inverse Compton Scattering at MESA

The Institute for Nuclear Physics (KPH) of the Johannes Gutenberg University (JGU) Mainz has a history of successful particle accelerator research, development and operation. Available to experimenters since 1979, the Mainz Microtron (MAMI) race track electron accelerator, was gradually upgraded and modified over the years. At this time, MAMI can deliver an electron beam energy of 160 MeV to 1.6 GeV at 100 µA with optional polarization. While experiments A2 and X1, concerning tagged photons and detector tests, are ongoing, the A4 experiment has concluded and it's underground facilities provide an excellent opportunity for a new experiment. For this reason, a smaller scale accelerator based on novel designs was conceptualized: The Mainz Energy Recovering Superconducting Linear Accelerator "MESA". The following description of MESA was written on the basis of the summarized works of [3–8] in no particular order.
For MESA, the electron beam will be generated by the synchronized rf DC photoguns. While the Small Thermalised Electron Source (STEAM) can only generate $I_{el} = 150$ to 1000 µA, it also allows for spin polarization above 85% efficiency by utilizing superlattice GaAs photocathodes. The MESA Inverted Source Two (MIST) on the other hand, does not allow for spin tuning, but uses multi alkali K_2CsSb based photocathodes to generate an electron flux of up to $I_{el} = 10$ mA. From there, MELBA transports the free electrons to their first acceleration step in the Milli-Ampere Booster MAMBO. For spin fine tuning in conjunction with STEAM, the MESA Low-energy Beam Apparatus (MELBA) is equipped with two Wien filters and one solenoid to rotate the polarization of the spin polarized electron beam in space. The MAMBO acceleration section is made up of four normal conducting biperiodic $\frac{\pi}{2}$ rf cavities of which only the first is β graded to adapt to the increasing electron velocity. Per section, MAMBO accelerates an electron bunch by $\Delta E_{el} = 1.25$ MeV, resulting in a net sum kinetic electron energy E_{kin} of 5 MeV at the end of the low energy beam transport section of MESA. To further accelerate the electron bunches, MESA uses $\Delta E_{el,ref} = 25$ MeV ELBE-type cryomodules containing two 9-cell TESLA RF cavities in it's recirculated main accelerator section.
MESA is being built to run in two modes of operation for two respective experiments. In the Extracted Beam (EB) mode, the electron beam goes through each cavity thrice before being extracted from the main recirculation and entering the External Beamline. Then, at $E_{el} = 155$ MeV, the electron beam is used in the P2 experiment. Here, high-precision measurements of the Weinberg mixing angle are taken by detecting parity violations (PV) of electron-proton scattering in the elastic

regime. Afterwards, the electron bunches come to a stop in the P2 beam dump, which in itself is part of another experiment, called Dark MESA which runs parasitically while the P2 experiment is active [8]. Bremsstrahlung processes inside of the beam dump can result in the generation of a dark photons that can decay into dark matter particles ($\gamma' \rightarrow \chi\overline{\chi}$ which are then detected by the Dark Mesa calorimeter system. As the External Beamline and P2 are designed for $I_{el} = 150\,\mu A$, $E_{el} = 155\,MeV$ electron bunches, no pion production is expected, which should ensure, that the detected background is mainly composed off of cosmic background radiation.
In the energy-recovery (ER) mode, a beam current of $I_{el} = 1\,mA$ in MESA construction phase1 and 10 mA in phase 2 will be accelerated to an energy of 105 MeV. The path diverges from the EB mode after two recirculations. Here, the beam line leads through the MESA Gas Internal Target Experiment (MAGIX) where electron bunches interact with a gas jet of customizable makeup ranging from hydrogen up to xenon to investigate proton radii and search for particles beyond the standard model. The MAGIX section of the beam line leads back into the recirculation but introduces a 180° phase shift. After the experiment, the spent electron bunches re-enter the accelerating cavities with the now introduced phase shift of 180° with respect to the RF field. Now synchronized to the cavity RF in deceleration phase, the electron beam energy transfers back to the cavity's RF fields by $\Delta E_{el} = 25\,MeV$ per cryomodule. After passing through the cryomodules twice, this leaves only 5 MeV, the injection energy, to be disposed at the ER beam dump. The higher beam current is possible only in ER mode, as it reliefs the limited RF budget by the relativistic electron energy re-transferred to the cavity's EM field [9]. Energy-recovering accelerators can be an economic solution if bunch quality degradation is low enough to safely reuse post experiment particles.

Alongside MAGIX, an experiment that allows for energy recovery could be Inverse Compton Scattering (ICS). It can be described as either a two particle collision between a photon and a relativistic fermion or as a fermion being excited by an electromagnetic field. The partial descriptor "inverse" differentiates ICS from the standard Compton Effect [10], in which a photon scatters on free electrons. In the inverse Compton effect, a relativistic charged particle interacts with a photon of lower kinetic energy. The transfer of energy goes from the fermion to the photon and leads to the scattered photon having a shorter wavelength corresponding to the energy loss of the fermion. The energy of the scattered gamma radiation can potentially reach a maximum of $E'_{ph,max} = 4\gamma^2 E_{ph}$, a significant increase over the initial photon energy E_{ph} defined by the Lorentz factor γ of the accelerated fermion. Typically, the cross section for this scattering event is given by the classical Thomson cross section $\sigma_{Th} = \frac{8\pi}{3} r_e^2 \approx 6,6524587321 \cdot 10^{-29}\,m^2$ [2]. This is equal to about 0.665 b and constitutes a constant approximation of a variable that depends on a multitude of factors. As part of this thesis, a thorough investigation of the Compton cross section in simulation studies (sec. 5.1) and mathematical derivations (sec. 3.2&4.5.2) will be presented. These will convey the complexity and interdepence of

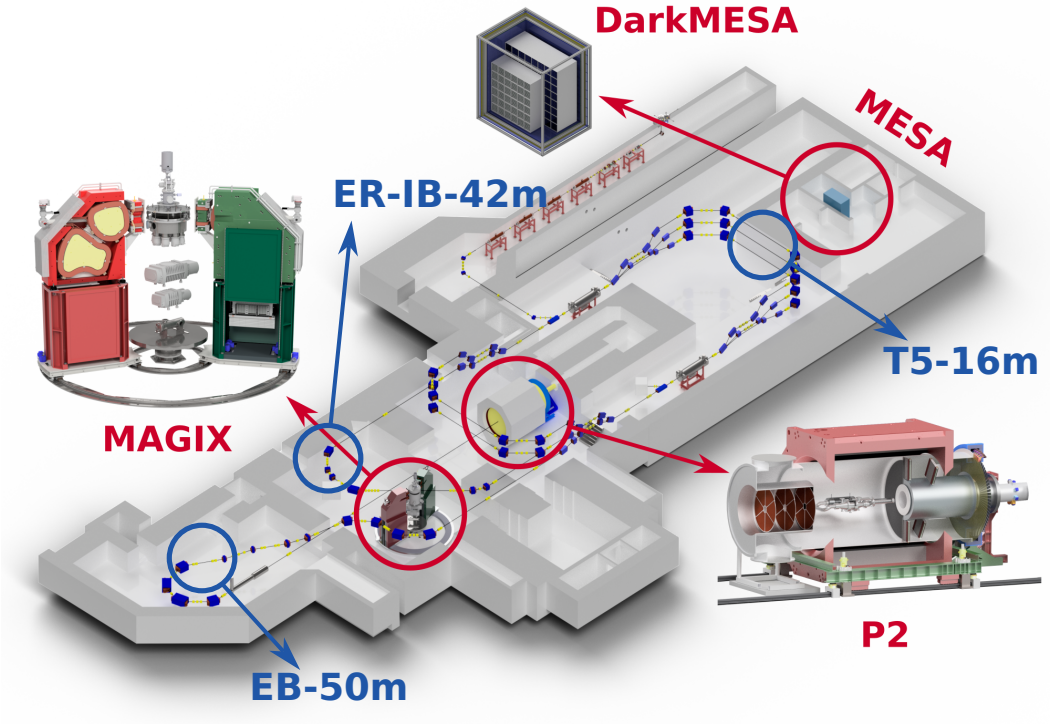

Figure 2.1.: MESA layout as planned and under construction in 2024 with highlighted experiments P2, Magix and DarkMESA. Figure taken from Figure 1. of [5]. Additionally, the 3 beam line locations investigated for this study, ER-IB-42m, T5-16m and EB-50m, have been highlighted in blue.

the Inverse Compton Cross section in a variety of scenarios.

2.1. Thomson, Compton and Inverse Compton Scattering

An attentive reader may wonder why the cross section for Inverse Compton Scattering is given by the Thomson cross section. The reason for that is, that in a simplified model, these terms describe the same process. Thomson scattering is understood to refer to the low fermion energy scenario of Compton scattering, where a free resting charged particle is excited by electromagnetic (EM) radiation, causing it to emit a photon of the same energy but different trajectory [11]. It can thus be described as an elastic collision between a photon and a fermion, as the fermion's rest energy is considerably higher than the energy transferred in the scattering process. Due to the low impact nature of the collision/excitation, the fermion must be in an unbound state to be affected.
We no longer refer to Thomson scattering, but Compton scattering instead, when a measurable recoil is exchanged between photon and fermion. Classically, a free

fermion at rest before the collision is transferred a fraction of the photon's momentum, which results in a net positive kinetic fermion energy corresponding to a lengthened photon wavelength. This recoil X can be estimated as $X = \frac{4E_{ph}}{m_{par}c^2}$, however, in a later chapter, we will present a more accurate expression in section 3.1.3. The energy transfer is strongly dependent on the scattering angle θ between the initial and emitted photon.
Finally, inverse Compton scattering refers to the scenario, in which the free fermion is not at rest. If it possess a significant velocity, then the energy transfer inverts and the emitted photon has a higher energy than the initial one. This is the scenario described above and what we will refer to when talking about ICS or even just Compton scattering in this thesis.
With it's low cross section, ICS is an ideal candidate for an ERL, where experiments destructive to the electron beam are impractical and the high intensity, high brilliance beam current is required for meaningful scattered photon statistics. In this thesis. we will investigate the potential ICS experiment conditions possible at MESA, the impact of various ICS implementations on the electron beam as well as the quality and quantify of the scattered gamma radiation. This work represents the foremost comprehensive theoretical investigation of Inverse Compton Scattering at the JGU Mainz.

2.2. Thesis Structure

This thesis is organized as follows.
Chapter 2 concludes the introduction to ICS feasibility studies at MESA.
In Chapter 3, the theoretical background of ICS as a relativistic collision between a fermion and a photon of variable momentum and polarization direction is given.
Chapter 4 introduces the semi analytical simulation code written to conduct ICS studies named Comparse. The chapter gives an overview of the program and explains the key implementation concepts.
Chapter 5 represents the purpose of this work. In it, a number of detailed ICS scenario studies are presented for MESA and valued for potential performance and feasibility. Additionally, the practical limitations and fringe cases of ICS experiments are studied on the basis of MESA and other particle accelerators. Among the investigated topics are the effects of incident angles and polarization as well as the potential and limitations of pinhole collimators as a spectrum improvement component.
Lastly, chapter 6 concludes the thesis by a giving one last summary of the conducted studies.

3. Theory of Inverse Compton Scattering

Inverse Compton Scattering can be understood as a polarization dependent elastic particle collision between a photon distribution and an ultrarelativistic free electron bunch. Within the limits of this interpretation, this chapter aims to provide a mathematically complete path from the initial to the scattered state. It will require the introduction of a number of different reference systems and concepts. We will start at the micro level with the single photon - electron collision at predetermined incoming and outgoing scattering angles and only afterwards zoom out to the macro level, where we describe the mathematical approach of determining which photon scatters into what direction and the effect electron and photon polarization has on the process. In this chapter, we will explain Compton scattering between electrons and photons. Note, however, that similar scattering processes can occur between protons and photons. As the software written for this thesis, Comparse, can accommodate both electrons and protons for all calculations, we will refer to fermions instead, when writing about its functions in chapter 4.

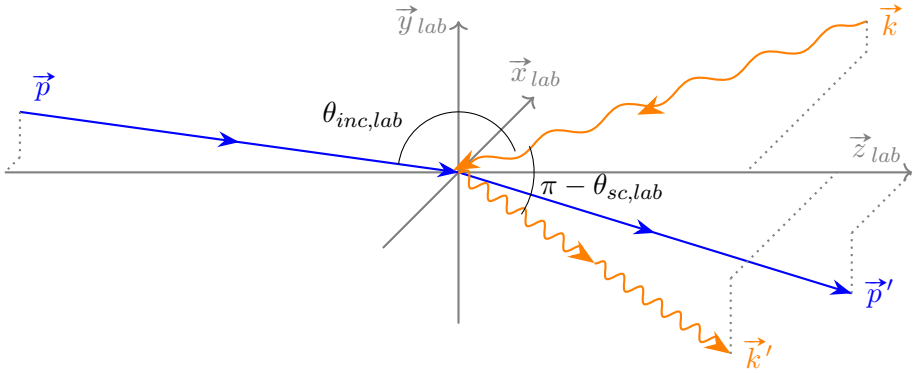

Figure 3.1.: Compton scattering with angles in the Laboratory Frame

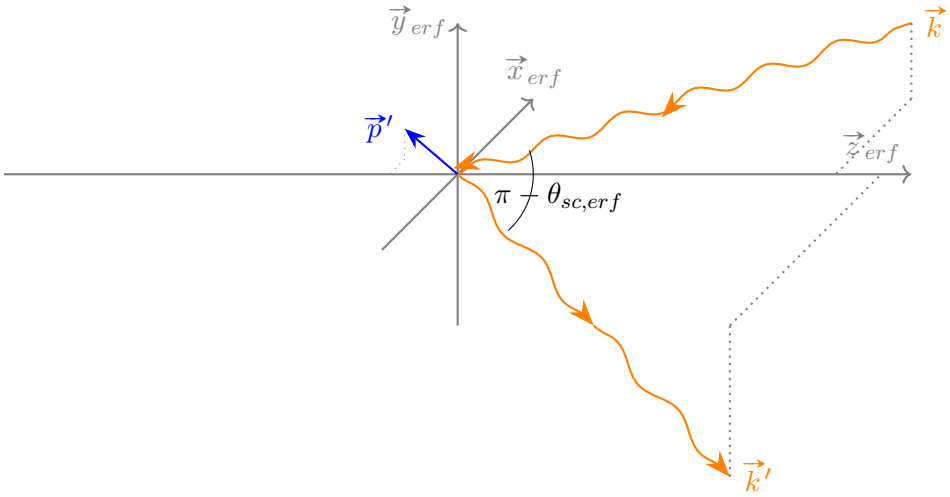

Figure 3.2.: Compton scattering with angles in Electron Rest Frame. Note that for historical reasons, this system is named in reference to electrons in this thesis. Despite the name, the mathematical principles can be applied to fermions in general, namely protons.

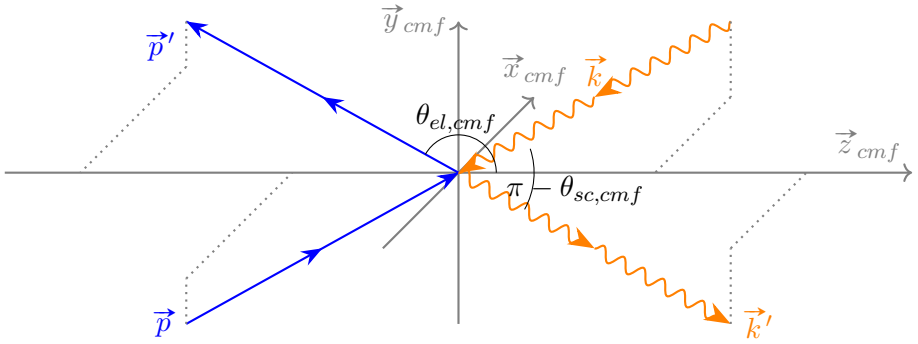

Figure 3.3.: Compton scattering with angles in Center of Mass Rest Frame

3.1. Relativistic Collision Kinematics

In the physical framework of the particle aspect of photons, an electron - photon interaction can be mathematically expressed as an elastic collision following the rules of kinematics.

3.1.1. Four-Vector Energy Expression

Using Cartesian coordinates, both electron and photon relevant attributes can be expressed in the four-vector notation as four-momenta: [12]

$$\mathbf{v}_{el} \equiv \mathbf{p} \equiv \begin{bmatrix} cp_0 \\ cp_1 \\ cp_2 \\ cp_3 \end{bmatrix} = \begin{bmatrix} E_{el} \\ p_x \\ p_y \\ p_z \end{bmatrix} \quad \text{and} \quad \mathbf{v}_{ph} \equiv \mathbf{k} \equiv \begin{bmatrix} k_0 \\ k_1 \\ k_2 \\ k_3 \end{bmatrix} = \begin{bmatrix} E_{ph} \\ \hbar c k_x \\ \hbar c k_y \\ \hbar c k_z \end{bmatrix} \tag{3.1}$$

Per definition, the length of a general four-vector $\mathbf{v} = (v_0, v_1, v_2, v_3)$ is:

$$|\mathbf{v}| \equiv v_o^2 - v_1^2 - v_2^2 - v_3^2 \tag{3.2}$$

Applied to the electron and photon in eq. 3.1, we obtain:

$$\begin{aligned} |\mathbf{v}_{el}| &\equiv E_0 \\ |\mathbf{v}_{ph}| &\equiv 0 \end{aligned} \tag{3.3}$$

We write the photon momentum four-vector with a $\mathbf{k}$, due to it's direct relation to the photon wave four-vector $k = \frac{2\pi}{\lambda}$ through $\mathbf{p}_{ph} = \hbar\mathbf{k}$.
The absolute length of a four-vector can be interpreted as the inner energy or rest mass of the respective particle. Importantly, this value is conserved under any rotation or transformation of the four-dimensional coordinate system such as Lorentz transformations, which are of particular relevance to this work.
Using k for the photon momentum simplifies the differentiation to the fermion momentum four-vector $\mathbf{p}$ as we don't have to specify the particle type through indices alike to $\mathbf{p}_{ph}$ and $\mathbf{p}_{el}$. Regarding the notation of thesis, be aware that four-vectors are written in bold, such as $\mathbf{p}_{el}$, while momentum vectors with only 3 spatial components are written with a vector arrow above, as $\vec{p}$. Given that the p_0 , k_0 energy component of the four-vector accounts for relativity in Lorentz transformations, we can now express the conservation of energy through four-momenta before ($\mathbf{p}$, $\mathbf{k}$) and after scattering ($\mathbf{p}'$, $\mathbf{k}'$) in any reference system by:

$$\mathbf{p} + \mathbf{k} = \mathbf{p}' + \mathbf{k}' \tag{3.4}$$

This is one of the six Lorentz invariants that can be constructed in four-vector scattering kinematics. They will be explored in the next section 3.1.2. With known emitted photon direction, we can express the scattered state of both electron and photon as a combination of their initial state four-vectors and the scattering direction. This description is variable in various reference systems, as shown in figures 3.1, 3.2 and 3.3.

3.1.2. Retreading Kinematic Invariants of Four-Vector Particle Scattering

The conservation of four-momentas in a scattering process does not require one to distinguish between initial and final particles for the general equation to hold true [13].

$$\mathbf{q}_1 + \mathbf{q}_2 + \mathbf{q}_3 + \mathbf{q}_4 = 0 \tag{3.5}$$

where $\mathbf{q}_i$ are the momentum four-vectors and $\mathbf{q}_i^2 = m_a^2$ are the particle mass squares for a given particle type. Eq. 3.5 leaves any of the four-vectors $\mathbf{q}_i$ dependent on the three other independents. Since no specific identity has been assigned yet, we can let $\mathbf{q}_1$,$\mathbf{q}_2$ and $\mathbf{q}_3$ be the ambiguous three four-momentas with which we define the six invariants $\mathbf{q}_1^2, \mathbf{q}_2^2, \mathbf{q}_3^2, \mathbf{q}_1\mathbf{q}_2, \mathbf{q}_1\mathbf{q}_3, \mathbf{q}_2\mathbf{q}_3$ of which the latter three are bound by the relation

$$(\mathbf{q}_1 + \mathbf{q}_2 + \mathbf{q}_3)^2 = \mathbf{q}_4^2 = m_4^2 \tag{3.6}$$

that can be used to express the three symmetric invariants s, t, u

$$\begin{aligned} s &= (\mathbf{q}_1 + \mathbf{q}_2)^2 = (\mathbf{q}_3 + \mathbf{q}_4)^2 \\ t &= (\mathbf{q}_1 + \mathbf{q}_3)^2 = (\mathbf{q}_2 + \mathbf{q}_4)^2 \\ u &= (\mathbf{q}_1 + \mathbf{q}_4)^2 = (\mathbf{q}_2 + \mathbf{q}_3)^2 \end{aligned} \tag{3.7}$$

that are related to quantity

$$h = m_1^2 + m_2^2 + m_3^2 + m_4^2 \tag{3.8}$$

the square sum of the individual particle masses by

$$s + t + u = h \tag{3.9}$$

When assigning parameters of index 1 and 2 as colliding particles, invariant s represents the square of the total energy in the two-particle center of mass rest frame where $\vec{p_1} + \vec{p_2} = 0$. We shall use invariant mass s to construct recoil factor X, a measure of the transferred energy between electron and photon, as one of the key parameters of our ICS scattering calculation. It will be used in place of terms of multiple variables in many of the equations that the simulations described in this thesis are built upon.

Special Case: Electron & Photon

An electron - photon collision described as four-momenta $\mathbf{p}$ & $\mathbf{k}$ before and after scattering by $\mathbf{p} + \mathbf{k} = \mathbf{p}' + \mathbf{k}'$ allows us to express the previously defined invariants via the electron rest mass E_0. Thus, in eq. 3.7, s, u and t become

$$s = (\mathbf{p} + \mathbf{k})^2 = (\mathbf{p}' + \mathbf{k}')^2 = E_0^2 + 2\mathbf{pk} = E_0^2 + 2\mathbf{p}'\mathbf{k}' \tag{3.10}$$

$$t = (\mathbf{p} - \mathbf{p}')^2 = (\mathbf{k}' - \mathbf{k})^2 = 2(E_0^2 - \mathbf{pp}') = -2\mathbf{kk}' \tag{3.11}$$

$$u = (\mathbf{p} - \mathbf{k}')^2 = (\mathbf{p}' + \mathbf{k})^2 = E_0^2 - 2\mathbf{pk}' = E_0^2 - 2\mathbf{p}'\mathbf{k} \tag{3.12}$$

and as a photon possesses no mass. eq. 3.8 sums to

$$h = 2E_0^2 \tag{3.13}$$

The path to the post-scattering results requires several relativistic Lorentz transformations and starts with the relative energy $\gamma_{el,lab}$ [14] derived from the electron energy of the accelerated beam in the laboratory frame divided by the electron rest energy:

$$\gamma_{el,lab} = \frac{E_{el,lab}}{m_e c^2} \tag{3.14}$$

3.1.3. Deriving ICS Recoil

From the general scattering formulation of s in eq. 3.7, an expression for an electron - photon pair has been derived as outlined below. Let

$$\mathbf{p} \equiv \begin{bmatrix} \frac{E_{el}}{c} \\ p_x \\ p_y \\ p_z \end{bmatrix} \quad \text{and} \quad \mathbf{k} = \begin{bmatrix} \frac{h\nu}{c} \\ \hbar k_x \\ \hbar k_y \\ \hbar k_z \end{bmatrix} \tag{3.15}$$

with absolute energy E_{el} and electron rest energy $E_0 = m_e c^2$

$$\begin{aligned} E_{el}^2 &= E_x^2 + E_y^2 + E_z^2 + E_0^2, \\ &= (p_x c)^2 + (p_y c)^2 + (p_z c)^2 + m_e^2 c^4 \end{aligned} \tag{3.16}$$

and photon

$$\begin{aligned} h^2\nu^2 &= (\hbar k_x c)^2 + (\hbar k_y c)^2 + (\hbar k_z c)^2, \\ &= \left(\hbar \vec{k}\right)^2 \end{aligned} \tag{3.17}$$

whereas $\vec{p}$ is pointing in opposite direction of $\vec{k}$. Now, invariant mass s can be expressed as

$$\sqrt{s} = \sqrt{c\mathbf{p}_s \cdot c\mathbf{p}_s} \tag{3.18}$$

where $\mathbf{p}_s = \mathbf{p} + \mathbf{k}$. Because of the direction of $\vec{p}$ and $\vec{k}$, $\mathbf{p}_s^2$ is

$$\mathbf{p}_s = \left[\frac{E_{el} + h\nu}{c}, (p_x - \hbar k_x), (p_y - \hbar k_y), (p_z - \hbar k_z)\right] \tag{3.19}$$

which when squared produces four-vector product

$$(\mathbf{p}_s)^2 = \left(\frac{E_{el} + h\nu}{c}\right)^2 - (p_x - \hbar k_x)^2 - (p_y - \hbar k_y)^2 - (p_z - \hbar k_z)^2 \tag{3.20}$$

Solving the square of each four-vector and moving c^2 to the left side of the equation gives us

$$\begin{aligned} (c\mathbf{p}_s)^2 = E_{el}^2 + h^2\nu^2 + 2h\nu E_{el} - \overbrace{c^2(p_x^2 + p_y^2 + p_z^2)}^{E_{el}^2 - E_0^2} - \overbrace{c^2\hbar^2(k_x^2 + k_y^2 + k_z^2)}^{h^2\nu^2} \\ + 2\hbar c^2(k_x p_x + k_y p_y + k_z p_z) \end{aligned} \tag{3.21}$$

Factoring out E_0 brings the equation to the form of

$$(c\mathbf{p}_s)^2 = E_0^2\left[\frac{2h\nu E_{el}}{E_0^2} + 1 + \frac{2\hbar c^2}{E_0^2}(k_x p_x + k_y p_y + k_z p_z)\right] \tag{3.22}$$

Let's recall 3.18 to arrive at the final shape, for our purposes, of the invariant mass s expression

$$\sqrt{s} = \sqrt{(c\mathbf{p}_s)^2} = E_0\sqrt{1 + \frac{2h\nu\gamma_{lab}}{E_0} + \frac{2\hbar c^2}{E_0^2}(k_x p_x + k_y p_y + k_z p_z)} \tag{3.23}$$

We will call the specific electron and laser beam parameter dependent parts of 3.23 recoil factor X for convenient repeated use in further calculations.

$$\boxed{X \equiv \frac{2h\nu\gamma_{lab}}{E_0} + \frac{2\hbar c^2}{E_0^2}(k_x p_x + k_y p_y + k_z p_z)} \tag{3.24}$$

Which shortens 3.23 to

$$\sqrt{s} = E_0\sqrt{1+X} = E_{cmf} \tag{3.25}$$

s and by extension X is, as a Lorentz invariant, constant under arbitrary Lorentz transformation and can be used in any reference system.

3.1.4. Center of Mass Frame Parameters

To bring the electron and photon four-vectors into the center of mass frame (CMF) where the analytical solution to the quasi-elastic collision is easy to express via energy-momentum-conservation, we first require the relativistic Lorentz factor of the respective system's center mass system, meaning the total combined kinetic and rest energies of both particles. This is calculated via the combined electron and photon energies

$$\boxed{\gamma_{cmf} = \frac{E_{lab}}{E_{cmf}} = \frac{E_{el} + h\nu}{m_e c^2\sqrt{1+X}} \approx \frac{\gamma_{lab}}{\sqrt{1+X}}} \tag{3.26}$$

Other parameters that we need to bring into the CM system are total electron energy E_{el}, total photon energy $E_{ph} = h\nu$ and the scattering (= observation) angle θ_{ph}. Due to the multitude of ways one can interpret the term "scattering angle", we will use the term "observation angle" when talking about the angle between the scattered photon and the laboratory system's longitudinal z-axis. To limit the length of the following equations, observation angle $\theta_{ph,lab}$ will be shortened to θ and the Lorentz transformed $\theta_{ph,cmf}$ to θ^*. Both are plotted alongside the the corresponding scattering momenta in figures 3.1 and 3.3.
Let us start by expressing the Lorentz transformed observation angle θ^* by the reference system's gamma factor γ_{cmf} and the laboratory observation angle θ:

$$\boxed{\cos\theta^* = \frac{-\gamma_{cmf}\sqrt{\gamma_{cmf}^2 - 1}\tan^2\theta \pm \sqrt{1+\tan^2\theta}}{1+\gamma_{cmf}^2\tan^2\theta}} \tag{3.27}$$

where " $\pm$ " := " $+$ " if $\theta < \frac{\pi}{2}$ and " $\pm$ " := " $-$ " if $\theta > \frac{\pi}{2}$ [15]. Due to momentum conservation in the center of mass frame, the scattered electron moves in opposite direction of the photon:

$$\theta_{el}^* = \pi - \theta_{ph}^* \tag{3.28}$$

3.1.5. Energy Conservation in Center of Mass Frame

The inherent momentum symmetry of the CMF, as discussed in section 3.1.2 allows the expression of the electron and photon energy and total momentum as relations that hold before and after scattering:

$$\vec{p}_{tot} = \vec{p} + \hbar\vec{k} = 0 \rightarrow |\vec{p}^{*}| = \hbar\left|\vec{k}^{*}\right| \tag{3.29}$$

$$E^{*}_{ph} = E_{cmf} - E^{*}_{el} = m_e c^2\sqrt{1+X} - E^{*}_{el} = h\nu^{*} \tag{3.30}$$

The energy of a photon, due to it having no mass and therefore rest energy, can be expressed solely by it's absolute momentum $|\vec{k}|$:

$$h\nu^{*} = \hbar\left|\vec{k}^{*}\right| c = |\vec{p}^{*}|\, c \tag{3.31}$$

Analogously, the electron energy is:

$$E^{*}_{el} = \sqrt{m_e^2 c^4 + |\vec{p}^{*}|^2\, c^2} \tag{3.32}$$

Starting with 3.30, 3.31 and 3.32, we can express the scattered photon energy in the center of mass frame $h\nu^{*}$ via recoil factor X and electron rest energy $E_0 = m_e c^2$ after a few mathematical steps:

$$\begin{aligned}
h\nu^{*} &= E_0\sqrt{1+X} - \sqrt{E_0^2 + h^2\nu^{*2}} && |\rightleftarrows \\
E_0\sqrt{1+X} - h\nu^{*} &= \sqrt{E_0^2 + h^2\nu^{*2}} && |^2 \\
E_0^2(1+X) - 2E_0 h\nu^{*}\sqrt{1+X} + h^2\nu^{*2} &= E_0^2 + h^2\nu^{*2} && |-h^2\nu^{*2}, \rightleftarrows \\
E_0(1+X) - E_0 &= 2h\nu^{*}\sqrt{1+X} && |E_0(), \frac{1}{2\sqrt{1+X}} \\
E_0[(1+X)-1]/2\sqrt{1+X} &= h\nu^{*} && |1-1=0 \\
\boxed{m_e c^2 \frac{X}{2\sqrt{1+X}} = h\nu^{*}} & && |E_0 = m_e c^2
\end{aligned} \tag{3.33}$$

The absolute values of the momenta $|\vec{p^{*}_e}|$ and $\hbar|\vec{k^{*}_{ph}}|$ can also easily be derived from eq. 3.33 with $p = \frac{E}{c}$.

$$|\vec{p}^{*}_e| = m_e c \frac{X}{2\sqrt{1+X}} = |\vec{k}^{*}_{ph}| \tag{3.34}$$

Using eq. 3.33's expression of the scattered CMF photon energy and by recalling eq. 3.30, we can construct a similar expression for E^*_{el}:

$$\begin{aligned}
E^*_{el} &= E_0\sqrt{1+X} - E_0\frac{X}{2\sqrt{1+X}} && |\rightleftarrows \\
&= E_0\left(\sqrt{1+X} - \frac{X}{2\sqrt{1+X}}\right) && |\text{insert}\frac{2\sqrt{1+X}}{2\sqrt{1+X}} = 1 \\
&= E_0\left(\sqrt{1+X}\cdot\frac{2\sqrt{1+X}}{2\sqrt{1+X}} - \frac{X}{2\sqrt{1+X}}\right) && |\rightleftarrows \\
&= E_0\left(\frac{2+2X}{2\sqrt{1+X}} - \frac{X}{2\sqrt{1+X}}\right) && |\rightleftarrows
\end{aligned}$$

$$\Rightarrow \boxed{E^*_{el} = m_e c^2\frac{2+X}{2\sqrt{1+X}}} \tag{3.35}$$

For a general observation polar angle $\theta*$ and observation azimuth angle ϕ^* the four-momenta can be constructed in the center of mass frame by using the previously derived absolute momenta and energies for both scattered electron

$$\mathbf{p'}^* = \begin{bmatrix} E^*_{el} \\ p^*_x \\ p^*_y \\ p^*_z \end{bmatrix} = \begin{bmatrix} E^*_{el} \\ |p^*_x|\sin\theta^*_e\cos\phi^* \\ |p^*_y|\sin\theta^*_e\sin\phi^* \\ |p^*_z|\cos\theta^*_e \end{bmatrix} = \begin{bmatrix} m_e c^2\frac{2+X}{2\sqrt{1+X}} \\ m_e c\frac{X\sin\theta^*_e\cos\phi^*}{2\sqrt{1+X}} \\ m_e c\frac{X\sin\theta^*_e\sin\phi^*}{2\sqrt{1+X}} \\ m_e c\frac{X\cos\theta^*_e}{2\sqrt{1+X}} \end{bmatrix} \tag{3.36}$$

and emitted photon

$$\mathbf{k'}^* = \begin{bmatrix} E^*_{ph} \\ \hbar k^*_x \\ \hbar k^*_y \\ \hbar k^*_z \end{bmatrix} = \begin{bmatrix} m_e c^2\frac{X}{2\sqrt{1+X}} \\ \frac{E^*_{ph}}{c}\sin\theta^*\cos\phi^* \\ \frac{E^*_{ph}}{c} * \sin\theta^*\sin\phi^* \\ \frac{E^*_{ph}}{c}\cos\theta^* \end{bmatrix} = \begin{bmatrix} m_e c^2\frac{X}{2\sqrt{1+X}} \\ m_e c\frac{X\sin\theta^*\cos\phi^*}{2\sqrt{1+X}} \\ m_e c\frac{X\sin\theta^*\sin\phi^*}{2\sqrt{1+X}} \\ m_e c\frac{X\cos\theta^*}{2\sqrt{1+X}} \end{bmatrix} \tag{3.37}$$

3.1.6. Lorentz Transformation From CM to Lab Frame

To transform a four-vector between the lab frame a and a boosted reference system a', one can employ the general Lorentz boost matrix $\mathbf{\Lambda}$.

$$a^* = \mathbf{\Lambda}_{cmf}a \tag{3.38}$$

We will express $\mathbf{\Lambda}_{cmf}$ using the relativistic Lorentz and beta factor of the center of mass frame γ_{cmf} and $\beta_{cmf} = (\beta_x, \beta_y, \beta_z)$:

$$\mathbf{\Lambda}_{cmf} = \begin{pmatrix} \gamma_{cmf} & -\gamma_{cmf}\beta_x & -\gamma_{cmf}\beta_y & -\gamma_{cmf}\beta_z \\ -\gamma_{cmf}\beta_x & 1+(\gamma_{cmf}-1)\frac{\beta_x^2}{\beta_{cmf}^2} & (\gamma_{cmf}-1)\frac{\beta_x\beta_y}{\beta_{cmf}^2} & (\gamma_{cmf}-1)\frac{\beta_x\beta_z}{\beta_{cmf}^2} \\ -\gamma_{cmf}\beta_y & (\gamma_{cmf}-1)\frac{\beta_y\beta_x}{\beta_{cmf}^2} & 1+(\gamma_{cmf}-1)\frac{\beta_y^2}{\beta_{cmf}^2} & (\gamma_{cmf}-1)\frac{\beta_y\beta_z}{\beta_{cmf}^2} \\ -\gamma_{cmf}\beta_z & (\gamma_{cmf}-1)\frac{\beta_z\beta_x}{\beta_{cmf}^2} & (\gamma_{cmf}-1)\frac{\beta_z\beta_y}{\beta_{cmf}^2} & 1+(\gamma_{cmf}-1)\frac{\beta_z^2}{\beta_{cmf}^2} \end{pmatrix} \tag{3.39}$$

To transform back, from a Lorentz boosted reference system to the lab frame, one needs to invert Λ

$$\mathbf{a} = \mathbf{\Lambda}_{cmf}^{-1T} a' = \mathbf{\Lambda}_{lab} a' \tag{3.40}$$

$$\mathbf{\Lambda}_{cmf}^{-1T} = \mathbf{\Lambda}_{lab} = \begin{pmatrix} \gamma_{cmf} & \gamma_{cmf}\beta_x & \gamma_{cmf}\beta_y & \gamma_{cmf}\beta_z \\ \gamma_{cmf}\beta_x & 1+(\gamma_{cmf}-1)\frac{\beta_x^2}{\beta_{cmf}^2} & (\gamma_{cmf}-1)\frac{\beta_x\beta_y}{\beta_{cmf}^2} & (\gamma_{cmf}-1)\frac{\beta_x\beta_z}{\beta_{cmf}^2} \\ \gamma_{cmf}\beta_y & (\gamma_{cmf}-1)\frac{\beta_y\beta_y}{\beta_{cmf}^2} & 1+(\gamma_{cmf}-1)\frac{\beta_y^2}{\beta_{cmf}^2} & (\gamma_{cmf}-1)\frac{\beta_y\beta_z}{\beta_{cmf}^2} \\ \gamma_{cmf}\beta_z & (\gamma_{cmf}-1)\frac{\beta_z\beta_x}{\beta_{cmf}^2} & (\gamma_{cmf}-1)\frac{\beta_z\beta_y}{\beta_{cmf}^2} & 1+(\gamma_{cmf}-1)\frac{\beta_z^2}{\beta_{cmf}^2} \end{pmatrix} \tag{3.41}$$

We derived the two boosted four-vectors after scattering in the CMF that will be inserted for a' in the last subsection in 3.36 and 3.37. Using 3.40, one can now calculate the four-momenta of both electron and photon after scattering in the laboratory frame, $\mathbf{p}'$ and $\mathbf{k}'$.

$$\mathbf{p}' = \mathbf{\Lambda}_{lab} \cdot \mathbf{p}'^{*} =$$

$$\begin{bmatrix} E_{e,s} \\ p_{x,s} \\ p_{y,s} \\ p_{z,s} \end{bmatrix} = \begin{bmatrix} \frac{\gamma_{cmf} m_e c^2}{2\sqrt{1+X}} \left(2 + X + \frac{\beta_x}{c} X \sin\theta_e^* \cos\phi^* + \frac{\beta_y}{c} X \sin\theta_e * \sin\phi^* + \frac{\beta_z}{c} X \cos\theta_e *\right) \\ \gamma_{cmf}\beta_x \frac{E_{el}^*}{c} + \left(1 + \frac{\gamma_{cmf}^2}{\gamma_{cmf}+1}\beta_x^2\right) p_x^* + \frac{\gamma_{cmf}^2}{\gamma_{cmf}+1}\beta_x\beta_y p_y^* + \frac{\gamma_{cmf}^2}{\gamma_{cmf}+1}\beta_x\beta_z p_z^* \\ \gamma_{cmf}\beta_y \frac{E_{el}^*}{c} + \frac{\gamma_{cmf}^2}{\gamma_{cmf}+1}\beta_y\beta_x p_x^* + \left(1 + \frac{\gamma_{cmf}^2}{\gamma_{cmf}+1}\beta_y^2\right) p_y^* + \frac{\gamma_{cmf}^2}{\gamma_{cmf}+1}\beta_y\beta_z p_z^* \\ \gamma_{cmf}\beta_z \frac{E_{el}^*}{c} + \frac{\gamma_{cmf}^2}{\gamma_{cmf}+1}\beta_z\beta_x p_x^* + \frac{\gamma_{cmf}^2}{\gamma_{cmf}+1}\beta_z\beta_y p_y^* + \left(1 + \frac{\gamma_{cmf}^2}{\gamma_{cmf}+1}\beta_z^2\right) p_z^* \end{bmatrix} \tag{3.42}$$

$$\mathbf{k}' = \mathbf{\Lambda}_{lab} \cdot \mathbf{k}'^{*} =$$

$$\begin{bmatrix} E'_{ph} \\ \hbar k'_x \\ \hbar k'_y \\ \hbar k'_z \end{bmatrix} = \begin{bmatrix} \gamma_{cmf}\left(E^*_{ph} + k^*_x c\beta_x + k^*_y c\beta_y + k^*_z c\beta_z\right) \\ \gamma_{cmf}\beta_x \frac{E^*_{ph}}{c} + \left(1 + \frac{\gamma^2_{cmf}}{\gamma_{cmf}+1}\beta^2_x\right)k^*_x + \frac{\gamma^{*2}_{cmf}}{\gamma_{cmf}+1}\beta^*_x\beta_y k^*_y + \frac{\gamma^{*2}_{cmf}}{\gamma_{cmf}+1}\beta_x\beta_z k^*_z \\ \gamma_{cmf}\beta_y \frac{E^*_{ph}}{c} + \frac{\gamma^2_{cmf}}{\gamma_{cmf}+1}\beta^*_y\beta_x k^*_x + \left(1 + \frac{\gamma^{*2}_{cmf}}{\gamma_{cmf}+1}\beta^2_y\right)k^*_y + \frac{\gamma^{*2}_{cmf}}{\gamma_{cmf}+1}\beta^*_y\beta_z k^*_z \\ \gamma_{cmf}\beta_z \frac{E^*_{ph}}{c} + \frac{\gamma^2_{cmf}}{\gamma_{cmf}+1}\beta_z\beta_x k^*_x + \frac{\gamma^{*2}_{cmf}}{\gamma_{cmf}+1}\beta^*_z\beta_y k^*_y + \left(1 + \frac{\gamma^{*2}_{cmf}}{\gamma_{cmf}+1}\beta^2_z\right)k^*_z \end{bmatrix} \tag{3.43}$$

Let us analyze our general result for the specific case of a head-on collision on the longitudinal z-axis in the laboratory frame ($\vec{k} = (0, 0, \hbar k_z)$, $\beta_{cmf} = (0, 0, \beta_z)$ by writing out the energy term E'_{ph}:

$$\begin{aligned} E'_{ph} &= \gamma_{cmf}\left(m_e c^2 \frac{X}{2\sqrt{1+X}} + m_e c \frac{X}{2\sqrt{1+X}}\cos\theta^*\beta_z\right) \qquad \left|\beta_z = \sqrt{1 - \frac{1}{\gamma^2_{cmf}}}\right. \\ &= m_e c^2 \frac{\gamma_{cmf} X}{2\sqrt{1+X}}\left(1 + \cos\theta^*\sqrt{1 - \frac{1}{\gamma^2_{cmf}}}\right) \end{aligned} \tag{3.44}$$

We further specialize the scenario and approximate the formula for a small observation angle $\theta = \pi - \theta$. If $\theta_{lab} \to 180°$, then according to eq. 3.27, $\cos\theta* \to -1$. Equation 3.44 simplifies to

$$E'_{ph,max} = m_e c^2 \frac{\gamma_{cmf} X}{2\sqrt{1+X}}\left(1 + 1\sqrt{1 - \frac{1}{\gamma^2_{cmf}}}\right) \tag{3.45}$$

which, assuming $\sqrt{1 - \frac{1}{\gamma^2_{cmf}}} \approx \beta_z \approx 1$, can be further reduced to

$$E'_{ph,max} = m_e c^2 \frac{\gamma_{cmf} X}{2\sqrt{1+X}}(1+1) = m_e c^2 \frac{\gamma_{cmf} X}{\sqrt{1+X}} \tag{3.46}$$

Recall from eq. 3.26 that $\gamma_{cmf} = \frac{\gamma_{lab}}{\sqrt{1+X}}$ and you will find that

$$E'_{ph,max} = m_e c^2 \gamma_{lab} \frac{X}{1+X} \tag{3.47}$$

We shall now substitute recoil factor X in the numerator with it's expression in eq. 3.24 where we define $k_x, k_y \to 0$ to obtain the following equation.

$$E'_{ph,max} = \frac{m_e c^2 \gamma_{lab} \frac{4h\nu\gamma_{lab}}{m_e c^2}}{1+X} = \frac{4h\nu\gamma^2_{lab}}{1+X} \tag{3.48}$$

For a low recoil factor $X \to 0$, which describes the quasi-elastic case, we can now derive the final version of the approximated maximum scattered photon energy:

$$\boxed{E'_{ph,max} = 4h\nu\gamma^2_{lab}} \tag{3.49}$$

The elastic collision regime of low recoil ICS is known as Thomson scattering and describes the result of potential applications in dual digit MeV accelerators to a reasonably well approximation.

3.2. 3D Polarized Angular Cross Section

In the previous section, we derived the energy and momentum transfer between an electron and a photon for a given observation angle θ_{lab} as the result of a relativistic, elastic collision from their initial four vectors. We shall now formulate a definition of an angular and polarization dependent Thomson cross section in the form of a 4D Stokes vector transformation matrix. In this, we will recap and condense the often cited reference works by William H. McMaster [16, 17] as well as sections of the "Course of Theoretical Physics" by Lev Landau and Evgenii Lifshitz [12, 13] in so far as they concern themselves with Compton scattering.
In line with the original expression by William H. McMaster, you may consider $\hbar$ to be 1 for the purposes of thesis from this point onward. We shall henceforth express four-momentum related equations and values using the Minkowsky four-momentum norm multiplied by light speed c:

$$\mathbf{v}_{el} = \left(\frac{E}{c}, \vec{p}\right) \cdot c = (E, c\vec{p}) \tag{3.50}$$

This is introduced for legibility. The following mathematical equations are based on transformation matrix algebra with multiple variables in each cell. For this reason, we wish to write the individual variables as short as possible and substitute photon energy E_{ph} with k.

$$E_{ph} \equiv k \tag{3.51}$$

3.2.1. Unpolarized ICS Cross Section

Before including polarization attributes in our calculations, we shall start by re-treading the more widely utilized expressions of the unpolarized Klein-Nishina Cross Section σ_{KN}. A common starting point is the angular dependent electron - photon cross section summed over all polarization configurations written down eq.(86.6) of [13], here reprinted in eq. 3.52.

$$\begin{aligned} d\sigma =& 8\pi \frac{r_e^2}{E_0} \frac{E_0^2 dt}{(s-E_0^2)^2} \left[\left(\frac{E_0^2}{s-E_0^2} + \frac{E_0^2}{u-E_0^2} \right)^2 \right. \\ &\left. + \left(\frac{E_0^2}{s-E_0^2} + \frac{E_0^2}{u-E_0^2} \right) - \frac{1}{4} \left(\frac{s-E_0^2}{u-E_0^2} + \frac{u-E_0^2}{s-E_0^2} \right) \right] \end{aligned} \tag{3.52}$$

This version can be derived from Walter Heitler's form of the σ_{KN} as a quantum mechanical scattering matrix S published in his work "The Quantum Theory Of

Radiation" [18].
S-matrices as a concept were introduced in 1937 by John Archibald Wheeler [19] and independently formalized by Werner Heisenberg in 1943 [20] and are expansions of equations developed by Paul Dirac in 1928 [21,22]. For quantum mechanical processes, S-matrices describe the scattering amplitude and direction of plane waves around a scattering center. In [18] on p.86, Heitler states, that as in quantum mechanics, states of negative energy cannot be excluded, one has "altogether four independent solutions" of a wave equation and thus, "in all applications of relativistic quantum mechanics to radiation problems we shall find it necessary to evaluate matrix elements of operators which are defined as products" of matrices with four rows and four columns. S-matrices are formulated as unitary matrices that connect the initial to the final state of a quantum mechanical process, in our case a scattering event between a photon and an electron. When solved for a set start and end states via four vectors, they quantify the probability of that specific state transition occurring. Thus, they can be used to express the scattering cross section $d\sigma$ of eq. 3.52.
As the cross section is dependent on Mandelstam invariants, the calculated value for $d\sigma$ holds in any frame of reference. We can thus calculate $d\sigma$ in a frame that simplifies the calculation process. We shall choose the laboratory frame in which the initial electron is at rest (ERF), as visualized in fig. 3.2. We will once again clarify, that while for historical reasons, this system is named in reference to electrons, the mathematical principles apply to fermions in general, namely protons as well.
Here, the electron four momentum eq. 3.15 is $\mathbf{p} = (E_0, 0, 0, 0)$ and the Mandelstam invariants eq. 3.10 and eq. 3.12 simplify to:

$$s - E_0^2 = 2E_0 k \quad \text{and} \quad u - E_0^2 = -2E_0 k' \tag{3.53}$$

For a convenient equation encompassing $\mathbf{k}, \mathbf{k}'$ and $\mathbf{p}$, we will square momentum conservation eq. 3.4 reshaped to $\mathbf{p}' = \mathbf{p} + \mathbf{k} - \mathbf{k}'$ and make use of the fact, that the inner product of a four-vector is always constant and equal to it's rest mass in any reference frame:

$$0 = \mathbf{p} \cdot \mathbf{k} - \mathbf{p} \cdot \mathbf{k}' - \mathbf{k} \cdot \mathbf{k}' \tag{3.54}$$

See Appendix section A.1.1.1 for a full derivation of equation 3.54. Because squaring a vector involves it's internal dot product, this equation can be resolved to a scalar form. We express the momentum terms of the four-vectors as the product of the energy with the 3D unit vector $\vec{u}$ pointing into the direction of the particle's momentum.

$$\vec{k} = (k, k \cdot \vec{u}_k) \tag{3.55}$$

When in the electron rest frame, then $vbp = (E_0, 0 \cdot \vec{u}_p)$, and we can write

$$\begin{aligned} 0 &= E_0 k - E_0 k' - k k' (1 - \vec{u}_k \cdot \vec{u}_{k'}) \\ 0 &= E_0 (k - k') - k k' (1 - \cos(\theta_{sc,erf}) \end{aligned} \tag{3.56}$$

where $\theta_{sc,erf}$ is the scattering angle in the electron rest frame: the angle between the incoming and outgoing photon path. We can now describe the change in photon energy in relation to the scattering angle $\theta_{sc,erf}$:

$$\begin{aligned} \frac{k-k'}{kk'} &= \frac{1-\cos\theta_{sc,erf}}{E_0} \\ \frac{1}{k'}-\frac{1}{k} &= \frac{1}{E_0}\left(1-\cos\theta_{sc,erf}\right) \end{aligned} \tag{3.57}$$

Finally, using electron - photon collision invariant t from eq. 3.11, we can write

$$t = -2\mathbf{k}\mathbf{k}' = -2kk'(1-\cos\theta_{sc,erf}) \tag{3.58}$$

To take the derivative dt as a function of dk', we first substitute $1-\cos\theta_{sc,erf}$ in eq. 3.58 using eq. 3.56:

$$t = -2E_0(k-k')$$

For a known incoming photon, energy k is a constant for dt, while the emitted photon energy k' remains variable depending on scattering angle $\theta_{sc,erf}$. The derivation $\frac{dt}{dk'}$ of t is therefore:

$$\frac{dt}{dk'} = 2E_0$$

The derivative dk' is defined to the change in scattering angle $d\cos\theta_{sc,erf}$.

$$\begin{aligned} \frac{dk'}{d\cos\theta_{sc,erf}} &= d\left(\frac{mk}{E_0+k(1-\cos\theta_{sc,erf})}\right)\cdot\frac{1}{d\cos\theta_{sc,erf}} \\ &= \frac{E_0k}{E_0+(1-\cos\theta_{sc,erf})k}\cdot\frac{k}{E_0+(1-\cos\theta_{sc,erf})k} \\ &= k'\cdot\frac{k'}{E_0} \\ dk' &= \frac{k'^2}{E_0}d\cos\theta_{sc,erf} \end{aligned} \tag{3.59}$$

With eq. 3.2.1 and eq. 3.59, derivative dt can be formulated:

$$dt = 2k'^2 d\cos\theta_{sc,erf} = \frac{1}{\pi}k'^2dk' \quad \text{with} \quad dk' = 2\pi\sin\theta_{sc,erf}d\theta_{sc,erf} \tag{3.60}$$

Having constructed and assembled all substitution variables in eq. 3.53, eq. 3.56 and eq. 3.60, we insert them into eq. 3.52 starting with eq. 3.53. For improved

clarity, substitution insertions are highlighted in teal.

$$
\begin{aligned}
d\sigma =& \frac{8\pi r_e^2 E_0^2 dt}{(2E_0 k)^2}\left[\left(\frac{E_0^2}{2E_0 k}+\frac{E_0^2}{-2E_0 k'}\right)^2\right.\\
&\left.+\left(\frac{E_0^2}{2E_0 k}+\frac{E_0^2}{-2E_0 k'}\right)-\frac{1}{4}\left(\frac{2E_0 k}{-2E_0 k'}+\frac{-2E_0 k'}{2E_0 k}\right)\right]\\
=& \frac{2\pi r_e^2 dt}{k^2}\left[\left(\frac{E_0}{2k}+\frac{E_0}{-2k'}\right)^2+\left(\frac{E_0}{2k}-\frac{E_0}{2k'}\right)+\frac{1}{4}\left(\frac{k}{k'}+\frac{k'}{k}\right)\right] && \text{|eq.3.60}\\
=& \frac{2\pi r_e^2 k'^2 dk'}{k^2\pi}\left[\frac{E_0}{2}\left(\frac{1}{k}+\frac{1}{k'}\right)^2+\frac{E_0}{2}\left(\frac{1}{k}-\frac{1}{k'}\right)+\frac{1}{4}\left(\frac{k}{k'}+\frac{k'}{k}\right)\right] && \text{|eq.3.56}\\
=& \frac{2r_e^2 k'^2 dk'}{k^2}\left[\left(\frac{E_0}{2}\frac{\cos\theta_{sc,erf}-1}{E_0}\right)^2+\frac{E_0}{2}\frac{\cos\theta_{sc,erf}}{E_0}+\frac{1}{4}\left(\frac{k}{k'}+\frac{k'}{k}\right)\right]\\
=& \frac{2r_e^2 k'^2 dk'}{k^2}\left[\left(\frac{1}{4}(\cos^2\theta_{sc,erf}-2\cos\theta_{sc,erf}+1)\right)\right.\\
&\left.+\frac{1}{2}\cos\theta_{sc,erf}-\frac{1}{2}+\frac{1}{4}\left(\frac{k}{k'}+\frac{k'}{k}\right)\right]\\
=& \frac{1}{2}\frac{r_e^2 k'^2 dk'}{k^2}\left[\left(\cos^2\theta_{sc,erf}-1+\frac{k}{k'}+\frac{k'}{k}\right)\right]\\
\frac{d\sigma}{dk'} =& \frac{1}{2}r_e^2\left(\frac{k'}{k}\right)^2\left(\frac{k}{k'}+\frac{k'}{k}-\sin^2\theta_{sc,erf}\right)
\end{aligned}
\tag{3.61}
$$

This is the classical Klein-Nishina Compton Cross Section in the form commonly presented in modern textbooks.

3.2.1.1. Total ICS Cross Section

An important parameter for the numerical code developed as part of this thesis, Comparse, is the total ICS cross section σ_{tot} that depends only on initial scattering parameters and is integrated over all scattering results. This value gives us a probability for a scattering event of two known particles taking place, regardless of scattering direction. Comparse calculates this value in the first step of the simulation routine in order to greatly reduce the number of fermion - photon pairs to be simulated precisely with observation of scattering direction and polarization. For this purpose, we prefer a swiftly solvable 1 dimensional equation over the more complex transformation matrix approach described further below. A formula satisfying the requirements of considering incoming particle momentum and energies can be derived from eq. 3.52.
For this version of the ICS cross section, following the path laid out in [13] §86, we shall move into the center of mass rest system (fig. 3.3). Here, the Mandelstam invariants can be simplified by considering that $\mathbf{p}+\mathbf{k}=0$. We can thus express

the s, t, u in terms of energy as follows:

$$\begin{aligned} s &= (E_{el} + k)^2 = E_0^2 + 2k(k + E_{el}) \\ u &= E_0^2 - 2k(k\cos\theta_{sc,erf} + E_{el}) \\ t &= -2k^2(1 - \cos\theta_{sc,erf}) \end{aligned} \tag{3.62}$$

The Mandelstam invariants used to express eq. 3.52 are limited by a set of inequalities:

$s \geq E_0^2$ because the inner product of $\mathbf{p} \cdot \mathbf{k} \geq 0$ in eq. 3.10

$t \leq 0$ because the inner product of $\mathbf{p} \cdot \mathbf{p}' \geq E_0^2$ in eq. 3.11

$us \leq E_0^4$ proof given in appendix A.1.1.2

As we intend to calculate σ_{tot} knowing the initial particle's energies, we have a given s in the set of equations. We can thus replace the integration of eq. 3.52 over t with one over $u = 2E_0^2 - s - t$ in the range $\frac{E_0^4}{s} \leq u \leq 2E_0^2 - s$. We will substitute the remaining invariants s and u with recoil X (eq. 3.24) and the analogously formulated $Y = \frac{E-0^2-u}{E_0^2}$:

$$\sigma_{tot} = \frac{8\pi r_e^2}{X^2} \int_{X/(X+1)}^{X} \left[\left(\frac{1}{X} - \frac{1}{Y} \right)^2 + \frac{1}{X} - \frac{1}{Y} + \frac{1}{4} \left(\frac{X}{Y} + \frac{Y}{X} \right) \right] dY \tag{3.63}$$

This integral needs to be resolved in order to obtain a version of the total ICS cross section σ_{tot} that can be valued merely by incoming initial particle parameters.

$$\sigma_{tot} = \frac{8\pi r_e^2}{X^2} \left[\underbrace{\int_{X/(X+1)}^{X} \left(\frac{1}{X} - \frac{1}{Y} \right) dY}_{\text{A}} + \underbrace{\int_{X/(X+1)}^{X} \frac{1}{X} dY}_{\text{B}} + \underbrace{\int_{X/(X+1)}^{X} -\frac{1}{Y} dY}_{\text{C}} + \underbrace{\int_{X/(X+1)}^{X} \left(\frac{X}{Y} + \frac{Y}{X} \right) dY}_{\text{D}} \right] \tag{3.64}$$

We shall solve each of the integral summands marked above:

$$\begin{aligned} \text{A} &= \int_{X/(X+1)}^{X} \frac{1}{X^2} + \frac{1}{Y^2} - \frac{2}{XY} dy \\ &= \left[\frac{Y}{X^2} \right]_{X/(X+1)}^{X} + \left[-\frac{1}{Y} \right]_{X/(X+1)}^{X} - \left[\frac{2}{X} \ln(Y) \right]_{X/(X+1)}^{X} \\ &= 1 + \frac{1}{X} - \frac{1}{X(X+1)} - \frac{2}{X} \ln(X+1) \end{aligned} \tag{3.65}$$

$$\text{B} = \left[\frac{Y}{X} \right]_{X/(X+1)}^{X} = \frac{X}{X+1} \tag{3.66}$$

$$\mathrm{C} = [-\ln(Y)]_{X/(X+1)}^{X} = -\ln(X+1) \tag{3.67}$$

$$\begin{aligned}\mathrm{D} &= \frac{1}{4}\left([X\ln(Y)]_{X/(X+1)}^{X} + \left[\frac{Y^2}{2X}\right]_{X/(X+1)}^{X}\right) \\ &= \frac{X}{4}\left(\ln(X+1) + \frac{1}{2} + \frac{1}{2(X+1)^2}\right)\end{aligned} \tag{3.68}$$

Now, we insert the A, B, C and D into eq. 3.64 to at last obtain:

$$\begin{aligned}\sigma_{tot} &= \frac{8\pi r_e^2}{X^2}\left[\mathrm{A}+\mathrm{B}+\mathrm{C}+\mathrm{D}\right] \\ &= \frac{8\pi r_e^2}{X^2}\left[\ln(X+1)\left(-1-\frac{2}{X}\right)+1+\frac{1}{X}+\frac{X}{X+1}-\frac{1}{X(X+1)}+\mathrm{D}\right] \\ &\qquad +\ln(X+1)+\frac{1}{2}+\frac{1}{2(X+1)^2}\Big] \\ &= \frac{2\pi r_e^2}{X}\left[\ln(X+1)\left(1-\frac{4}{X}-\frac{8}{X^2}\right)+\frac{1}{2}+\frac{1}{2(X+1)^2}\right. \\ &\qquad \left.+\frac{4}{X}\left(1+\frac{1}{X}+\frac{X}{X+1}-\frac{1}{X(X+1)}\right)\right] \\ &= \frac{2\pi r_e^2}{X}\left[\ln(X+1)\left(1-\frac{4}{X}-\frac{8}{X^2}\right)+\frac{1}{2}+\frac{1}{2(X+1)^2}\right. \\ &\qquad \left.+\frac{4}{X}\left(\frac{1}{X(X+1)}\left[X(X+1)+(X+1)+X^2-1\right]\right)\right] \\ &= \frac{2\pi r_e^2}{X}\left[\ln(X+1)\left(1-\frac{4}{X}-\frac{8}{X^2}\right)+\frac{1}{2}+\frac{1}{2(X+1)^2}\right. \\ &\qquad \left.+\frac{4}{X}\left(\frac{1}{X(X+1)}\left(2X(X+1)\right)\right)\right]\end{aligned}$$

$$\sigma_{tot} = \frac{2\pi r_e^2}{X}\left[\ln(X+1)\left(1-\frac{4}{X}-\frac{8}{X^2}\right)+\frac{1}{2}+\frac{1}{2(X+1)^2}+\frac{8}{X}\right] \tag{3.69}$$

This final equation is, as mentioned earlier, executed in Comparse for all fermion - photon pairs before polarization and scattering angle information is included. The latter two attributes will only be considered for those particle pairs that get selected by a weighted random selection. σ_{tot} of eq. 3.69 constitutes one of the key factors that make up the stochastic weight. For more details see section 4.5.

3.2.2. Stokes Parameters

The four Stokes parameters were presented in 1851 by Sir George Gabriel Stokes as an analytical tool for problems involving polarized electromagnetic radiation [23]. In Stokes parameters, the light is described in 4 physically measurable properties that

Stokes Parameter	Photon Observable		Particle Observable	
I	[0,1] 	Intensity	[0,1] 	Intensity
P_1	+1 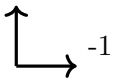 -1	transversal polarization	+1  -1	Spin in z
P_2	+1 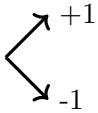 -1	transversal polarization at an angle of $\frac{\pi}{4}$ to the right	+1 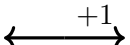 -1	Spin in x
P_3	+1 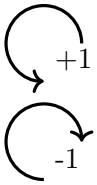 -1	circular polarization	+1 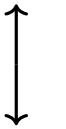 -1	Spin in y

Figure 3.4.: Stokes Parameters of photons and fermions and they're interpretation in this thesis.

can be written as Stokes vector $S = (I, P_1, P_2, P_3)$, illustrated in fig. 3.4. Written as four vectors, one can perform a number of useful calculations as transformation matrix multiplications, called Mueller calculus. [24]

$$\begin{pmatrix} I \\ P_1' \\ P_2' \\ P_3' \end{pmatrix} = \boldsymbol{M} \begin{pmatrix} I \\ P_1 \\ P_2 \\ P_3 \end{pmatrix} \tag{3.70}$$

Matrix $\boldsymbol{M}$ can stand for both transformations that do not represent actual changes to the intrinsic state of photons, such as reference frame translations or rotations, and polarization dependent interactions of photons with particles, fields or each other, for example optical elements or scattering events.
Let us now introduce the concept of probability in Stokes vector notation. We start with a photon beam characterised by a defined set of Stokes parameters $\boldsymbol{S}_i = \boldsymbol{P} = (I, \vec{P})$. In case of or monochromatic radiation, $\boldsymbol{P}$ constitutes a definite combination of values that follow $P_1^2 + P_2^2 + P_3^2 = I^2$. However, if the photon beam is incoherent, then $P_1^2 + P_2^2 + P_3^2 \leq I^2$ and Stokes parameters represent mean values of the whole beam. Let $\boldsymbol{P}$ be the initial photon beam. To determine the probability W of detecting a single photon ($I = 1$) of known polarization defined by Stokes vector

$\boldsymbol{S}_Q = (1, \vec{Q})$, we calculate the fractional intensity:

$$W = \frac{1}{2}(1 + \boldsymbol{P} \cdot \boldsymbol{Q}) = \frac{1}{2}(1, \vec{Q}) \begin{pmatrix} I \\ \vec{P} \end{pmatrix} \tag{3.71}$$

The results range from $W = 0$ in the case of pure opposed polarization, when $\vec{P} \cdot \vec{Q}$ becomes -1 and $W = 1$ when both unit vectors $\vec{P} \cdot \vec{Q} = 1$ are the same, indicating the polarization of detector and beam photons points in the exact same direction.

3.2.2.1. Polarization Vector Value Space

Some distinctions are necessary for the possible values of $\boldsymbol{Q}$ and $\boldsymbol{P}$. Representing the initial photon beam of arbitrary polarization, the absolute value of the components $|\vec{P}|$ cannot exceed I.

$$\boldsymbol{S}_i = \begin{pmatrix} I \\ \vec{P} \end{pmatrix} = \begin{pmatrix} I_0 \\ I_0 p P_1 \\ I_0 p P_2 \\ I_0 p P_3 \end{pmatrix} \tag{3.72}$$

$$\sqrt{(I_0 p P_1)^2 + (I_0 p P_2)^2 + (I_0 p P_2)^2} \leq I_0 \tag{3.73}$$

Factor p represents the degree of polarization and can assume values $[0, 1]$. When calculating single particle events, e.g. Comparse, I_0 is normalized to 1. Therefore, the 3 polarization components can be set to $[-1, 1]$ but $\vec{P}$ cannot exceed unit vector length.
This is different for the detector $\boldsymbol{Q}$. We can visualize the effect of $\boldsymbol{Q}$ as either a polarising filter set to a specific polarization or a polarization insensitive screen. When filtering for polarization, the polarising filter let's only light of a certain oscillation direction pass, filtering out the orthogonal oscillation in the process. Filtering a polarization in the particle regime is always absolute: a partial polarising filter in a single component conceptually does not make sense without statistic effects. $\boldsymbol{Q}$ is always "fully polarised". Due to $p \stackrel{!}{=} 1$, the set of components Q_1, Q_2, Q_3 has to always satisfy unit vector definition. In the latter case, we define $\boldsymbol{S}_{Q,unpol} = (1, 0, 0, 0)$ and in that decision, remove the polarization sensitive factors P_1, P_2, P_3 from the equation. An important remark has to be made here: Setting the polarization components of the polarization filter Stokes vector $\boldsymbol{Q}$ to zero is equivalent to measuring over both perpendicular polarization possibilities. Therefore, in the unpolarised case, we sum the same cross section value twice over the θ value space, losing the multiplier $\frac{1}{2}$ in the process:

$$W = (1, 0, 0, 0) \begin{pmatrix} 1 \\ 0 \\ 0 \\ 0 \end{pmatrix} \tag{3.74}$$

The mathematical proof is presented in Appendix sec. A.1.2.1.

3.2.2.2. Coordinate Transformation of Stokes Vectors

As the Stokes parameter components define a directed polarization state in 3D space, their values must change under coordinate system transformation. This change from the initial state $\boldsymbol{S} = (I, \vec{P})$ to the Stokes vector's rotated form $\boldsymbol{S}' = (I, \vec{P}')$ can be performed via multiplication with a rotation matrix $\mathbf{M}$. As the transversal components of a Stokes vector P_1 and P_2 isolated are not conserved over changes of the polarization vector direction, $\mathbf{M}$ typically takes the shape of a euclidean rotation matrix with a main diagonal $D = (1, a, b, 1)$, affecting only the two middle dimensions of the Stokes vector containing P_1 and P_2. As an example, see eq. 3.75 which will perform a clockwise rotation about the direction of the propagation at an angle ϕ.

$$\mathbf{M} = \begin{pmatrix} 1 & 0 & 0 & 0 \\ 0 & \cos 2\phi & \sin 2\phi & 0 \\ 0 & -\sin 2\phi & \cos 2\phi & 0 \\ 0 & 0 & 0 & 1 \end{pmatrix} \tag{3.75}$$

We shall discuss in more detail the Stokes vector rotations we have to perform in order to calculate ICS in continuous angle space in section 4.6.2.

3.2.3. Stokes Transformation Matrix for Compton Scattering Cross Section

Of utmost importance in the analytical approach to Compton scattering is the Klein-Nishina cross section σ_{KN}. Derived from the Dirac equation and one of the first confirmed predictions of Quantum Electrondymics, σ_{KN} expresses the angular dependent scattering cross section of radiation described by two incoherent elliptical waves, thus incorporating the concept of partial polarization. Converted to the Stokes formalism and written for the case of a specific initial electron spin direction $\vec{s}$, σ_{KN} can be expressed via a transformation matrix $\mathbf{T}$ [25,26]. When $\mathbf{T}$ is applied to Stokes vectors before and after the event in matrix multiplications, it resolves into the scattering probability or fractional intensity W for that scattering event configuration.

$$W = \frac{1}{2}(1, \vec{Q})\mathbf{T}\begin{pmatrix} I \\ \vec{P} \end{pmatrix} \tag{3.76}$$

$$\mathbf{T} = \frac{1}{2}\left(\frac{1}{4\pi\epsilon_0}\frac{e^2}{m_e c^2}\right)^2 \left(\frac{k'}{k}\right)^2 \times$$

$$\begin{pmatrix} 1+\cos^2\theta+(k-k')(1-\cos\theta) & \sin^2\theta & 0 & -(1-\cos\theta)(\vec{k}\cos\theta+\vec{k}')\cdot\vec{s} \\ \sin^2\theta & 1+\cos^2\theta & 0 & (1-\cos\theta)(\vec{u}'\times\vec{u})\cdot(\vec{k}\times\vec{s}) \\ 0 & 0 & 2\cos\theta & (1-\cos\theta)(\vec{k}\times\vec{u}')\cdot\vec{s} \\ -(1-\cos\theta)(\vec{k}'\cos\theta+\vec{k})\cdot\vec{s} & (1-\cos\theta)(\vec{u}\times\vec{u}')\cdot(\vec{k}'\times\vec{u})\vec{s} & (1-\cos\theta)(\vec{k}'\times\vec{u})\cdot\vec{s} & 2\cos\theta+(k-k')(1-\cos\theta)\cos\theta \end{pmatrix} \tag{3.77}$$

where

$(\frac{1}{4\pi\epsilon_0}\frac{e^2}{mc^2})^2$	classical electron radius squared
k, k'	energies of photon before and after scattering
$\vec{k}, \vec{k}'$	momentum three vectors of photon before and after scattering
$\vec{u}, \vec{u}'$	unit vectors of $\vec{k}, \vec{k}'$
θ	scattering angle between incoming and outgoing photon momentum
$\vec{s}$	spin direction of the initial electron

3.2.4. ICS Cross Section Transformation Matrix Unpolarized

We shall confirm the validity of this matrix approach by attempting to construct the classical σ_{KN} using the $\mathbf{T}$-matrix as a starting point. This initially complex matrix $\mathbf{T}$ is reduced to its top-left cell in unpolarized scattering scenarios which leaves behind a common expression of the unpolarized σ_{KN}. Note, that for a full picture of the scattering cross section, we sum probabilities over two perpendicular polarization directions. Therefore, we can simply remove multiply $\frac{1}{2}$ from the single direction measurement equation and take the top left cell of $\mathbf{T}$ to obtain the total cross section measurement formula. A proof of this is derived in appendix section A.1.2.1.

$$W = (1,0,0,0)\mathbf{T}\begin{pmatrix}1\\0\\0\\0\end{pmatrix} \tag{3.78}$$

$$= \frac{1}{2}r_e^2\left(\frac{k'}{k}\right)^2\left[1+\cos^2\theta(k-k')(1-\cos\theta)\right] \tag{3.79}$$

$$= \frac{1}{2}r_e^2\left(\frac{k'}{k}\right)^2\left[\frac{(k-k'_0)^2}{kk'_0}+1+\cos^2\theta\right]$$

$$= \frac{1}{2}r_e^2\left(\frac{k'}{k}\right)^2\left[\frac{k'^2}{kk'}-\frac{2kk'}{kk'}+\frac{k'^2}{kk'}+2-\sin^2\theta\right]$$

$$\boxed{W = \frac{1}{2}r_e^2\left(\frac{k'}{k}\right)^2\left[\frac{k}{k'}+\frac{k'}{k}-\sin^2\theta\right]} \tag{3.80}$$

This equation mirrors our solution eq. 3.61 derived earlier in subsection 3.2.1

3.2.5. Polarized ICS Cross Section Transformation Matrix

To illustrate the polarized ICS cross section calculation capability of the Stokes transformation matrix $\mathbf{T}$, we will consider the relatively simple example of a fully linearly polarized laser. As shown in fig. 3.4, the incoming polarization vector $\boldsymbol{P}$ of a fully linearly polarized photon beam includes a Stokes vector of the form

$$\boldsymbol{P}_{lin} = \begin{pmatrix}1\\1\\0\\0\end{pmatrix} \tag{3.81}$$

Applying $\boldsymbol{P}_{lin}$ onto $\mathbf{T}$ in eq. 3.76 results in eq. 3.82:

$$
\begin{aligned}
W =& \frac{1}{2}\left[\frac{1}{2}\left(\frac{1}{4\pi\epsilon_0}\frac{e^2}{m_e c^2}\right)^2\left(\frac{k}{k}\right)^2\right]\boldsymbol{Q}\cdot \\
& \begin{pmatrix}
\left[1+\cos^2\theta+(k-k)(1-\cos\theta)\right]+\left[-\sin^2\theta\right] \\
\left[-\sin^2\theta\right]+\left[1+\cos^2\theta\right] \\
0 \\
\left[-(1-\cos\theta)(\vec{k}\cos\theta+\vec{k}_0)\cdot\vec{s}\right]+\left[(1-\cos\theta)(\vec{u}_0\times\vec{u})\cdot(\vec{k}\times\vec{u}_0)\vec{s}\right]
\end{pmatrix} \\
=& \frac{1}{2}\left[\frac{1}{2}\left(\frac{1}{4\pi\epsilon_0}\frac{e^2}{m_e c^2}\right)^2\left(\frac{k}{k}\right)^2\right]\boldsymbol{Q}\cdot \\
& \begin{pmatrix}
2\cos^2\theta+(k-k)(1-\cos\theta) \\
2\cos^2\theta \\
0 \\
\left[-(1-\cos\theta)(\vec{k}\cos\theta+\vec{k}_0)\cdot\vec{s}\right]+\left[(1-\cos\theta)(\vec{u}_0\times\vec{u})\cdot(\vec{k}\times\vec{u}_0)\vec{s}\right]
\end{pmatrix}
\end{aligned}
\tag{3.82}
$$

We will give the vector to which Stokes matrix $\mathbf{T}$ reduced the variable name "$\boldsymbol{S}_f$". It can be interpreted as the Stokes vector defining the photon polarization after ICS scattering. As opposed to $\boldsymbol{P}$, $\boldsymbol{S}_f$ shows a scattering angle θ_{cmf} dependence. You may notice, that this example calculation does not show a dependence on azimuthal scattering angle ϕ. It is implicitly there, however, because the photon polarization is defined on the photon momentum or wave vector. An Euler rotation that transforms the incoming photon into the emitted photon direction has to be applied onto the polarization vector as well. This can project part or all of $\boldsymbol{S}_{f,1}$ onto $\boldsymbol{S}_{f,2}$ as per rotation matrix $\mathbf{M}(\phi)$:

$$
\mathbf{M}(\phi) := \begin{pmatrix}
1 & 0 & 0 & 0 \\
0 & \cos 2\phi & \sin 2\phi & 0 \\
0 & -\sin 2\phi & \cos 2\phi & 0 \\
0 & 0 & 0 & 1
\end{pmatrix}
\tag{3.83}
$$

In a realistic scenario in which photons of a laser pulse have a certain emittance, this implicit rotation needs to be applied twice: Once onto $\boldsymbol{P}$ and once onto $\boldsymbol{S}_f$. For generalized particle and laser collision events, we thus expand scattering probability W of eq. 3.76 to W_R.

$$
W_\mathrm{R} = \frac{1}{2}\boldsymbol{Q}\cdot(\mathbf{T}\cdot\boldsymbol{P}\cdot\mathbf{M}(\phi))\cdot\mathbf{M}'(\phi') \tag{3.84}
$$

$$
= \frac{1}{2}\boldsymbol{D}\cdot\boldsymbol{S}_f\cdot\mathbf{M}'(\phi') \tag{3.85}
$$

As the last requirement to resolve the equation for the scattering probability W_R, polarization detector vector $\boldsymbol{Q}$ has to be defined. We discussed how $\boldsymbol{Q}$ can be

interpreted earlier in section 3.2.2.1 and later proved in section 3.2.4 that a detector set to unpolarized photons $\boldsymbol{Q} = (1, 0, 0, 0)$ is the sum of two linear polarization detectors set to opposite index values and that detecting fully unpolarized photons that way results in the classical Klein-Nishina cross section σ_{KN} (eq. 3.61, eq. 3.80).
A detailed overview of how we incorporate spatial rotation in the calculation of polarized ICS can be found in section 4.6.2 where we discuss the implementation of Stokes ICS transformation matrix $\boldsymbol{T}$ into in Comparse. With it, a number of different polarization and angle scenarios have been investigated, the results of which are presented in section 5.3.

4. Comparse

In order to support quick iteration scenario studies of Inverse Compton Scattering (ICS) at fermion accelerators with the inclusion of polarization effects, a semi-analytical numerical simulation code was written as part of this thesis at the KPH of the JGU Mainz. The full source code of the **Com**pton **P**olarized **A**nalytical **R**adiation **S**tatistics **E**nvironment (**Comparse**) is based on the mathematical foundation laid out in chapter 3. In this chapter, only key implementation aspects are explained.

The complete code including all past versions can be found in the Rheinland-Pfalz state gitlab respository under `https://gitlab.rlp.net/clorey/thomson-scattering-phd`. A version compiled for Windows that does not require a python installation can be downloaded from the Rheinland-Pfalz Seafile server accessed via the following URL and the QR code.

`https://seafile.rlp.net/f/16841b6e9a084840b8d8/`

4.1. Comparse Overview

Comparse was written in Python with the goal of providing a user friendly tool to apply the analytical principles of ICS described in chapter 3 on large data sets with enough precision and performance to be used in swift iteration studies. With it, users can generate or read pre-made fermion distributions, define and match a laser beam and then simulate every step of ICS from the stochastic selection of which fermion - photon pairs result in scattering over the calculation of the momenta and energies after scattering to the detected gamma radiation on a defined detector screen including collimation. It relies on the libraries "DearPyGui" by Jonathan Hoffstadt [27] for the user interface (UI), "Matplotlib" by John D. Hunter [28] for all image visualizations. Comparse predominantly relies on "NumPy" [29] for parallel array calculations to achieve performance targets. For mathematical operations that do not need to occur in successive order, loops are avoided entirely.

When executing the program, every fermion or photon distribution initiates a `Fermion` or `Laserbeam` class instance. In these classes, all variables and functions directly related to either fermions and photons are saved and can be called specifically through that class instance. There can be several instances of fermion and photon class created and loaded in memory during runtime, representing different accelerator or laser types or modes to be investigated. Users can switch between these classes by pressing the corresponding class button that appeared in the UI upon creation of a new class instance. This "activates" the selected class, meaning

whenever a method requires a fermion or photon class, the one designated "active" is used. Note that, when creating a fermion class, the UI will replace every mention of "fermion" with either "electron" or "proton". Through this, users can work with several fermon and photon distributions in parallel, quickly switching between one combination to another. In this text, we will always refer to the class with "fermion". A third class, `Neutral`, is mainly used to save UI state values unrelated to the physics of ICS.
Comparse consists of altogether 15 files that are listed and described in Appendix A.5.The standard user is not expected to interact with any of the files outside. The functions and methods within are called by the UI started by running compton_main.py in a python interpreter or through a pre-compiled operating system specific executable. Advanced users may change the values found in constants.py and utilize the import and export functions of Comparse together with auxiliary files in the "inputfiles" and "outputfiles" local folders. Only experts of ICS that have deeply familiarized themselves with the functions and logic of Comparse should attempt to make changes to any other file.

Figure 4.1 shows the essential Comparse calculation routines in logical order. Functions must be executed in numerical stage order. One can, for example, not trace photons to a screen, stage 6, before the scattered photon data has been created in stage 5. All side modules are associated with a stage of the Comparse execution order and are highlighted as active as soon as that stage is reached. For the purposes of keeping the flowchart readable and this chapter brief, data save/load and import/export functionality as well as functions relating to the user interface as well as makros, executing more complex multi stage calculations using the existing Comparse modules, have been omitted and will not be described in detail. You may refer to appendix section sec. A.4 for a detailed step-by-step user manual to Comparse.

4.1.1. Comparse User Interface

Comparse is a program that is required to be executed in a certain order (see fig. 4.1) and the user interface is designed to guide through these logical steps. On opening, the user is presented with a window primarily kept in a blue-grey color scheme (fig. 4.2). Initially, several UI elements are red and one button reading "ENTER" is green. Interacting with any red UI element will not work or lead to errors. Comparse internally keeps track of the current stage of the simulation. At any point, interacting with the green highlighted UI element will lead from the current to the next stage, starting with the highlighted "ENTER" button that loads an Astra file and creates a new fermion class. This action will bring Comparse from Stage 0 to Stage 1, at which point the green highlighted fermion "ENTER" button will change to the default UI color while the red photon class "ENTER" button turns green. This indicates that it is active and a photon class can be created and matched to the fermion distribution. The principle continues analogously from Stage 0 to Stage 6, in which the scattered photons are traced to a defined screen

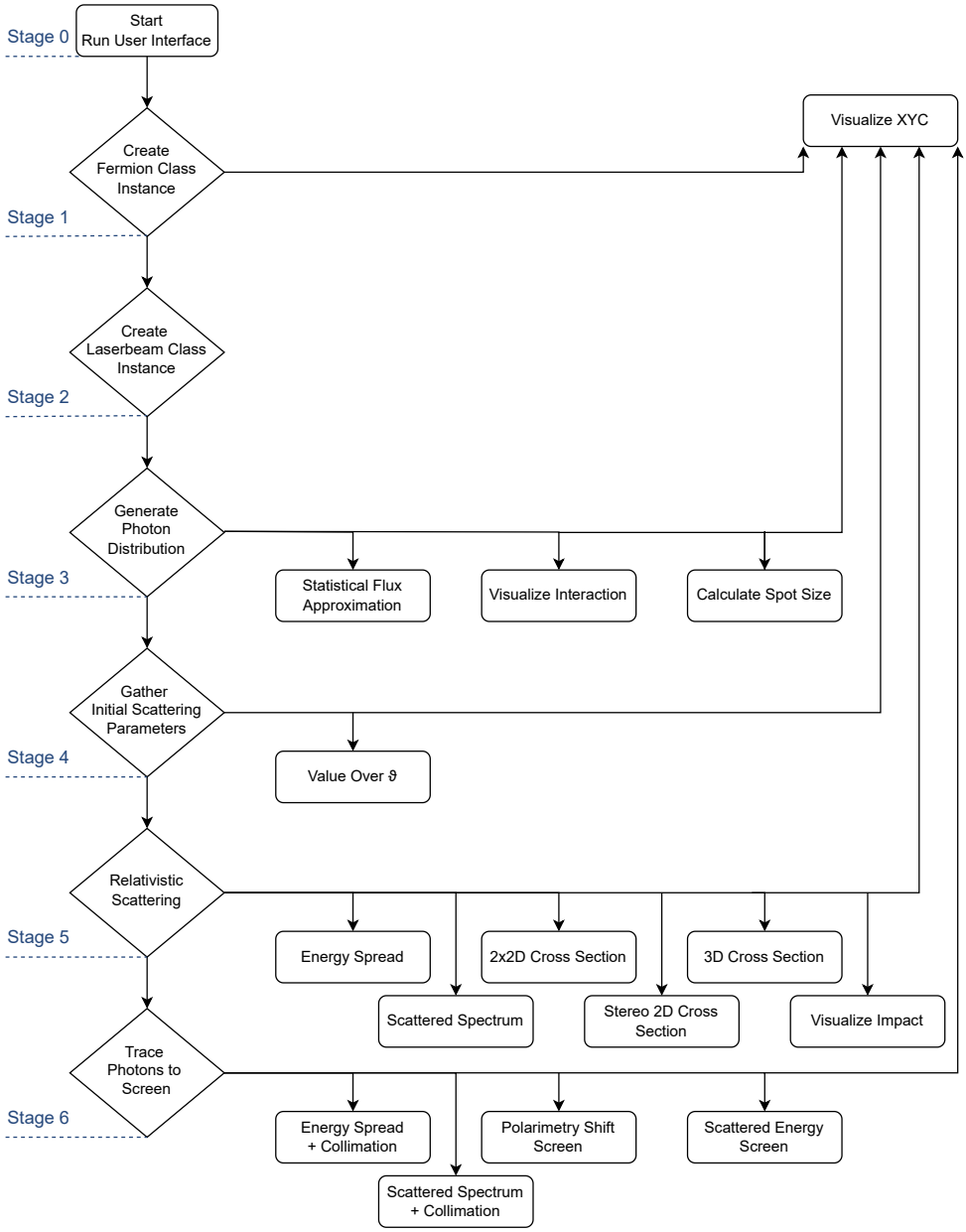

Figure 4.1.: Comparse Flow Chart showing the main and side calculation routines and after which major step they become available. "Visualize XYC" lets users plot any combination of parameters taken from all steps of the simulation in a 2D scatter plot with optional additional color value axis.

in space. On the way, the visualization and data analysis modules found under the "Data Analysis & Visualization" will change color from red to the UI theme default at the stage that they can be first executed. See fig. 4.3 for an example screenshot of Comparse at internal Stage 5 after the relativistic scattering simulation has concluded. Perception and knowledge of the color guidance system is not required to use Comparse, but it might serve in a supportive function as a reminder of the simulation's current progress for those familiar with it.

Furthermore, whenever changes are made and confirmed to values in earlier than

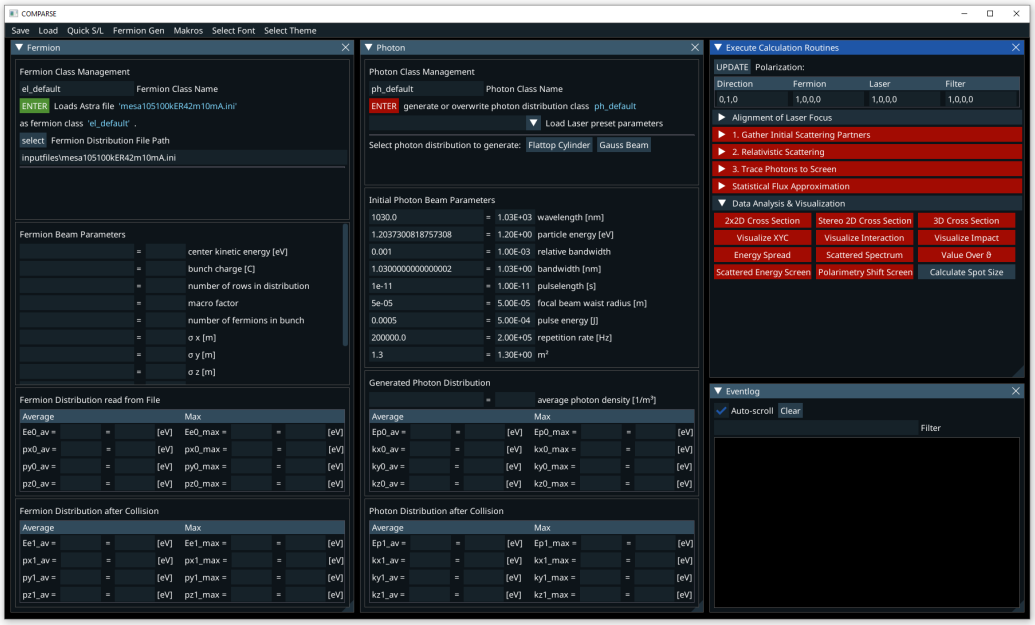

Figure 4.2.: Comparse default user interface on startup as of version 1.0.

current stages, Comparse will automatically revert the UI to this earlier stage and delete values calculated before in higher stages, preventing unnoticed errors. Loading a previously saved fermion and photon class automatically sets the UI to the highest stage reached in the simulation at the time.

4.1.2. Comparse Data Export

Comparse can calculate, simulate and approximate a wide range of variables related to various aspects of Compton scattering in potentially large data sets. Naturally, there is a clear requirement for users to be able to save, analyze and visualize the data outside of the program's routine. To fulfill this requirement, Comparse features a number of data export functions.

The most obvious way to export data is the "Save Fermion/Photon" method found in the window top header "Save" menu shown in fig. 4.4. Users can define the filename, choose the save location via a file selection dialog and selected between only

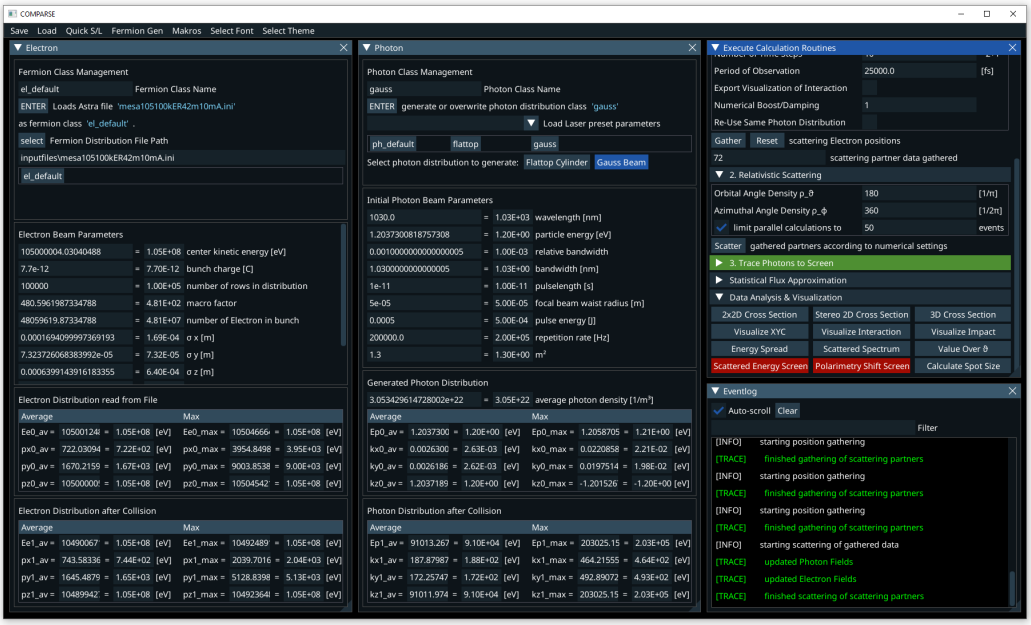

Figure 4.3.: Comparse default user interface after execution "Relativistic Scattering" as of version 1.0.

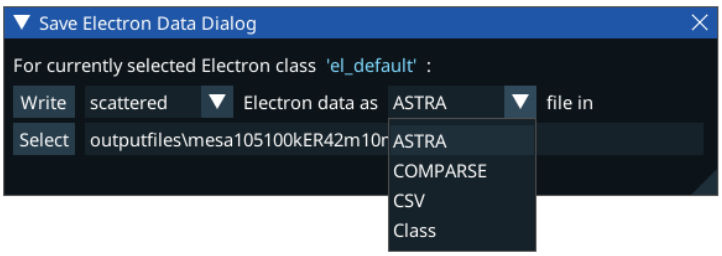

Figure 4.4.: Comparse fermion save dialog as of version v1.0. In this screenshot, the currently active fermion class has particle type "electron".

	1	2	3	4	5	6	7	8	9	10
Parameter	x	y	z	px	py	pz	clock	macro charge	particle index	status flag
Unit	m	m	m	eV/c	eV/c	eV/c	ns	nC		

Table 4.1.: Structure of Astra format particle distribution files as shown in [30] on p.2.

the scattered, unscattered or alternatively the combined scattered and unscattered data. Furthermore, the file format can be selected from a drop down menu containing menu items "Astra", "Comparse", "CSV" and "Class".
Aside from that, data type specific export formats and functions are accessible in their respective Comparse module. All file formats are explained in Appendix A.6. All graphs, plots and tables of simulations in this thesis have been created in Comparse or using Comparse data export.

4.2. Electron Input

4.2.1. Importing an External Input Format Electron Distribution

For most of the studies in this thesis, the default first step was the generation of an electron bunch distribution in "A Space Charge Tracking Algorithm" or Astra [30]. Astra was written in Fortran, a procedural programming language in development since 1957 [31], by Klauss Floettmann for DESY (Deutsches Elektronensynchrotron) in Hamburg, Germany. With Astra and it's various subroutines, users can define charged particle distributions, beam line sections, track particles through these sections and finally perform a series of data analysis operations on the initial, intermediate or final state of the particle distribution. For the purposes of this work, the particle distribution generation application named "generator" was of primary interest. Refined, applied and validated over decades, it has a high measure of trust and understanding in the accelerator community and allows for low discrepancy quasirandom Hammersley sequence injection in it's Gaussian distribution generator. The latter was enabled for all electron distributions created for this work, as it prevents close clustering of like-charged particles that should in actuality repel each other due to space charge effects. In Astra, electron distributions are defined via a Fortran 90 namelist written into an input file ending in ".in", where key particle distribution parameters and filename are defined. You may refer to [30] p.93-97 for a complete list of input options. Once defined, the input file ending in .in can be read by the Astra program "generator" in order to generate a particle distribution file ending in ".ini". This file is structured as a tab separated value (TSV) table of 10 columns as laid out in 4.1 and an arbitrary number of rows, each corresponding to a macro particle. As of version 1.0, Comparse only makes use of columns 1 to 6, 8 and 10 of 4.1. Comparse uses the first three, "x", "y" and "z" for the particle position, "px", "py" and "pz" for the particle momenta in 3D, "macro

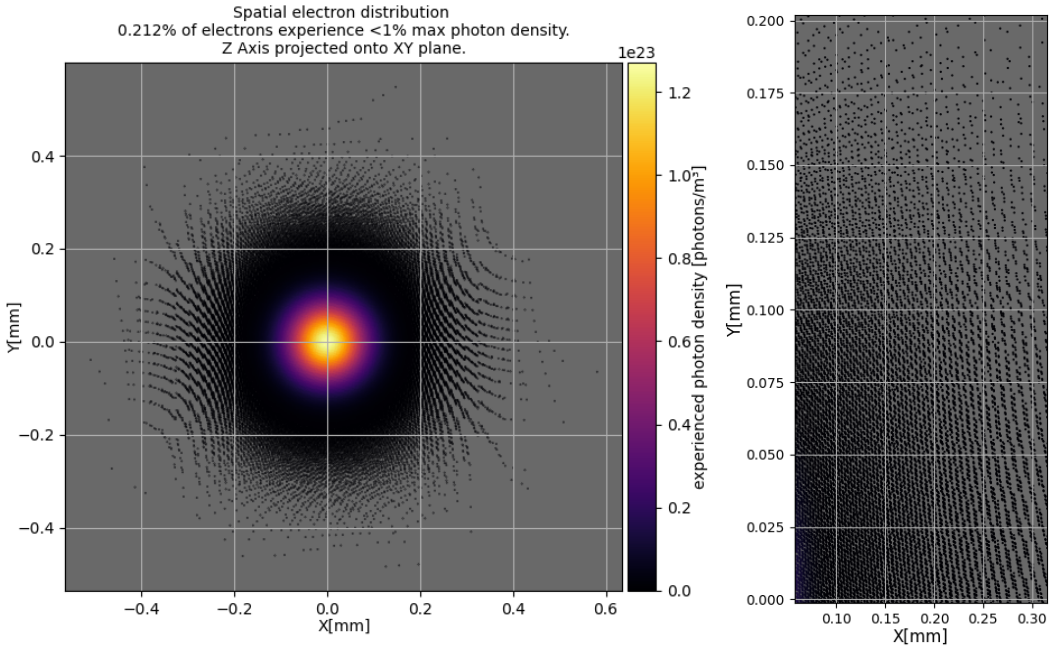

(a) Wave-like structures are visible in the outer area

(b) Close-up of electron distribution fine structure

Figure 4.5.: Astra generated electron distribution with Hammersley injection activated displayed via Comparse "Visualize Interaction". The quasi numerical distribution avoids clustering of electron placement but leaves distinct traces.

charge" for the Comparse internal `macro_particle` parameter used to correctly calculate scattering probabilities per line of data and finally "particle index". While Astra has 4 pre-built particle types, 1: electrons, 2: positrons, 3: protons and 4: hydrogen ions, Comparse v1.0 can only adjust the calculations between proton and electron beams and is thus limited to values 1 and 3 in the "particle index" column.

Notes on the Astra Format Energy Reference Row

In the Astra particle distribution format, the first row is defined as a reference row. It represents the bunch center and can be used as the reference particle. All other rows represent particles defined in reference to the first row, meaning that the values of these particles are defined in the reference particle frame. This allows Astra to keep value precision high despite limiting the column width. An example: Using Astra Generator without activating the `high_res` flag limits the data in each column to 4 decimal values in exponential notation. For relativistic particle distributions of low energy spread, this limit would make it impossible to write Gaussian distribution variance originating in energy into the longitudinal momentum. For instance, let us consider a 250 MeV electron bunch with less than

0.01% relative deviation. One example particle may have a momentum deviation of $\Delta p_z = 0.2411\,\text{keV}$. This value would be written as `2.5002+E06` in Astra, rounding all decimal places of Δp_z to the zeroth. Using a reference row solves this issue. With it, the first row contains `2.5000+E06` and the particle row corresponding to this example `2.4111E+02`, preserving the precision in the longitudinal momentum column.
The example above was meant to illustrate the use of a reference row, but does not accurately describe Astra's implementation. Perhaps confusingly, the Astra reference row does not directly contain the longitudinal momentum or kinetic energy in the longitudinal momentum column `pz`. Instead, in the reference row, column `pz` displays the total particle momentum p_{total} in units of $[mc^2]$ [32]:

$$p_{total} = \sqrt{\left(\frac{E_{kin}}{mc^2} + 1\right)^2 - 1} \tag{4.1}$$

Internally, Comparse handles particle distributions without reference row. To convert the Astra format data file to a Comparse data array, Comparse first copies and saves all Astra position columns as Comparse `position` $(3,N_{par})$-dimensional array and saves each momentum column as it's own array of dimension $(1,N_{par})$: `hor_mom`, `ver_mom` and `lon_mom`. Afterwards, Comparse saves the Astra reference row `pz` value as float type variable `astra_row_1_e` $= p_{total}$. From this, reference kinetic energy variable $E_{kin,ref}$ = `ekin_ref` is calculated through

$$E_{kin,ref} = \sqrt{p_{total}^2 + E_0^2} - E_0^2 \tag{4.2}$$

where $E_0 = mc^2$. In the next step, this kinetic energy $E_{kin,ref}$ is added to all non-reference row p_z values in direct summation. Additionally, $E_{kin,ref}$ is set as the first value `lon_mom[0]` of Comparse array `lon_mom`. The absolute particle energy E_{par} required for four-vector algebra is then calculated by

$$E_{par} = \sqrt{p_x^2 + p_y^2 + p_z^2 + E_0^2} \tag{4.3}$$

Finally, a four-vector array of dimension $(4,N_{par})$ is created from the 4 energy and momentum vectors. Every value is in units of electron volt. The conversion described above is written in Comparse as:

```
astra_row_1_e = np.copy(el_lon_mom[0])
ekin_ref = np.sqrt(astra_row_1_e**2+self.E0**2)-self.E0
el_lon_mom = el_lon_mom + ekin_ref
el_lon_mom[0] = ekin_ref
el_abs_energy = np.sqrt(
    el_hor_mom ** 2 + el_ver_mom ** 2 + el_lon_mom ** 2 + self.E0 ** 2)
vier_el_ak_lab = np.array(
    [el_abs_energy, el_hor_mom, el_ver_mom, el_lon_mom])
```

There is still a matter of precision left to be aware of. Reshaping eq.4.1 to

$$E_0 = \frac{p_{total}^2 - E_{kin}^2}{2E_{kin}} \tag{4.4}$$

allows us to check if Astra's rest mass expression is accurate by overwriting E_{kin} with the reference energy entered into the Astra Generator input file.
A series of electron distributions has been created in Astra. Energy spread was left at `sig_z=0.64` for all, while `Ref_Ekin` was set to 0.5, 5, 100 and 10000 MeV. For each value, particle distributions were created with `High_res = True` and `High_res = False`. The calculated rest energies E_0 reveal the issue: As one can

Input Configuration	**Calculated Astra E_0 [eV]**
10 GeV High Prec.	511002.9955366912
10 GeV Low Prec.	1000049.9999997952
100 MeV High Prec.	511002.99998447
100 MeV Low Prec.	511300.5
5 MeV High Prec.	511003.0000003719
5 MeV Low Prec.	511046.129
0.5 MeV High Prec.	511002.9999999733
0.5 MeV Low Prec.	510994.5225

Table 4.2.: Calculated electron rest energy E_0 used by Astra to create energy reference row value p_{total}

see in tab.4.2, the calculated Astra E_0 value, assuming that E_{kin} is as declared in the input file, is inconsistent and often deviates considerably from the current literature value of 0.510 998 95 MeV. This indicates that despite using a reference row to improve precision, Astra still introduces a measure of value deviation due to a limited column width of only 4 decimals in low precision and 12 in high precision mode. The deviation increases with the reference energy, as the E_0 value is written into higher decimal places. An extreme example is "10 GeV Low Prec." in tab. 4.2, where the 511 keV was apparently rounded up to 1 MeV before further imprecision was added in the data processing. As a result, when read by Comparse, the particle distribution's reference kinetic energy $E_{kin,ref}$ will deviate from the intended value in it's lower post decimal positions. To visualize the effect in a concrete example, loading a `High_res = True` Astra electron distribution with a set `Ref_Ekin = 105`(MeV reference kinetic energy results in a `"center kinetic energy [eV]"` of $E_{kin,ref}$ = 105000004.03040488 in Comparse. While users may expect Comparse to mirror the reference electron energy defined in Astra's "generator" module, 105 MeV, in the translation to Comparse's data structure, the reference kinetic energy is re-calculated using the literature value for E_0 in float128 precision. Despite this deviation, the file import is working as intended and as best as possible under Astra precision constraints.

Let us emphasize, that the electron distribution .ini file, despite using the Astra output format, does not need to originate in Astra. As long as the correct value type is found in each column, any TSV file can be read. Furthermore, in Comparse, scattered electron distributions can be exported as an Astra format TSV.ini file for data analysis in Astra or use as a new input file in Comparse. Should users generate Astra format particle distribution of higher precision by any other means, then $E_{kin,ref}$ calculated in Comparse will be closer to the initially set value. In lieu of this, we strongly recommend using Astra Generator with the `High_res` flag set to `True`, to limit additional sources for errors and imprecision.
Comparse's internal, rudimentary Gaussian distribution generation module "Fermion Generator" does not include this behavioural quirk and generates particles around the precise value of the initially declared $E_{kin,ref}$. As of v1.0, it lacks Hammersley sequence injection in the Gaussian distribution sampling.

4.2.2. Generating the Electron Distribution in Comparse

As an alternative to importing fermion particle distributions written in the Astra format, Comparse features it's own Gaussian distribution generator. This is intended for users wishing to make spontaneous changes to their fermion distribution and those currently without access to Astra.

4.2.2.1. Fermion Generator User Interface Input Mask

The input UI for the Fermion Generator method of Comparse is accessed via the "Fermion Generator" menu item of the "Fermion Gen" window top header menu. The small window shown in fig. 4.6 has an expandable menu initially labelled "Fermion" in which users can select between "Electron" and "Proton". This decides the particle type of the distribution to be generated. Internally, Comparse adjusts particle dependent constants such as rest mass and base charge. Below, there are 9 input fields defining the initial parameters of the distribution: the reference kinetic energy E_{par}, bunch charge Q_{par}, number of macro particles N_{par}, three input fields for the spatial position distribution variances σ_x, σ_y and σ_z as well as three variances for the momentum distribution $p_{x,\sigma}, p_{y,\sigma}$ and $E_{par,\sigma}$.
At the bottom of the input fields, a button labelled "Mirror" copies the corresponding main fermion window values from an already active fermion distribution and pastes them into the generator input fields. This way, users can make quick adjustments to parameters of currently investigated particle distributions.
Finally the "Generate" button calls Comparse's `generate_gaussian_electron_⌋distribution(...)` method from `fermion_class.py`.

4.2.2.2. Mathematical Realization of Fermion Generator

Comparse's internal Gaussian particle distribution generator uses method `gen_⌋gauss_xyz(...)` located in `fermion_class.py` for both position and momentum in 3D space. The method's input parameters are described in tab. 4.3. As of

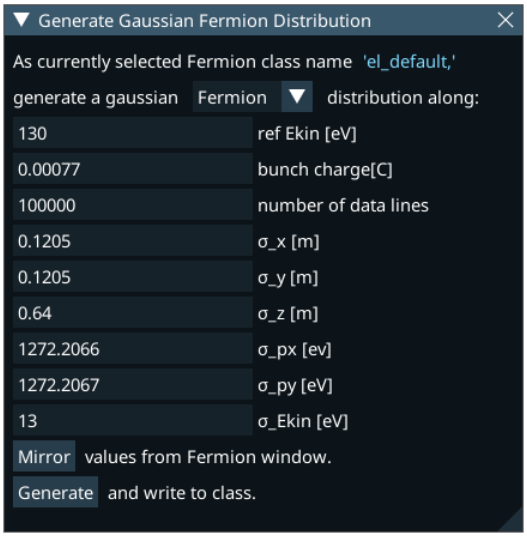

Figure 4.6.: Gaussian fermion distribution generator window of Comparse v1.0.

Name	Shape	Description
`sigs`	(3)	3 variances corresponding to 3 dimensions $\sigma_x, \sigma_y, \sigma_z$
`num`	(1)	the number of particles N_{par}
`correl`	(3)	3 correlation factors corresponding to 3 dimensions. If no value is given, the factors are set to zero. C_{xy}, C_{xz}, C_{yz}
`mean`	(3)	3 mean values around which the Gaussian distribution is created in the 3 corresponding dimensions. If no value is given, the means are set to zero. $\overline{x}_{el}, \overline{y}_{el}, \overline{z}_{el}$

Table 4.3.: Input variables of Comparse method `gen_gauss_xyz(...)`.

v1.0, Comparse creates Gaussian particle position and momentum distributions without dimensional correlation. In the backend however, correlation factors are already implemented. Upon executing `gen_gauss_xyz(...)`, a covariance matrix is created [33]. As the expected value of each dimension is included one step later, this covariance matrix is simplified and can be written as:

$$\mathbf{M}_{cov} = \begin{pmatrix} \sigma_x^2 & C_{xy}\sigma_x\sigma_y & C_{xz}\sigma_x\sigma_z \\ C_{xy}\sigma_y\sigma_x & \sigma_y^2 & C_{yz}\sigma_y\sigma_z \\ C_{xz}\sigma_x\sigma_z & C_{yz}\sigma_y\sigma_z & \sigma_z^2 \end{pmatrix} \tag{4.5}$$

Here, covariance C_{ij} is introduced for dimension i and j. Next, numpy function `np.random.default_rng().multivariate_normal(...)` is executed with `mean`,

$\mathbf{M}_{cov}$ and N_{par} as input parameters. It generates N_{par} values sampled from a 3-dimensional Gaussian distribution around `mean` using the $\mathbf{M}_{cov}$ covariance matrix describing the dimensions of the Gauss curves in space. The returned data is assigned to variables x, y, z. Lastly, `gen_gauss_xyz(...)` returns an array containing x, y, z. The final returned data is written in the form of a numpy array with shape $(3 \times N_{par})$. This routine is executed twice to create the 3D particle position array and the 3d particle momentum array, each with the unit corresponding variances $\sigma_{par,i}$ respectively $p_{i,\sigma}$ or $E_{par,\sigma}$. The expected value array `mean` is set to $(x, y, z) = (0, 0, 0)$ for the particle position and to $(p_x, p_y, E_kin) = (0, 0, E_{par,ref})$ for the momentum.
This rudimentary approach to particle distribution generation is not meant to replace Astra import for high precision simulations, but instead for rapid iteration studies that only need to produce approximate results. Despite that, a python console health check printout shows, that the key parameter means are closely recreated from the Astra format input file. When calculating the variances $\sigma_x, \sigma_y, p_{x,\sigma}$ and $E_{el,kin,\sigma}$, using them as input parameters for Comparse's internal Gaussian distribution generator and then re-calculating them over the newly generated samples, one can expect deviations in the third decimal, as one example illustrates:

```
   electron generation health check:
sigx:0.0001694099997369193 vs  0.00016931537139022368
sigz:0.0006399143916183355 vs  0.0006370158599244747
sig_px:904.9105733912139 vs  905.2929850351863
sig_Ekin:10498.694211142114 vs  10439.79458518062
```

$$\Delta\sigma_x = 9.4628 \cdot 10^{-8} \quad \text{m} \qquad \Rightarrow \frac{\Delta\sigma_x}{\sigma_x} = 0.0559\%$$

$$\Delta\sigma_z = 2.8985 \cdot 10^{-6} \quad \text{m} \qquad \Rightarrow \frac{\Delta\sigma_z}{\sigma_z} = 0.4530\%$$

$$\Delta p_{\sigma,x} = -0.3824 \quad \text{eV} \qquad \Rightarrow \frac{\Delta p_{\sigma,x}}{p_{\sigma,x}} = 0.0423\%$$

$$\Delta E_{el,\sigma} = 58.8996 \quad \text{eV} \qquad \Rightarrow \frac{\Delta E_{el,\sigma}}{E_{el,\sigma}} = 0.5610\%$$

The original Astra input calculated values are written on the left side while the mirrored Comparse generated and then re-calculated values are on the right. During this study, a meaningfully greater deviation was not observed.

4.3. Photon Distribution Generation

As opposed to fermion distributions, photon distributions cannot be created or imported with arbitrary position data, instead, they are matched to a fermion

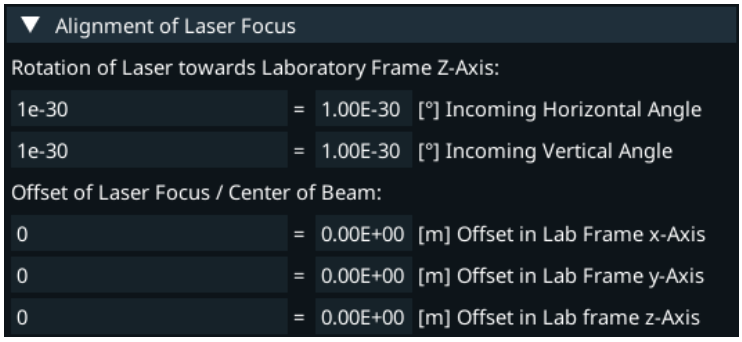

Figure 4.7.: Comparse user interface laser focus alignment section.

distribution already loaded into program. When selecting to generate a photon distribution using either the "Flattop Cylinder" or "Gauss Beam" button, the respective methods `cvi_photon_distribution(...)` (Gauss) and `flattop_cylinder_distribution(...)` located in `laser_class.py` are executed. In every fermion macro particle position, a photon represented by a four-momentum vector $\mathbf{k}$ is created. Additionally, a value termed "experienced photon density ρ_{ph} is calculated at every fermion macro particle position. This term represents the density of photons in space ($[\frac{\text{ph}}{m^3}]$) at this location and heavily depends on the selected photon distribution model and parameters. There is no need to generate a 3D position in space array for the photon distribution. We are only interested in the photon description of electromagnetic fields in places where potential ICS scattering events take place, in other words, at the fermion positions. This means, that regardless of the number of photons indicated by the photon density, only photons colliding with electrons are generated. Thus, N_{par} also represents the number of photons in the generated distribution.

4.3.1. Gauß Beam Laser Model

Comparse's Gaussian laser beam model was developed on the basis of the description found in the oft referenced "Historic Technical Guide" published in 2009 by what was at the time a single company named "CVI Melles Griot" that since then split into "CVI Laser Optics" and "Melles Griot". It is still available on the website of the "IDEX Health & Science" company as it is popular among universities and colleges [34].

For the Gaussian beam laser simulation, `cvi_photon_distribution(...)` is called by users selecting the "Gauss Beam" option in the photon menu. As the initial step, a potential offset of the laser focus defined by the users in the "Alignment of Laser Focus" collapsible header menu (fig. 4.7) is taken into account. On the grounds that translation and Euler transformation of every Gauß beam defining function is complicated, we instead transport every macro fermion position from the laboratory frame to the laser focus center. Still, this operation is performed only if changes have been made to any of the default values of the Alignment of Laser Focus

input fields. If changes have been made, Comparse method `transfer_fermion_pos_to_laser_center(...)` located in `laser_class.py` is called, in which a simple $x' = x + x_{\text{offset}}$ addition that translates the fermion positions is followed by a matrix multiplication of the 3D position with the Euler rotation matrix $\mathbf{M}_{rot}$ constructed by the incoming Laser rotation angles defined in the UI. The latter is performed via `transfer_laser_xyz_to_lab_frame(...)` also located in `laser_class.py`:

```
def transfer_laser_xyz_to_lab_frame(self, compton_class, xyz):
    ec = compton_class
    xe = xyz[0] + self.offset[0]
    ye = xyz[1] + self.offset[1]
    ze = xyz[2] + self.offset[2]
    offset_pos = np.array([xe, ye, ze])
    rotated_pos = np.einsum('jk,ij', offset_pos,
        uv.euler_trafo_matrix_3x3(self.inc_angle_horz,
                                  self.inc_angle_vert,
                                  0))
    return rotated_pos
```

With this transformed position array, the distance to the longitudinal laser axis r is calculated via

$$r = \sqrt{x'^2 + y'^2} \tag{4.6}$$

Next, for every particle index, a corresponding photon wavelength λ_i is randomly determined from a normal distribution based on reference wavelength λ_{ref} and spectral bandwidth $\Delta\lambda$ input parameters. Instead of reference wavelength λ_{ref}, the particle index dependent array λ_i is inserted in the real laser beam propagation equation (2.27) of [34] for the longitudinally dependent Gauß beam waist $w_{\text{R}}(z)$:

$$w_{\text{R}}(z) = w_{0\text{R}} \sqrt{1 + \left(\frac{z \lambda_i M^2}{\pi w_{0\text{R}}^2} \right)^2} \tag{4.7}$$

Here w_0 is the beam waist at it's narrowest in the flat part of the wavefront, z is the longitudinal laser beam axis position and M^2 is the beam divergence factor, also known as beam quality factor, that describes the beam propagation ratio. w_0 and M^2 are defined by the user in the Comparse UI in the "focal beam waist radius" and M^2 input fields before the creation of the distribution is initiated.
Having defined the beam waist radius over z, we can calculate the spatially dependent irradiation intensity of the Gauß beam:

$$I(r, z) = I_0(t) \left(\frac{w_{0\text{R}}}{w_{\text{R}}(z)} \right)^2 e^{\frac{-2r^2}{w_{\text{R}}^2(z)}} \tag{4.8}$$

A few explanations regarding the newly introduced variables are in order. $I_0(t)$ is defined as the origin intensity in the Gauß beam center $r = 0, z = 0$ at time t.

Note that time dependence is discussed in it's own section 4.5.4, so for now, we will describe the equation for time $t = 0$ at the temporal zenith of the laser beam pulse.

$$I_0 = \frac{2}{\pi w_0^2} \tag{4.9}$$

The unit of I_0 as defined in eq. 4.9 and implemented in Comparse is $[\frac{\mathrm{ph}}{m^3}]$. In it's common form, I_0 is defined with an added total beam power P in the numerator of the fraction, resulting in unit $[\frac{\mathrm{W}}{\mathrm{m}^2}]$. However, we are evaluating the Gauß beam intensity to target photon density experienced by fermions ρ_{ph}. With the single particle pair cross section W (eq. 3.76), we can then calculate the probability $W_{ics,norm}$ (eq. 4.25) of a fermion scattering with any photon of the laser pulse. Thus, we calculate ρ_{ph} from $I(r, z)$ as:

$$\rho_{ph} = N_{ph} I(r, z) \tag{4.10}$$

After calculating one of the key attributes we require from the photon distribution in ρ_{ph}, we shall continue with the photon four-momentum creation. In service of this, we first calculate the far field divergence angle of the Gauß beam θ_{ff}.

$$\theta_{ff} = \frac{\lambda_{ref} M^2}{2\pi w_0} \tag{4.11}$$

Now, a θ_{ff} scale normal distribution is created from which a random angle $\theta_{g,i}$ is selected for every particle index i. This constitutes the orbital angle of a photon towards the longitudinal center axis $\vec{z}_g$ of it's Gauß beam. For the corresponding azimuthal angle $\phi_{g,i}$ around $\vec{z}_g$, a simple random choice between 0 and 2π is performed. As a last step before formulating photon four vector $\mathbf{v}_{ph}$, the photon specific wave number is created from the bandwidth defined initial wavelength array.

$$k_i = 2\pi\lambda_i \tag{4.12}$$

Following this, `build_vier_ph_ak_lab(...)` of `laser_class.py` is executed for all particle indexes i. In this method, first, the specific initial photon energy E_{ph} is calculated from wavenumber k_i.

$$E_{ph} = \hbar c k_i \tag{4.13}$$

Photon momentum vector $\vec{v}_{ph}$ can now be expressed as

$$\begin{aligned} k_x &= \quad E_{ph} \sin\theta_{g,i} \cos\phi_{g,i} \\ k_y &= \quad E_{ph} \sin\theta_{g,i} \sin\phi_{g,i} \\ k_z &= -E_{ph} \cos\theta_{g,i} \\ \vec{v}_{ph} &= \quad (k_x, k_y, k_z) \end{aligned} \tag{4.14}$$

As it stands, $\vec{v}_{ph}$ is derived in the laser Gauß beam frame. For the photon four-vector to be congruent in the fermion defined laboratory frame, we need to rotate it's 3D momentum components $\vec{k} \cong$ `drei_ph_ak_lab` with the inverse Euler rotation we used to transport the fermion positions into the laser Gaussian beam center frame.

```
drei_ph_ak_lab = np.einsum('ij,jk',
                           uv.euler_trafo_matrix_3x3(self.inc_angle_horz,
                                                     self.inc_angle_vert, 0),
                           drei_ph_ak_lab)
```

The code above executes rotations around two axes (horizontal and vertical) over the momentum vectors belonging to all photons using vectorized implementation. See sec. 4.4.2 for a detailed explanation of these operations.
Now at last, the Euler transformed $\vec{v}_{ph,rot}$ array is used to define the photon four-momentum $\mathbf{v}_{ph}$ and unit vector $\vec{u}_{ph}$ arrays.

$$\mathbf{v}_{ph} = \begin{pmatrix} E_{ph} \\ k_{x,rot} \\ k_{y,rot} \\ k_{z,rot} \end{pmatrix} \tag{4.15}$$

$$\vec{u}_{ph,i} = \vec{v}_{ph,rot,i} / \left(\sqrt{\sum_i |\vec{v}_{ph,rot,i}|^2} \right) \tag{4.16}$$

An example result of a laser Gauß beam with 1 mm center translation and 10° incoming angle rotation offset is shown in fig. 4.8.

Comparse's laser Gauß beam has been used for all studies conducted for this thesis, except when explicitly stated otherwise.

4.3.2. Short Flattop Pulse

Once the default model, due to it's oversimplification, the Flattop Cylinder photon distribution generator now serves only for debugging solutions and simulations interested solely in the reference scattered energy. Once the "Flattop Cylinder" button is pressed inside of the "Photon Distribution" window, `flattop_cylinder_distribution` is activated. In it, a cylinder volume $V_{cylinder}$ is calculated as follows:

$$l = 6\sigma_{ph,z}c \tag{4.17}$$

$$r = w_0 \tag{4.18}$$

$$V_{cylinder} = l\pi r^2 \tag{4.19}$$

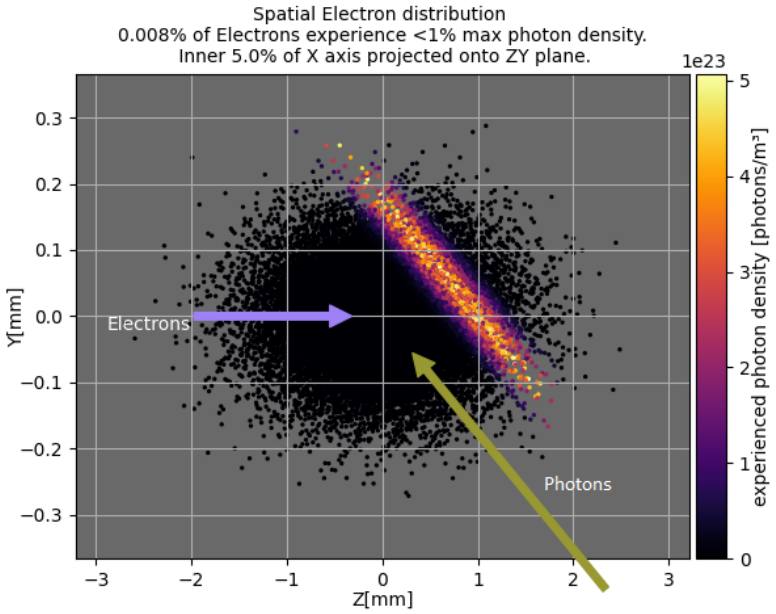

Figure 4.8.: Interaction of laser Gauß beam with electron distribution. Simulated and generated in Comparse using a MESA ER-IB-42m-nominal (App. tab. A.2) Astra generated electron distribution and Tangor-100-IR-focused (App. tab. A.8) presets.

The top C_1 and bottom C_2 center position of the cylinder is defined in the laser focus frame as:

$$C_1 = \left(0, 0, -\frac{l}{2}\right) \tag{4.20}$$

$$C_2 = \left(0, 0, \frac{l}{2}\right) \tag{4.21}$$

$$\tag{4.22}$$

Both center points are then transferred into the fermion lab frame analogously to the way described in sec. 4.3.1 using rotation and translation offset input values. C_1, C_2 and r now constitute the base cylinder data given to `check_cylinder(...)` executed from `unit_vectors_angles.py` in which the mathematical solutions detailed in section 4.7 are combined as visualized in fig 4.16. This method returns the indices of the particles found inside of the cylinder volume defined by C_1, C_2 and r. For these indices, a photon density

$$\rho_{ph,cylinder} = \frac{N_{ph}}{V_{cylinder}} \tag{4.23}$$

is calculated while those indices pointing to fermions outside of the cylinder are assigned $\rho_{ph} = 0$. This means,that only fermions found inside of the cylinder volume can experience ICS scattering.

To close the Flattop Cylinder distribution generation, a photon four-vector is created using the same `build_vier_ph_ak_lab(...)` method used in the Gauß beam generation. Here, however, there is no gaussian momentum angle distribution: All photons initially point the same direction defined by the alignment input values. Only a gaussian wave number distribution derived from the incoming laser spectral bandwidth $\Delta\lambda$ inserts a measure of variation into the photon four-vector $\mathbf{k}$. Naturally, the bandwidth can be set to zero by the user, if they wish to investigate all identical incoming photons.
An example result with offset and angle can be seen in fig. 4.9

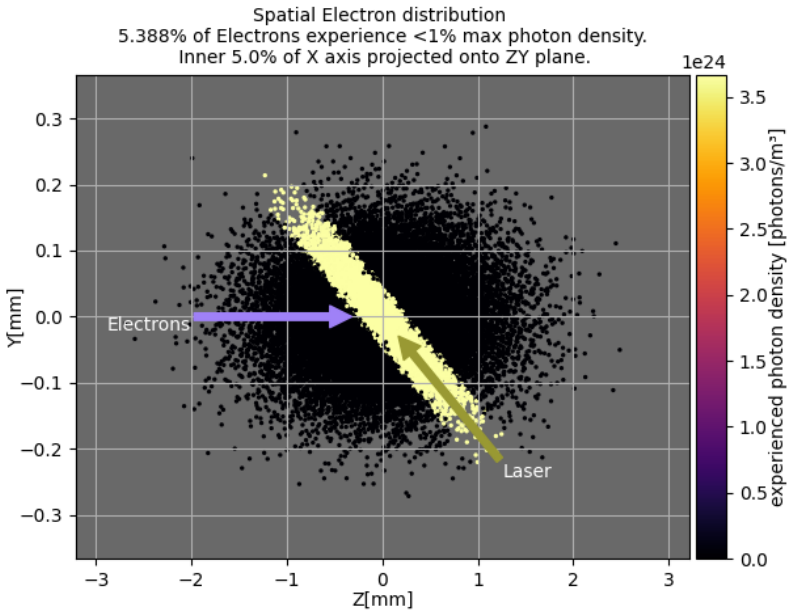

Figure 4.9.: Interaction of Flattop Cylinder photon distribution model with electron distribution. Simulated and generated in Comparse using a MESA-ER-IB-42m-nominal (App. tab. A.2) Astra generated electron distribution and Tangor-100-IR-focused (App. tab. A.8) presets.

4.4. Comparse Data Dimensions

The first step of every Comparse simulation routine is the generation, import or loading of a fermion class containing a macro particle distribution. This distribution has a certain finite size corresponding to the number of macro particles N_{par}. As a result, every macro particle is assigned a specific numerical value referred to as "index" in this work. Most Variables used in Comparse are stored internally as NumPy arrays [29], that can assume an arbitrary dimensional data shape. The NumPy Python module contains many functions to facilitate parallel calculations of multi dimensional variables. This is called vectorized algebra and a key requirement

of writing efficient code for numerics. The meaning of these data dimensions and the mechanics of NumPy arrays are best illustrated by example.

4.4.1. NumPy Array Shape Examples

The overall kinetic energy of a particle i is a one dimensional scalar E_i. If the task requires the differentiation between different particles, the usual approach is an index i referencing each individual entity. Written as a NumPy array, one can assign all particles to one variable $E_{all} = [E_0, E_1, E_2 ... E_{n-1}]$ which in Python code would be `e_array = np.array([e_0, e_1, e_2 ... e_n])`. This array object has the shape `(n)` and it's indices i are comprised of the natural numbers $\mathbb{N}$ from 0 to $n-1$. Any single value stored that way in the array can be accessed via the standard Python indexing notation: `e_array[i]` returns E_i, `e_array[:]` returns all values.
Let us now consider the result of replacing energy scalar E_i with a multi-dimensional variable such as momentum $\vec{p} = (p_x, p_y, p_z)$. Constructing an array of momentum vectors $\vec{p}$ for each particle would result in an array of shape $(n, 3)$. We shall call it `momentum_array`. The new variable represents a tensor of *rank* 2, as 2 indices are required to fully specify a value entry. If one requires just the p_x components of the array, a view can be created and linked to a variable `all_p_x` by slicing the array as such: `all_p_x = momentum_array[:,0]`. Here, ":" in the first index position referred to number of particles dimension "n" and returned all, while "0" referred to the vector component dimension and returned the first of 3, defined as x in Comparse notation (x,y,z = 0,1,2). This new variable `all_p_x` has shape (n) and therefore rank 1. It is a view, not an entirely new object, which means that it still points to the same location in the computer memory. As a result, creating a view of an n sized array does not require more memory capacity for greater n. Analogously, if one wanted to create a view of the three dimensional momentum vector of a specific particle $\vec{p}_i =$ `v_pi`, one would write `v_pi = momentum_array[0,:]`.
The complexity of the array shapes can be considerably higher. As of v1.0, Comparse's most complicated NumPy array shape is the coded Stokes transformation matrix T of eq. 3.77. T represents a tensor of rank 5 and it's shape is $(4, 4, N_{par}, \rho_\phi, \rho_\theta)$, whereas $(4, 4)$ is due to the algebraic shape of a 4×4-matrix, (N_{par}) is the number of fermion - photon macro particle pairs that the calculation is executed over at once and (ρ_ϕ, ρ_θ) refer to the two spherical coordinate angles azimuth (ϕ) and orbital (θ) that span a direction grid in 3D space. For further details on this angle grid, see sec. 4.6.1.1.

4.4.2. NumPy Arrays as Part of Equations

As a consequence of Comparse being based on analytical equations and written in order to solve numerical tasks, it is formulated in vectorized algebra realized through NumPy arrays. In ideal scenarios, authors can formulate equations for arrays verbatim as they would for single scalar variables. NumPy then executes

the mathematical operations using highly efficient methods written in C for all values found inside of an array. In practise, programmers often have to provide extra instructions to NumPy to unambiguous define their intention.

(a) Array to Scalar **(b)** Array to Array

Figure 4.10.: Default calculation mapping when using NumPy arrays without explicit dimension commands. Note that fig. 4.10b only resolves if the dimension of both arrays has the same size.

4.4.2.1. NumPy Arrays and Single Value Variables

An array object of any shape interacts with a float or integer single value scalar object the same way a single value scalar object would with another. For illustration purposes, we will once again use the $(n, 3)$-shaped `momentum_array` from before. Multiplication with a factor 2 is written the same way one would write single value $\times$ single value multiplication: `momentum_array_2 = momentum_array * 2`. This multiplies every value `momentum_array` with 2 at once as visualized in fig. 4.10a. All basic algebraic operations with single value scalars work similarly.

4.4.2.2. NumPy Array on Array Operations

Array $\times$ array operations function differently depending on the shape of the arrays. If both arrays have the same shape, then the mathematical operation is executed for each corresponding value pair. See fig. 4.10a. Two arrays of different shapes cannot perform mathematical operations on another without further definitions. The NumPy module features a large number of common mathematical operations in the form of methods in which users can define the axi upon which the operation is supposed to be executed on. In NumPy terminology, an axis refers to the position in the array shape expression. As a concrete case, for shape $(n, 3)$ of `momentum_array` array, axis 0 refers to the number of particles n and axis 1 refers to the 3 momentum components. As an example, the average vector length of each particle is calculated by mapping NumPy function for the norm of an array over axis 1 by writing `np.linalg.norm(momentum_array, axis=1)`. This operation returns a new array of shape (n). The explanation of common Python broadcasting rules is outside the scope of this thesis. However, as the mathematical requirements of Comparse are very complex, more advanced techniques had to be employed in

order to vectorize the analytical equations of ICS.

4.4.2.3. Einstein Sum Convention Defined Operations on NumPy Arrays

NumPy features a module that executes mathematical operations defined by Einstein sum convention. This convention was proposed by Albert Einstein in his 1916 article "Die Grundlage der allgemeinen Relativitätstheorie" [35] in order to simplify the expression of tensor based equations. The main decision related to the index sum notation, for which Einstein defined, that repeated indices always constitute summation only over the repeated index and thus, the sum sign can be left out. This often applies when solving matrix or vector products, as those operations can be formulated via summation over rank indices. As an example, the matrix & vector product $\mathbf{M} \cdot \vec{v}$ can be expressed as $\sum_i M_{ij} v_j$ which in Einstein sum notation becomes $M_{ij} v_j$. With knowledge of this notation, vector algebraic operations can be precisely defined for specific indices of higher ranked arrays using NumPy's `einsum` method. It requires two arrays and an Einstein sum convention compliant index string reduced to only the indices. We shall present two concrete examples of implementation in Comparse.

4.4.2.4. Product of Transformation Matrix and polarization Array

A unique feature of Comparse is the calculation of the angle and polarization dependent scattering probability through vectorized resolution of the Stokes transformation matrix $\mathbf{T}$ (eq. 3.76) on large data sets. The first step to resolve the equation requires matrix - vector product $\mathbf{T} \cdot \boldsymbol{P}$. Both $\mathbf{T}$ and $\boldsymbol{P}$ are saved as high rank tensors in Comparse. The dimensions and rank indices are defined as

$$\texttt{mcm\_trafo\_matrix\_T} : (\overbrace{4}^{i}, \overbrace{4}^{j}, N_{par}, \rho_\phi, \rho_\theta)$$

$$\texttt{pol\_array} : (N_{par}, \rho_\phi, \rho_\theta, \underbrace{4}_{j})$$

and with this, we can write the vectorized matrix - vector product in Python as:

```
S_f = np.einsum('ij...,...j', mcm_trafo_matrix_T, pol_array)
```

A shortcut was taken: Only the matrix and vector shape defining indices are explicitly given. Writing an ellipsis is interpreted as "assign non repeating indices to all ranks before or after the given indices". Thus, only j repeats, and we execute Matrix - vector product $\sum_i^4 \mathbf{T}_{ij} \boldsymbol{P}_j$ over all combinations of N_{par}, ρ_ϕ and ρ_θ at once. The resulting array of the Stokes parameters after scattering `S_f` has the shape $(N_{par}, \rho_\phi, \rho_\theta, 4)$.

4.4.2.5. Outer Product over Arrays in Equations

In other scenarios, Einstein sum convention can be used for tasks that are originally not vector based in nature. One such tasks is the product of the scattered photon energy in the electron rest frame k and the scattering direction $\vec{n}$ that results in the 3 vector momentum $\vec{k}$ used in Stokes transformation T in eq. 3.77. In the analytical equation form, this is a trivial scalar and unit vector multiplication, but in Comparse's vectorized approach, energy scalar k has the array shape $(N_{par}, \rho_\phi, \rho_\theta)$ whereas unit vector $\vec{n}$ is shaped $(3, \rho_\theta, \rho_\phi)$ due to their dependence on the scattering direction and in k's case the initial particle's momenta. The desired shape of the product's result should be a 3 component vector depending on particle index and angle densities. For this, we can formulate an outer product with the Einstein sum convention string in NumPy as follows:

```
kmcmv = np.einsum('inm,jmn->jmni', space_point_vector_cart, kmcm)
```

Using the optional arrow `"->"` defines the target shape of the resulting array. By keeping `"mn"` representing ρ_ϕ & ρ_θ in the result to the right of arrow `"->"`, we explicitly state that these rank indices should be summed. By doing this, we create a $\vec{k}$ product matrix of uneven dimensions $(3, N_{par})$ for every ρ_ϕ & ρ_θ combination at once. The result referenced internally as `"kmcmv"` has the shape $(N_{par}, \rho_\phi, \rho_\theta, 3)$.

4.4.2.6. Performance Improvements due to Vectorization using NumPy

NumPy's backend is implemented in C, which greatly improves performance compared to native Python code [36]. For the Python programmer, Numpy vectorization appears to calculate every value of an array at once. Despite that, calculations are still performed using loops. Due to the C level execution of these NumPy loops, the benefits over Python loop operations are still considerable. Time of execution improvements vary between tasks and hardware, but are usually in the range of 2 magnitudes. Recreating every vectorized operation in native Python loops was outside of the scope of this thesis, however, as an example, outer product `kmcmv = np.einsum('inm,jmn->jmni', space_point_vector_cart, kmcm)` was recreated using for-loops over all dimensions and timed. The result, shown in 4.4 shows that this single operation would take over 180 times longer if written as a Python loop compared to it's currently implemented NumPy vectorized form.

For this thesis, studies were conducted using Comparse v1.0 with default values for

Python Loop Execution Time	19.8869 s
NumPy Einsum Execution Time	0.1101 s

Table 4.4.: Comparison of the outer product calculation of an array of shape $(3, 181, 360)$ and an another shaped $(221, 360, 181)$ between native Python loops and NumPy Einstein sum convention vectorization.

the spherical coordinate direction grid in the range of $\rho_\theta \cdot \rho_\phi \approx 65,000$ and macro

particle distribution sizes of generally $N_{par} = 100,000$. Depending on the target of the simulation, studies generally took between 1 to 45 minutes to complete. Using Comparse for rapid iteration, parameter scan or optimization studies would not be possible, if every mathematical step of the calculation were not vectorized. Assuming `kmcmv` is an example that can be projected upon all vectorized operations, study completion times recorded during the work on this thesis would increase from 1 to 45 minutes to an unfeasible length from 3 hours to 5+ days. It is clear, that without vectorization, the simulation data for this thesis could not have been assembled to it's current level of comprehensiveness.

4.5. Stochastic Scattering Decision with Recoil

As detailed in the overview section in fig. 4.1, a set of initial scattering parameters has to be gathered before the fermion - photon scattering can be simulated in detail. This set contains the four-momenta $\mathbf{p}$ & $\mathbf{k}$, photon density ρ_{ph} and fermion positions r_{par}. The gathering of scattering particles happens in Stage 4 of Comparse. In this step, the indices of the scattering particle pairs are determined per collision of a fermion bunch and a laser pulse via a stochastic check executed in method `stochastic_selection_of_scattering_particles(...)` described in section 4.5.1 following below. The initial scattering parameters of the particles referenced by the determined scattering indices are written to new arrays denoted with "`red_`" indicating a "reduced" subset of fermoions and photons, as the number of scattering particles N'_{par} has to be less or equal than the initial number of macro particles N_{par}.

$$N'_{par} = N_{par,scattering} \leq N_{par,macro} = N_{par,real} \cdot M_{par} = N_{par} \tag{4.24}$$

In eq. 4.24, we hint at a potential numerical issue: The initial particle distribution N_{par} is a macro particle distribution down sampled from a theoretical actual number $N_{par,real}$ that would be found in the fermion bunch according to it's bunch charge. In the macro particle distribution, one line of data is representative of a possibly higher number $M_{par} = (0–\infty)$ of fermions. However, in Comparse, scattering events are calculated for a group of "real" particles N'_{par} of macro factor $M_{par} = 1$. We will discuss the resulting problems and circumvention methods in section 4.5.3.
Depending on the experiment setup, the selection of scattering particles N'_{par} can reduce the data size significantly. With lasers at the lower end of the industrial pulse energy, it is possible, that of a $N_{par} = 100 \cdot 10^6$ fermion distribution, only less than one is expected to scatter. For this reason, Comparse has two ways of acquiring a sufficiently large scattering statistic without changing the experiment parameters.

1. Adjustable number of collisions n_{sim} of fermion bunches with laser pulses to be simulated
2. Numerical boost & damping factor B used in the scattering probability formula eq. 4.25

Users can configure over how many collisions Comparse is gathering scattering data. As the statistic check, described in section 4.5.1, completes extremely fast even for large data sets, a loop over a multitude of iterations is workable within a standard length simulation approach. Experience has shown, that the time to gather scattering indices almost never exceeds the length of the subsequent simulation steps. Only very low cross section ICS experiments can make the collection of large scattering data sets impracticable.
For these cases and those with the opposite problem, Comparse injects an artificial boost or damping factor in the scattering probability calculation. In it's default value $B = 1$, it has no effect on the simulation. For values above 1, it increases the scattering probability. That increase is afterwards removed from values dependent on the scattering probability, such as the scattered photon flux $\mathfrak{F}_\gamma$, to ensure an accurate evaluation of the simulation results. Generally, the value of B is a direct multiplicator to the expected number of scattering fermions per collision. As such, fractional values below 1 will lower the scattering probability. Values below zero are invalid. This too will be mentioned again when we discuss numerical issues and their solutions in subsec. 4.5.3.

4.5.1. Stochastic Selection of Scattering Particles

The core method of collecting the fermion and photon (FP) scattering data is Comparse method `stochastic_selection_of_scattering_particles(...)` that is part of `routines.py`. It is passed an instance of each internal class type, neutral, fermion and photon class and returns an array of shape (n) that contains all scattering indices of one macro collision. For single collisions, the initial distributions are sampled according to the scattering probability function. In case of looped executions over multiple collisions, the sampled and copied values are accumulated. After this, no reference has to be made to the initial fermion and photon distribution arrays. This avoids issues related to index repeats in NumPy list comprehensions when referencing the same initial particle pair multiple times.
The first physics related step is the calculation of the 4-dimensional recoil factor X according to 3.24 derived in section 3.1.3 for every macrofermion - photon combination. With this X as array, the particle pair specific cross section σ_{ics} is calculated. We have implemented the σ_{tot} expression solely dependent on recoil X of eq. 3.69 that was created by integrating over all scattering directions. The single variable dependence supports vectorization (sec. 4.4.2.6) for swift execution times but includes effects related to values of the fermion and photon four-vectors before scattering. σ_{tot} and is one factor of many that are part of the normalized scattering probability:

$$W_{ics,norm} = \sigma_{tot} \cdot n_{p,k} \cdot \rho_{ph} \cdot M_{par} \cdot Q_{u,par} \cdot B \cdot T_{rad} \tag{4.25}$$

whereas

σ_{tot} (N_{par}) Array; total ICS cross section eq. 3.69

$n_{p,k}$ (N_{par}) Array; normalized collision factor $n_{p,k} = c\,(1 - \vec{u}_{par} \times \vec{u}_{ph})$

ρ_{ph} (N_{par}) Array; photon density eq. 4.10 or eq. 4.23

M_{par} (N_{par}) Array; macro factor introduced above in eq. 4.24

$Q_{u,par}$ (N_{par}) Array; particle type charge sign adjust factor $Q_{u,el} = 1$, $Q_{u,pr} = -1$

B 1-D Scalar; user defined numerical boost factor

T_{rad} 1-D Scalar; irradiation time. Equals laser pulse length T_{pulse} in temporally static calculation mode, equals time step duration when simulating with temporal dynamics (sec. 4.5.4).

As all variables in this equation are implemented in either scalars or one dimensional N_{par} length NumPy arrays, the calculation is easily vectorized and the product quickly calculated for all particle pairs. The returned data is another 1-D NumPy array of length N_{par} with the total scattering probability for onefermion - photon macro particle pair $W_{ics,norm}$ in all fields. Note, that $W_{ics,norm} = 0$ represents no chance of and $W_{ics,norm} = 1$ guaranteed scattering. The array is saved as local variable "`cond`", referencing the scattering probability condition.
To introduce a measure of randomized variance that is intrinsic to Compton scattering experiments when conducted in a real setting, a NumPy array of equal length is created in which each field contains a random value between 0 and 1 using the NumPy built in function `random.uniform`:

```
rando_list = np.random.uniform(low=0, high=1, size=ec.el_amount)
numerical_index = np.where(rando_list <= cond)[0].tolist()
```

Finally, using the NumPy method `numpy.where`, a reduced list of only the particle indices where the random number between 0 and 1 is as great or greater than the scattering probability is returned. These indices representfermion - photon pairs that perform ICS as a result of the probability weight $W_{ics,norm}$ and the random chance introduce through the NumPy random number generator. Internally, the list is saved as local method variable `numerical_index`. The list of indices can then be used to access and copy all data related to the specific particles into new "`red_`" labelled NumPy arrays that can easily be appended with the data of further collisions. This way, the initial data of only the scattering particles is gathered in a fast performing routine that usually reduces the data size significantly for subsequent spatial simulations of higher complexity.

Notes on the Implementation of the Stochastic Selection Method

`stochastic_selection_of_scattering_particles(...)` described above is embedded in a Comparse method called `callback_gather_scattering_positions(...)`. In this, the selection method is executed within a loop of length n_{sim} defined by the user. This loop has two modes. By default, the photon distribution is newly created for each collision. The reason for that, lies in the randomized selection of

wavelength and wave vector angle described in section 4.3. For each collision, a fermion is matched to a new photon created with values randomized within the confines determined by the initial photon parameters. To improve the scattering data collection speed, this can be turned off. If the users removes the check mark from the checkbox labelled "Re-Use Same Photon Distribution", then the multiple collision loop with execute only the stochastic decision method described in this section while the initial photon distribution remains static. Throughout all studies conducted for this thesis, the execution speed of the gathering of scatteringfermion - photon pairs was always insignificant in comparison to scattering direction calculation time despite a new photon distribution being generated for every collision. The re-use of the generated photon distribution was thus left deactivated.
While generally, Python loops are avoided in Comparse, here, an exception is made. With large input data sets of single to triple digit megabytes, even calculating one collision can approach hardware limitations. Furthermore, many use cases have to work for an undefined number n_{sim} of collisions. One example is users spontaneously adding more collisions in order to accumulate a higher number of scatteringfermion - photon partners N_{par} while another is the flux estimation routine described in detail in the next subsection.

4.5.2. Statistical Flux Estimation Routine

Alongside the gathering of scattering partner data, the stochastic scattering selection method describe in the last section (sec. 4.5.1), is used for another key feature of Comparse: The statistical flux estimation routine `estimate_flux(...)`. Here, it is embedded in a looped routine with an undefined number of loops, only stopping when the iteratively averaged mean scattering particles per collision $\overline{\mathfrak{N}}_{ph,ics}$ is considered static. For this, only the length of `numerical_index` is saved to iteratively build $\overline{\mathfrak{N}}_{ph,ics}$ over looped collision simulations while no array of scattering indices is retained. This routine is the basis for gamma flux studies presented in this thesis, as it incorporates energy spread, momentum divergence and spatial distribution through the relativistic 4D recoil factor X (eq. 3.24) and photon density distribution ρ_{ph} (eq. 4.10), unlike commonly used luminosity formulas that often assume ideal collision scenarios. Our explanation will as usual focus on the mathematical aspects of the implementation. Methods and variables related to the user interface or internal data management will be omitted.
Comparse method `estimate_flux` requires an instance of all 3 class types, neutral, fermion and photon, as well as two variables named `criterion_runs` ($n_{sim,c}$) and `criterion_distance` ($\Delta\overline{N}_c$). These variables will define the stop criterion for the loop. In practise, this means that Comparse must have progressed to stage where both a fermion and photon distribution exists and is active. "Stochastical Flux Estimation Routine" becomes available at the same time as "Gather Scattering Partners". Before entering the loop, the following variables are locally declared for the `estimate_flux(...)` method as float data type with value 0: Every loop starts with the stochastic selection of scattering partners as described above up to

Name	Shape	Description
`sum_scattered`	(1)	total amount of scattered photons $N_{ph,acc}$
`runs_static`	(1)	counter for number of collisions during which $\overline{\mathfrak{N}}_{ph,ics}$ is considered static $n_{sim,s}$
`sim`	(1)	counter of all collisions simulated so far n_{sim}
`current_mean`	(1)	average number of scattered photons per collisions as currently iterated $\overline{\mathfrak{N}}_{ph,ics,i}$
`last_mean`	(1)	average number of scattered photons per collisions as per the previous iteration step $\overline{\mathfrak{N}}_{ph,ics,i-1}$

Table 4.5.: Internal variables of Comparse method `estimate_flux(...)`.

the point of returning the list of scattering indices `numerical_index`. It's length represents the number of scattering particles. This number is then added to local variable "`sum_scattered`". Next, the counter of simulated collisions is increased by 1 as per `runs += 1`. Now, the `current_mean` number of scattering particles per collision can be calculated via `current_mean = sum_scattered/runs`.
Next, the newly calculated `current_mean` is compared to the previously calculated `last_mean`. Different operations are performed depending on a condition check:

```
if np.abs(last_mean - current_mean) < criterion_distance:
    runs_static += 1
else:
    resets += 1
    dpg.set_value(nc.text_stochastic_flux_exp, resets)
    runs_static = 0
```

Let us explain this part: The absolute value of the difference between current and last mean iteration $\Delta_{i-1,i}\overline{\mathfrak{N}}_{ph,ics}$ is compared with input variable `criterion_distance`. If $\Delta_{i-1,i}\overline{\mathfrak{N}}_{ph,ics}$ is lower value, then $\overline{\mathfrak{N}}_{ph,ics}$ is considered static for this iteration and variable n_{sim} is increased by 1. If $\Delta_{i-1,i}\overline{\mathfrak{N}}_{ph,ics}$ is greater, then n_{sim} is reset to zero. This marks the end of one loop.
For the next loop to start, a new criterion has to be met. The number of loops considered static n_{sim} has to be lower or equal than input value `criterion_runs`. Until that condition is no longer met, the number of scattering particles $\sum \mathfrak{N}_{ph,ics}$ increases alongside the number of collisions. Every iteration, a new mean scattering particles value

$$\overline{\mathfrak{N}}_{ph,ics} = \frac{\sum_i \mathfrak{N}_{ph,ics,i}}{\sum_i i} \tag{4.26}$$

is calculated until the statistical variance between iterations decreases to the point that within a `criterion_runs` number of iterations the difference between iterations does not exceed `criterion_distance`. This way, users can define their mean

value stability criterion with the two input variables, depending on whether a swift or a precise estimation is preferred.

4.5.3. Numerical Issues

Routines related to the stochastic selection of scattering partners require a certain balance between the initial fermion macro particle distribution size and the scattering probability. As briefly mentioned earlier in reference to eq. 4.24, Comparse starts with an initial unscattered macro particle distribution and determines a number of scattering particles that are no longer macro particles. While the amount of real particles scattering in a single fermion bunch - photon pulse collision cannot exceed the number of particles before scattering, it can exceed the amount of macro particles before scattering, depending on the distribution's macro factor and ICS cross section.
Even before, when between 20 and 100% of macro particles are resulting in a scattering event, the statistic is likely erroneous. As photon and fermion distributions are usually Gaussian in nature and the laser beam is concentrated in the fermion distribution's center, as visualize in fig. 4.11, when most macro particles are resulting in a scattering event, it is possible that the inner area surrounding the center is "maxed out" on scattering events and could have resulted in more, if more macro particles would be present. Comparse includes a check that displays a warning

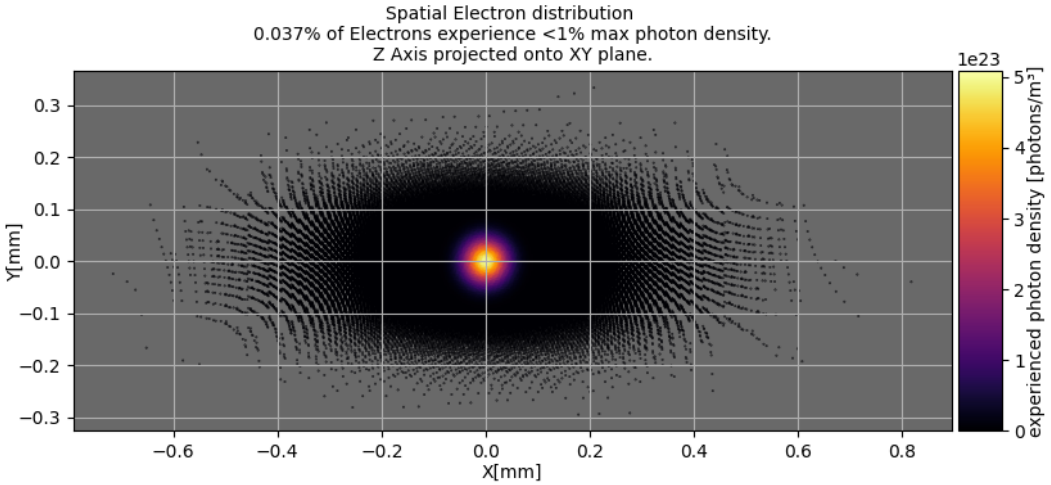

Figure 4.11.: Scattering probability colorized in transversal projection standard Gaussian electron distribution. Simulated and generated in Comparse using a MESA-ER-IB-42m-nominal (App. tab. A.2) Astra generated electron distribution and Tangor-100-IR-focused (App. tab. A.8) presets.

popup to the user if more than 20% of Macro particles result in a scattering event. In the popup, two methods of combating this numerical limit issue are suggested: Increase the initial macro particle distribution size N_{par} or decrease the boost and damping factor B. Adjusting B is a quick solution that can restore numerical bal-

ance. However, a sense of how many fermions are scattering per collision now must be gained from the flux estimation module. The user no longer obtains a representative amount of scattering data when using the gather scattering partners routine. There is no loss of simulation precision, as that is defined by the input distribution density and that remains unchanged.
The other solution raises said input density by increasing the initial particle distribution size N_{par} while lowering M_{par}. As a result, flux estimations and the gathering of scattering partner data will take longer. Data is sampled to a finer degree however, which is beneficial to the simulation precision. While many software applications in the field of physics limit a particle distribution macro factor to $M_{par} \geq 1$, Comparse can accommodate values between 0 and 1. In principle, a macro particle distribution generated on the basis of spatial Gauß curves is a list of samples taken from a continuous probability curve. Comparse adjusts the weight of each sample depending on it's macro factor, which represents the granularity of the sampling. There is no fundamental difference between samples taken from a curve with granularity factor $M_{par} = 1$, $M_{par} > 1$ or $M_{par} < 1$. Just the same as there is no fundamental difference between adding the scattering results of two macro particle distributions of size $N_{par} = n$ with $M_{par} = m$ on one hand and simulating the scattering data of a single macro particle distribution of size $N_{par} = 2n$ with $M_{par} = m$ on the other hand, as long as both cases are sampled from the same formula and it is understood to the user and in the simulation how the results came to be.

4.5.4. Temporal Dynamics Approximation

Earlier, we alluded to a more complex mode for the selection of scattering fermions that would include an approximation of temporal dynamics. This can be activated by the user in the "Gather Initial Scattering Parameters" submenu. By default, it is assumed, that the fermion bunch is not moving significantly enough during the ebb and flow of the laser pulse to leave traces in the ICS scattering result. In this case, irradiation time T_{rad} in the normalized scattering probability function $W_{ics,norm}$ defined in eq. 4.25 is set to the value of the laser pulse length in units of seconds. We thus calculate $W_{ics,norm}$ as if only when the center of the electron bunch passes the middle of the laboratory frame, which we defined by the given fermion bunch distribution center, the laser pulse flashes for an instant at it's maximum and only intensity $P_{pulse,staticICS} = T_{pulse} \cdot E_{pulse,max}$. Note, that by convention, Comparse's "pulselength" input field has it's value interpreted as the "full width at half-maximum" (FWHM) of a Gauß beam pulse. This value is about 2.355σ, the variance of a distribution, and covers about 76% of the area below the curve.
In principle, the temporally dynamic scattering position gathering routine, `temporal_scattering_positions_para(...)` in `routines.py`, is similar to the static version described earlier in section A.4.4. Fundamentally it executes the same `stochastic_selection_of_scattering_particles(...)` that includes $W_{ics,norm}$, but with different values for T_{rad} and E_{pulse}. There are multiple models for the

intensity and amplitude change of a laser pulse over time. Comparse uses the Gaussian approximation [37].

$$I_{pulse}(t_i) = I_0 \exp\left\{-4 \ln 2 \left(\frac{t_i}{T_{pulse}}\right)^2\right\} \tag{4.27}$$

whereas

I_0 zenith intensity of laser pulse eq. 4.9

t_i point in time with $t_0 = 0$ corresponding to pulse maximum convention

T_{pulse} FWHM pulse length defined in Comparse

To work with a non-zero t parameter in vectorized calculations over all initial fermion - photon[ ] pairs, we start by dividing a time period into smaller time steps. For this, the user is presented with two input fields, labelled "Period of Observation" (T_{obs}) and "Number of Time Steps" ($N_{t,input}$). The latter input field is further labelled with the algebraic expression "$\cdot 2 + 1$", indicating how the period of observation is sampled. Now, when temporal dynamics are activated, Comparse method `gen_timestep_data(...)` starts off by calculating the length of a single time step

```
step_s = period_s/(num_neg+num_pos+1)
```

where for now, as of Comparse v1.0, the number of time steps entered by the user is inserted for both `num_neg` and `num_pos` in order to keep the simulation setup simple. In the future, the code may be expanded to allow for more customization of the observation time, in the backend, the functionality is already implemented and tested. The implementation with $N_t = N_{t,input} \cdot 2 + 1$ ensures, that no matter what value user enters, there is a time step with value $t_0 = 0$ in the middle of the time step array that we will now construct. When calling NumPy method `numpy.arange(A,B)`, an array of integers from `A` to just before `B` is created. This is now performed twice, once from $-N_{t,input}$ to 0, and once from 0 to $N_{t,input} + 1$. Both arrays are multiplied by the time step length $t_{i-1,i}$ and combined to one larger array. This results in an array $\boldsymbol{t}$ of points in time ranging from $\boldsymbol{t}(1) = t_1 = -T_{obs}$ to $\boldsymbol{t}(N_t) = t_{N_t} = T_{obs}$ with guaranteed value $t = 0$ in the middle of the array. Continuing in the code:

```
n = np.arange(-num_neg,0)*step_s
p = np.arange(0,num_pos+1)*step_s
t_arr_t_s = np.append(n,p)
t_arr_idx = np.arange(num_neg+num_pos+1)

data = [step_s, t_arr_t_s, t_arr_idx]

return data
```

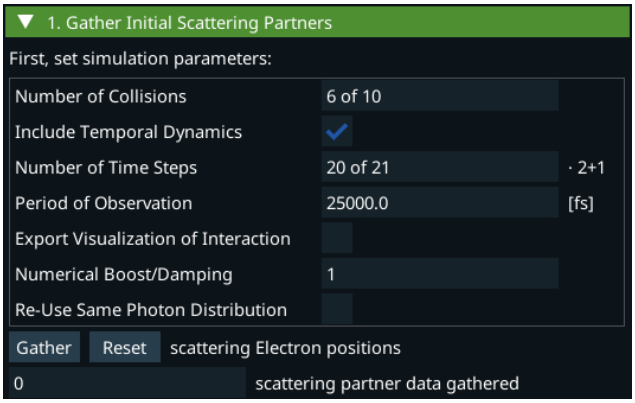

Figure 4.12.: Comparse user interface during active gathering of scattering information with active temporal dynamics. During the gathering process, the "Number of Collisions" and "Number of Time Steps" user input fields content is replaced with the corresponding current status.

Comparse method `gen_timestep_data(...)` returns the step size of a single timestep $t_{i-1,i}$, the array of timesteps in units of seconds $\boldsymbol{t}$ and an array of the same length iterating from 0 to N_t, representing the timestep indices that are required for the usual Python list comprehension access method of NumPy arrays.
Having generated the time step data, Comparse then overwrites photon class variable `irradiation_time_s` T_{rad}, previously set to photon class variable `pulselength_s` by default, with the calculated time step length $t_{i-1,i}$. From this point, calculations are taking place within a loop through the fields of the array of time step indices initiates, starting from the first index $i_t = 0$.

1. the "current" time t_i is recalled from array $\boldsymbol{t}$
2. the fermion positions are shifted to their position at current t_i
3. either a flattop cylinder or a Gauß beam photon distribution is created, generating photon data at every newly shifted position of all fermions in 3D
4. the stochastic selection of scattering fermions is executed

The time dynamics come from the shift of fermion positions and the current time step t_i given to the photon distribution as an input variable. Otherwise, the temporal dynamic approach uses the same methods as the static case.
When attaching a time step value t_i to the inputs of Comparse method `cvi_photon_distribution` that generates a Gauß beam distribution according to sec. 4.3.1, the default value $t_0 = 0$ in eq. 4.27 that is used in the absence of an input value is replaced with the current t_i. As the values of t_i range from negative to positive in units of seconds, crossing $t_0 = 0$, we obtain a rising and then falling laser intensity over the time step loop iterations.
On the fermion side, as of Comparse v1.0, no space charge effects are considered.

The fermion positions are simply traced along the trajectories in space-time before and after $t = 0$ given by their corresponding four-momenta as per eq. 4.5.4.

$$r_{par,t_i} = \boldsymbol{r}_{par,0} + \vec{\boldsymbol{u}}_{par} \cdot \boldsymbol{\beta}_{par,lab} \cdot c \cdot t_i \tag{4.28}$$

The fermion positions will be unambiguously defined by the initial distributions position array $\boldsymbol{r}_{par,0}$ and the trajectory calculated by $\vec{\boldsymbol{u}}_{par} \cdot \boldsymbol{\beta}_{par,lab} \cdot c \cdot t_i$. As we re-use the same fermion bunch distribution and none of the variables in eq. posses randomization aspects, the shifted r_{par,t_i} positions will be identical for every iterative collision calculated in a simulation run. This enables performance optimization by limiting the number of time shifts to be calculated for a simulation of multiple collisions.
When scattering events occur, then the arrays collecting the positions and momenta of the scattering fermion - photon pairs are filled with new values as described earlier in sec. 4.5.1. Once the loop has concluded, all time state dependent values are reset to the input values defining time $t_0 = 0$. In this implementation, when the user sets the number of bunch - pulse collisions from which data is to be collected to more than one, each time step of the temporal loop is collided the requested number of times before the system is transferred to the next temporal state. This way, the time shift calculations only have to be performed once per t_i. The user interface reflects this by displaying both the current time step and collision to be calculated, as shown in fig. 4.12.
When referring to the temporal dynamics in Comparse, we wish to emphasize the approximation nature of the approach. It can, however, provide a hint of how varying laser pulse lengths influence the inverse Compton scattering results in unexpected ways. In support of this, users can activate the export of a visualization. When activated, a plot of the interaction is saved to the "outpufiles/tseries" for each time step, highlighting the previously and currently recorded scattering positions over the moving fermion distribution colorized to display their experienced photon density ρ_{ph}. See fig. 4.13 for two example plots corresponding to $t_5 = -59.524\,\text{fs}$ and $t_10 = 0\,\text{fs}$ and A.8 for the complete set of 21 time steps $\boldsymbol{t}$. Adding to that, studies section 5.5 represents a brief evaluation of the effects of non-instant laser pulse simulations.

4.6. Inverse Compton Scattering Simulation Routine

Once a set of initial four vector and position parameters has been sampled and assembled for the fermion - photon pairs determined to be scattering, the scattering itself can be simulated. In the internal logic of Comparse, this constitutes stage 5, which only becomes available if stage 4, the gathering of initial scattering parameters described in sec. A.4.4, has successfully concluded. In the scattering routine, `scattering_routine_reduced(...)`, we will finally take the step from just before the scattering event to just after. Based on the theory summarized in chapter 3, the relativistic four momenta and polarization vectors of the scattered photons and

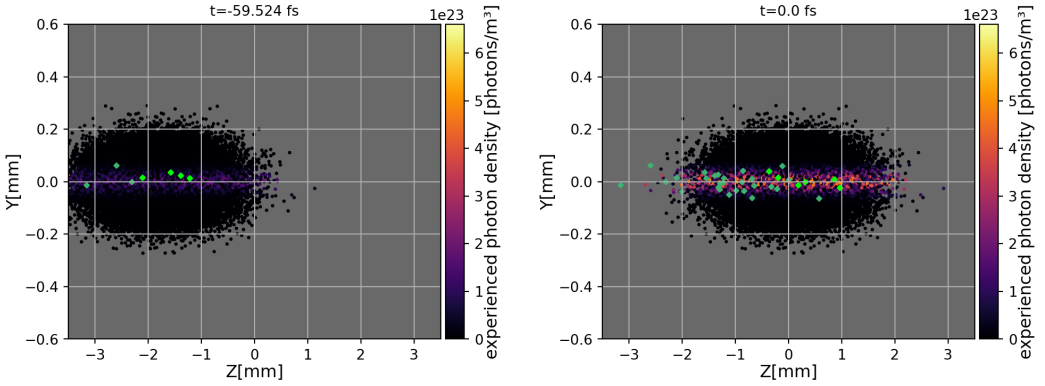

(a) Interaction at $t_5 = -59.524\,\mathrm{fs}$ **(b)** Interaction at $t_10 = 0\,\mathrm{fs}$

Figure 4.13.: Time dependent interaction of laser Gauß beam with electron distribution. Scattering events of 100 collisions corresponding to the current timestep are highlighted in bright green, while previously recorded scattering positions are highlighted in a darker green. Figure 4.13b shows how approximating fermion distribution trajectories can lead to scattering positions in longitudinal positions that temporally static simulations would not allow for. Simulated and generated in Comparse with activated temporal dynamics using a MESA-ER-IB-42m-nominal (App. tab. A.2) Astra generated electron distribution and Tangor-100-IR-focused (App. tab. A.8) presets. The full example series is shown in App. sec. A.8

fermion will be calculated. Once again, we will focus on the mathematical core of the scattering routine in Comparse. It is embedded in higher level functions related to staging, data management and the UI of which the explanation will be omitted for the sake of brevity. As always, the complete source code can be found in [38].

4.6.1. Selection of Scattering Direction

In theory section 3.2.3, we have introduced the Stokes transformation matrix $\mathbf{T}$ (eq. 3.77) in order to calculate the scattering cross section with inclusion spatial direction and polarization effects and then used a much simplified total cross section σ_{tot} (eq. 3.69) to decided which fermion - photon pair scatters. We have not forgotten about $\mathbf{T}$, but as it's correct application in a large data set simulation is a complex operation, we will only use it on the reduced subset of scattering particles in order to determine their scattering direction. Through the unit vectors created from the initial four-vectors and the rotated (see sec. 4.6.1.2), the set of necessary pre-scattering parameters $\vec{u}_{ph}$, k_0 and $\vec{k}$ is given. Missing for the evaluation of $\mathbf{T}$ is the corresponding set of post-scattering parameters $\vec{u}'_{ph}$, k'_0, $\vec{k}'$ and θ.

4.6.1.1. Polar & Azimuthal Spatial Angle Grid

The scattering direction of the photons is determined via a weighted random selection over a grid of possible scattering angles. This grid, defined by an azimuthal

angle ϕ and an orbital angle θ samples the surface of a unit sphere. Users can define the azimuthal ρ_ϕ and orbital ρ_θ density of the direction grid in the Comparse UI. When executing the method, first a numerical fix factor `num_fix` $:= a_{num}$ is declared and defined as the smallest possible float value via

```
num_fix = np.finfo(float).tiny
```

which equals $2.2250738585072014 \cdot 10^{-308}$ in scientific notation. The need for this measure comes from some equations resulting in divide by zero errors for perfect head-on collisions of scattering angles 0° or 180°.
Immediately, the numerical fix is put to use in the creation of NumPy arrays of shape $(\rho_\theta + 1)$ and (ρ_ϕ) respectively. Their value ranges are $\theta = a_{num}$ to $\pi + a_{num}$ and $\phi = 0$ to 2π. The two angle arrays are then reshaped into a common dimension shape $(\rho_\theta + 1, \rho_\phi)$ using NumPy method `meshgrid`. This keeps the values of the 1-dimensional arrays but allows for 2-dimensional vectorized operations that include all possible combinations of θ and ϕ. It's effect is visualized below for a θ_{array} of example length $\rho_\theta = 3$ and a ϕ_{array} with length $\rho_\phi = 4$:

$$\theta_{array} = \begin{pmatrix} \theta_1 \\ \theta_2 \\ \theta_3 \end{pmatrix}; \phi_{array} = \begin{pmatrix} \phi_1 \\ \phi_2 \\ \phi_3 \\ \phi_4 \end{pmatrix} \rightarrow \theta_{grid} = \begin{pmatrix} \theta_1 & \theta_2 & \theta_3 \\ \theta_1 & \theta_2 & \theta_3 \\ \theta_1 & \theta_2 & \theta_3 \\ \theta_1 & \theta_2 & \theta_3 \end{pmatrix}; \phi_{grid} = \begin{pmatrix} \phi_1 & \phi_1 & \phi_1 \\ \phi_2 & \phi_2 & \phi_2 \\ \phi_3 & \phi_3 & \phi_3 \\ \phi_4 & \phi_4 & \phi_4 \end{pmatrix} \tag{4.29}$$

In order to complete the spherical coordinates of all sampled points on a unit sphere, a smiliarly $(\rho_\theta + 1, \rho_\phi)$ shaped NumPy array filled with value 1 in every field is created. This represents distance r in the classic spherical coordinate convention. Now, the angle and r grids are combined into `space_point_vector_spher`, a 3-dimensional NumPy array with shape $(3, \rho_\theta + 1, \rho_\phi)$ representing all possible unit vectors of the scattering photon $\vec{u}'$ of ICS Stokes transformation matrix $\mathbf{T}$ from eq. 3.77 in spherical coordinates. Using Comparse's coordinate conversion function `spher_to_cart(...)`, the values are transformed into cartesian coordinate values and saved as variable `space_point_vector_cart`. From this point onward in Comparse, the mathematics are formulated in vector algebra, avoiding the use of angles.

4.6.1.2. Rotation of polarization Vectors

It is only possible after the grid of scattering photon directions and the corresponding 3-dimensional cartesian unit vector array $\vec{u}'$ has been created to include the aspect of polarization into the simulation. Photons entering the ICS interaction location and scattered photons being emitted from it have different wave vectors given by $\vec{u}$ and $\vec{u}'$. The polarization Stokes vector of light is defined in a right-handed coordinate system aligned with said wave vector. This necessitates careful tracking of the coordinate systems and transformation of the Stokes vectors before and after scattering for all scenarios except for the most trivial of a head-on collision

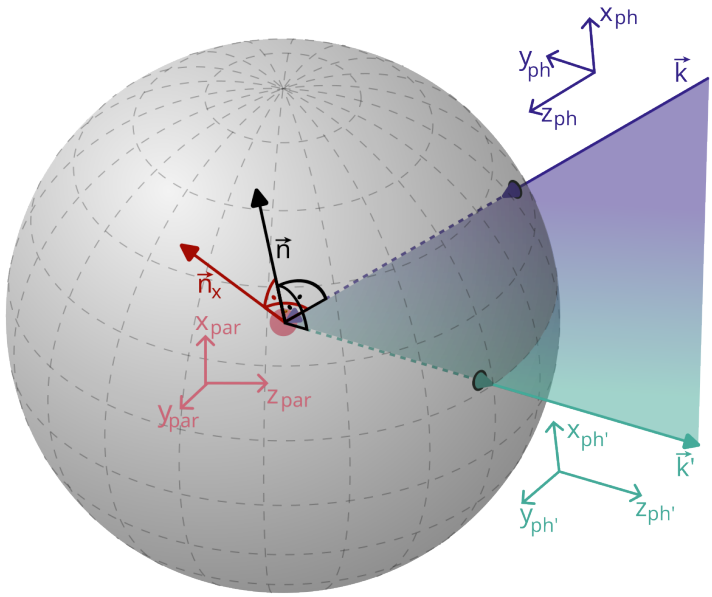

Figure 4.14.: Visualization of fermion and photon coordinate systems in the fermion rest frame. The fermion is located at the center of it's rest frame and has no momentum. Despite having no momentum, the fermion and accordingly the ERF, is defined in it's own salmon colored $(x_{par}, y_{par}, z_{par})$ coordinate system. This system is separate from those of the photons which are defined by the photon momentum or wave vector. For the incoming photon, the right-handed system (x_{ph}, y_{ph}, z_{ph}) must be aligned with it's momentum vector $\vec{k}$ to quantify the Stokes parameters as introduced in 3.2.2. Equally, the polarization of the emitted photon is aligned with it's momentum vector $\vec{k}'$, which defines a third right-handed coordinate system $(x'_{ph}, y'_{ph}, z'_{ph})$ colored in teal.
To transform the polarization from incoming photon over the ERF to the emitted photon's system, the two normal vectors $\vec{n}$ and $\vec{n}_x$ are constructed. $\vec{n}$ stands as the normal vector of the vector plane defined by $\vec{k}$ and $\vec{k}'$ and is located in the center of the ERF. It is therefore perpendicular to both $\vec{k}$ and $\vec{k}'$. The second normal vector $\vec{n}_x$ is in turn perpendicular to $\vec{n}$ and $\vec{k}$.

with perfect $\theta = 180°$ reflection, in which the Stokes parameters before and after are both defined to the same axis sans a sign change.

4.6.2. Definition of right-handed cartesian systems in 3D space used for polarized ICS simulations

Initially, photon polarization Stokes vector $\boldsymbol{P}$ is defined in the cartesian system of the photon (x_{ph}, y_{ph}, z_{ph}) where the z_{ph} axis points in the direction of the photon wave vector. Linear polarization is defined transversely to the photon momentum

in x_{ph} and y_{ph}.

$$\boldsymbol{P} = \begin{pmatrix} I \\ P_1 \\ P_2 \\ P_3 \end{pmatrix} \widehat{=} \begin{pmatrix} \\ x_{ph} \\ y_{ph} \\ z_{ph} \end{pmatrix} \tag{4.30}$$

It follows, that just as the incoming cartesian system (x_{ph}, y_{ph}, z_{ph}) has to be rotated in 3D-space to transform into the one on the scattered photon $(x'_{ph}, y'_{ph}, z'_{ph})$, one can rotate the polarization vector $\boldsymbol{P}$ similarly.
Before we can work with Stokes parameters, we have to start by defining a polarization direction vector $\vec{u}_P$ in the incoming photon system (x_{ph}, y_{ph}, z_{ph}). This vector has to be perpendicular to the photon's momentum and thus the z_{ph} axis shown in fig. 4.14. It defines to which transversal direction the polarization Stokes vector is written in reference to. Depending on notation, this may differ. Recall figure 3.4 and how P_1 stands for the transversal polarization of the photon and P_2 for the transversal polarization at an angle of $\frac{\pi}{4}$ to the right. Vector $\vec{u}_P$ defines what P_2 is to the right off. One has to be aware of the polarization direction definition before and after scattering to properly use the Stokes notation. Furthermore, when calculating scattering events in 3D space, one needs to automatically adjust $\vec{u}_P$ alongside the change in photon momentum direction. Thus, we attempt to calculate an individual Euler rotation matrix derived from the change in photon momentum direction for every scattering photon and apply it to the polarization vector $\vec{u}_P$ and in doing so to the Stokes vector $\boldsymbol{P}$.
Since we're calculating the angle dependent ICS cross section in the electron rest frame, the electron momentum is zero at the outset and our initial directional data consists of the photon momentum vectors, respectively, their unit vector form. Hence, we begin by calculating $\vec{n}$, the unit vector that is perpendicular to both $\vec{k}$ and $\vec{k}'$, respectively their corresponding unit vectors $\vec{u}$ and $\vec{u}'$

$$\vec{n} = \frac{\vec{u} \times \vec{u}'}{|\vec{u} \times \vec{u}'|} \tag{4.31}$$

and a second vector $\vec{n}_x$ that is perpendicular to $\vec{k}$ and $\vec{n}$ both.

$$\vec{n}_x = \frac{\vec{u} \times \vec{n}}{|\vec{u} \times \vec{n}|} \tag{4.32}$$

These normal vectors are then applied to the photon polarization vector $\vec{u}_P$ to transport it onto a new system that is orthogonal to both the incoming and the emitted photon momentum by forming the dot product between $\vec{u}_P$ and the normal vectors and then projecting this value onto both normal directions.

$$\vec{u}'_P = \vec{n} \cdot (\vec{u}_P \cdot \vec{n}) + \vec{n}' \cdot (\vec{u}_P \cdot \vec{n}') \tag{4.33}$$

Let's recall, that the circular polarization does not represent a polarization in any specific direction, but a periodic change in transversal polarization. It is therefore

invariant under Euler transformations. We only aim to quantify the change in the transversal polarization defining Stokes parameters P_1 and P_2. We do this by quantifying the rotation in both components by

$$\tau' = \arccos \begin{pmatrix} 1 \\ 0 \\ 0 \end{pmatrix} \cdot \vec{u}'_P \tag{4.34}$$

$$\phi' = \arccos \begin{pmatrix} 0 \\ 1 \\ 0 \end{pmatrix} \cdot \vec{n}' \tag{4.35}$$

and combine both to rotation angle

$$\alpha = 2\tau' - 2\phi' \tag{4.36}$$

construct the particle and scattering direction specific Euler rotation matrix affecting only the transversal components of $\boldsymbol{P}$ as shown below.

$$\mathbf{M}_{rot} = \begin{pmatrix} 0 & 0 & 0 & 0 \\ 0 & \cos\alpha & \sin\alpha & 0 \\ 0 & -\sin\alpha & \cos\alpha & 0 \\ 0 & 0 & 0 & 0 \end{pmatrix} \tag{4.37}$$

With this rotation matrix $\mathbf{M}_{rot}$, incoming photon Stokes vector $\boldsymbol{P}$ can now be transformed into the emitted photon cartesian system as Stokes vector $\boldsymbol{P}_{rot}$.

$$\boldsymbol{P}_{rot} = \boldsymbol{P} \cdot \mathbf{M}_{rot} \tag{4.38}$$

We shall use this $\boldsymbol{P}_{rot}$ instead of $\boldsymbol{P}$ to calculate the angle and polarization dependent normalized inverse Compton scattering cross section W of eq. 3.76, as we intend to find the probability of an emitted photon of a certain polarization landing on a detector screen.

4.6.3. Calculating Electron Rest Frame Parameters

To complete the set of variables required to evaluate Stokes transformation matrix $\mathbf{T}$, only the scattered photon momentum k' is missing. In the electron rest frame (erf), where the calculation of the ICS cross section is easiest, the scattered photon energy k'_{erf} as a function of scattering angle θ_{erf}, as shown in fig. 3.2 is given by

$$k'_{erf} = \frac{k_{erf}}{1 + k_{erf}\,(1 - \cos\theta_{erf})} \tag{4.39}$$

We will multiply every scattering photon unit vector $\vec{u}'_{ph}$ with this energy k'_{erf} to obtain the scattered photon 3D momentum vector $\vec{k}'$.

$$\vec{k}' = k'_{erf}\,\vec{u}_p h' \tag{4.40}$$

4.6.4. Randomized Selection of Scattering Direction

Having assembled all variables required to evaluate $\mathbf{T}$ for all sampled potential scattering directions per initial laser photon, including their specific polarization properly transformed onto the emitted photon system, we can now interpret solution $W = \boldsymbol{Q} \cdot \mathbf{T} \cdot \boldsymbol{P}_{rot}$ as the weight for a random choice function over the $\rho_{\theta+1} \times \rho_{\phi}$ size grid of scattering momenta $\vec{k}'$.
Because we have already stochastically determined in sec. 4.5 that the group of particles N'_{par} is scattering, we require that the random choice function selects exactly one scattering direction per index. In Comparse, this is realized by first normalizing W to $\sum_i W_n(i) = 1$ and then reshaping the 3-dimensional W_n array from shape $(N'_{par}, \rho_\theta+1, \rho_\phi)$ to a 2-dimensional array of length $(N'_{par}, (\rho_\theta+1)\cdot(\rho_\phi))$. The array still contains the same values, only no longer in a two angle grid. Each index of the $(\rho_\theta+1)\cdot(\rho_\phi)$ sized second dimension can be traced to and restored into a $(\rho_\theta + 1)$ and a (ρ_ϕ) index pair. Next, Comparse creates a new array $W_{n,cumsum}$ from W_n.

$$W_{n,cumsum}(i) = \sum_{1}^{i} W_n(i) \tag{4.41}$$

$W_{n,cumsum}$ is an array in which each fields represents the next iteration step of the cumulative sum over all values of W_n. For instance, in the first index $i = 1$, both arrays are identical as $W_{n,cumsum}(1) = W_n(1)$, however, they deviate starting with index $i = 2$, because $W_{n,cumsum}(2) = W_n(1) + W_n(2)$. Through this logic, $W_{n,cumsum}$ contains values ranging from $W_{n,cumsum}(1) = W_n(1)$ to $W_{n,cumsum}(\rho_\theta + 1) \cdot (\rho_\phi)) = 1$ in step sizes ranging from $W_{n,min}$ to $W_{n,max}$, where greater steps between $W_{n,cumsum}$ indices constitute higher scattering probabilities. We shall now roll a random number a_R between 0 and 1 for each of the scattering particles. This number will be compared with the values in $W_{n,cumsum}$ using a greater than condition to create a new array consisting of zeros for all $W_{n,cumsum}(i) < a_R$ and ones for all $W_{n,cumsum}(i) > a_R$. Of this array filled with only zeros followed by only ones, after the random condition has been fulfilled, NumPy function `argmax(axis=1)` is executed over reshaped scattering angles dimension $(\rho_\theta+1)\cdot(\rho_\phi))$ (`axis=1`), to return the first index that contains the array's maximum value "1" for each scattering particle. Recall, that higher scattering probabilities lead to greater cumulative sum steps and thus a higher likelihood of being the first index to fulfill the $W_{n,cumsum}(i) > a_R$ value condition.
Lastly, the 1-dimensional angles indices selected in the weighted random choice are restored to a θ and a ϕ index and two arrays named `theta_selected` and `phi_selected` of shape (N'_{par}) are saved. These will form the scattering angles of the relativistic quasi-elastic collision in the final step of the scattering routine.

4.6.5. Vectorized Relativistic Quasi-Elastic Fermion - Photon Collision

After completion of the operations in the previous sec. 4.6.4, we obtained the four-vectors of the initial photons and fermions as well as the scattering direction

of the emitted photon, with full consideration of arbitrary aligned and quantified momentum and polarization in space. To finish the simulation routine, we transport momentum four vectors $\boldsymbol{v}_{ph}$ and $\boldsymbol{v}_{par}$ from the laboratory frame (lab) to the center of mass system (cms), and the selected orbital scattering angle θ_{erf} from the electron rest frame into the cms as well. As the azimuthal angle ϕ_{erf} is contained under Lorentz boost, it does not need to be transformed for use in the following calculations.
We start by transforming θ_{erf} into the laboratory frame using the formula for the relativistic aberration of light eq.(5.6) in [12].

$$\theta_{lab} = \frac{\cos\theta_{erf} + \beta_{par,lab}}{1 + \beta_{par,lab} \cdot \cos\theta_{erf}} \tag{4.42}$$

$\beta_{par,lab}$ in this equation is the velocity of the fermion in the laboratory frame relative to the speed of light $\beta_{par,lab} = \frac{v_{par,lab}}{c}$. From the laboratory frame, we can use eq. 3.27 to calculate the photon scattering angle $\cos\theta_{cmf}$. Of this center of mass system scattering angle we save both the cosine expression and $\theta_{cmf} = \arccos(\cos(\theta_{cmf}))$ in their own local variables. θ_{cmf} often appears in equations as it's cosine and re-calculating the cosine from the arcus cosine would slow down the program.
Comparse will now calculate the four-vectors after the collision following the equations presented in theory sections 3.1.5 and 3.1.6. For electrons, a Comparse method named `vierervektor_el_pk_lab` first calculates the center of mass four-vector of the scattering fermions eq. 3.36 and with it implements eq. 3.42. Following the same principle, the photon four-vector after scattering in the laboratory frame is calculated by `vierervektor_ph_pk_lab` which uses eq. 3.37 to build eq. 3.43.
With the polarization, momentum and positional information of the fermions and photons immediately before and after scattering now completely assembled, this signifies the end of the simulation aspects related to Inverse Compton Scattering. From this point onward, the calculations all serve evaluation purposes such as the tracking of the scattered photons through space onto a screen and the analysis of the scattered photon and fermion attributes under various experiment related aspects, including the gamma spectrum and polarization distribution.

4.6.6. Optional Parallelisation Limit

We mentioned before, that the polarization dependent and relativistic scattering routine discussed in this section can easily be the most complex and demanding on the hardware found in Comparse, depending on user setting and data size. For instance, the matrix - vector dot product of the Stokes ICS transformation matrix $\mathbf{T}$, eq. 3.77, and polarization vector $\boldsymbol{P}$ can easily overwhelm the memory of a computer. With angle densities left at default input for the θ-ϕ-angle grid, $\rho_\theta = 181$ and $\rho_{phi} = 360$ and $N'_{par} = 1000$ particle pairs to be scattered, Comparse has to perform a $(4 \times 4)\cot(4)$ matrix - vector multiplication over $1000 \cdot 360 \cdot 181 = 65,160,000$ combinations at once. This constitutes an astonishing number

of floating point values kept in the working memory at once. As of Comparse v1.0, simulations are calculated using the "longdouble" data type which, on common modern hardware, is equivalent to a 128 Bit floating point value.

$$\begin{aligned} \text{size}\left(\mathbf{T}\cdot\boldsymbol{P}\right) &\widehat{=} \left(4\cdot 4\cdot N_{par}\cdot\rho_{\phi}\cdot\rho_{\theta}\right)+\left(N_{par}\cdot\rho_{\phi}\cdot\rho_{\theta}\cdot 4\right) \\ \text{size}\left(\mathbf{T}_{ex}\cdot\boldsymbol{P}_{ex}\right) &\widehat{=} \left(4\cdot 4\cdot 1000\cdot 360\cdot 181\right)+\left(1000\cdot 360\cdot 181\cdot 4\right) \\ &= 3.65\cdot 10^{8}\ \text{float128} \\ &\approx 5.84\ \text{Gigabyte} \end{aligned}$$

Any of the variables not set by the analytical equation that's the basis of this vectorized calculation can easily exceed the conservative example and default values given above. It is because of this, that by default Comparse limits the number of particles to be scattered at once to 50. Users can change the parallelisation limit or turn limits off altogether in the Comparse User Interface.
When a limit is activated, then calculation in the "scatter gathered" routine is handled in a loop. For this, the particle number dimension of all position and momentum arrays is split into smaller arrays with the $N_{par,sub}$ dimension size given by the limit $N_{par,limit}$ with the remainder kept in it's own group of likely smaller size $N_{par,sub}=1$ to $N_{par,limit}$. The looped execution through the sub-arrays is straight forward. At each iteration, the fermion and photon class position and momenta variables are overwritten by the current subset and restored after the loop has concluded, with all results appended to arrays of restored particle index dimension length N_{par}.
Special attention needs to be given to the calculated values that are saved as photon class variables in it's average over all scattered particles, such as polarization and scattering angle dependent cross section W of eq. 3.76. For visualization purposes, we aim to average over all particles, to prevent single deviations from defining the overall picture. With a parallelisation limit in place, Comparse needs to automatically calculate the average value of all scattering events over subsets of differing size correctly. The solution starts with the declaration of a list of arrays named `ave_cs_pol`, referencing the average cross section with polarization. This list only has a length of 2, but a NumPy array filled with the $\overline{W}$ results averaged over the particle dimension in each cell. Their array shape is $(\rho_{\theta},\rho_{\phi})$. In the first loop, the current $\overline{W}$ is saved to the first list field and the loop comes to a close and restarts. In subsequent loops, the current $\overline{W}$ is saved to the second field. There we determine the current array size $N_{\overline{W},i}$ and write this array to the second cell of `ave_cs_pol`. We proceed to define an averaging weight factor a_f.

$$a_f = \frac{N_{\overline{W},i}}{N_{par,limit}} \tag{4.43}$$

Lastly, the current average is calculated over the `ave_cs_pol` list dimension NumPy method `numpy.average(...)`, which allows for the addition of statistical weights to the averaging. The array dimension to be averaged over only has two fields in

which two weights are inserted: The iteration number of the current loop i and the previously calculated weight factor a_f. If two subsequent arrays of the same size are averaged over, then $a_f = 1$ and the weight is only dependent on how many sub arrays' average value is already contained in `ave_cs_pol` field 1. The more iterations the loop operations goes through, the smaller will be the change of $\overline{W}$ due to one current $\overline{W}_i$. If the initial group of scattering particles was not a multiple of the parallelisation limit $N_{par,limit}$, then the final sub array will be $0 < N_{par,sub} < N_{par,limit}$ and averaging weight factor a_f will not value 1 for the first time.
This implementation of a parallelisation limit reduces the execution speed, but can run quasi indefinitely due to it's constant overwriting of most data positions with limited sized sub arrays. Special attention was put on the memory usage of the scattering routine during the programming of Comparse. As of v1.0, there is no known memory leak and close to hour long scattering simulations have been performed at constant working memory usage, providing scattered photon and fermion data for 100k+ particle pairs.

4.7. Raytracing of Scattered Photons with Collimation

In a real experimental setup, gamma radiation is usually not measured or utilized in the location of it's creation, but a distance away in a detector or different experiment setup. To adequately perform a feasibility study using simulated data, including experiment optimizations, we need to be able to transport the scattering results from the ICS interaction point to any location in space in a way that mirrors real conditions. For this, we trace the trajectory of every scattered photon towards a screen of arbitrary rotation and plane center position in space. Optionally, we can place a physical collimator in form of a cylinder of arbitrary length, rotation and position in space and activate the condition, that every photon must pass through the cylinder in order to not be deleted.
In Comparse, the tracing of photons is realized through a method named `trace_ph_to_screen(...)`, found in `routines.py`, which takes a neutral, a fermion and a photon class instance as input. It is initiated in the Comparse UI via the "Trace" button found in the "Trace Photons to Screen" submenu, shown in fig. 4.15, of the "Execute Calculation Routines" window. The same submenu contains input fields for the collimator and screen defining variables as well as a checkbox to activate and deactivate the physical collimation. A slider enables users to rapidly adjust the collimator radius, by triggering a new execution of the method at every value change. Below, output fields display the number of photons, average energy and energy variance for both the uncollimated and collimated groups of scattered photons. Further still below, the percentage of scattered photons lost due to collimation as well as the relation of the average energy of the collimated photons to all gamma photons is shown for the purposes of collimation optimization.

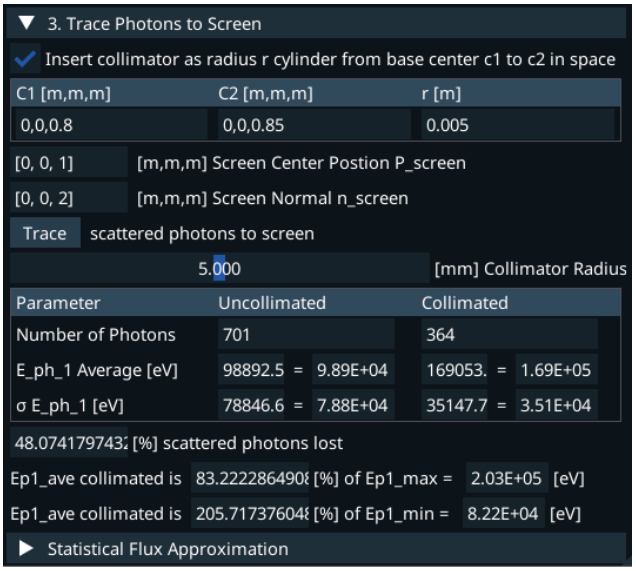

Figure 4.15.: Comparse UI submenu related to the tracing of scattered photons with optional physical collimation.

4.7.1. Vectorized Plane Projection

At the core of all photon tracing operations lies Comparse method `uv_project_to_plane()`, located in `unit_vectors_angles.py`, of which the input variables are listed in tab. 4.6.

It starts by calculating the normal vector starting from plane point r_c to point

Name	Shape	Description
`unit_vector`	$(3, N'_{par})$	unit vectors of scattered photons $\vec{u}'_{ph}$
`unit_vector_origin`	$(3, N'_{par})$	positions r_{par} of scattering fermions
`projection_point1`	(3)	location of "center" point r_c of infinite plane
`projection_point2`	(3)	point in space r_n defining normal of plane

Table 4.6.: Input variables of Comparse methode `uv_project_to_plane(...)`.

in space r_n. These two variables are UI input parameters. Through them, the user can define the location and rotation of a photon detector screen in space at will. For example, a screen perpendicular to the reference fermion direction in 1 m distance from the laboratory frame origin can be defined through $r_c = (0, 0, 1)$ and $r_n = (0, 0, 2)$. As the plane is infinite for our purposes, there are infinite combinations of defining it through it's normal vector.

$$\vec{r}_{cp} = r_n - r_c \tag{4.44}$$

In order to ensure the calculation works for every user input, the unit vector $\vec{u}_{cp}$ of plane normal vector $\vec{v}_{cp}$ is calculated. It will replace $\vec{v}_{cp}$ in all local method

operations. Next, a vector pointing from the plane point r_c towards the photon unit vector origin r_{par} is created similar to $\vec{v}_{cp}$ ealier.

$$\vec{v}_{oc} = r_{par} - r_c \tag{4.45}$$

Subsequently, two vector projections are performed along the plane normal axis:

$$d_o = \vec{v}_{oc} \cdot \vec{u}_{cp} \tag{4.46}$$
$$d_v = \vec{u}'_{ph} \cdot \vec{u}_{cp} \tag{4.47}$$

These products quantify the vector approach when we set their scalar results in relation as

$$d_{ov} = \frac{d_0}{d_v} \tag{4.48}$$

The intersection between the photon vectors $\vec{u}'_{ph}$ starting in r_{par} and the plane is now calculated as

$$r_{pp} = r_{par} - \vec{u}'_{ph} d_{ov} \tag{4.49}$$

and is returned as the result of method `uv_project_to_plane(...)`.

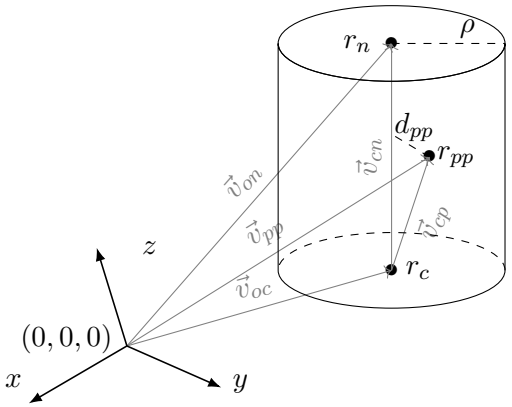

Figure 4.16.: Vector geometry for check if a xyz-position is found within a cylinder arbitrarily rotated and translated in 3D space. Same principles and variables are used to project a vector onto a plane in space. The two cylinder face center points r_c and r_n correspond to the plane normal construction points introduced in sec. 4.7.1. Both cylinder and plane orientation can be defined in the same way.

4.7.2. Vectorized Radius to Line in 3D Space Check

With the goal of implementing a ray based collimation check in the Comparse simulation environment, we require a method that finds the shortest distances to an arbitrary line in 3D space for any point distribution given. As a return value, we wish to obtain an N'_{par} length array of ones and zeros with which we can combine several conditional checks in a simple vectorized NumPy array multiplication.

Name	Shape	Description
`position_array`	$(3, N'_{par})$	positions r_{ph} of scattered photons
`cylinder_data`	(3)	array containing 2 (3) shaped position arrays r_c, r_n and one radius float value ρ

Table 4.7.: Input variables of Comparse methode `check_radius(...)`.

Comparse method `check_radius(...)` only requires input variables: As before, positions of all scattering particles are given. Here, the positions are not necessarily the scattering positions of the initial fermion distribution, but the positions of photons at a previously calculated point on their trajectory in space. First, the parameters contained in `cylinder_data` are extracted and saved as local method variables. The mathematical operations begin with the construction of the cylinder axis $\vec{v}_{cn}$ and cylinder base center to position vector $\vec{v}_{cp}$ shown in fig. 4.16.

$$\vec{v}_{cn} = r_n - r_c \tag{4.50}$$

$$\vec{v}_{cp} = r_{pp} - r_c \tag{4.51}$$

Of this vector $\vec{v}_{cp}$, the component square sum for every particle index is calculated.

$$\vec{v}^2_{cp} = \left(x^2_{cp} + y^2_{cp} + z^2_{cp}\right) \tag{4.52}$$

Next, the squares of the cylinder height h and radius ρ are calculated and saved as their own local variables.

$$h^2 = \vec{n}_{cn} \cdot \vec{n}_{cn} \tag{4.53}$$

We are once again using the orthogonal projection method to the cylinder/normal axis, this time to quantify the distance of origin position r_{pp} to it.

$$d_{pn} = \vec{v}_{cp} \cdot \vec{v}_{cn} \tag{4.54}$$

Now, the squared closest distanced d_{pp} from position r_{pp} to the cylinder axis $\vec{d}_{cn}$ is calculated via

$$d^2_{pp} = \vec{v}^2_{cp} - \frac{d_{pn}}{h^2} \tag{4.55}$$

Finally, condition array `cond_r` of length N'_{par} is filled with zeros in every index i at which the smallest squared distance is evaluated as $d^2_{pp} > \rho^2$ and ones in every other case. This represents one of the two collimation condition arrays created in the higher level method `trace_ph_to_screen` when physical collimation is activated.

4.7.3. Conditional Ray-Tracing with Physical Collimator

Having discussed the core mathematical functions of the photon tracing in Comparse, we shall now present the logic of the conditional tracing. After activating method `trace_ph_to_screen(...)`, the first mathematical task is checking if a

scattered photon points towards the screen and has a chance of reaching it even if it is infinite. This is not guaranteed, as there is a non zero chance that the scattering angle θ_{lab} is so big, that the scattered photon will only increase it's distance to the screen, with it's ICS interaction point being the closest point.
In Comparse, this is checked by first comparing the sign of the orthogonal vector projection between photon unit vector and plane normal vector

$$d_1 = \vec{u}'_{ph} \cdot \vec{v}_{cn} \tag{4.56}$$

with the vector projection of the plane normal with the vector $\vec{v}_{pc}$ pointing from the photon origin position r_{ph} to the plane center r_c used as the origin of the normal vector

$$d_2 = \vec{v}_{cn} \cdot \vec{v}_{pc} \tag{4.57}$$

It is enough to work with the signs of the two inner products while disregarding the numerical values. d_1 quantifies if the photon's momentum vector points into the same hemisphere of the plane normal, while d_2's sign indicates if the photon position is in the space into which $\vec{v}_{cn}$ points. The photon will intersect with the plane if both d_1 and d_2 possess the same sign. Thus, we can create a 1-dimensional array of N'_{par} length in which every index is filled with either "1" if the photon's vector intersects and "0" if it doesn't. This condition array is locally saved as `cond_points_to_screen`.
More conditions are then added. If the user chooses to insert a collimator into the ICS gamma ray, a short sequence of Comparse method executions is initiated. First, two positions are calculated using through execution of `uv_project_to_plane(...)` of subsection 4.7.1 with almost identical input values. Both method calls are given the scattered photon unit vectors $\vec{u}'_{ph}$ as `unit_vector` and the fermion distribution position r_{par} array as `unit_vector_origin`. We will recall, that the method requires a plane center point `projection_point1` and `projection_point2`. Here the inputs differ, as the two inputs are given by the two possible combinations of the user defined collimator points r_{c1} and r_{c2}, corresponding to the two circular faces of a cylinder. In this, the photon trajectory is traced to the infinite plane parallel to the collimator entrance and the one parallel to the collimator exit both. On the obtained intersection position arrays $r_{ph,c1}$ and $r_{ph,c2}$, we perform the radius to line check `check_radius(...)` explained in subsection 4.7.2. The returned condition arrays filled with 1 for inside and 0 for outside are too saved locally as N'_{par} length arrays `cond_coll_c1` and `cond_coll_c2`. Should the user have chosen not to insert a collimator, then both arrays are simply filled with ones. The conditional array form of N'_{par} length 1-D NumPy arrays filled with ones and zeros is chosen, because we can now simply perform a vectorized multiplication of all three condition arrays and save only the indices in which the value is equal to 1 as a new array termed `coll_index`:

```
coll_index = np.where(cond_points_to_screen * cond_coll_c1 *
                      cond_coll_c2 == 1)[0].astype(int)
```

This array constitutes a list of array indices pointing to the photons that fulfill all three conditions of

1. eventually intersecting with the screen plane
2. being within the collimator radius at the collimator entrance
3. being within the collimator radius at the collimator exit

We use the array `coll_index`, saved as a photon class variable and thus made available outside of the photon tracing method, containing their indices to reduce all scattered photon data to only those detectable on an arbitrarily placed and aligned screen in space after collimation. Separately, a condition array formed by the `cond_points_to_screen` alone is saved as photon class variable `to_screen_index` to allow direct comparison of collimated and uncollimated values.
As the last mathematical operation, we once again make use of `uv_project_to_plane()` to finally trace all photons towards the screen. The result is saved as photon class variable `vector_to_screen`.
All methods and operations used in this routine are written fully vectorized. As a result, tracing scattered photons towards a screen is extremely performant. In usual simulation scenarios, the tracing is fast enough to use the collimator radius slider with little to no delay of the calculated results, allowing for efficient optimization of the scattered photon energy spectrum. It is tempting for physicists to assume a high potential for bandwidth optimization through collimation, due to the strong scattering angle θ dependence of the ICS gamma energy. In reality, however, each scattered photon is emitted from the position of a fermion that's itself part of a bunch spread out over a certain volume. Even with negligible transversal momentum effects on the scattering process, this spatial distribution alone can limit the effectiveness of physical collimation to the point of making achieving a desired gamma bandwidth impossible. See section 5.4 for a deeper simulation investigation of the potential and limitation of collimation in ICS.

5. Studies of Inverse Compton Scattering at MESA

As the stated intent of this PhD work, several studies have been carried out using the semi-analytical simulation environment Comparse outlined in chapter 4 based on the theory of Inverse Compton Scattering as presented in chapter 3. The version used for all studies is v1.0 that is linked in the introduction of chapter 4. It is foreseeable, that Comparse will receive updates and undergo changes in the future. For the purpose of reproducibility, the Seafile upload of the v1.0 executable will be kept online for as long as possible alongside the GitLab RLP repository, the GitLab repository hosted by the universities and colleges of the state of Rheinland-Pfalz, hosting the full history of versions including v1.0 [38].
MESA beamline simulations conducted by Daniel Simon using the KPH Mainz internal software BeamOptik 2000 [39] and CERN's MAD-X [40–42] in September 2020 [43] were analyzed for suitable implementation locations. An exemplary transversal bunch size plot representative of the Internal Beamline in ERL mode is shown in figure 5.1.

Three locations found in different modes of operation and parts of the beamline have been selected:

- "T5-16m" found in the turn 5 track of the recirculation beam line at around 16.7 m
- "EB-50m" found in the external beamline at 50.42 m
- "ER-IB-42m" found in the internal beamline at 42.19 m when in ERL operation mode

5.1. Focus Flux Optimization Studies

Of great importance to ascertain the benefits of an ICS gamma source is the collision rate that directly relates to the produced gamma flux $\mathfrak{F}_\gamma$ and luminosity $\mathfrak{L}_\gamma$. Here, we define luminosity following [44] as the proportionality factor between the number of scattering events per second and the ICS cross section:

$$\frac{d\mathfrak{N}_{ICS}}{dt} = \mathfrak{L} \cdot \sigma_{ICS} \tag{5.1}$$

Optimization of Laser parameters can prevent overfocus or unnecessary beam widening with accompanying photon intensity loss experienced by the electron bunch.

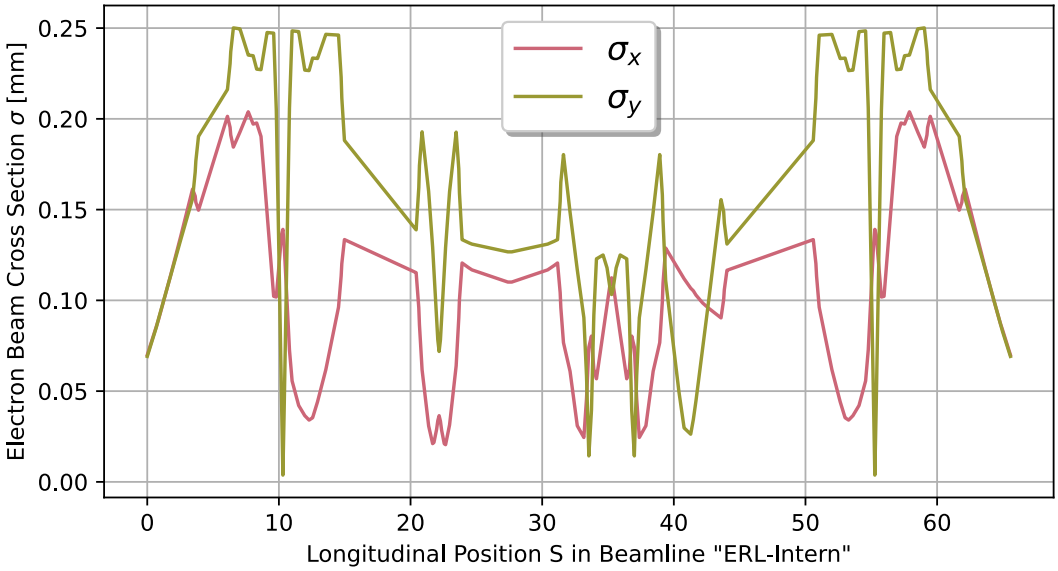

Figure 5.1.: Transversal beam size σ for electron beam of MESA ERL-mode Internal beamline. Generated from Daniel Simon's September 2020 beamline simulations in Beamoptik.

Various scenarios have been investigated to optimize laser focusing settings for provided electron beam parameters.

5.1.1. Electron Beam Focus Study

A study to ascertain the optimal electron beam focus for a high luminosity ICS gamma source was carried out using Comparse based on the 3D recoil cross section eq. 3.76 implemented in Comparse via eq. 4.25.
Every simulation in this section was carried out in Comparse's statistical flux estimation routine described in section 4.5.2 using the following parameters to determine the average number of scattering electrons per collision $\overline{\mathfrak{N}}_{ics}$:

- $n_{runs} = 1000$ consecutive collisions required for $\overline{\mathfrak{N}}_{ics}$ to be considered stable
- $\Delta\overline{\mathfrak{N}}_{ics,i} <= 0.001$ absolute difference between two iteratively calculated $\overline{\mathfrak{N}}_{ics,i}$ values for the the current one to be considered stable
- $n_{ave} = 3$ mean values of $\overline{\mathfrak{N}}_{ics}$ to be calculated and afterwards averaged to one final $\overline{\mathfrak{N}}_{ics}$
- $B = 1000$ scattering probability boost set in order to obtain a reliable scattering statistic

The Laser parameter set used is "Tangor-100-IR-focused" and the electron beam is set to "MESA-ER-IB-42m-nominal" with exception of σ_x & σ_y which are the subject of optimization. See appendix tables A.1 and A.8 for an overview of the

respective underlying electron and photon beam parameters.

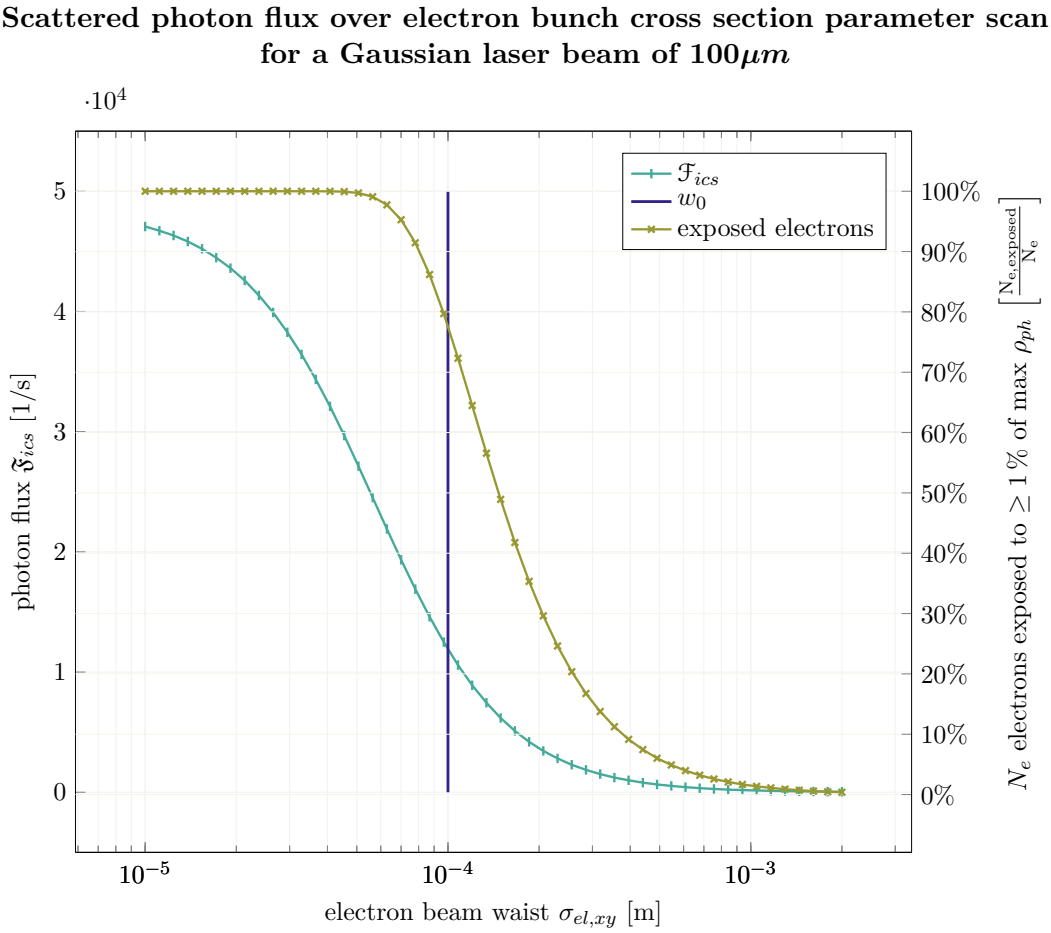

Figure 5.2.: Scattered photon flux calculated using the Comparse Estimate Flux function. Laser parameters were set to Tangor-100-IR-focused (App. tab. A.8) settings with a laser focus waist of $w_0 = 100\,\mu m$. The electron distribution series was generated in Astra using the MESA-EB-50m preset (App. tab. A.5) but with symmetrical σ_x & σ_y transversal beam diameter varying over the horizontal axis value range from 10 to 2000 µm. The photon density distribution model is "Gauss Beam". The curve titled "exposed electrons" displays the percentage of electrons that are exposed to an EM laser field of more than 1 % of the maximum field intensity $I_{ph,max}$.

Scattered photon flux over electron bunch cross section parameter scan for a Gaussian laser beam of 50 μm

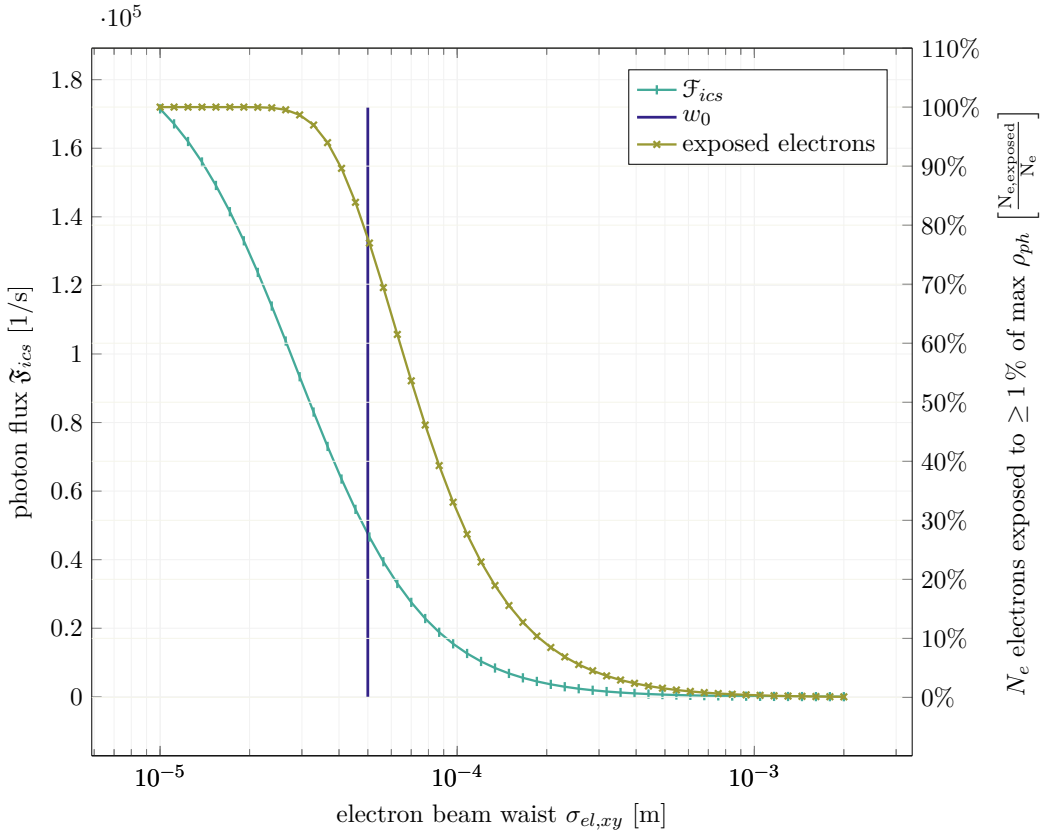

Figure 5.3.: Scattered photon flux calculated using the Comparse Estimate Flux function. Laser parameters were set to Tangor-100-IR-focused (App. tab. A.8) settings with a laser focus waist of $w_0 = 50\,\mu m$. The electron distribution series was generated in Astra using the MESA-EB-50m preset (App. tab. A.5) but with symmetrical σ_x & σ_y transversal beam diameter varying over the horizontal axis value range from 10 to 2000 µm. The photon density distribution model is "Gauss Beam". The curve titled "exposed electrons" displays the percentage of electrons that are exposed to an EM laser field of more than 1 % of the maximum field intensity $I_{ph,max}$.

A pair of electron focus parameter scan studies was carried out for the Tangor 100 IR laser focused to $w_0 = 50\,\mu m$ and $w_0 = 100\,\mu m$. The electron bunch distributions were generated using the "MESA-EB-50m" preset (App. tab. A.5) with $\sigma_{el,xy}$ ranging from 10 to 2000 µm in 50 logarithmically scaled values. The plots in figures 5.2 & 5.3 show that within that range, the flux $\mathfrak{F}$ always increases with a tighter electron beam focus. When plotted logarithmically however, a slow down in effective luminosity improvement can be observed. The flux curve trends towards a plateau in the logarithmic value space. This is more pronounced in the $w_0 = 100\,\mu m$ study, where the transversal electron bunch size decreases to the point of approaching a laser underfocus scenario visualized in fig. 5.4b. As in accelerator

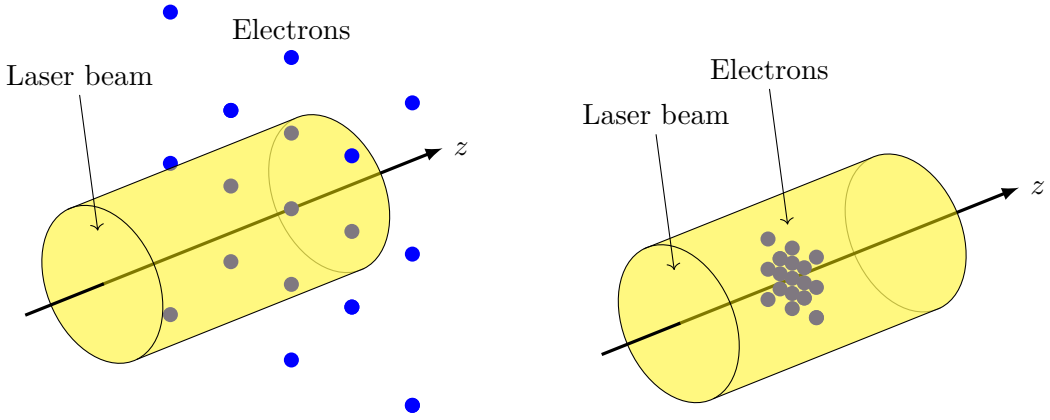

(a) Potential overfocus **(b)** Potential underfocus

Figure 5.4.: Pictured are two potential cases of misfocus. 5.4a shows a laser with a beam waist radius smaller than the electron bunch transversal expansion. This results in a lowered effective electron population in respect to our scattering calculations as a number of electrons cannot interact with the high intensity inner part of the gaussian beam, instead only with the close to zero laser intensity of the outer area. 5.4b on the other hand presents a potential underfocus scenario in which the laser beam waist could be decreased to increase the photon density per volume unit with no electrons dropping out of the high intensity laser beam zone.

physics, greater beam focus comes with exponentially greater effort and complications, we deem the logarithmic scaling appropriate.
When optimizing for photon flux, a smaller $\sigma_{el,xy}$ should be targeted within reasonable effort. Our plots suggest that the greatest flux increase per electron beam focus improvement can be obtained just beyond the state where $\sigma_{el,xy} = w_0$, as the logarithmic $\mathfrak{F}_{ics}$ curve is steepest between $\sigma_{el,xy} = w_0$ and $\sigma_{el,xy} = 0.2 \cdot w_0$, after which it approaches saturation.

5.1.2. Laser Beam Focus Study

Studies were carried out in Comparse to ascertain optimal Laser beam focus settings for the simulated electron bunches expected to represent MESA after completion.
The Gaussian laser beam model has a fixed number of photons per pulse. With narrower focus, the photon density per volume unit ρ_{ph} increases within laser beam diameter w_0 (FWHM). However, the narrowing of Laser focus will eventually result in an increasing number of electrons falling outside of w_0, potentially lowering the average electron specific photon density that determines the scattering of electrons. See fig. 5.4 for a visualization.

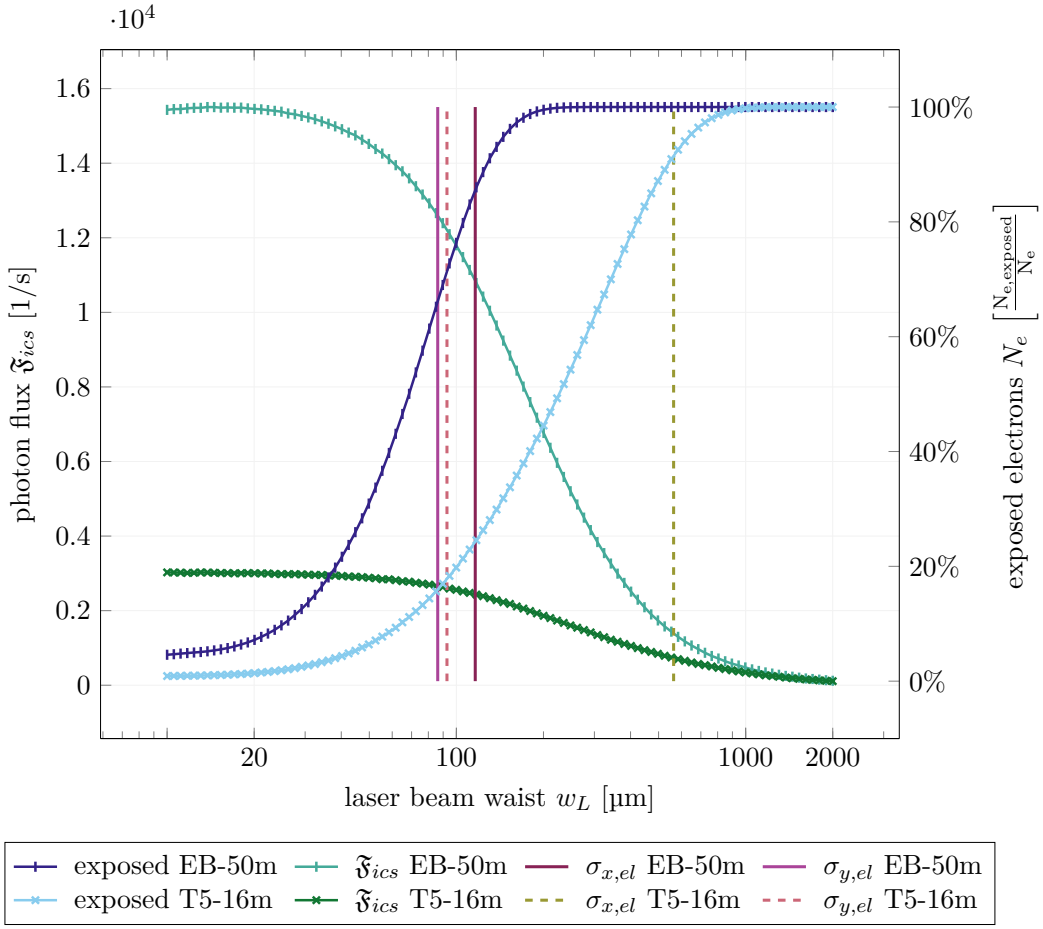

Figure 5.5.: Scattered photon flux calculated using the Comparse Estimate Flux function. Laser parameters were left at Tangor-100-IR-focused (App. tab. A.8) settings while the laser focus waist was scanned in 100 logarithmically scaled steps from $w_0 = 10$ to 2000 µm. The electron distributions were generated in Astra using the MESA T5-16m (App. tab. A.6) and EB-50m (App. tab. A.5) presets. Simulations were conducted using the "Gauss Beam" photon density distribution model. Vertical lines indicate the horizontal σ_x and vertical σ_y bunch diameters at the specified location in MESA. The curve titled "exposed electrons" displays the percentage of electrons that are exposed to an EM laser field of more than 1 % of the maximum field intensity $I_{ph,max}$.

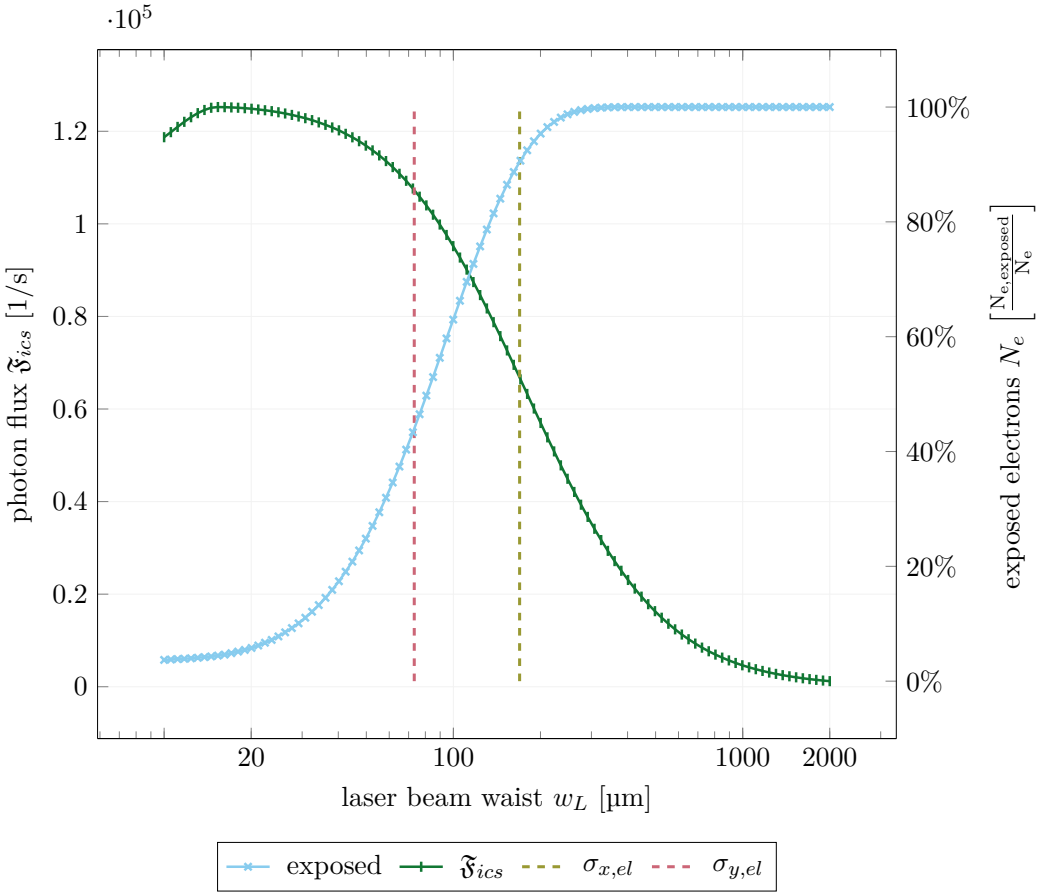

Figure 5.6.: Scattered photon flux calculated using the Comparse Estimate Flux function. Laser parameters were left at Tangor-100-IR-focused (App. tab. A.8) settings while the laser focus waist was scanned in 100 logarithmically scaled steps from $w_0 = 10$ to 2000 µm. The electron distribution series was generated in Astra using the MESA ER-IB-42m preset (App. tab. A.1). Simulations were conducted using the "Gauss Beam" photon density distribution model. Vertical lines indicate the horizontal σ_x and vertical σ_y bunch diameters at $s = 42.19$ m in the Internal Beamline when operating MESA in Energy Recovery mode. The curve titled "exposed electrons" displays the percentage of electrons that are exposed to an EM laser field of more than 1 % of the maximum field intensity $I_{ph,max}$.

Parameter scan simulations were carried out over the Laser focus transversal beam waist w_0. The flux was calculated for 100 w_0 values ranging logarithmically from 10 µm to 2000 µm to identify optimal laser focus settings. The parameters of the stochastical Comparse calculation are:

- $n_{runs} = 10000$ consecutive collisions required for $\overline{\mathfrak{N}}_{ics}$ to be considered stable

- $\Delta\overline{\mathfrak{N}}_{ics,i} <= 0.001$ absolute difference between two iteratively calculated $\overline{\mathfrak{N}}_{ics,i}$ values for the the current one to be considered stable
- $n_{ave} = 5$ mean values of $\overline{\mathfrak{N}}_{ics}$ to be calculated and afterwards averaged to one final $\overline{\mathfrak{N}}_{ics}$
- $B = 1000$ scattering probability boost set in order to obtain a reliable scattering statistic

The results have been plotted in figures 5.5 and 5.6. Due to the aggressive laser focus value $w_0 = 10\,\mu m$ that constitutes the narrow end of the w_0 value range, we can clearly observe a plateauing of the generated ICS gamma flux for all investigated MESA locations. Furthermore, we can even identify the beginning of overfocus for MESA EB-50m (fig. 5.5) and IB-42m (fig. 5.6) in the reduction of flux at narrower laser beam waist focus.
The σ_x and σ_y transversal electron bunch sizes simulated at the MESA locations are included as vertical lines in each figures 5.5 and 5.6. Plotted logarithmically, we can observe, that generally the greatest flux $\mathfrak{F}_{ics}$ gains from relative laser focus improvement effort can be obtained when w_0 is between σ_x and σ_y. Improving laser focus beyond the smaller electron bunch size σ and onwards still increases the flux, but with diminishing returns. This is especially pronounced for MESA T5-16m. The electron distribution at this location is simulated to be the least circular in it's transversal dimension of all three investigated locations, with $\sigma_x = 564\,\mu m$ and $\sigma_y = 93\,\mu m$ resulting in a eccentricity of more than $e = 6$. See table 5.1 for a complete list of all transversal bunch size parameters.

Location	$\boldsymbol{\sigma_x}$	$\boldsymbol{\sigma_y}$	**Eccentricity** $\boldsymbol{e_{xy}}$
EB-50m	116 µm	86 µm	1.35
T5-16m	564 µm	93 µm	6.06
ER-IB-42m	169 µm	73 µm	2.31

Table 5.1.: Transversal bunch dimension of Gaussian electron distributions at three locations investigated for MESA.

Both flux and flux improvements due to laser focus benefit from a low eccentricity. In figure 5.5, we can observe, that location EB-50m can provide a much higher flux than T5-16m due to the strong elongation of the latter into its y-dimension. For a bright ICS gamma source, we can recommend an electron bunch distribution of narrow bunch size transversal and low eccentricity. As providing this to the ICS experiment is not guaranteed to be possible, every electron distribution needs to be investigated for laser focus improvement potential, as spending effort on narrowing the waist of a Gaussian beam might not produce an appropriate brightness increase and in extreme cases even lower the gamma flux $\mathfrak{F}$.

ν_{RF}	Q_{el}	$E_{el,ref}$	$E_{el,\sigma}$	σ_x	σ_y	σ_z
1.3 GHz	7.7 pC	105 MeV	0.01 %	169 µm	73 µm	640 µm

Table 5.2.: Electron distribution parameters for nominal operation mode of MESA in ERL mode in the internal Beamline at $s \approx 42\,\mathrm{m}$.

5.2. MESA as a Driver for a Inverse Compton Scattering Gamma Source

Of the three potential ICS experiment locations within the MESA layout discussed earlier at the beginning of this section 5, we decided to focus on the drift section within the so-named "Internal Beamline" at 42.19 m as it is reachable in nominal Energy Recovery mode. This allows for a beam current of $I_{el} = 10\,\mathrm{mA}$ without modifications as opposed to only 1 mA in the external beam mode. The increase in potential gamma flux accompanying the higher beam current is significantly important for a low-cross-section experiment such as Inverse Compton Scattering. As such, MESA ER-IB-42m is chosen for detailed parameter and performance studies for an ICS gamma source. Here, according to simulations, the transversal cross-section will be relatively small at about $\sigma_x = 169\,\mu\mathrm{m}$ and $\sigma_y = 73\,\mu\mathrm{m}$. In the Internal Beamline, the bunch is assumed to be long, at a longitudinal bunch size of $\sigma_z = 640\,\mu\mathrm{m} \approx 2.13\,\mathrm{ps}$. In this mode, MESA accelerates electrons to a reference kinetic energy of $E_{el,ref} = 105\,\mathrm{MeV}$ with an $\frac{\sigma_{E,el}}{E_{el,ref}} = 0.01\,\%$ relative energy spread. The acceleration takes place at a frequency of $\nu_{RF} = 1.3\,\mathrm{GHz}$. As the beamline is designed to accommodate beam currents of up to $I_{el} = 10\,\mathrm{mA}$, at $\nu_{RF} = 1.3\,\mathrm{GHz}$, the electron bunch charge is limited to $Q_{el} = 7.7\,\mathrm{pC}$. In order to reach $E_{el,ref} = 105\,\mathrm{MeV}$, an electron bunch has to traverse both of MESA's 25 MeV cryomodules twice. After four cryomodule passes, the targeted final beam energy of 105 MeV is reached and we expect a normalized transversal emittance of $\epsilon_{x/y,n} = 0.3\,\pi\,\mathrm{mrad\,mm}$ in the internal beamline.
Based on this location, a series of implementation scenarios were simulated. We shall spread the studies over the following subsections. A summary of the results can be found in section 5.2.6. All initial electron distributions were created using Astra Generator [30].

5.2.1. Nominal MESA ERL internal Beamline & off-the-shelve 1030 nm IR Laser

We will start our investigation of ER-IB-42m, assuming MESA operates at nominal parameters and is built according to current plans as of 2024. The electron bunch distribution was created according the parameters mentioned in the previous subsection, a summary of which is available in tab. 5.2 with the corresponding Astra generator namelist values listed in App. tab. A.1.
For the laser pulse side of the ICS experiment, the commercial sector has a number

Laser Variant	$\boldsymbol{\lambda_\nu}$ [nm]	$\boldsymbol{\sigma\lambda_\nu}$ [nm]	$\boldsymbol{E_{pulse}}$ [mJ]	$\boldsymbol{\nu_{ph,rep}}$ [kHz]	$\boldsymbol{\overline{P}}$ [W]	$\boldsymbol{\sigma_{x/y}}$ [mm]	$\mathbf{m^2}$
1	1030 nm	< 3	0.5	200	100	0.05	< 1.3
2	1030 nm	< 3	4	200	100	0.05	< 1.3
3	193 nm	< 2	20	1	10	0.05	35
4	193 nm	< 2	160	1	10	0.05	35

Table 5.3.: Overview of investigated laser solutions for this study.
1. Tangor 100 IR baseline + focus optics
2. Tangor 100 IR + SMILE + focus optics
3. EX10IN + focus optics
4. EX10IN + SMILE + focus optics

of models readily available. One of the lasers considered for this study is the Tangor 100 IR femtosecond laser made by the french company Amplitude. It is used for ICS based beam diagnostics at the TU Darmstadt Superconducting Darmstadt Linear Accelerator (S-Dalinac) [45]. Darmstadt's setup aims to focus the emitted laser pulse down to a $\sigma_{ph,x} = \sigma_{ph,y} = 50\,\mu\text{m}$ spot size. The laser is rated for a small spectral bandwidth of $\Delta\lambda < 3\,\text{nm}$. See tab. 5.3 for a summary of all Laser solutions considered, including the Tangor 100 laser, described above and used in the simulation in this section.

Simulation Results

20,000 collisions were simulated in Comparse. They correspond to an experiment duration of $T_{ics} = 0.1\,\text{s}$, as the collision frequency is limited and given by the lower laser pulse repetition rate of $\nu_{ph,rep}$ 200 kHz. Each collision is defined as a λ =1030 nm laser pulse of a Tangor 100 IR laser focused down to $\sigma_{ph,x/y} = 50\,\mu\text{m}$ irradiating a $E_{el,ref} = 105\,\text{MeV}$ MESA electron bunch in the Internal Beamline at 42 m in energy recovery mode. The number of collisions is independent from whether or not a scattering event takes place. In this experiment configuration, the peak scattered photon energy achieved is $E'_{ph,max} \approx 204\,\text{keV}$, however the uncollimated average scattered photon energy is merely $\overline{E}_{ph} \approx 102\,\text{keV}$. Plotting the gamma ray spectrum fig. 5.10 shows that most scattered photons are found well below the maximum energy $E'_{ph,max}$. When projecting the scattered photons towards a screen positioned in $d_s = 1\,\text{m}$ distance, one can see the cause of the halved averaged energy and identify a potential for bandwidth improvement.
The total scattered radiation combined has a very broad bandwidth, as it's energy approximately ranges from $E'_{ph,max}$ to $\frac{1}{2} \cdot E_{ph,max}$. However, due to the strong scattering angle dependence of the projected spatial energy gradient, one can physically limit the area of of which the gammas are used to significantly narrow the spectrum at a loss of overall photon flux $\mathfrak{F}$. Figure 5.8 illustrates the gamma-distribution on

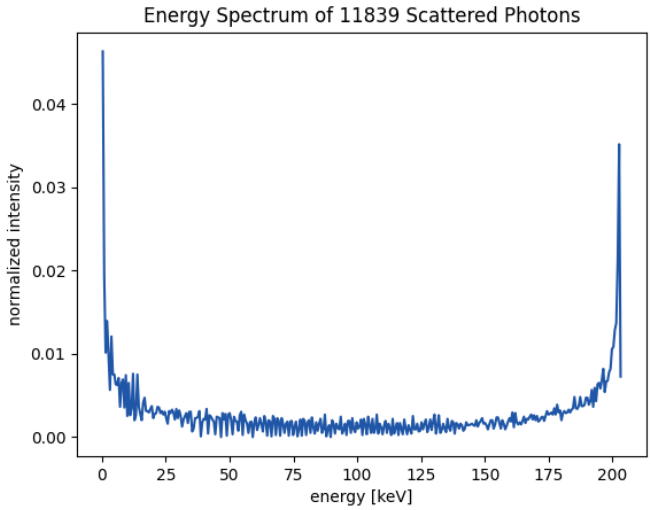

Figure 5.7.: Scattered photon spectrum simulated and generated in Comparse using a MESA ER-IB-42m-nominal (App. A.2) Astra generated electron distribution and Tangor-100-IR-focused (App. A.8) presets.

the screen including the gamma energies. The radial dependence of energy E'_{ph} to scattering angle θ_{lab} is clearly visible. If the defined goal of the experiment is to produce narrow bandwidth gamma radiation and some flux loss is acceptable, one can install a collimator within the scattered photon path. In it's basic form, a collimator can be a simple pinhole element, a body that blocks gamma radiation from reaching the detector or screen, with a small hole that lets only a subset of photons pass. In this way, the observed radiation can be limited to only the highest energy inner section of the scattering image. In our ICS simulations, for example in fig. 5.8, the scattering angle θ_{lab} dependence of E'_{ph} can be observed clearly. This is despite the fact, that the simulation takes into account all transversal properties of the Gaussian electron distribution in momentum and position as well as a simple model of the transversal momentum distribution of a Gaussian laser. Significant transversal momentum and and position deviations from the ideal reduce the effectiveness of collimation and in extreme cases even limit the potential for bandwidth improvements via pinhole collimator. For an investigation of such scenarios, see subsection 5.4.
High flux in a small bandwidth is often a requirement for gamma-ray-experiments. To study the impact of electron and laser emittances on the potential gamma bandwidth, we have simulated the effect of using a pinhole collimator to take advantage of the energy-angle correlation of the gamma-rays. Especially of interest was the percentage of photons lost to collimation under realistic laboratory conditions. For this, we have attempted to collimate the gamma-ray until the average scattered photon energy is $\overline{E}'_{ph}/E'_{ph,max} = 95\,\%$ and $99\,\%$ respectively. The simulations were

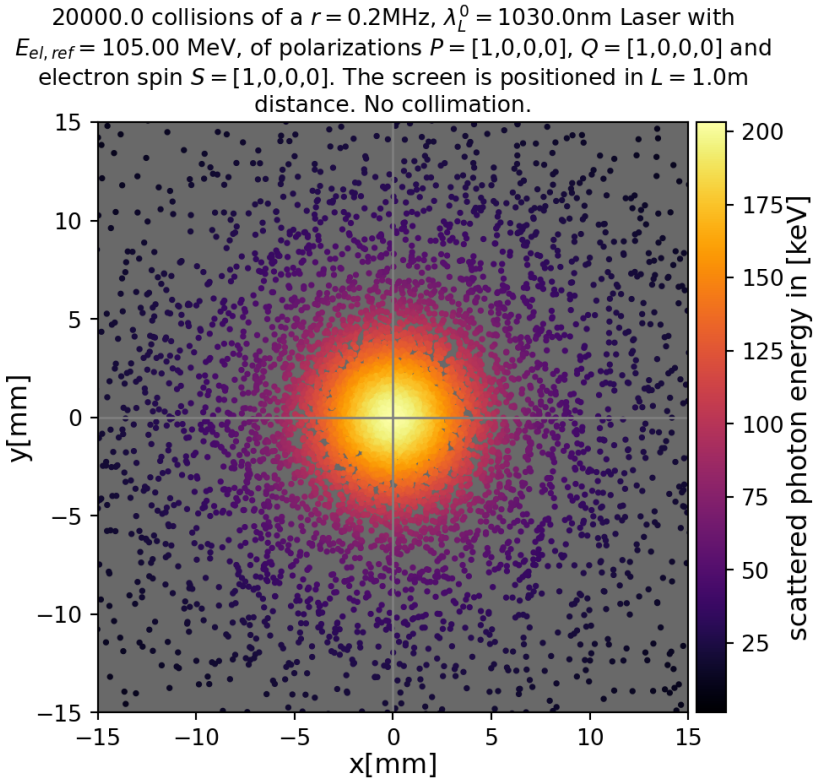

Figure 5.8.: Scattering image simulated and generated in Comparse using a MESA ER-IB-42m-nominal (App. tab. A.2) Astra generated electron distribution and Tangor-100-IR-focused (App. tab. A.8) presets.

performed Comparse using the "Trace Photons to Screen" module with activated collimator. There, we have opted to insert a virtual cylindrical collimator of length $l_{col} = 5\,\text{cm}$ within the scattered gamma beam in $d_{col} = 80\,\text{cm}$ distance from the ICS interaction center. The collimator radius r was then gradually decreased until Comparse's calculation produced the desired average scattered photon energy E_{ph}. For the set of scattering photons, two radii were found that each ensure one of the chosen bandwidths. Photons of an average energy of $\overline{E}'_{ph,95\%} = 193\,\text{keV}$ pass, if the collimator radius is set to $r_{col,95\%} = 1.735\,\text{mm}$. For $\overline{E}'_{ph,99\%} = 201\,\text{keV}$, the collimator radius needs to be narrowed to $r_{col,99\%} = 606\,\mu\text{m}$.

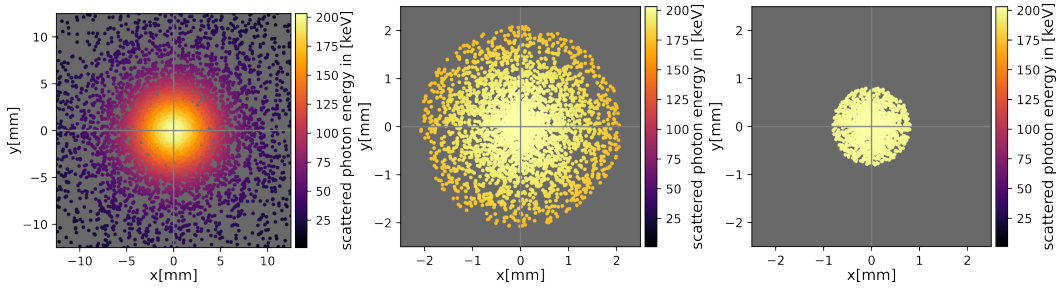

(a) Uncollimated **(b)** Collimated to $E'_{ph,lab,95\%}$ **(c)** Collimated to $E'_{ph,lab,99\%}$

Figure 5.9.: Comparision of collimation levels on a screen in 1 m distance. Scattering images simulated and generated in Comparse using a MESA ER-IB-42m-nominal (App. tab. A.2) Astra generated electron distribution and Tangor-100-IR-focused (App. tab. A.8) presets.

The collimation results of MESA ER-IB-42m and a focused Tangor 100 IR laser are shown in figure 5.9 and summarized in table 5.4. We can see, that the ER-IB-42m drift section position in it's nominal state has a sufficiently focused and aligned electron bunch distribution to enable collimation of the gamma spectrum to a 5% or even 1% bandwidth. However, a further focusing or reduction of emittance of the electron beam and laser pulse could be beneficial to improve flux at these values.
In Comparse's ICS simulation routine, a set of scattering electrons and photons is gathered via a stochastically afflicted process that produces slightly different results on every run of finite length. For the data set of this simulation, the collimator radii discussed above produce the desired average gamma energy but reduce the amount of scattered photons to $\mathfrak{N}_{ph,col,95\%}/\mathfrak{N}_{ph,uncol} = 32.25\,\%$ and $\mathfrak{N}_{ph,col,99\%}/\mathfrak{N}_{ph,uncol} = 12.48\,\%$ of the original entirety. Naturally, this lowers the estimated gamma flux of the ICS experiment. Utilizing Comparse's "Statistical Flux Estimation" module, we determine the expected uncollimated photon flux to be $\mathfrak{F}_\gamma \approx 1.17 \cdot 10^5 \mathrm{ph/s}$, a result of the approximated mean scattered photons per collision $\mathfrak{N}_\gamma \approx 0.5831\,\mathrm{ph/collision}$ multiplied by the laser pulse frequency of $\nu_{ph} = 200\,\mathrm{kHz}$. This simple calculation is possible, because for the frequency of collisions, the limiting factor is ν_{ph}, which is much lower than MESA's bunch frequency of $\nu_{RF} = 1.3\,\mathrm{GHz}$.
With this $\mathfrak{F}_\gamma$ and the simulated fractional photon loss factor $\mathfrak{N}_{ph,col,any\%}/\mathfrak{N}_{ph,uncol}$, we can calculate the collimated photon flux for any average gamma energy collimation target by simply taking their product:

$$\mathfrak{F}_{\gamma,col,95\%} = \mathfrak{F}_\gamma \cdot \frac{\mathfrak{N}_{ph,col,95\%}}{\mathfrak{N}_{ph,uncol}} \approx 3.67 \cdot 10^4 \left[\frac{\mathrm{ph}}{\mathrm{s}}\right] \tag{5.2}$$

$$\mathfrak{F}_{\gamma,col,99\%} = \mathfrak{F}_\gamma \cdot \frac{\mathfrak{N}_{ph,col,99\%}}{\mathfrak{N}_{ph,uncol}} \approx 1.46 \cdot 10^4 \left[\frac{\mathrm{ph}}{\mathrm{s}}\right] \tag{5.3}$$

To investigate the quality of the gamma bandwidth that can be achieved through pinhole collimation, let us once again plot the gamma spectrum, but for a collimation to $\overline{E}'_{ph,95\%}$. We observe in fig. 5.9, that the spectral curve is behaving as

	Uncollimated	$\overline{E}'_{ph,95\%}$	$\overline{E}'_{ph,99\%}$
average energy $\overline{E}'_{ph}$	102 keV	193 keV	201 keV
remaining photons $\mathfrak{N}$	100 %	32.25 %	12.48 %
resulting flux $\mathfrak{F}_\gamma$	$1.17 \cdot 10^5$ph/s	$3.67 \cdot 10^4$ph/s	$1.46 \cdot 10^4$ph/s

Table 5.4.: Average scattered gamma energy and collimation requirements for nominal ERL mode MESA in the IB at 42 m and a focused Tangor 100. Energies and flux approximations simulated in Comparse using a MESA ER-IB-42m-nominal (App. tab. A.2) Astra generated electron distribution and Tangor-100-IR-focused (App. tab. A.8) presets.

previously without collimation, fig. 5.10, in the immediate vicinity of the Compton peak at the ideal reference scattering energy of $E'_{ph,ref} = 4\gamma^2 E_{ph} = 203\,\text{keV}$. At around 175 keV, a sudden drop to zero normalized intensity is visible, it's cutoff being located at approximately 171 keV. This drop to cut-off is caused by the pinhole collimation. With it, researchers can fine tune the emitted ICS gamma spectrum to their bandwidth requirements, as long as scattered photon divergence and origin point distribution is small enough to allow for it's effective use.

The results presented in this subsection are also found in the ER-IB-42m position studies summary table tab. 5.10 in the row labelled "Case A".

As this study investigates a scenario in which MESA operates in ERL mode, the recoverability of electron beam energy is an important attribute to keep in mind. In this case, with laser pulse frequency $\nu_{ph,rep} = 200\,\text{kHz}$ and electron bunch frequency $\nu_{RF} = 1.3\,\text{GHz}$, only 200 thousand of 1.3 billion electron bunches potentially experience ICS. We can express this frequency mismatch as a frequency synchronisation factor $\nu_{ics,\%}$ which quantifies the percentage of the pulses or electron bunches of the higher frequency scattering partner that can be used in the ICS experiment. For MESA in nominal ER mode in the Internal Beamline at 42 m and an off-the-shelve Tangor 100 IR with applied focus optics, we obtain:

$$\nu_{ics,\%} = \frac{2 \cdot 10^5}{1.3 \cdot 10^9} = 0.0001538 = 0.01538\% \tag{5.4}$$

Let us further consider, that the average expected scattering photons per collision are approximately $\mathfrak{N}_\gamma \approx 0.5831\,\text{ph/collision}$. Now, we can calculate the expected average scattering electrons per bunch as

$$\mathfrak{N}_{el,ics} = \nu_{ics,\%} \cdot \mathfrak{N}_\gamma = 8.97 \cdot 10^{-5} \quad \left[\frac{\text{electrons}}{\text{bunch}}\right] \tag{5.5}$$

According to the Comparse simulation, the average energy of the scattering electrons is $\overline{E}'_{el} \approx 104.90\,\text{MeV}$ as opposed to $\overline{E}_{el} \approx 105.00\,\text{MeV}$ before scattering, indicating an average energy loss due to ICS of $\overline{E}'_{el,los} \approx 100\,\text{keV}$. As the average scattered photon energy is simulated to be $\overline{E}'_{ph} \approx 102\,\text{keV}$ and incoming photons possess $\overline{E}_{ph,ref} = 1.20\,\text{eV}$, an energy loss in this range is to be expected. One can

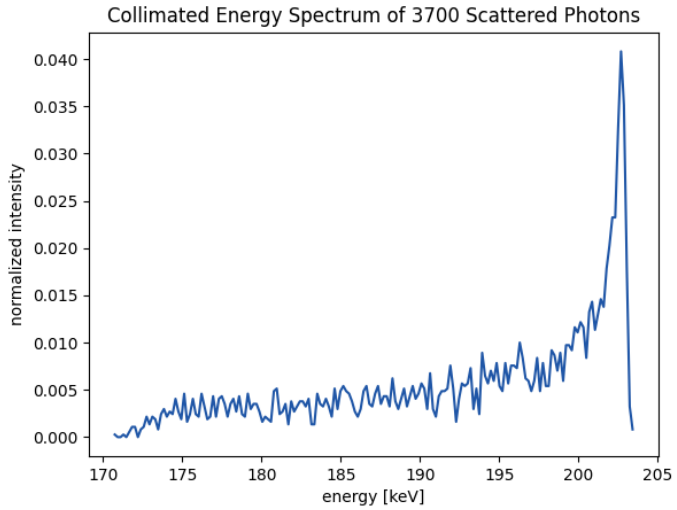

Figure 5.10.: Scattered photon spectrum of nominal ERL mode MESA in the IB at 42 m and a focused Tangor 100 laser. The scattered photons were collimated with the target average energy $\overline{E}_{ph,95\%} = E'_{ph,max}$. This plot was simulated and generated in Comparse using a MESA ER-IB-42m-nominal (App. tab. A.2) Astra generated electron distribution and Tangor-100-IR-focused (App. tab. A.8) presets.

plot the energy loss $\overline{E}'_{el,los}$ to the unscattered electron energy E_{el} and recoil factor X to see, that the experience energy loss is heavily related to X (fig. 5.11).

To visualize the impact on the electron phase space and analyze whether the scattering electrons can be used for energy recovery, we export the Comparse simulation data as a combined unscattered and scattered file and plot it using Astra Postpro [30]: fig. 5.12. The scattered electrons are found clear outside of the unscattered longitudinal phase space. Assuming the worst case scenario, in which none of the scattering electrons can be recirculated and thus their kinetic energy not be recovered, consider, that they make up only

$$\frac{\mathfrak{N}_{el,ics}}{N_{el}} = \frac{\mathfrak{N}_{el,ics}e}{Q_{el}} = \frac{8.97 \cdot 10^{-5}}{4.81 \cdot 10^{7}} = 1.86 \cdot 10^{-10}\% \tag{5.6}$$

of all accelerated electrons. Even a total loss would not meaningfully influence ERL efficiency in this experiment configuration.

5.2.2. Nominal MESA ERL Internal Beamline & Laser Cavity Configuration

To increase the ICS gamma flux, at first, an efficient method to improve laser intensity was considered. For this purpose, typically solutions akin to a Fabry-Pérot cavity (fig. 5.13) are considered [46]. When applying a cavity concept to an accelerator driven ICS source, one has to consider the limitations imposed by the

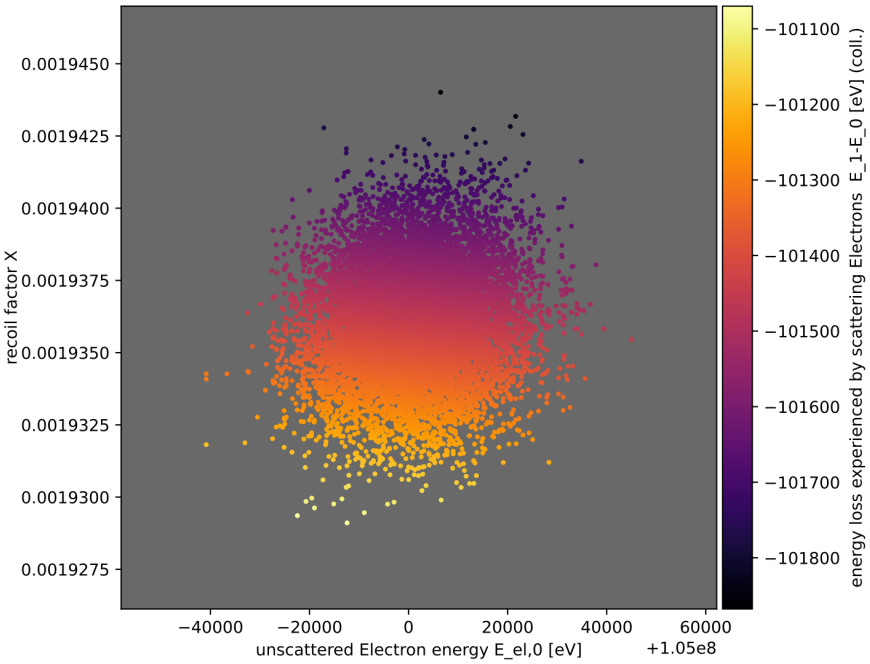

Figure 5.11.: Experienced electron energy loss $\overline{E}'_{el,los}$ to unscattered electron energy E_{el} and recoil factor X. Plot simulated and generated in Comparse using a MESA ER-IB-42m-nominal (App. A.2) Astra generated electron distribution and Tangor-100-IR-focused (App. A.8) presets. The horizontal axis shows electrons with an initial energy E_el in units of eV around reference kinetic energy 105 MeV, as indicated by the "+1.05e8" exponential summand below.

accelerator operation parameters the interaction between laser intensity and cavity material. Fundamentally, there are two principles for boosting the intensity of a pulsed laser: increasing the repetition rate or pulse energy. When the reflected laser pulses in an optical cavity are arriving in the experiment location at the same time, the intensity of the individual pulses add up, thus essentially increasing the energy contained within one pulse while keeping the pulse repetition rate constant. For accelerator ICS experiments, this has the advantage that no modification has to be made to the electron bunch repetition rate. However, the fraction of electron bunches that experience laser pulses now are affected by a pulse intensity multiplied by the number of overlapping pulses. This multiplication factor directly affects the scattering probability and accordingly the likelihood of a single electron undergoing multiple scattering events. Should a single electron scatter more often than once, the ICS impact on it can be arbitrarily high, depending on the number of scattering events. Eventually, it would drop out of any beam guidance condition. Furthermore, multi scattering events broaden the ICS gamma spectrum, as the space of possible initial scattering parameters includes already scattered photons or elec-

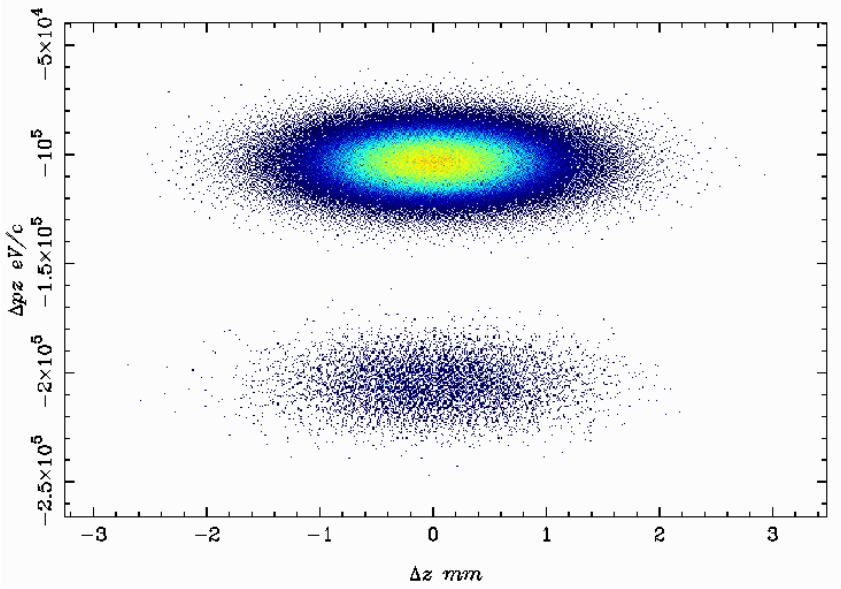

Figure 5.12.: Longitudinal phase space of one unscattered MESA electron bunch combined with the scattered electrons of 20k ICS collisions. Data simulated and generated in Comparse using a MESA ER-IB-42m-nominal (App. tab. A.2) Astra generated electron distribution and Tangor-100-IR-focused (App. tab. A.8) presets. Plot created in Astra postpro.

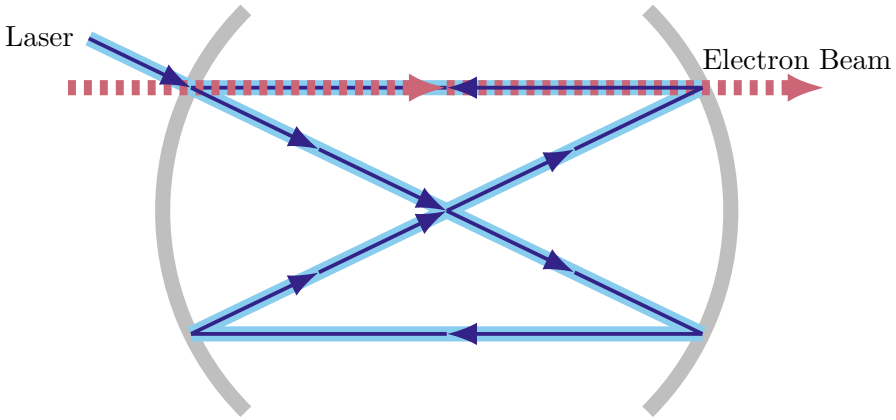

Figure 5.13.: Basic scheme of a Fabry-Pérpt cavity amplified ICS experiment layout, drawn in reference to [46].

trons. For a high base laser pulse intensities, this effect can be expected to occur. However, in this study, we focused on detailed inverse Compton scattering simulations without multiple scattering effects. Calculations determining if an electron can still be guided in the accelerator beamline after scattering assume an energy loss caused by only one scattering event. To ensure the validity of the exclusion of multi-scattering effects, we focus on optical cavity concepts that avoid boosting

individual laser pulses while keeping the pulse repetition rate.
In the other variant, that of reflected pulses arriving one after another without overlap, the effective repetition rate $\nu_{ph,rep}$ is multiplied. This can benefit the generated photon flux only if the particle accelerator can match the new $\nu_{ph,rep}$. On a per bunch - pulse collision basis, this leaves the impact on the electron beam unchanged.
A sophisticated particle accelerator usually operates at a much higher repetition rate than commonly available industry lasers. This general rule can be well applied to MESA during nominal operation as planned in 2024, where the electron bunch repetition rate ν_{RF} = GHz is higher than the pulse frequency range of the Tangor 100 IR laser $\nu_{ph,rep} = 200\,\text{kHz}$ to $40\,\text{MHz}$ by multiple orders of magnitude. However later on we will discuss a speculative high bunch charge Q_{el} - low repetition rate ν_{RF} modification to MESA. This study assumes that the cavity solution can be adjusted and constructed to facilitate both laser amplification modes or even a combination, as required by the accelerator setting.
Taking advantage of the developments discussed in [47] and [48], a novel optical cavity's performance reports were chosen as the basis for boosting ICS flux at MESA. The "System of Multipass optical beam for Interaction between Laser and Electrons" (SMILE) cavity consists of two sets of seven spherical mirrors. They are placed in equal distance on both sides to the laser - electron interaction focus on circular plates with large openings for the electron beam. While there are seven mirrors on each side, each circular plate has 8 inlets symmetrically aligned around the electron beam axis, 7 of which are filled with optical mirrors and two of which are left empty: One opening for the laser pulse to enter and one for it to exit. With well adjusted alignment, one laser pulse travels eight times through the electron interaction point, ideally increasing the laser repetition rate by a factor of 8. See fig. 5.14 for a sketch of the optical scheme.
In [47], the 8 laser pulse reflections are synchronized to arrive at the ICS interaction point at the same time. To keep the compact cavity design of about $s = 1\,\text{m}$ along the electron beam axis, we keep this synchronisation for this laser study and consider the laser pulse intensity to be amplified 8-fold, rather than the repetition rate. The entire ICS experiment of [48] is 1 m in length, small enough for implementation at MESA. Therefore, we shall consider an 8-fold amplified laser pulse intensity from $E_{pulse} = 0.5\,\text{mJ}$ to $4\,\text{mJ}$ for this study.
Changing neither laser wavelength $\lambda = 1030\,\text{nm}$ nor reference electron energy $E_{el,ref} = 105\,\text{MeV}$, we can expect the same scattered photon energy of $E'_{ph,max} \approx 204\,\text{keV}$, although at a much higher flux. Simulation results listed in tab. 5.5 confirm the expectation. See fig. 5.15 for a visual comparison of the scattered photons one can expect from 100 collisions between MESA in nominal configuration and a Tangor 100 IR laser with or without SMILE style optical cavity. Smaller differences in the percentage of lost photons in the attempt to obtain a target average energy by inserting a physical collimator in the scattered gamma path are due to statistical variation in simulations. Every scattering electron and photon have a randomized initial four vector and scattering position, which causes changes in the

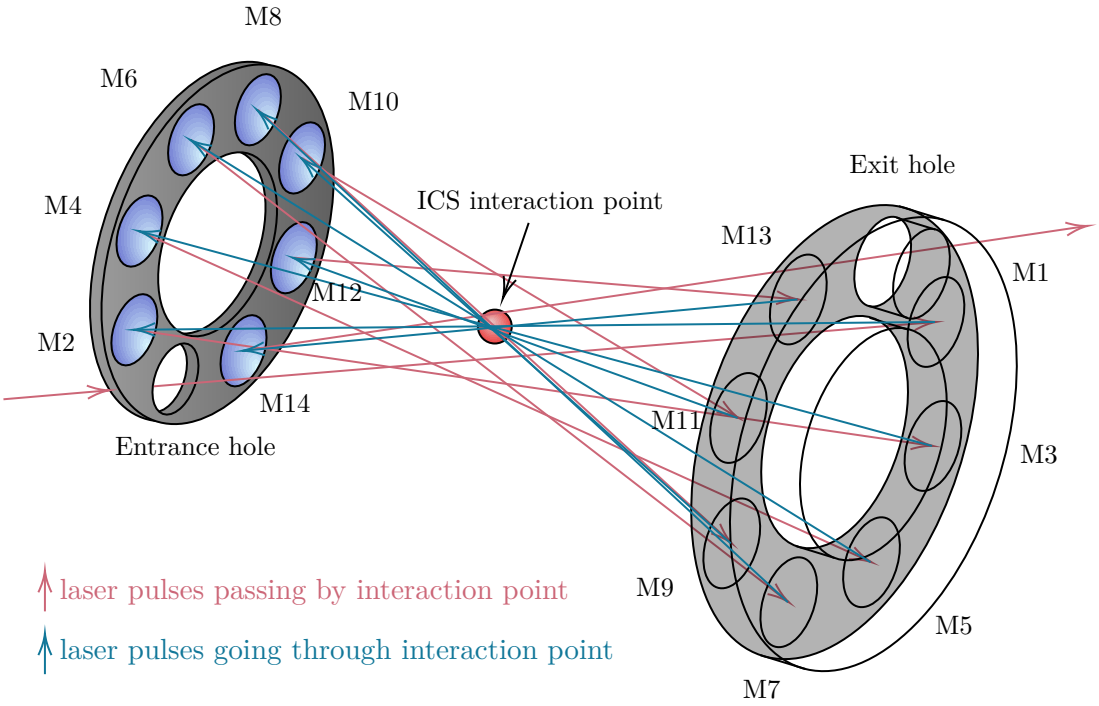

Figure 5.14.: Sketch of SMILE system optical cavity scheme. This figure was recreated for this thesis based on Fig.3 on p.115 in [47].

$E_{ph,max} \approx 204\,\mathrm{keV}$	**Uncollimated**	$\overline{E}'_{ph,95\%}$	$\overline{E}'_{ph,99\%}$
average energy $\overline{E}'_{ph}$	102 keV	193 keV	201 keV
remaining photons $\mathfrak{N}$	100 %	30 %	12.14 %
resulting flux $\mathfrak{F}_\gamma$	$9.32 \cdot 10^5$ph/s	$2.8 \cdot 10^5$ph/s	$1.13 \cdot 10^5$ph/s

Table 5.5.: Average scattered gamma energy and collimation requirements for nominal ERL mode MESA in the IB at 42 m and a 8-fold SMILE amplified focused Tangor 100. Energies and flux approximations simulated in Comparse using a MESA ER-IB-42m-nominal (App. tab. A.2) Astra generated electron distribution and Tangor-100-IR-focused (App. tab. A.9) presets.

traced scattering image on screen, even before the weighted random selection of the scattering photon direction. This indicates a level of uncertainty and limitation inherent to bandwidth fine tuning through the use of a collimator. See section 4.7 for an explanation of how Comparse's collimation simulations work and section 5.4 for a study focusing on collimation potential and limitations. There is another source of variation: 95% of the maximum energy is defined in reference to an $E'_{ph,max}$ that itself is the result of a randomization affected simulation:

$$\overline{E}'_{ph,95\%} := 0.95 \cdot E'_{ph,max} \tag{5.7}$$

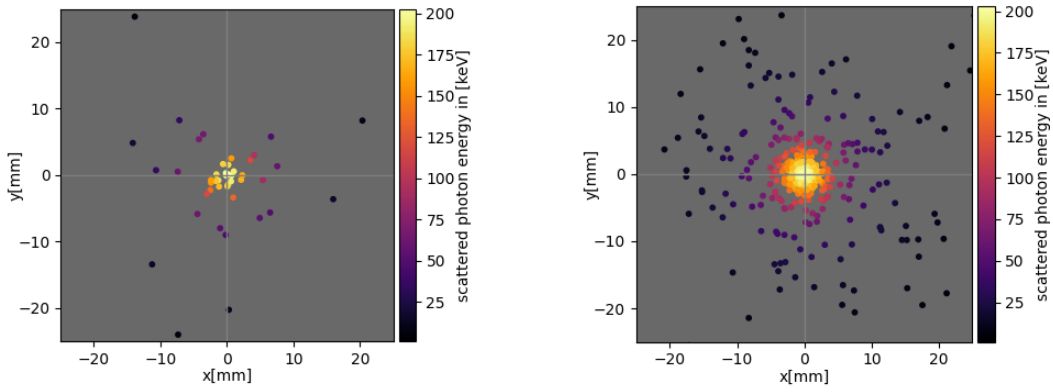

(a) Tangor 100 IR

(b) Tangor 100 IR & SMILE cavity

Figure 5.15.: Scattering photons produced in 100 MESA IB42m nominal collisions traced to a 50 mm edge length square screen positioned in 1 m distance from the ICS interaction point. Scattering images simulated and generated in Comparse using a MESA ER-IB-42m-nominal (App. tab. A.2) Astra generated electron distribution and Tangor-100-IR-focused (fig. 5.15a, App. tab. A.8) and Tangor-100-IR-focused-SMILE (fig. 5.15b, App. tab. A.9) presets.

As the highest scattered photon energy will vary from collision to collision, so will the criteria for $\overline{E}'_{ph,95\%}$ and with it the collimation requirements.

5.2.3. Nominal MESA ERL Internal Beamline & 193 nm Excimer Laser

With a Laser wavelength of $\lambda = 1030\,\text{nm}$ and MESA at 105 MeV, the generation of ICS gamma radiation up to $E'_{ph} = 4E_\nu\gamma^2 = 203\,\text{keV}$ is possible. For higher scattered photon energies, we have to consider a different wavelength. Excimer lasers produce $\lambda_\nu = 193\,\text{nm}$ wavelength UV light by generating excited unstable Argon Fluorid pseudo-molecules termed "excimer" [49]. The market holds several manufacturers of high pulse energy $E_{pulse} > 100\,\text{mJ}$ excimer lasers, and a broader range of models one magnitude lower in energy. For this study, we investigated the GAM Laser Inc EX10UIN from tab. A.10 focused to a pulse waist of $\sigma_{ph,x} = \sigma_{ph,y} = w_0 = 50\,\mu\text{m}$. According to the spec sheet [50], it can produce $E_{pulse} = 0.2\,\text{mJ}$ laser pulses at a $\nu_{ph,rep} = 1\,\text{kHz}$ repetition rate and is rated for Laser beam quality factor $M^2 = 35$. Using a high-end $\lambda = 193\,\text{nm}$ excimer laser model enables the production of MeV range gamma radiation at MESA. The flux is subject to the same inefficiencies of a Tangor 100 IR laser setup where most of the electron bunches do not experience laser pulses. Here, the repetition rate difference is even greater. Of the 1.3 billion electron bunches that MESA accelerates per second ($\nu_{RF} = 1.3\,\text{GHz}$), only 1000 ($\nu_{ph,rep} = 1\,\text{kHz}$) can potentially experience ICS. While a greater repetition rate related flux

$E_{ph,max} \approx 1.075\,\mathrm{MeV}$	**Uncollimated**	$\overline{E}'_{ph,95\%}$	$\overline{E}'_{ph,99\%}$
average energy $\overline{E}'_{ph}$	537 keV	1.023 MeV	1.064 MeV
remaining photons $\mathfrak{N}$	100 %	31.09 %	13.79 %
resulting flux $\mathfrak{F}_\gamma$	$2.36 \cdot 10^6$ph/s	$7.33 \cdot 10^5$ph/s	$3.25 \cdot 10^5$ph/s

Table 5.6.: Average scattered gamma energy and collimation requirements for nominal ERL mode MESA in the IB at 42 m and a focused 193 nm excimer laser. Energies and flux approximations simulated in Comparse using a MESA ER-IB-42m-nominal (App. tab. A.2) Astra generated electron distribution and EX10IN-excimer-focused (App. tab. A.11) presets.

inefficiency lowers the gamma flux, the higher pulse energy of $E_{pulse} = 20\,\mathrm{mJ}$ more than compensates for it. The scattered photon flux of the nominal MESA ERL Internal Beamline and 193 nm excimer laser experiment, $\mathfrak{F}_\gamma = 2.36 \cdot 10^6 \left[\frac{\mathrm{ph}}{s}\right]$, is an order of magnitude and twice as high as the nominal MESA and off-the-shelve IR laser one of section 5.2.1.
The character of the effect on the electrons changes. While with a $\nu_{ph,rep} = 200\,\mathrm{kHz}$ & $E_{pulse} = 0.5\,\mathrm{mJ}$ laser just over 100 thousand of 1.3 billion electron bunches have one or two electrons scattering on average, here, only 1000 electron bunches can experience ICS, but of those, about 2360 electrons exceed the nominal phase space volume as a result of ICS momentum transfer.
Due to the increased scattering photon energy E'_{ph}, the impact of ICS on individual scattering electrons is raised. As shown in fig. 5.16, impacted electrons are losing about $\overline{E}'_{el,los} = 537\,\mathrm{keV}$, a logical match with the average scattered photon energy $\overline{E}'_{ph}$ whose value is mostly defined by the ICS energy transfer. In comparison to the same plot created for the Tangor 100 simulation fig. 5.11, one can observe a more pronounce oblong shape along the bottom left corner to upper right corner diagonal. This diagonal in the recoil factor X to initial electron energy E_{el} represents the linear dependence of X to E_{el}, as seen in eq. 3.24, where Lorentz factor γ_{el} is a direct multiplier. In an ideal scattering scenario of zero laser energy spread ΔE_{ph} and only head-on collisions, the dots in the graph would all be located on the middle diagonal. With an increase in photon energy E_{ph} of the excimer laser in fig. 5.16 over the Tangor 100 IR laser of fig. 5.11, the recoil to electron energy spread dependence is boosted as per $X \propto E_{el} \cdot E_{ph}$. It follows, that the plot's diagonal relation must be more apparent for higher energies, which is the effect that we observe.
As a consequence, the spectrum of ICS gamma sources using higher energy incident lasers will be more sensitive to the fermion beam's energy spread and extra attention must be placed on keeping ΔE_{el} low.

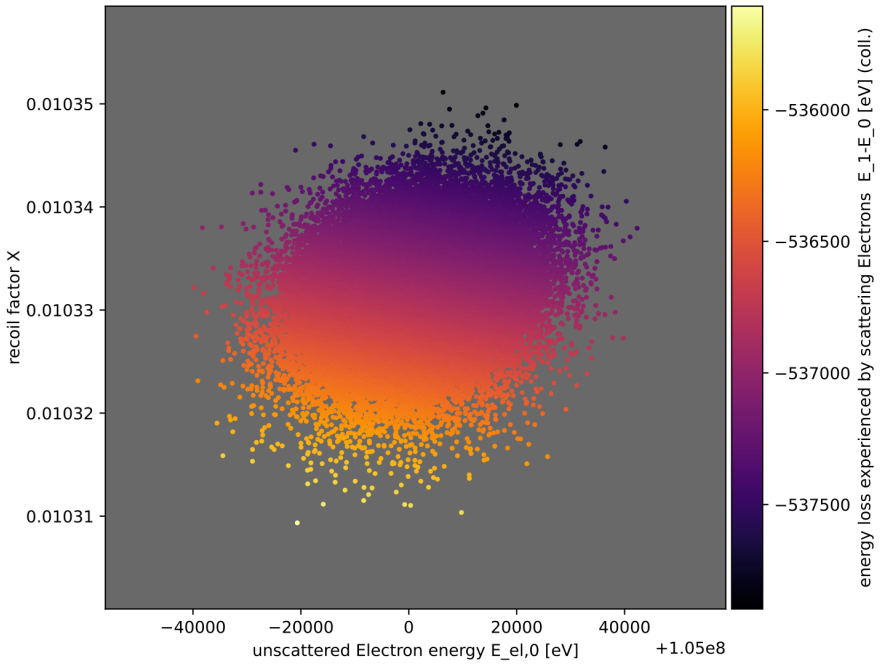

Figure 5.16.: Experienced electron energy loss $\overline{E}'_{el,los}$ to unscattered electron energy E_{el} and recoil factor X. Plot simulated and generated in Comparse using a MESA ER-IB-42m-nominal (App. tab. A.2) Astra generated electron distribution and EX10IN-Excimer-focused (App. tab. A.11) presets. The horizontal axis shows electrons with an initial energy E_el in units of eV around reference kinetic energy 105 MeV, as indicated by the "+1.05e8" exponential summand below.

5.2.4. Nominal MESA ERL Internal Beamline & Amplified 193nm Excimer Laser

When amplifying a laser of high pulse energy E_{pulse} and low repetition rate $\nu_{ph,rep}$, it can be easier to increase $\nu_{ph,rep}$ rather than E_{pulse}. With MESA operating at $\nu_{RF} = 1.3\,\text{GHz}$, there is plenty of synchronization leeway to accommodate a higher $\nu_{ph,rep}$ in full. Furthermore, as an ICS experiment with a EX10IN excimer laser would constitute a more extensive setup, the potential loss of compactness on the laser cavity side is justified by the reduction of multiple scattering events.
For the nominal MESA ERL IB and 8-fold amplified 193 nm excimer study, we shall only discuss the flux related changes compared to the last subsection's study of the unamplified excimer laser. Table 5.7 lists the newly simulated scattering statistics in the same way as before. In the uncollimated case, we can see the flux increase from $\mathfrak{F}_\gamma = 2.36 \cdot 10^6\text{ph/s}$ to $1.89 \cdot 10^7\text{ph/s}$. As expected, the flux improvement is equivalent to the increase of the laser pulse energy E_{pulse} by a factor 8. In this setup, one could produce narrow spectral bandwidth $\overline{E}'_{ph,99\%}$ MeV gamma rays at MESA with a flux of $2.59 \cdot 10^6$ ph/s. Further improvements on the laser side are

$E_{ph,max} \approx 1.075\,\mathrm{MeV}$	**Uncollimated**	$\overline{E}'_{ph,95\%}$	$\overline{E}'_{ph,99\%}$
average energy $\overline{E}'_{ph}$	537 keV	1.021 MeV	1.064 MeV
remaining photons $\mathfrak{N}$	100 %	31.23 %	13.71 %
resulting flux $\mathfrak{F}_\gamma$	$1.89 \cdot 10^7$ph/s	$5.89 \cdot 10^6$ph/s	$2.59 \cdot 10^6$ph/s

Table 5.7.: Average scattered gamma energy and collimation requirements for nominal ERL mode MESA in the IB at 42 m and a focused 193 nm excimer laser with 8-fold amplified E_{pulse}. Energies and flux approximations simulated in Comparse using a MESA ER-IB-42m-nominal (App. tab. A.2) Astra generated electron distribution and EX10IN-excimer-focused-SMILE (App. tab. A.12) presets.

difficult unless major laser development work takes place. Therefore, for the next studies, we will investigate the benefits of a theoretical low repetition rate - high bunch charge mode of operation for MESA.

5.2.5. MESA ERL 1nC Study

We have made mention of how the low ICS efficiency factor $\nu_{ics,\%} = 0.01538\%$ of eq. 5.4 between MESA at nominal operation and the investigated lasers limits the potential gamma flux of the experiments. We are thus considering modifications to MESA that would lower it's repetition rate ν_{RF} to bring it more inline with the lasers. The benefit comes from the fact, that one can lower ν_{RF} while keeping the average current constant by compensating with a proportional increase of the bunch charge Q_{el}. For this, an assumed $Q_{el} = 1\,\mathrm{nC}$ operation mode at a much lowered frequency of 100 kHz is investigated. A modification of the "MESA Low energy Beam Apparatus" (MELBA) will be needed for this mode of operation. This is because the "Milliampere Booster" (MAMBO) cannot boost electron bunches above a maximum bunch charge of $Q_{e,max} = 8\,\mathrm{pC}$ while keeping beam quality within MESA beamline constraints. However, national research institutes are working with 5 MeV & 1 nC electron injectors. See for example the electron source at the Photo Injector Test Facility at DESY Zeuthen ([51], [52]) that can generate 6000 $Q_e = 1\,\mathrm{nC}$ electron bunches per second. One can envision, that with a new room, some support by colleagues and maybe even pre-existing hardware, this implementation scenario could be realized as a new low frequency mode of operation for MESA. A higher bunch charge can go along with an increase in space charge effects that threaten to defocus and destabilize the electron bunch beyond the focusing capabilities of the MESA beamline. Thus, in order to conduct ICS studies for MESA at 1 nC, we first have to confirm the electron beam parameter's feasibility.
In Astra, a Gaussian electron bunch distribution was generated using the same parameters as MESA ER-IB-42m-nominal, except for bunch charge $Q_{el} = 1\,\mathrm{nC}$. To confirm that we can maintain the hereto assumed beam quality at $Q_{el} = 1\,\mathrm{nC}$, we make use of Astra's space charge routine to simulate a drift over $s = 1\,\mathrm{m}$ for the macro electron distribution and observe the changes every 20 cm. The results

are then plotted using the "lineplot" module that is part of Astra's data analysis tools [30].

As we can see in fig. 5.17, the transversal divergence is very low in the already

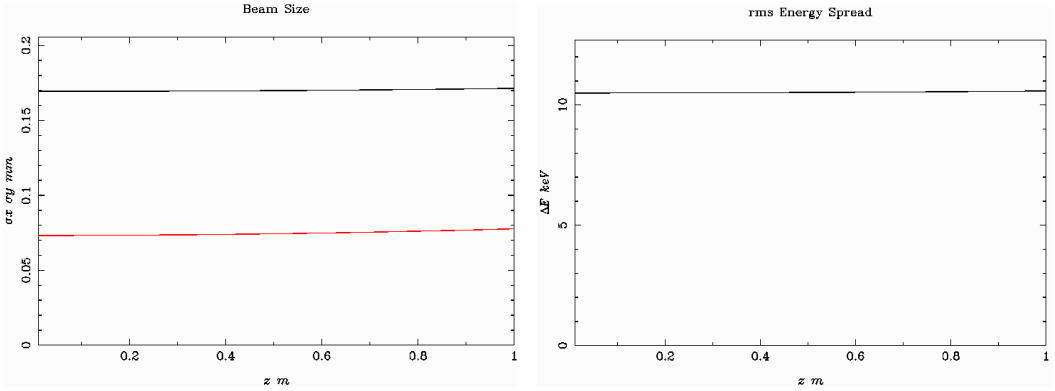

(a) Transversal bunch sizes $\sigma_{el,x}$ & $\sigma_{el,y}$. **(b)** Kinetic energy spread $E_{el,\sigma}$

Figure 5.17.: Changes in transversal bunch sizes and energy spread of a hypothetical $Q_{el} = 1\,\text{nC}$ bunch charge at MESA in the Internal Beamline at around $s = 42\,\text{m}$ over a 1 m drift. Drift simulation conducted using Astra, plots generated using Astra's lineplot module. Base electron distribution generated in Astra using the MESA ER-IB-42m-1nC (App. tab. A.4) preset.

wider x-component, rising from $\sigma_{el,x} = 169.4\,\mu\text{m}$ to $171.4\,\mu\text{m}$ over the 1 m, while in the tightly focused y-component, the bunch size increases from $\sigma_{el,y} = 73.2\,\mu\text{m}$ to $77.6\,\mu\text{m}$. Additionally, one can observe a slight diffusion of the energy spread from $E_{el,\sigma} = 10.50\,\text{keV}$ to $10.58\,\text{keV}$ over the drift. In the simulation, a lengthening of the longitudinal bunch size was calculated but remained imperceptible by Astra output precision. All parameters of interest before and after are listed alongside their relative change in tab. 5.8. The simulations indicate that at MESA's planned

	$\boldsymbol{\sigma_{el,x}}$	$\boldsymbol{\sigma_{el,y}}$	$\boldsymbol{\sigma_{el,z}}$	$\boldsymbol{E_{el,\sigma}}$
$\boldsymbol{s = 0\ \text{m}}$	169.4 µm	73.2 µm	639.9 µm	10.50 keV
$\boldsymbol{s = 1\ \text{m}}$	171.4 µm	77.6 µm	639.9 µm	10.58 keV
relative change	+1.18%	+6.01%	+0%	+0.76%

Table 5.8.: Time dependent electron bunch quality parameters in absolute values before and after a $s = 1\,\text{m}$ long drift section in absolute values and relative change.

Internal Beamline electron beam dimensions, a higher bunch charge is well within nominal acceptance.

It should be mentioned, that the initial electron distribution parameters were taken from within a drift section of the MESA beamline simulation as it is planned in 2024. This means, that the layout features no focusing elements in front of the investigated location. The electron bunch dimensions therefore constitute conservative

estimations of achievable beam focus. We are thus confident that the ICS studies conducted for a $Q_{el} = 1\,\text{nC}$, $\nu_{RF} = 100\,\text{kHz}$ operation mode using the settings listed in tables 5.9 and A.4 are not based on unrealistically optimistic expectations.

ν_{RF}	Q_{el}	$E_{el,ref}$	$E_{el,\sigma}$	σ_x	σ_y	σ_z
100 kHz	1 nC	105 MeV	0.01 %	169 µm	73 µm	640 µm

Table 5.9.: Electron distribution parameters for a hypothetical high bunch charge operation mode of MESA in the internal Beamline at $s \approx 42\,\text{m}$.

5.2.5.1. Laser Cavity Amplification in Combination with MESA in 1nC Operation Mode

On the topic of the laser cavity amplification, changes were made to the setups described in the previous sections 5.2.2 and 5.2.4 for MESA ER-IB-42m nominal. As the electron bunch frequency was greatly decreased to $\nu_{RF} = 100\,\text{kHz}$, we decided to configure the SMILE cavity for the repetition rate boost variant in combination with the $\nu_{ph,rep} = 1\,\text{kHz}$ laser. This combination still offers sufficient room for pulse - bunch synchronisation.
All four laser implementation scenarios were simulated again for the $Q_{el} = 1\,\text{nC}$ configuration. For the reason that the reference kinetic electron energy $E_{el,ref}$ was left unchanged, we did not expect and eventually observe any different maximum scattered photon energy $E_{ph,max}$. The spectra too appear to similar, as seen in fig. 5.18 showing the uncollimated spectrum of both MESA nominal and 1 nC with the EX10IN excimer laser. The sharper Compton edge in the nominal MESA case fig. 5.18a can be explained by the overall lower statistic. When the gamma energy spread $\sigma E'_{ph}$ nears zero, the Compton edge approaches a vertical drop.
The results so far are well within expectation. The high bunch charge modification was envisioned with for the purpose of increasing the scattered photon flux to improve the gamma source potential of MESA. Flux estimation simulations were carried out for MESA in $Q_{el} = 1\,\text{nC}$ & $\nu_{RF} = 100\,\text{kHz}$ scattering on Tangor 100 IR and EX10IN excimer laser, both with and without SMILE cavity amplification. The results are summarized alongside the MESA nominal studies in summary table 5.10. In all corresponding laser and collimation scenarios, we now obtain a scattered photon flux that is more than two magnitudes higher than before. This too is expected, as the increase in bunch charge Q_{el} without effective reduction of the repetition rate ν_{RF} should linearly increase the scattering probability:

$$\mathfrak{F}_{\gamma,1\text{nC}} = \frac{1\text{nC}}{7.7\text{pC}} \cdot \mathfrak{F}_{\gamma,7.7\text{pC}} = 130 \tag{5.8}$$

Indeed, when comparing flux values of corresponding rows and cells in table 5.10, we can confirm a boost of approximately 130 in all scenarios. For example, the

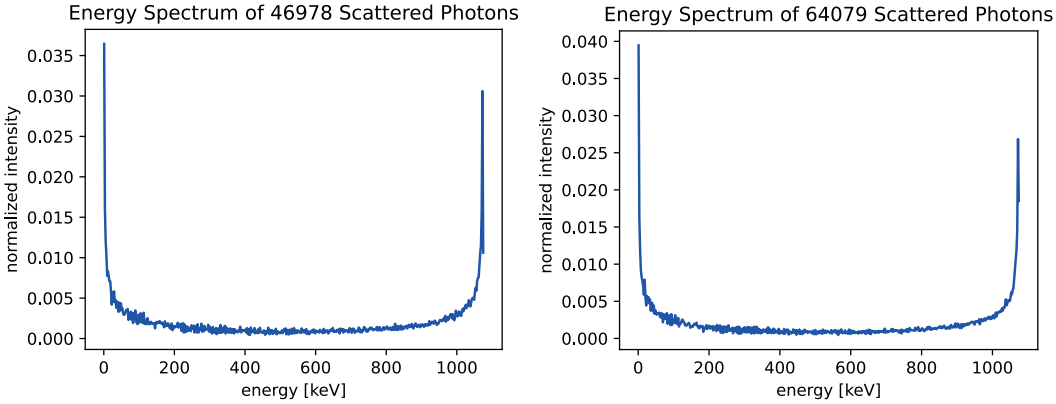

(a) Nominal MESA IB@42m **(b)** 1 nC MESA IB@42m

Figure 5.18.: Comparison of ICS gamma spectra of MESA IB@42m in nominal and high bunch charge configuration. Plots simulated and generated in Comparse using a MESA ER-IB-42m-nominal (App. tab. A.2) and MESA ER-IB-42m-1nC (App. A.4) Astra generated electron distributions with the EX10IN-Excimer-focused (App. A.11) laser preset.

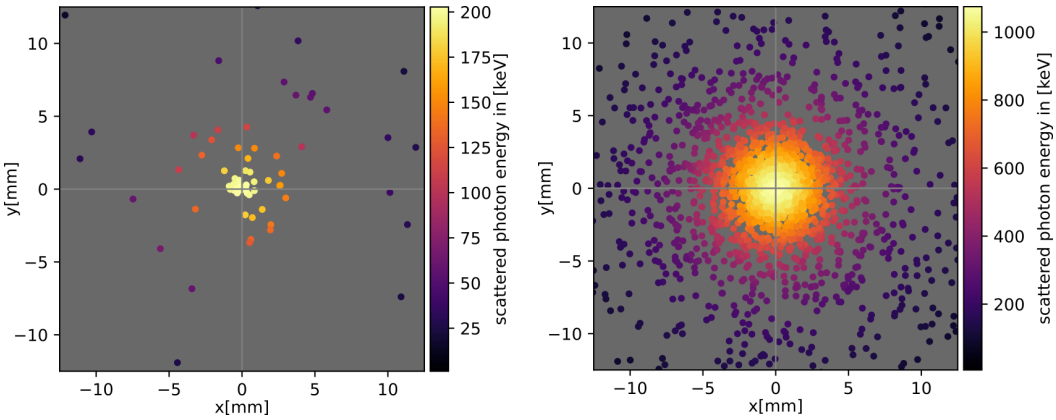

(a) Tangor 100 IR with focus optics **(b)** EX10IN Excimer with focus optics

Figure 5.19.: Scattering photons produced in collision with a MESA IB@42m $Q_{el} = 1\,\text{nC}$ and $\nu_{RF} = 100\,\text{kHz}$ electron bunch traced to a 50 mm edge length square screen positioned in 1 m distance from the ICS interaction point. fig. 5.19a displays the result of a single Tangor 100 IR laser pulse collision event, whereas fig. 5.19b displays the result of 1 % of a single EX10IN excimer laser pulse. The latter was simulated using boost/damping factor $B = 0.01$. No SMILE cavity or other method of laser pulse amplification was used. Scattering images simulated and generated in Comparse using a MESA ER-IB-42m-1nC (App. tab. A.4) Astra generated electron distribution and Tangor-100-IR-focused (fig. 5.19a, App. tab. A.8) and EX10IN-Excimer-focused (fig. 5.19b, App. tab. A.11) presets.

aggressively collimated flux $\mathfrak{F}_{\gamma,col,99\%}$ increases from $\mathfrak{F}_{\gamma,col,99\%,D} = 2.59 \cdot 10^6$ [ph/s] in row D to $\mathfrak{F}_{\gamma,col,99\%,H} = 3.29 \cdot 10^8$ [ph/s] in row H, a factor of $\frac{329}{2.59} \approx 127$.

5.2.6. MESA ERL baseline Study Summary

(A) MESA ER-IB-42m (tab. A.1) + Laser 1 (Tangor 100 IR baseline + focus optics) (tab. A.8)

(B) MESA ER-IB-42m (tab. A.1) + Laser 2 (Tangor 100 IR + SMILE + focus optics) (tab. A.9)

(C) MESA ER-IB-42m (tab. A.1) + Laser 3 (EX10IN + focus optics) (tab. A.11)

(D) MESA ER-IB-42m (tab. A.1) + Laser 4 (EX10IN + SMILE + focus optics) (tab. A.12)

(E) MESA ER-IB-42m-1nC (tab. A.4) + Laser 1 (Tangor 100 IR baseline + focus optics)(tab. A.8)

(F) MESA ER-IB-42m-1nC (tab. A.4) + Laser 2 (Tangor 100 IR + SMILE + focus optics) (tab. A.9)

(G) MESA ER-IB-42m-1nC (tab. A.4) + Laser 3 (EX10IN + focus optics) (tab. A.11)

(H) MESA ER-IB-42m-1nC (tab. A.4) + Laser 4 (EX10IN + SMILE + focus optics) (tab. A.12)

	$E'_{ph,max}$ [MeV]	$\mathfrak{F}_\gamma$ [ph/s]	$\overline{E}'_{ph}$ [MeV]	$r_{col,95\%}$ [mm]	$\mathfrak{N}_{ph,col,95\%}$ [%]	$\mathfrak{F}_{\gamma,col,95\%}$ [ph/s]	$\overline{E}'_{ph,95\%}$ [MeV]	$r_{col,99\%}$ [mm]	$\mathfrak{N}_{ph,col,99\%}$ [%]	$\mathfrak{F}_{\gamma,col,99\%}$ [ph/s]	$\overline{E}'_{ph,col,99\%,}$ [MeV]
A	0.204	$1.17 \cdot 10^5$	0.102	1.735	31.25	$3.67 \cdot 10^4$	0.193	0.606	12.48	$1.46 \cdot 10^4$	0.201
B	0.204	$9.32 \cdot 10^5$	0.0999	1.749	30.00	$2.80 \cdot 10^5$	0.193	0.614	12.14	$1.13 \cdot 10^5$	0.201
C	1.075	$2.36 \cdot 10^6$	0.537	1.786	31.09	$7.33 \cdot 10^5$	1.023	0.689	13.79	$3.25 \cdot 10^5$	1.064
D	1.075	$1.89 \cdot 10^7$	0.537	1.797	31.23	$5.89 \cdot 10^6$	1.021	0.683	13.71	$2.59 \cdot 10^6$	1.064
E	0.204	$1.52 \cdot 10^7$	0.102	1.746	30.95	$4.64 \cdot 10^6$	0.193	0.609	12.6	$1.83 \cdot 10^6$	0.201
F	0.204	$1.21 \cdot 10^8$	0.101	1.759	31.14	$3.73 \cdot 10^7$	0.193	0.603	12.46	$1.51 \cdot 10^7$	0.201
G	1.076	$3.06 \cdot 10^8$	0.537	1.779	31.09	$9.52 \cdot 10^7$	1.022	0.665	13.22	$4.05 \cdot 10^7$	1.06
H	1.075	$2.45 \cdot 10^9$	0.537	1.78	31.13	$7.63 \cdot 10^8$	1.024	0.670	13.44	$3.29 \cdot 10^8$	1.065

Table 5.10.: ICS performance parameters of investigated implementation scenarios.

So far in this chapter, we presented simulations investigating the feasibility of an Inverse Compton Scattering experiment at three suitable locations inside of the MESA facility. All electron distributions were modelled after beamline simulations of MESA as currently under construction, featuring no additional focusing elements. It is for this reason, that we have a high level of confidence for achieving the results presented tab. 5.10 should the decision to realize one of the proposals be made.
Grading the flux potential of an ICS gamma source is dependent on the energy bandwidth requirements given by users of the experiment. In every scenario presented above, the ICS gamma spectrum generated with MESA can be collimated to average scattered photon energies $\overline{E}'_{ph}$ below single digit percentiles of $E'_{ph,max}$. As we can see in figures 5.20 and 5.21, in which we have shown collimator parameter scan studies simulated in Comparse, while gamma flux losses increase at narrower pinhole radii, average gammas of close to maximum scattered photon energy $E'_{ph,max}$ are in obtainable.

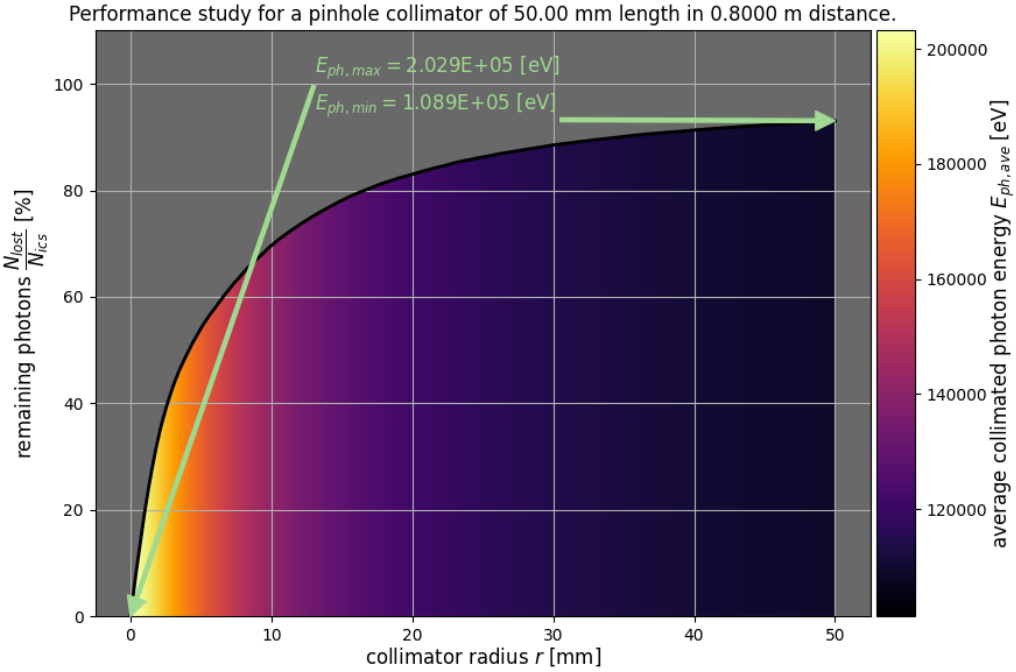

Figure 5.20.: Average scattered gamma energy $\overline{E}'_{ph}$ plotted in color over relative photon losses due to collimation $\frac{\mathfrak{N}_{lost}}{\mathfrak{N}_{ics}}$ to collimator radius r. Simulation and plot created in Comparse using a MESA ER-IB-42m-nominal (App. tab. A.2) Astra generated electron distribution and Tangor-100-IR-focused (App. tab. A.8) presets.

5.2.6.1. Sub MeV Gamma Radiation

Using off-the-shelve $\lambda = 1030\,\text{nm}$ Nd:YAG laser solutions such as the Amplitude Tangor 100 IR, MESA can produce gammas of up to $E'_{ph} = 204\,\text{keV}$. This energy

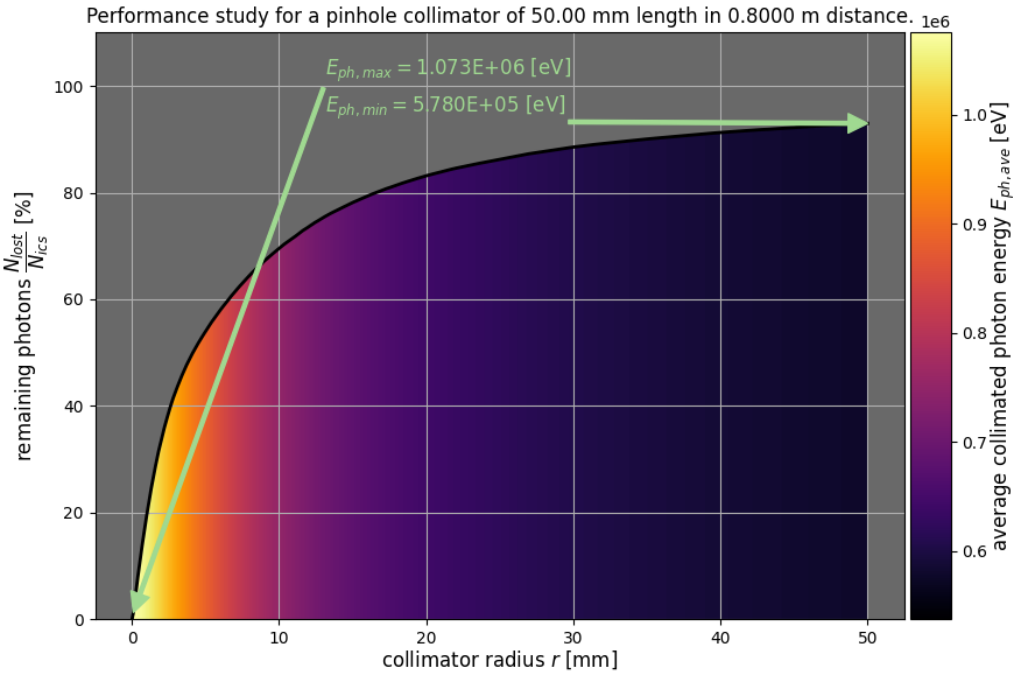

Figure 5.21.: Average scattered gamma energy $\overline{E}'_{ph}$ plotted in color over relative photon losses due to collimation $\frac{\mathfrak{N}_{lost}}{\mathfrak{N}_{ics}}$ to collimator radius r. Simulation and plot created in Comparse using a MESA ER-IB-42m-1nC (App. tab. A.4) Astra generated electron distribution and EX10IN-excimer-focused-SMILE (App. tab. A.12) presets.

range finds potential applications in medical applications and novel beam diagnostics.

For medical applications, one might consider using photon activation of gold nanoarticles (AuNP) [53]. Here, drugs are enriched with gold nano-particles which have a high photon absorption cross section above 81 keV compared to that of soft tissue [54]. Here, the photoelectric effect that occurs in the Au atom's k-shell can result in an Auger cascade, a that produces several low energy electrons which transfer their energy in the surrounding tissue. In this manner, a precise application of ionizing energy in deep tissue regions can be facilitated for radio therapy of cancer patients. Alternative uses for ICS sources in the field of medical applications include medical imaging. This too can involve gold nano-particles, where the k-shell edge is detectable in the the diffraction spectrum. Drug distribution in the human body can then be tracked if AuNP are added to the delivery agent. Outside of AuNP activation, ICS sources can stand in as replacement for conventional X-Ray sources, used for computed tomography imaging and high resolution material measurements [55]. They provide a bright, monochromatic alternative to conventional X-Ray sources at a smaller facility footprint than synchrotron sources.

ICS experiments in the sub MeV gamma energy range are used for beam diagnostics

in accelerator physics. Our exemplary Nd:YAG laser used in this study, the Tangor 100 IR, is installed in the S-Dalinac at the TU Darmstadt to use ICS for non destructive measurements of the electron beam energy and it's energy spread [45]. This method utilizes the Compton edge, the gamma intensity peak at the point of the maximum scattered photon energy generated by ICS. For incident lasers of sufficiently narrow bandwidth, the gamma energy can be derived to the incident electron's energy and the width of the peak originates in the electron's energy spread.
Beam diagnosis applications have only modest peak gamma energy requirements and can be successfully implemented using MESA in nominal operation mode and an off-the-shelve Tangor 100 IR laser. We have simulated, that in this configuration, we can obtain more than $\mathfrak{F}_{\gamma,col,99\%} > 1000$ ph/s of an average gamma energy $\overline{E}'_{ph,col,99\%,} > 200\,\mathrm{keV}$. Depending on the application, the generated gamma flux may be insufficient or necessitate long measurement times. A discussion of the possibility for a polarimetry beam diagnostic system can be found in sec. 5.3.2.3.
Irradiation therapy requires a higher gamma photon flux. For this, we assume a modification of MESA with a new $\nu_{RF} = 100\,\mathrm{kHz}$ RF frequency and $Q_{el} = 1\,\mathrm{nC}$ bunch charge mode of operation in combination with an 8-fold laser intensity amplification via SMILE style optical cavity. According to our simulations, implementing both would result in a gamma flux increase of more than three orders of magnitude. Of the same $\overline{E}_{ph,col,99\%,} = 201\,\mathrm{keV}$ as before, we would now generate $\mathfrak{F}_{\gamma,col,99\%} > 1.5 \cdot 10^7$ ph/s. This too falls short of medical irradiation therapy intensity baseline but exceeds optimal photon energies. A different laser of higher intensity but lower energy is required for MESA to be used in AuNP enhanced cancer therapy.

5.2.6.2. Low MeV Gamma Radiation

Additionally, we have conducted simulations with off-the-shelve industrial excimer laser parameters. Specialist manufacturers offer $\lambda = 193\,\mathrm{nm}$ in $E_{pulse} = 20\,\mathrm{mJ}$ pulses pulsed at $\nu_{ph,rep} = 1000\,\mathrm{Hz}$. When $E_{el,ref} = 130\,\mathrm{MeV}$ electrons scatter with $\lambda = 193\,\mathrm{nm}$ laser photons, they generate gammas of up to $E'_{ph,max} = 1.076\,\mathrm{MeV}$. Above 1 MeV, ICS applications enter into the range where nucleus measurements become possible. One such use case can be measurements of the Pygmy Dipole Resonance (PDR) [56] [57]. PDR refers to the lower dipole states in nuclei with excess neutrons. While significant progress was made in recent years in the investigation of their properties, the collective nature of PDR remains unquantified. Here, high brightness, low MeV gamma sources can yet contribute in the investigation of the lower isocalar response and it's interdependence with deformation.
Representative of industrial grade excimer lasers, we have chosen to conduct our study using the parameters given by GAM LASER, INC for their EX10IN model (App. tab. A.11). As expected, gamma energies exceed 1 MeV. Compared to the Tangor 100 IR, the EX10IN has a high beam quality factor of $m^2 = 35$, a measure

of how strong a laser beam diverges from an ideal Gaussian beam in the far-field. A high m^2 limits how narrow a beam can be focused. Despite that, we have calculated that the EX10IN can still be focused to $\sigma_{x,y} = 50\,\mu\text{m}$. Simulations conducted in this configuration show that an uncollimated flux of nearly $\mathfrak{F}_\gamma = 2 \cdot 10^7$ ph/s for MESA nominal and $\mathfrak{F}_\gamma = 2.5 \cdot 10^9$ ph/s for MESA at $\nu_{RF} = 100\,\text{kHz}$ and $Q_e = 1\,\text{nC}$ is in reach when using 8-fold SMILE cavity amplification. Similarly to the results obtained from simulations on the Tangor 100 IR proposal, aggressively collimating the generated gammas down to an average energy 1% below max energy $\overline{E}'_{ph,col,99\%} = 1.065\,\text{MeV}$ requires the filtering out of 86.29% of all scattered photons. Doing so leaves us with tunable, quasi-monochromatic gammas estimated to be generated at a high flux of $\mathfrak{F}_{\gamma,col,99\%} = 3.29 \cdot 10^8$ ph/s. ICS performance such as this is situated within the requirements of nuclear photonics and competes well with existing gamma source facilities such as the Extreme-Light-Infrastructure-Nuclear-Physics and the Tsinghua Thomson Scattering Source [55].

5.2.6.3. Conclusion in Short

Paired with a Tangor 100 IR or comparable laser, MESA can provide a monochromatic $\overline{E}'_{ph,col,99\%} \approx 200\,\text{keV}$ X-Ray source for medical and material imaging applications. The realization of this would require relatively little financial and person hour investment.
Using MESA as a driver for a high brightness monochromatic gamma source in the low-MeV range would require significantly more investment and modifications to MESA's beamline layout. However, $\overline{E}'_{ph,col,99\%} \approx 1.065\,\text{MeV}$ gammas produced with a flux of $\mathfrak{F}_{\gamma,col,99\%} = 3.29 \cdot 10^8$ ph/s are in reach. This would enable foundational research in the low-energy realm of nuclear photonics.
As currently planned, MESA is to provide electrons for two separate experiments, P2 and MAGIX. It therefore may not be desirable to add a third application that competes for uptime. In this case, ICS can be used as a non-destructive beam diagnostics tool for electron beam energy and energy spread. This can be facilitated by an off-the-shelve $\lambda = 1030\,\text{nm}$ in a small-footprint experiment setup.

5.3. Investigation of Spatial and Polarization Effects

Having implemented a comprehensive theoretical approach to Inverse Compton Scattering modelling that takes arbitrary photon and fermion polarizations and orientations into account in a fully vectorized numerical simulation code, we are enabled to investigate diverse scattering scenarios in quick succession. The following sections shall present standard and fringe case studies. In them, we will attempt to identify benefits and drawbacks of specific configurations and conditions. Unless stated otherwise, all studies will be based on the MESA-ER-IB-42m-nominal (tab. A.2) and Tangor-100-IR-focused (tab. A.8) parameter sets used for the baseline MESA studies in section 5.2.1. The default detector screen orientation will be center aligned perpendicular to the reference electron longitudinal beam axis and in

1 m distance.

5.3.1. Unpolarized Angle Dependent ICS Scattering Behavior

We will first present fully unpolarized scenarios drawn in the plot types used in this section. Note, that in this thesis, when describing a scattering process as "fully unpolarized", we describe an ICS experiment in which neither the initial nor the scattered photon and electron polarization are observed. We shall first discuss

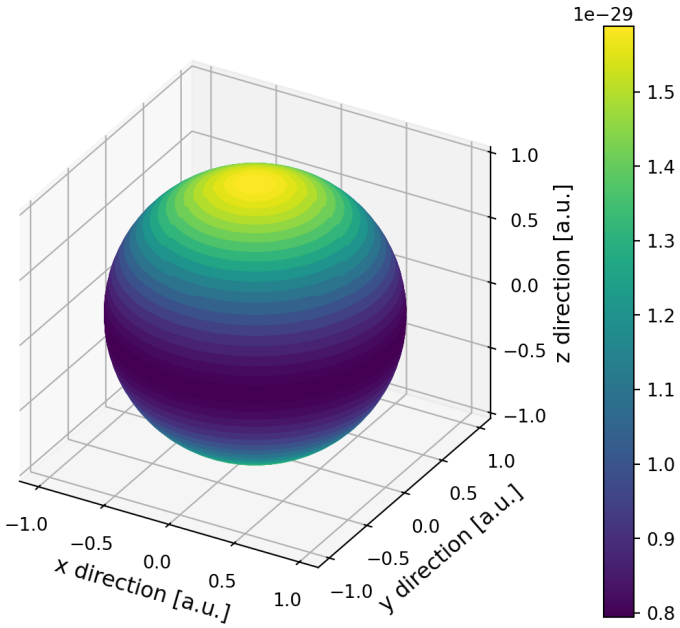

Figure 5.22.: Frontal collision $\theta_{inc} = 180°$ ICS without polarization. ICS cross section plot simulated and generated in Comparse using a MESA-ER-IB-42m-nominal (App. tab. A.2) Astra generated electron distribution and Tangor-100-IR-focused (App. tab. A.8) presets. For this plot, W was calculated for $\rho_\theta = 181$ & $\rho_\phi = 360$ scattering angles by way of averaging over $N'_{par} = 4$ scattering particle pairs chosen by weighted probability $W_{ics,norm}$.

the ICS scattering cross section for incident photon and electron momentum in alignment for head-on collision. The 3D cross section plot of fig. 5.22 visualizes the calculated ICS cross section in color over the defined scattering direction grid unit sphere. When using Comparse, this plot can rotated in real time. As a static plot, it does not convey the full data, as part of the unit sphere is always hidden. For this reason, Comparse can also generate two versions of 2D reflections: a 2D projection of each hemisphere, seen in fig. 5.24 and a stereographic projection [58] of the entire unit sphere in fig. 5.23.
In the 2D projections, we can clearly make out two maxima present in the fully

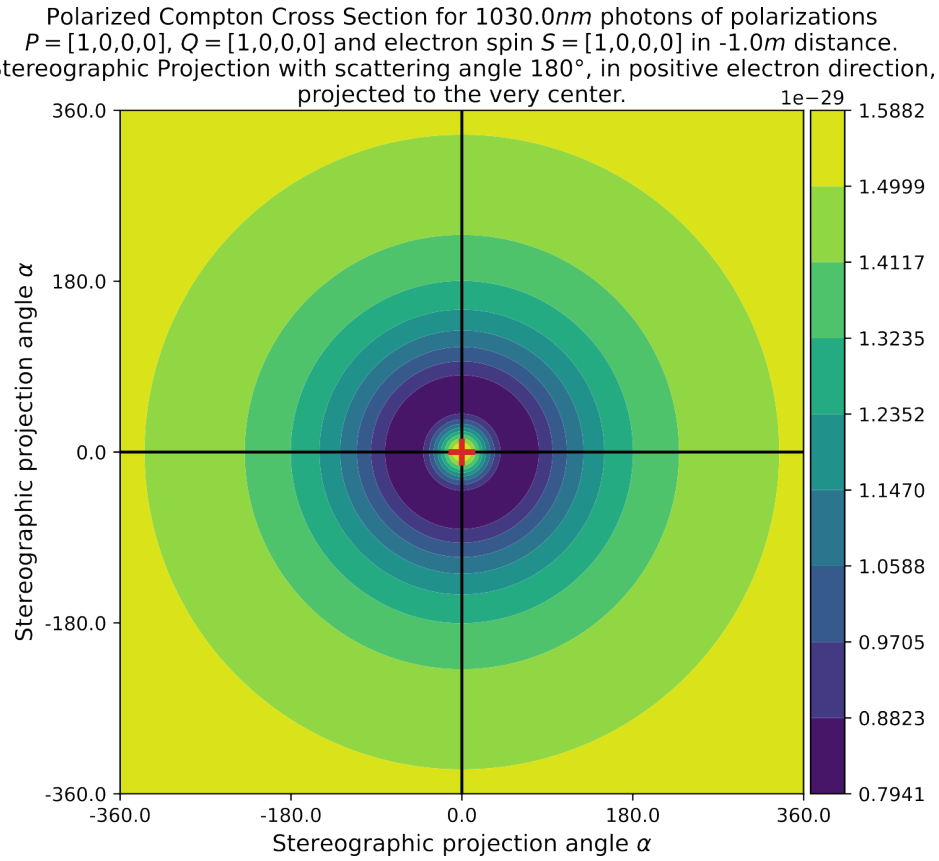

Figure 5.23.: Frontal collision $\theta_{inc} = 180°$ ICS without polarization. Stereographic projection ICS cross section plot simulated and generated in Comparse using a MESA-ER-IB-42m-nominal (App. tab. A.2) Astra generated electron distribution and Tangor-100-IR-focused (App. tab. A.8) presets. For this plot, W was calculated for $\rho_\theta = 181$ & $\rho_\phi = 360$ scattering angles by way of averaging over $N'_{par} = 4$ scattering particle pairs chosen by weighted probability $W_{ics,norm}$.

unpolarized observation of ICS scattering in the electron rest frame. On the scattering angle unit sphere, they are position similar to the north and south pole of planet earth if we align the earth's rotational axis with the longitudinal electron momentum axis. Correspondingly, the two maxima mark the scattering angles under which the scattered photon's direction is parallel to the electron's initial momentum, when scattering with incident angle $\theta_{inc,erf} = 180°$: One scattering maximum points into the direction of the electron's momentum and the other one points into the opposite direction, parallel but against the electron momentum. This represents scattering events in which the scattered photon can be seen as perfectly reflected or as scattered without change in direction. Both hemispheres, in positive and in negative electron z-direction, are identical in the electron rest frame. However, for accelerated electrons, all scattering photon directions are subject to a Lorentz transformation from the electron rest frame into the laboratory frame which com-

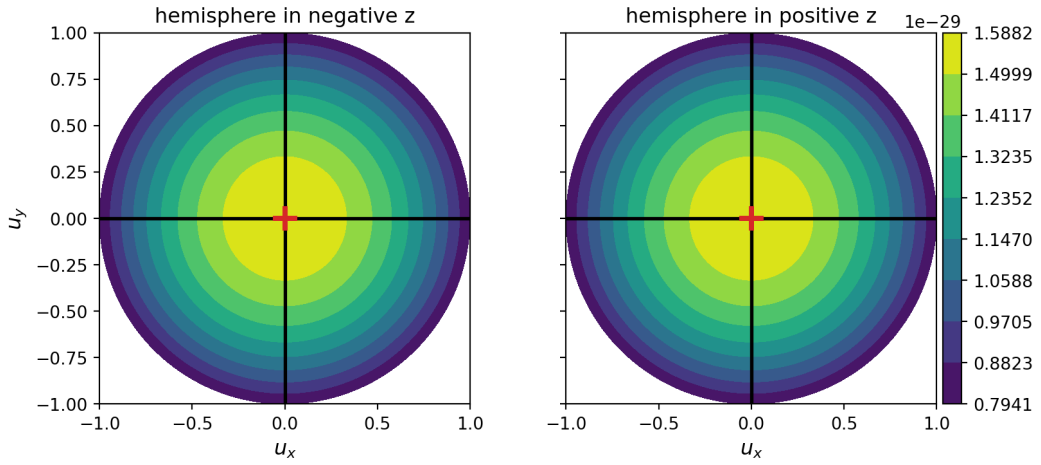

Figure 5.24.: Frontal collision $\theta_{inc} = 180°$ ICS without polarization. 2D ICS cross section plot simulated and generated in Comparse using a MESA-ER-IB-42m-nominal (App. tab. A.2) Astra generated electron distribution and Tangor-100-IR-focused (App. tab. A.8) presets. For this plot, W was calculated for $\rho_\theta = 181$ & $\rho_\phi = 360$ scattering angles by way of averaging over $N'_{par} = 4$ scattering particle pairs chosen by weighted probability $W_{ics,norm}$.

presses all angles towards the head-on scattering case of $\theta_{ph} = 180°$. In fact, for MESA at $E_{el,ref} = 105\,\text{MeV}$, of the electron rest frame hemisphere with negative electron z-direction components, most scattered photons end up in the positive electron z-direction hemisphere in the laboratory frame. See section 5.3.2.1 for a demonstration of this effect.
Frontal collisions constitute the ideal angle for unpolarized ICS gamma flux, as one of the scattering probability maxima is perfectly aligned with the scattering angle that provides the highest energy transfer from electron to photon: The head-on reflection. An example scattering image measured by a detector screen in 1 m distance perpendicular to the laboratory frame z-axis (already presented in fig. 5.19a) is shown in fig. 5.27a. The scattered photon density increases towards the middle, where the highest scattered photon intensity is observed.

When not scattering under frontal collision condition $\theta_{inc,erf} = 180°$, the position of the maxima on the scattering direction unit sphere in the electron rest frame shifts accordingly, as seen in figures 5.25 and 5.26. As in the electron rest frame, the electron's momentum is yet to be considered, this is to be expected. Some planners opt for a $\theta_{inc,erf} = 90°$ incident angle ICS experiment implementation due to an easier electron - laser beam separation or other physical constraints. Researchers should be aware, however, that the generated gamma spectrum will be degraded compared to the frontal $\theta_{inc,erf} = 180°$ implementation. The gamma spectrum comparison in figure 5.28 shows that the maximum scattered photon energy is halved to $E'_{ph,max,90°} \approx \frac{1}{2} E'_{ph,max,180°}$. The reduction of high energy photons is further aggravated through the significantly less pronounced Compton peak at

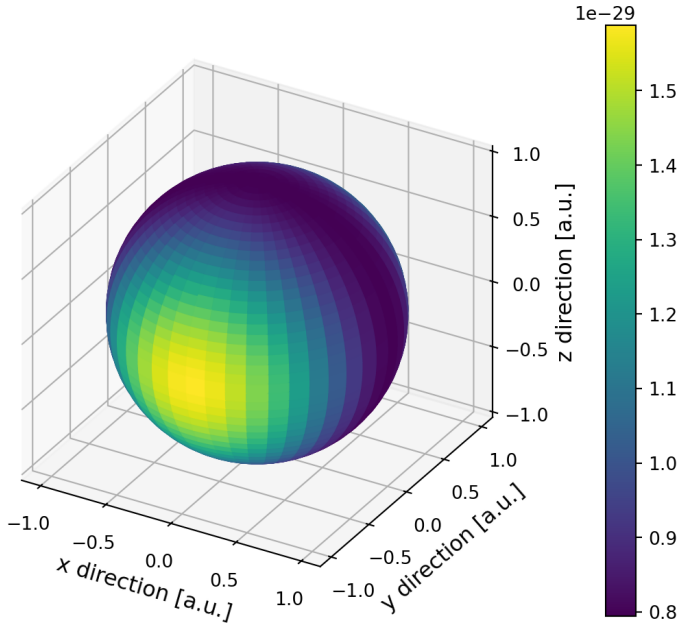

Figure 5.25.: Perpendicular collision $\theta_{inc} = 90°$ ICS without polarization. 3D ICS cross section plot simulated and generated in Comparse using a MESA-ER-IB-42m-nominal (App. tab. A.2) Astra generated electron distribution and Tangor-100-IR-focused (App. tab. A.8) presets. For this plot, W was calculated for $\rho_\theta = 181$ & $\rho_\phi = 360$ scattering angles by way of averaging over $N'_{par} = 4$ scattering particle pairs chosen by weighted probability $W_{ics,norm}$.

the upper end of the energy spectrum.

Naturally, the loss of brilliance is reflected in the scattered photon flux. For a frontal collision $\theta_{inc} = 180°$ aligned ICS experiment, we can expect a gamma flux of $\mathfrak{F}_\gamma \approx 1.19 \cdot 10^5$ ph/s derived from an average $\mathfrak{N}_{ph,ics} \approx 0.596$ photons emitted in one electron bunch - laser pulse collision. We simulate a stark drop to $\mathfrak{F}_{\gamma,90°} \approx 6.21 \cdot 10^3$ ph/s and $\overline{\mathfrak{N}}_{ph,ics,90°} \approx= 0.031$ for the same parameters except for a 90° incident angle.

5.3.2. The Effects of Spin Polarization in ICS

We've made mention earlier in the introduction chapter, that MESA is capable of spin polarized electron beam operation at a lowered beam current of $P_{el} = 150$ to 1000 µA. For this reason, we intended to quantify and summarize all effects of Spin polarization on ICS, starting with the straight forward effect of full spin polarization for a low recoil head-on collision.

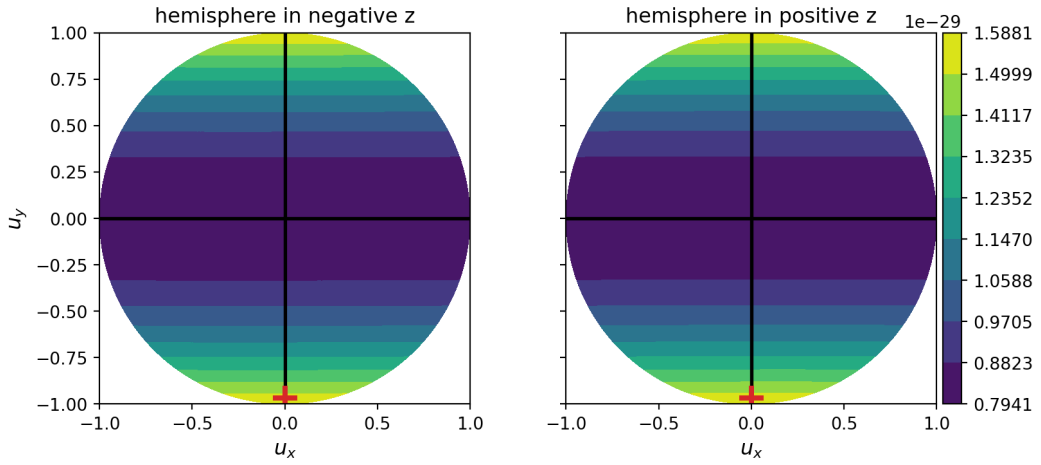

Figure 5.26.: Perpendicular collision $\theta_{inc} = 90°$ ICS without polarization. 2D ICS cross section plot simulated and generated in Comparse using a MESA-ER-IB-42m-nominal (App. tab. A.2) Astra generated electron distribution and Tangor-100-IR-focused (App. tab. A.8) presets. For this plot, W was calculated for $\rho_\theta = 181$ & $\rho_\phi = 360$ scattering angles by way of averaging over $N'_{par} = 4$ scattering particle pairs chosen by weighted probability $W_{ics,norm}$.

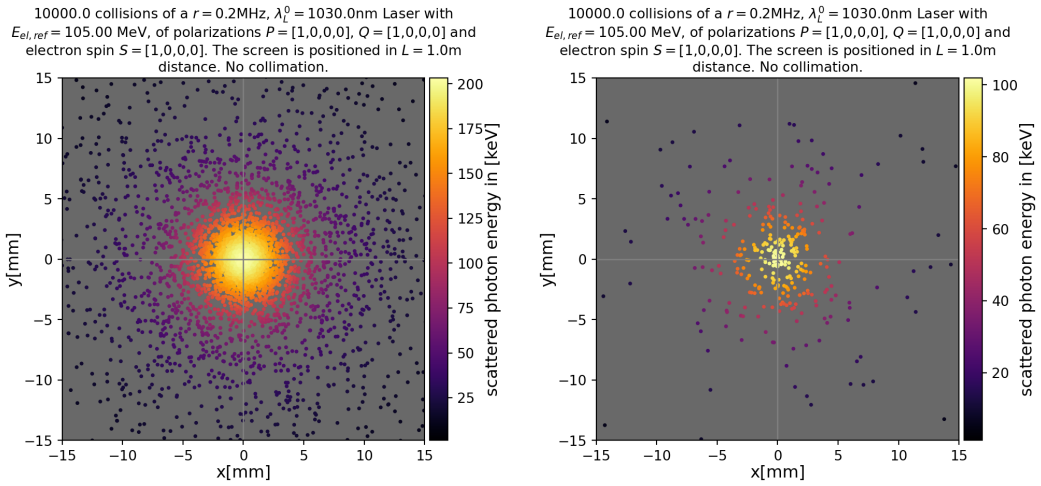

(a) Incident angle $\theta_{inc} = 180°$

(b) Incident angle $\theta_{inc} = 90°$

Figure 5.27.: Comparison of scattering photons projected onto a detector screen in 1 m distance perpendicular to the laboratory frame z-axis between head-on incident angle and 90° angle of the laser. Scattering images simulated and generated in Comparse using a MESA-ER-IB-42m-nominal (App. tab. A.2) Astra generated electron distribution and Tangor-100-IR-focused (App. tab. A.8) presets.

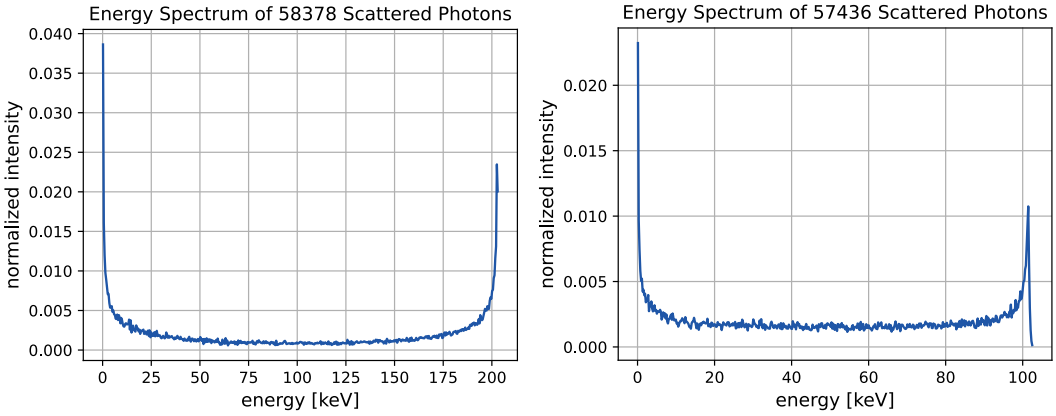

(a) Incident angle $\theta_{inc} = 180°$ **(b)** Incident angle $\theta_{inc} = 90°$

Figure 5.28.: Comparison of scattering photons projected onto a detector screen in 1 m distance perpendicular to the laboratory frame z-axis between head-on incident angle and 90° angle of the laser. Spectra simulated and generated in Comparse using a MESA-ER-IB-42m-nominal (App. tab. A.2) Astra generated electron distribution and Tangor-100-IR-focused (fig. 5.28a, App. tab. A.8).

5.3.2.1. Low-Recoil Head-On Spin-Polarized Low-E_{ph} ICS

Continuing with the default electron and photon beams tab. A.1 and tab. A.8, we summarize the dynamics of electron and circular polarization on ICS. Figure 5.29 shows, that in a low electron energy ICS collision such as with $E_{el,ref} = 105\,\mathrm{MeV}$ MESA nominal and a Tangor 100 IR $\lambda = 1030\,\mathrm{nm}$, the electron spin - photon circular polarization coupling is quasi undetectable, as no difference can be surmised between figures 5.29c and 5.29d to 5.29e and 5.29f where only the helicity of the electron spin was flipped. On the other hand, we can confirm, that the circular polarization Stokes parameter P_3 value is distributed over the direction unit sphere depending on scattering angle θ. This distribution inverts when we change the sign of the incident P_3, as seen in the change from 5.29a to 5.29c and from 5.29b to 5.29d. We have proven earlier in section 3.80, that the unpolarized cross section is made up of the sum of two measurements of polarization opposites. In figure 5.29, this is indicated by two collisions of identical incident polarization setting being measured in $\boldsymbol{Q} = (1, 0, 0, 1)$ and $(1, 0, 0, -1)$: Sub figures 5.29a and 5.29b, 5.29c and 5.29d and finally 5.29e and 5.29f together appear to cover the whole sphere.

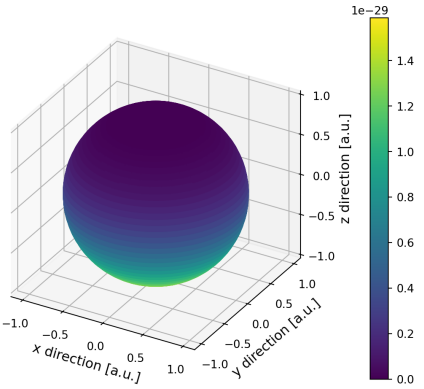

(a) $\boldsymbol{S}(1,0,0,1);\boldsymbol{P}(1,0,0,1);\boldsymbol{Q}(1,0,0,1)$

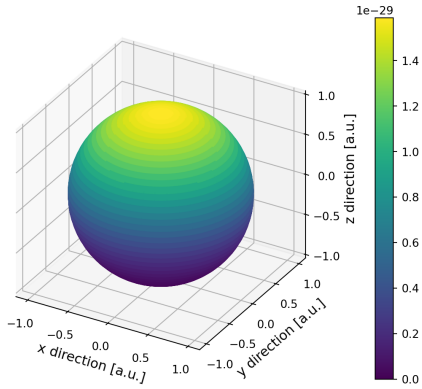

(b) $\boldsymbol{S}(1,0,0,1);\boldsymbol{P}(1,0,0,1);\boldsymbol{Q}(1,0,0,-1)$

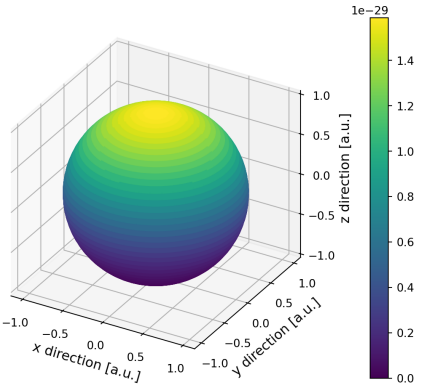

(c) $\boldsymbol{S}(1,0,0,1);\boldsymbol{P}(1,0,0,-1);\boldsymbol{Q}(1,0,0,1)$

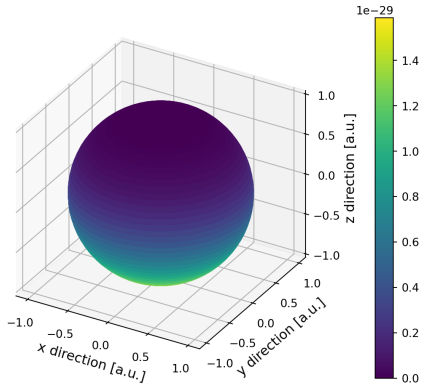

(d) $\boldsymbol{S}(1,0,0,1);\boldsymbol{P}(1,0,0,-1);\boldsymbol{Q}(1,0,0,-1)$

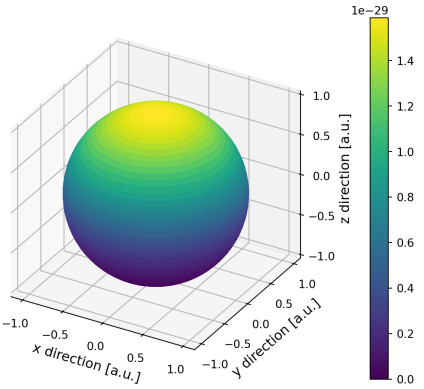

(e) $\boldsymbol{S}(1,0,0,-1);\boldsymbol{P}(1,0,0,-1);\boldsymbol{Q}(1,0,0,1)$

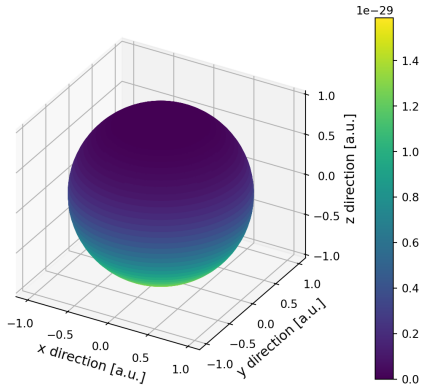

(f) $\boldsymbol{S}(1,0,0,-1);\boldsymbol{P}(1,0,0,-1);\boldsymbol{Q}(1,0,0,-1)$

Figure 5.29.: Comparison of Spin distribution over the scattering direction unit sphere in the electron rest frame for a frontal $\theta_{inc} = 180°$ ICS collision. Graphs are repeats of fig. 5.22 They were simulated and generated in Comparse using a MESA-ER-IB-42m-nominal (App. tab. A.2) Astra generated electron distribution and Tangor-100-IR-focused (App. tab. A.8) presets.

Said scattering direction unit sphere is still subject to the unpolarized maxima displyed in figures 5.22 to 5.24, but a closer look reveals, the the unpolarized minima drop to half of the scattering cross section of the maxima, while the polarization measured minima go to zero scattering probability, dominating the scattering dynamics.
We can confirm our observation, that the spin polarized cross section measured in opposite directions sums up to the unpolarized one by averaging over all azimuthal angles ϕ for all scattering particles and plotting the polarization dependent Compton scattering cross section W over scattering angle θ for the two polarized cases and the unpolarized one via Comparse's "Value Over θ" data analysis module. The results are presented in figure 5.30 and show clearly, that the two polarized measurements add up to the cross section without regard to polarization.
For head-on collisions, the scattering direction maxima on the unit sphere origi-

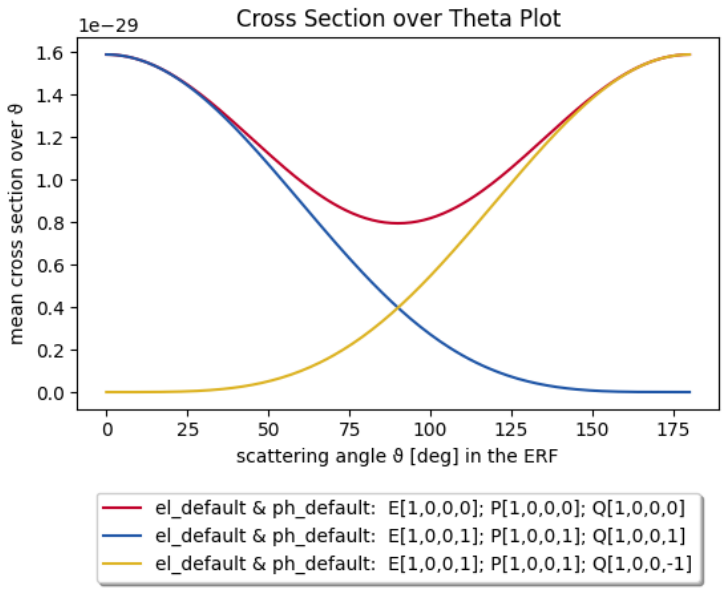

Figure 5.30.: ICS cross section W over scattering angle θ_{erf} for a fully unpolarized collision and two opposite circular polarization measurements of a fully circularly polarized collision. Lineplots simulated and generated in Comparse using a MESA-ER-IB-42m-nominal (App. tab. A.2) Astra generated electron distribution and Tangor-100-IR-focused (App. tab. A.8) presets. For this plot, W was calculated for $\rho_\theta = 181$ & $\rho_\phi = 360$ scattering angles for one ideal head-on scattering reference electron - reference photon pair.

nating from the circular polarization transformation overlap perfectly with the high and low energy scattering angle conditions. We can therefore overwhelmingly measure one Q_3 orientation in the high energy scattering maxima and the opposite $-Q_3$ in the low energy one. This improves the ideal ICS gamma spectrum for that specific polarization orientation. The effects on a screen perpendicular to the electron

beam axis in 1 m distance can be seen in figures 5.31 and 5.33. In case a certain

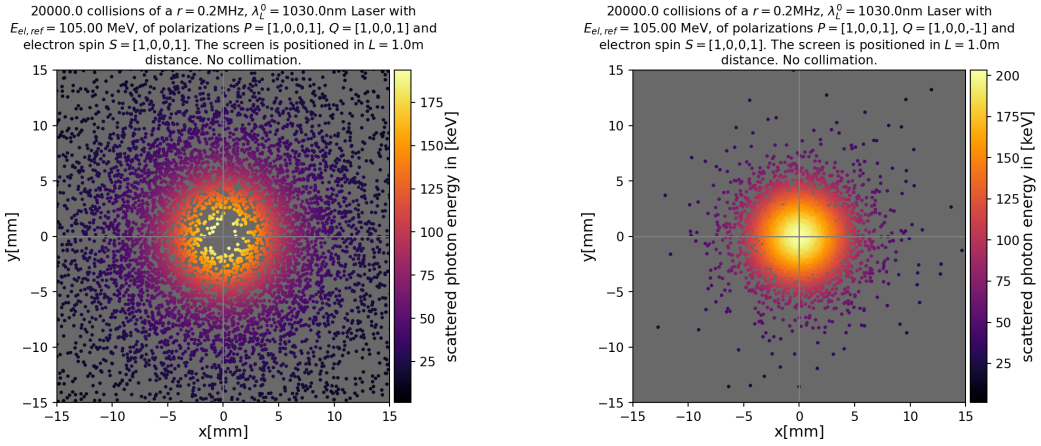

(a) $\boldsymbol{P}(1,0,0,1); \boldsymbol{Q}(1,0,0,1); \boldsymbol{S}(1,0,0,1)$ **(b)** $\boldsymbol{P}(1,0,0,1); \boldsymbol{Q}(1,0,0,-1); \boldsymbol{S}(1,0,0,1)$

Figure 5.31.: Comparison of scattering photons of two measureed circular polarizations projected onto a detector screen in 1 m distance perpendicular to the laboratory frame z-axis. Emitted photons originate from a fully circularly polarized ICS event. Scattering images simulated and generated in Comparse using a MESA-ER-IB-42m-nominal (App. tab. A.2) Astra generated electron distribution and Tangor-100-IR-focused (App. tab. A.8) presets.

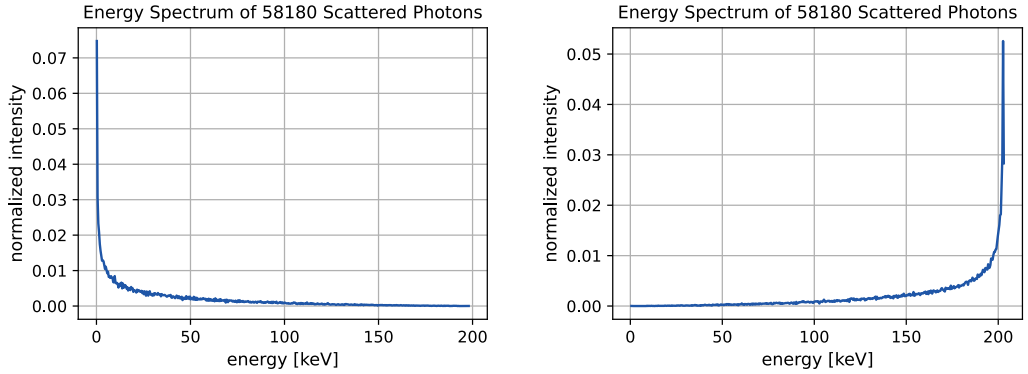

(a) $\boldsymbol{S}(1,0,0,1); \boldsymbol{P}(1,0,0,1); \boldsymbol{Q}(1,0,0,1)$ **(b)** $\boldsymbol{S}(1,0,0,1); \boldsymbol{P}(1,0,0,1); \boldsymbol{Q}(1,0,0,-1)$

Figure 5.32.: Comparison of uncollimated ICS gamma spectrum of scattering photons of two measureed circular polarizations projected onto a detector screen in 1 m distance perpendicular to the laboratory frame z-axis.. Emitted photons originate from a fully circularly polarized ICS event. Spectrum simulated and generated in Comparse using a MESA-ER-IB-42m-nominal (App. tab. A.2) Astra generated electron distribution and Tangor-100-IR-focused (App. tab. A.8) presets.

circular polarization is desired from the ICS gamma beam, it is recommended to

collect the emitted photons in the head-on collision configuration. At the same time, circular polarization filters can be used to make collimation towards a higher average gamma energy $\overline{E}'_{ph}$ or smaller spectrum bandwidth easier. We shall briefly consider the $\theta_{inc} = 90°$ case in which the circular polarization scattering maxima are least aligned with the high and low energy side of the scattering unit sphere in the next subsection.

5.3.2.2. Low-Recoil Spin-Polarized Low-E_{ph} ICS at 90° Incident Angle

Just as the unpolarized scattering direction maxima in the scattering direction unit sphere earlier in fig. 5.25, the circular polarization derived maximum is aligned with the incoming photon momentum in the electron rest frame. For 90° incident electron and photon collision angles, this results in a complete disappearance of the polarization dependence of the scattered gamma spectrum we earlier observed in fig. 5.33.

In this angle and experiment setup, researchers can neither separate the circular

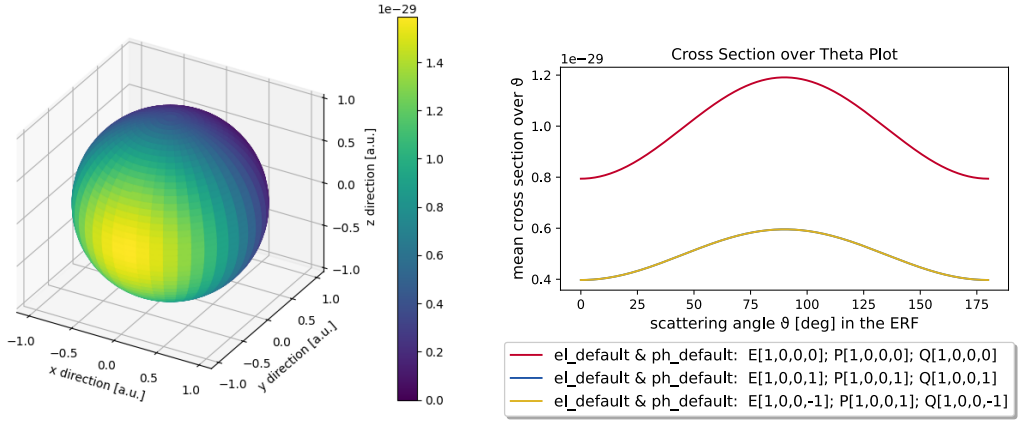

(a) $\boldsymbol{S}(1,0,0,1);\boldsymbol{P}(1,0,0,1);\boldsymbol{Q}(1,0,0,-1)$ **(b)** Value over θ_{erf} plot

Figure 5.33.: Scattering angle - polarization dependence of a $\boldsymbol{P}(1,0,0,1);\boldsymbol{S}(1,0,0,1)$ ICS event at a $\theta_{inc} = 90°$ incident collision angle. Figures simulated and generated in Comparse using a MESA-ER-IB-42m-nominal (App. tab. A.2) Astra generated electron distribution and Tangor-100-IR-focused (App. tab. A.8) presets.

polarizations from one another, nor use polarization filters to improve the spectrum. For legibility reasons, we shall refrain from retreading all resulting scattered photon statistics. At this point, the attentive reader is should be able to interpret the plots of fig. 5.33 based on connections drawn in previous sections.

5.3.2.3. High-E_{ph} Circular polarization Coupling in ICS

Even without polarization filtered photon detection, the circular polarization helicity of the laser photons scattering against a spin polarized fermion beam can

influence the scattering behavior [59, 60]. In order to visualize the effect, we shall begin with a hypothetical super-high-energy laser of $E_{ph} = 124\,\text{keV}$ corresponding to $\lambda = 10\,\text{pm}$ [61], otherwise modelled after Tangor-100-IR-focused, although for the purpose of this section, all macro parameters of the incoming laser pulse are irrelevant, as we will only be investigating a single electron - photon collision. Nonetheless, the full set of parameters used is listed in tab. A.13.

Figure 5.34 shows that an ICS cross section aberration occurs depending on

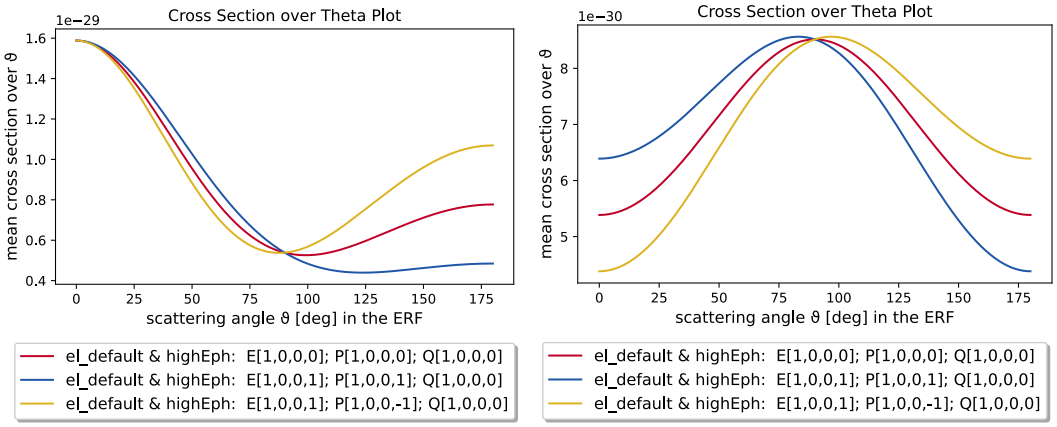

(a) Value over θ_{erf} plot for $\theta_{inc} = 180°$ incident collision angle

(b) Value over θ_{erf} plot for $\theta_{inc} = 90°$ incident collision angle

Figure 5.34.: Photon circular polarization to electron spin coupling of a hypothetical $\boldsymbol{P}(1,0,0,1)\lambda = 10\,\text{pm}$ incident photon ICS event at $\theta_{inc} = 90°$ and $180°$ collision angles. Figures simulated and generated in Comparse using a MESA-ER-IB-42m-nominal (App. tab. A.2) Astra generated electron distribution and hypthetical-10nm-photon (App. tab. A.13) presets.

whether the helicity $H_{inc} = P_3 \cdot S_3$ of photon and electron is aligned or not. For positive H_{inc}, scattering angle θ_{erf} values corresponding to a higher gamma energy, have a reduced probability for the higher energy area than without spin interaction. This is shown by the blue curve in fig. 5.34. The yellow curve representing a negative helicity product, occurring when electron and photon circular polarization are the inverse of each other, shows to an increased high gamma energy scattering chance. Researchers can use the deviation from the norm to ascertain the polarization rate of a fermion beam. When comparing the spectrum of a $P_3 = +1$ to a $P_3 = -1$ laser ICS collision, the difference becomes clearer. Through the measuring of this asymmetry, the degree of spin polarization S_3 of the electron beam can be calculated. This concept is known as ICS polarimetry and has been utilized at accelerator facilities including MAMI of the JGU Mainz [60].
Due to the low ICS cross section, ICS polarimetry is non-destructive the electron beam, but in turn requires long measuring times in most experimental configurations. Importantly, Compton polarimetry becomes increasingly difficult for lower energy incident photons [61]. For MESA at 105 MeV, a cost effective and low impact

1030 nm laser used for other types of beam diagnostics such as the often mentioned Tangor 100 IR, the value over scattering angle plots do not display any θ_{erf} aberration in the electron rest frame: fig. 5.35.

One can calculate the asymmetry curve

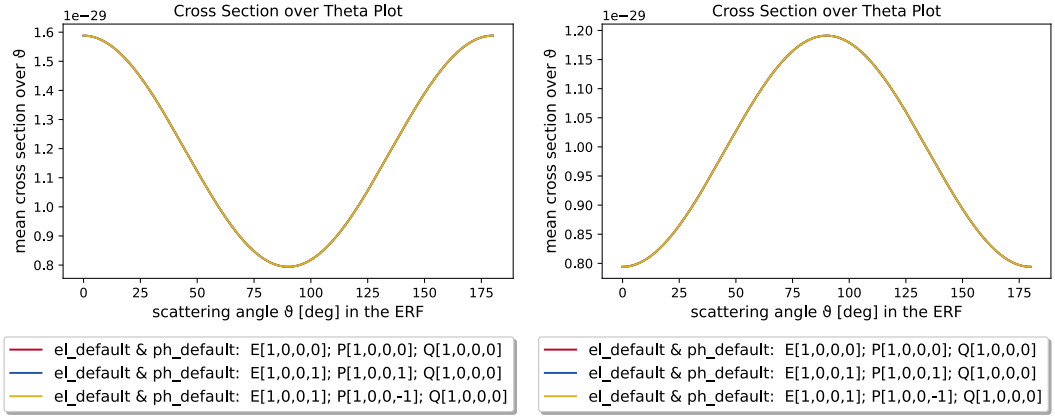

(a) Value over θ_{erf} plot for $\theta_{inc} = 180°$ incident collision angle

(b) Value over θ_{erf} plot for $\theta_{inc} = 90°$ incident collision angle

Figure 5.35.: Photon circular polarization to electron spin coupling of a $\boldsymbol{P}(1,0,0,1)$ polarized $\lambda = 1030\,\text{nm}$ laser similar to the Tangor 100 IR used for other beam diagnostics at $\theta_{inc} = 90°$ and 180° collision angles. Figures simulated and generated in Comparse using a MESA-ER-IB-42m-nominal (App. tab. A.2) Astra generated electron distribution and Tangor-100-IR-focused (App. tab. A.8) presets.

$$A = \frac{a - b}{a + b} \tag{5.9}$$

where a represents the intensity spectrum over θ for circular photon polarization $P_3 = 1$ and b represents the opposite $P_3 = -1$. Said curves a and b are the yellow and blue plots in previous figures 5.34a and 5.35a. The normalized asymmetry curves A calculated from both incident photon energy variations are shown in fig. 5.36.

While the asymmetry between positive and negative product helicity H_{inc} is clearly apparent in the high incident photon energy case shown in fig. 5.34a and impossible to discern at the scaling in fig. 5.35a, the same characteristic is underlying both plots. When plotting the normalized asymmetry curve A a similar dynamic emerges for both energy variations, albeit at different magnitudes. Up to $A \approx 4.71 \cdot 10^{-6}$ for $\lambda = 1030\,\text{nm}$ and $A \approx 0.38$ for $\lambda = 0.01\,\text{nm}$. For Compton polarimetry to be implemented in an accelerator, this magnitude of statistical deviation needs to be measured in a laboratory setting, ideally live during during operation.

For the expected ICS performance parameters possible at MESA without significant investment in reconstruction and expansion, case "A" and "B" in tab. 5.10, a relative asymmetry of less than $5 \cdot 10^{-6}$ would require extremely long measurement times of hours or days to be discernible over the intrinsic stochastic noise of the experiment.

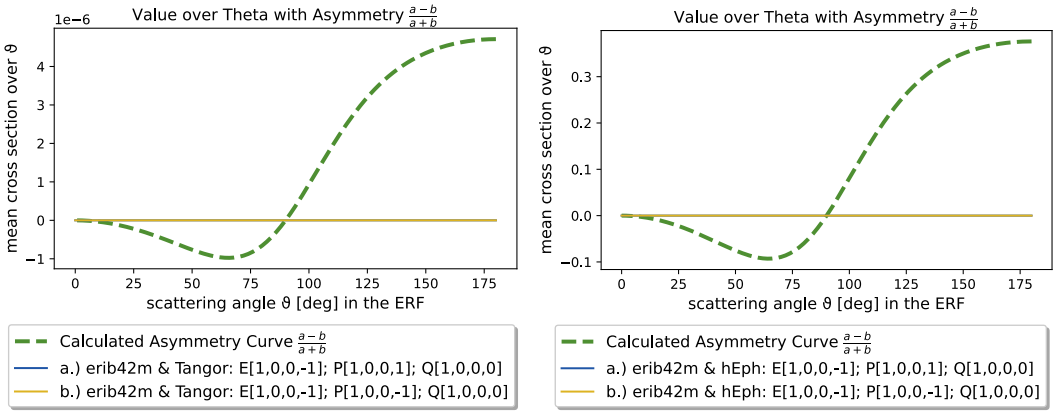

(a) $\lambda = 1030\,\text{nm}$ **(b)** $\lambda = 0.01\,\text{nm}$

Figure 5.36.: Photon circular polarization to electron spin coupling in ICS of a fully spin polarized MESA electron bunch. The incident laser in fig. 5.36a is a $\lambda = 1030\,\text{nm}$ nano meter industry laser whereas the laser in fig. 5.36b is a theoretical $\lambda = 0.01\,\text{nm}$ ($E_{ph} \approx 124\,\text{kHz}$ gamma source. Both plots are calculated for an incident collision angle of $\theta_{inc} = 180°$. Figures simulated and generated in Comparse using a MESA-ER-IB-42m-nominal (App. tab. A.2) Astra generated electron distribution and a single ideal head-on colliding photon of the aforementioned wavelengths.

Even using a high-end $\lambda = 193\,\text{nm}$ excimer laser, case "C" and "D" in tab. 5.10, would only increase the maximum asymmetry to $A \approx 2.5 \cdot 10^{-5}$. Due to the low electron energy $E_{el} = 105\,\text{MeV}$, an extensive design study and investigation of the potential for a polarimetry system at MESA was considered out of the scope for this thesis but could represent a possibility for future studies.

5.3.3. Linear Polarization Transmission in ICS

Linear polarization of the photons is subjected to transformations and incident angle dependence. In the simplest case, that a of a fully linearly $\boldsymbol{P} = (1, 1, 0, 0)$ polarized initial photon head-on scattering on an unpolarized fermion, a severe azimuth scattering angle ϕ modulation is observable. The scattering probability appears linearly aligned in the ERF as seen in fig. 5.37a and fig. 5.37b. However, when tracing the emitted photons towards a detector screen, the high energy region in yellow around the scattering center in (fig. 5.37c) does not show much of the ϕ modulation. The biggest difference appears to be in the middle energy region colored in orange and red, in which almost no emitted photons are traced towards the screen. Lastly, the low energy region in deep purple and black again barely exhibits a ϕ modulation of the scattering position density.

Let us analyse the ICS characteristic one layer deeper by applying virtually placing a polarization filter $\boldsymbol{Q}$ before the detector screen. Repeating the simulation for $\boldsymbol{Q} = (1, 1, 0, 0)$ and $(1, -1, 0, 0)$, the full linear polarization aligned with respectively perpendicular to the polarized laser $\boldsymbol{P} = (1, 1, 0, 0)$, results in figures 5.38 and 5.39.

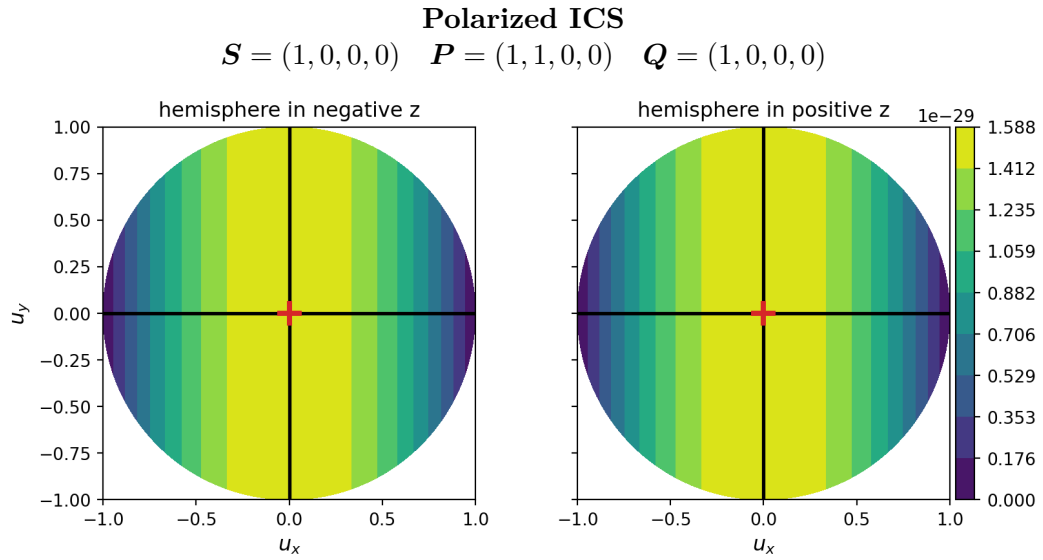

(a) 2D projection of polarized cross section in the Electron Rest Frame

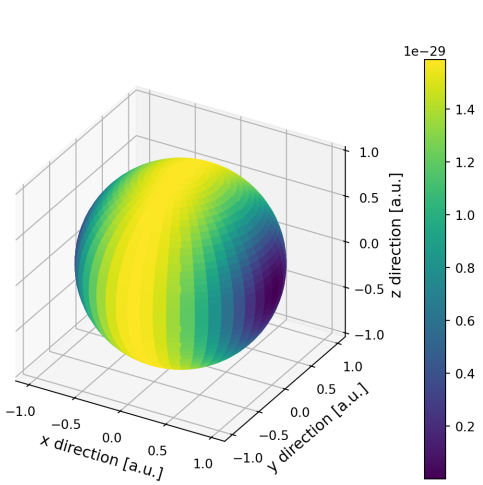

(b) 3D polarized ICS cross section (ERF)

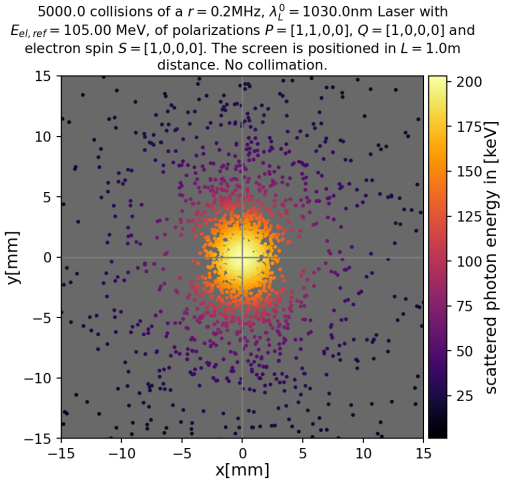

(c) ICS photons projected on a screen (LAB)

Figure 5.37.: Spatial characteristics of ICS emitted photons under the inclusion of polarization effects. Directional scattering probability W in the ERF and emitted photons of ICS with $\boldsymbol{P} = (1,1,0,0)$ polarized incident photons detected by a $\boldsymbol{Q} = (1,0,0,0)$ polarization filter. Calculated for a frontal collision $\theta_{inc} = 180°$. Plots simulated and generated in Comparse using a MESA-ER-IB-42m-nominal (App. tab. A.2) Astra generated electron distribution and Tangor-100-IR-focused (App. tab. A.8) presets. For this plot, W was calculated for $\rho_\theta = 181$ & $\rho_\phi = 360$ scattering angles by way of averaging over $N'_{par} = 11685$ scattering particle pairs chosen by weighted probability $W_{ics,norm}$.

Here, the two scattering distributions that superimpose to fig. 5.37 are visible, as is the cause for the scattering characteristic on the detector screen.

When setting the polarization filter to the same alignment as the incident's laser

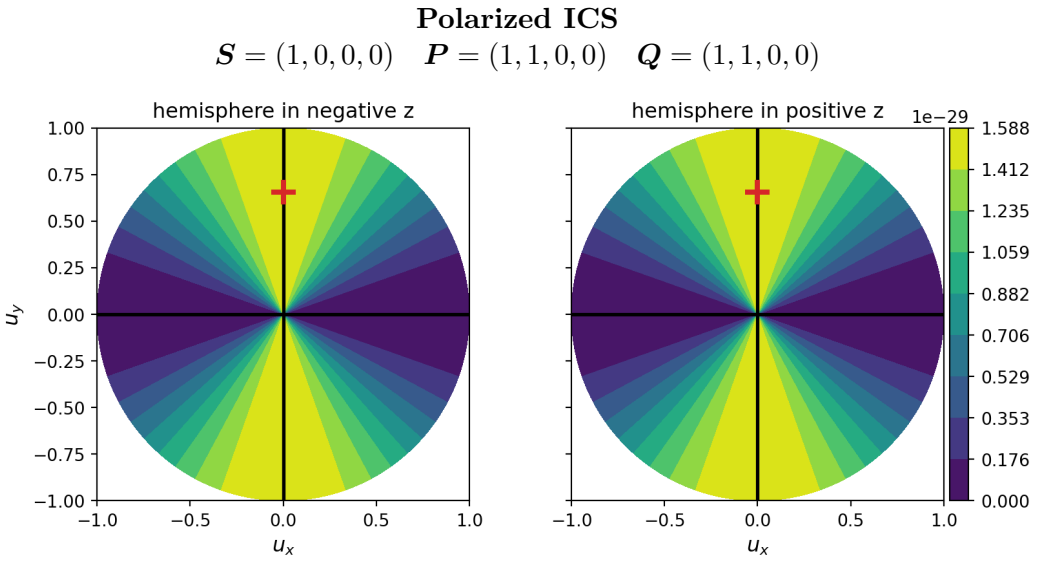

(a) 2D projection of polarized cross section in the Electron Rest Frame

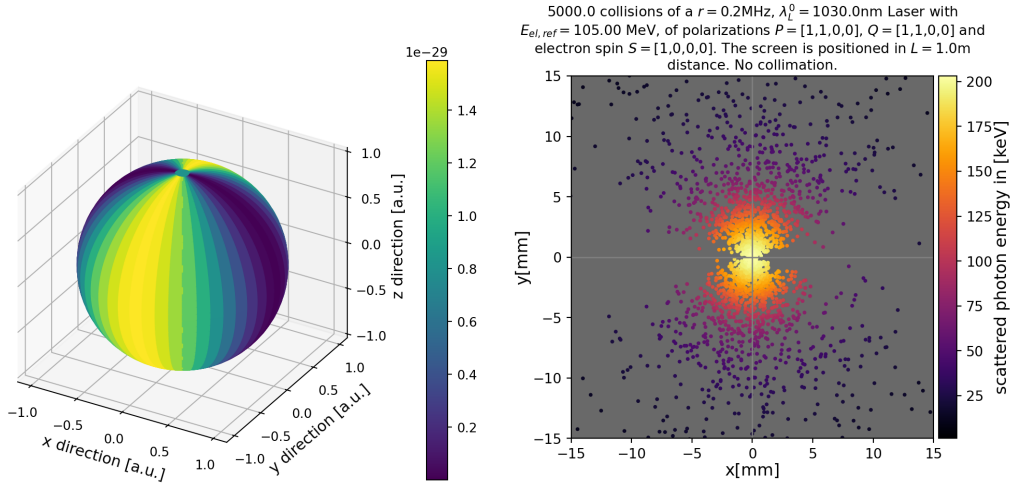

(b) 3D polarized ICS cross section (ERF) **(c)** ICS photons projected on a screen (LAB)

Figure 5.38.: Spatial characteristics of ICS emitted photons under the inclusion of polarization effects. Directional scattering probability W in the ERF and emitted photons of ICS with $\boldsymbol{P} = (1,1,0,0)$ polarized incident photons detected by a $\boldsymbol{Q} = (1,1,0,0)$ polarization filter. Calculated for a frontal collision $\theta_{inc} = 180°$. Plots simulated and generated in Comparse using a MESA-ER-IB-42m-nominal (App. tab. A.2) Astra generated electron distribution and Tangor-100-IR-focused (App. tab. A.8) presets. For this plot, W was calculated for $\rho_\theta = 181$ & $\rho_\phi = 360$ scattering angles by way of averaging over $N'_{par} = 11685$ scattering particle pairs chosen by weighted probability $W_{ics,norm}$.

polarization, gamma radiation probability W is centered around a specific angle ϕ

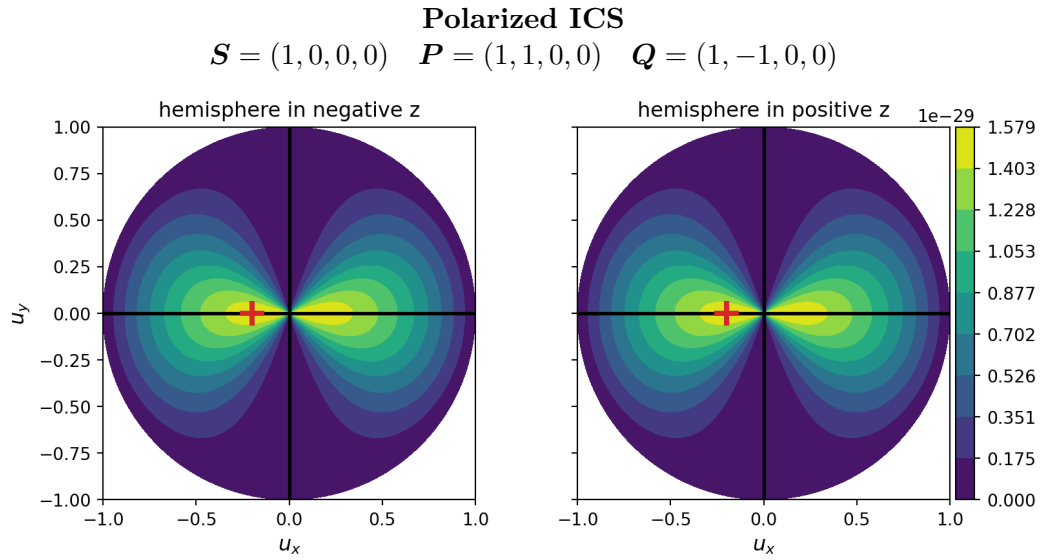

(a) 2D projection of polarized cross section in the Electron Rest Frame

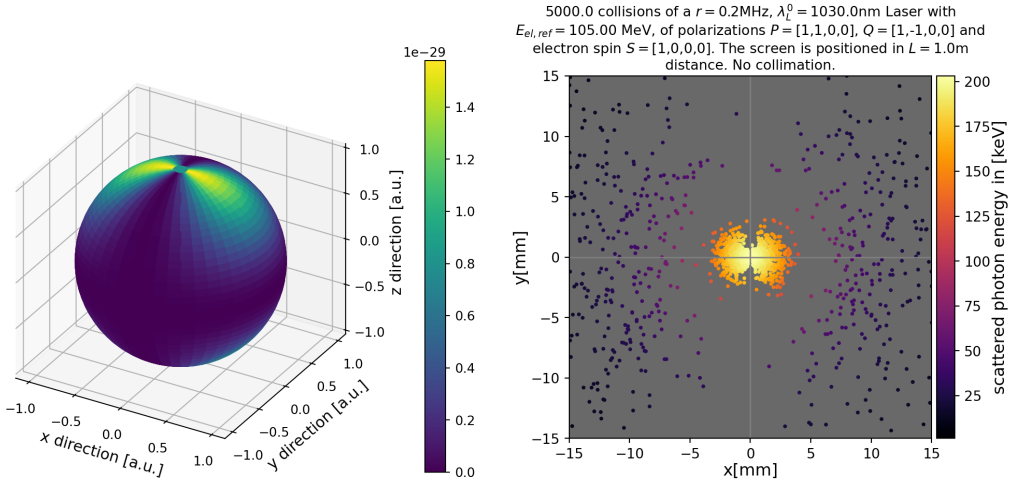

(b) 3D polarized ICS cross section (ERF) **(c)** ICS photons projected on a screen (LAB)

Figure 5.39.: Spatial characteristics of ICS emitted photons under the inclusion of polarization effects. Directional scattering probability W in the ERF and emitted photons of ICS with $\boldsymbol{P} = (1,1,0,0)$ polarized incident photons detected by a $\boldsymbol{Q} = (1,-1,0,0)$ polarization filter. Calculated for a frontal collision $\theta_{inc} = 180°$. Plots simulated and generated in Comparse using a MESA-ER-IB-42m-nominal (App. tab. A.2) Astra generated electron distribution and Tangor-100-IR-focused (App. tab. A.8) presets. For this plot, W was calculated for $\rho_\theta = 181$ & $\rho_\phi = 360$ scattering angles by way of averaging over $N'_{par} = 11685$ scattering particle pairs chosen by weighted probability $W_{ics,norm}$.

and it's $\phi + \pi$ opposite. On the chosen screen, these angles correspond with the vertical axis through the middle. As this W is modulated by the angle ϕ in the

ERF, the resulting scattered photons are most densely packed around the vertical screen axis near the center of the screen, where the $\Delta\phi$ sector radius is the smallest. Perhaps surprisingly, not all emitted ICS radiation is fully linearly polarized along the incident laser's polarization. In fig. 5.39c, we have filtered for the perpendicularly aligned linear polarization and can see, that photons with this polarization are still emitted. Just as the virtual polarization filter is set 90° perpendicular to $\boldsymbol{Q} = (1, 1, 0, 0)$, so too is the axis along which the scattered photons are packed. Now, the scattering image shows little to no photons along the vertical axis of the screen but around the horizontal axis. Here, however, the spatial characteristic is different in nature. Unlike the predominant ϕ modulation earlier for $Q = (1, 1, 0, 0)$, we now observe both a ϕ and θ dependence of W.
Let us briefly recall the interpretation of colored normalized scattering probability W plots such as fig. 5.39a and fig. 5.39b. Higher values indicate a greater probability of a photon of the defined polarization to be found scattering into that direction in the electron rest frame. Single photons in turn are always linearly polarized. In the framework of the corpuscle interpretation of light, when talking about an "unpolarized" beam, one expresses, that there is no statistically predominant linear polarization direction among the photons
With this, notice that both the W plots for $\boldsymbol{Q} = (1, 1, 0, 0)$ (fig. 5.38), nor $\boldsymbol{Q} = (1, -1, 0, 0)$ (fig. 5.39) show W value zero at $u_x = \pm 1$ and $u_y = 0$. It is thus impossible find a photon of either perpendicular linear polarization emitted into this exact direction, and thus, any photon in general. This W minimum is located on the equator of the directional sphere, furthest away from the dominant linear polarization axis. We can identify this probability sink on the detector image fig. 5.37a traced to approximately $x = 5\,\text{mm}$ and $y = 0\,\text{mm}$.
The severity of all polarization related spatial characteristic is reduced for linear polarization below maximum normalized Stokes parameter value $P_i = 1$ as shown in Appendix sec. A.7 fig. A.10.

Notes on the issues and benefits of ICS under linear polarization

Importantly, as explained in section 4.5, the stochastic probability of whether or not a fermion - photon pair results in an ICS event can be calculated independent of the aspects of polarization. Merely the scattering direction is determined in it's characteristic by the alignment of polarization. The locations on a spatial W sphere's equator in which the scattering probability is zero, therefore statistically attract the directions of the emitted photons towards this equator's equivalent meridian, the perpendicular surface axis dividing the sphere in halves. An equal flux of scattered photons compressed towards the center region can be beneficial for luminosity optimization in an experiment. In practise however, photon sources that allow for polarization tuning often come with intensity trade-offs compared to unpolarized emitters.
Off note as well, is that the emitted polarization from an ICS event between a fermion and a fully linearly polarized photon is not fully polarized in itself. The po-

larization direction of photons is spatially modulated through the interdependence of the scattering direction, Stokes parameters and cross section as per eq. 3.77. Experimentors planning an ICS based polarized gamma source should be aware of this. Simply using all emitted gamma radiation taken symmetrically around the longitudinal fermion momentum axis will not provide a predominantly linearly polarized beam. For this, the photons have to be collected from the azimuthal scattering angle ϕ region corresponding to the maximum scattering probability of the desired linear polarization alignment.
In turn, therein lie opportunities for polarization fine tuning in ICS gamma sources through spatial selection. As an example, a concept study is presented in fig. 5.40, in which a virtual pinhole collimator is placed in $d_{col} = 80\,\text{cm}$ distance to the experiment at a $\Delta x_{col} = 1.5\,\text{mm}$ shift towards the positive x-direction. Of the overall gamma radiation simulated in fig. 5.40a, we attempt to filter for the fraction that is linearly polarized in the $\boldsymbol{Q} = (1, -1, 0, 0)$ direction shown in fig. 5.40b. The collimator offset Δx_{col} is chosen due to the horizontal screen axis alignment of $\boldsymbol{Q} = (1, -1, 0, 0)$. First, we have set the collimator radius to $r_{col} = 1.5\,\text{mm}$. Now, filtering for $\boldsymbol{Q} = (1, -1, 0, 0)$ let's through roughly 63% of scattered collimated radiation, itself a reduction of 85% of the uncollimated gamma. This is plotted in 5.40c, which is a collimated version of fig. 5.38 (a), and 5.40d, in turn the collimated version of fig. 5.40b.
This $P_1 = 0.63$ degree of polarization can be improved upon by reducing r_{col} to $0.58\,\text{mm}$. Doing so further reduces the fraction of remaining photons $\mathfrak{N}_{ph,col}$ to approximately 96.5% when filtering for $\boldsymbol{Q} = (1, -1, 0, 0)$ and 99.93% for $\boldsymbol{Q} = (1, 1, 0, 0)$ respectively. While the gamma flux will be reduced by two orders of magnitude, we now obtain a linear polarization degree of $P_1 \approx 98\%$.
In regards to the loss of gamma Flux $\mathfrak{F}_\gamma$, it should be emphasized that the outlined concept above did not undergo careful optimization and was only intended to convey the approach. With collimator setup iterations, the flux to polarization efficiency ratio $\mathfrak{F}/P_i$ would improve. More advanced improvements can be gained from non circular pinhole collimator shapes, for instance a triangle shape that would more closely resemble the spatial ICS behavior.
Lastly, it should be mentioned that while conventional polarization filters provide the highest $\mathfrak{F}/P_i$, they may not be a suitable fit for a gamma source with a potentially high thermal load. Additionally, when filtering the uncollimated gamma radiation, the bandwidth of the spectrum will be very high. Commonly, ICS sources utilize collimation for bandwidth narrowing regardless of polarization considerations. Thus in principle, shifting the collimator to influence the degree of polarization may not be as costly as it appears on paper.

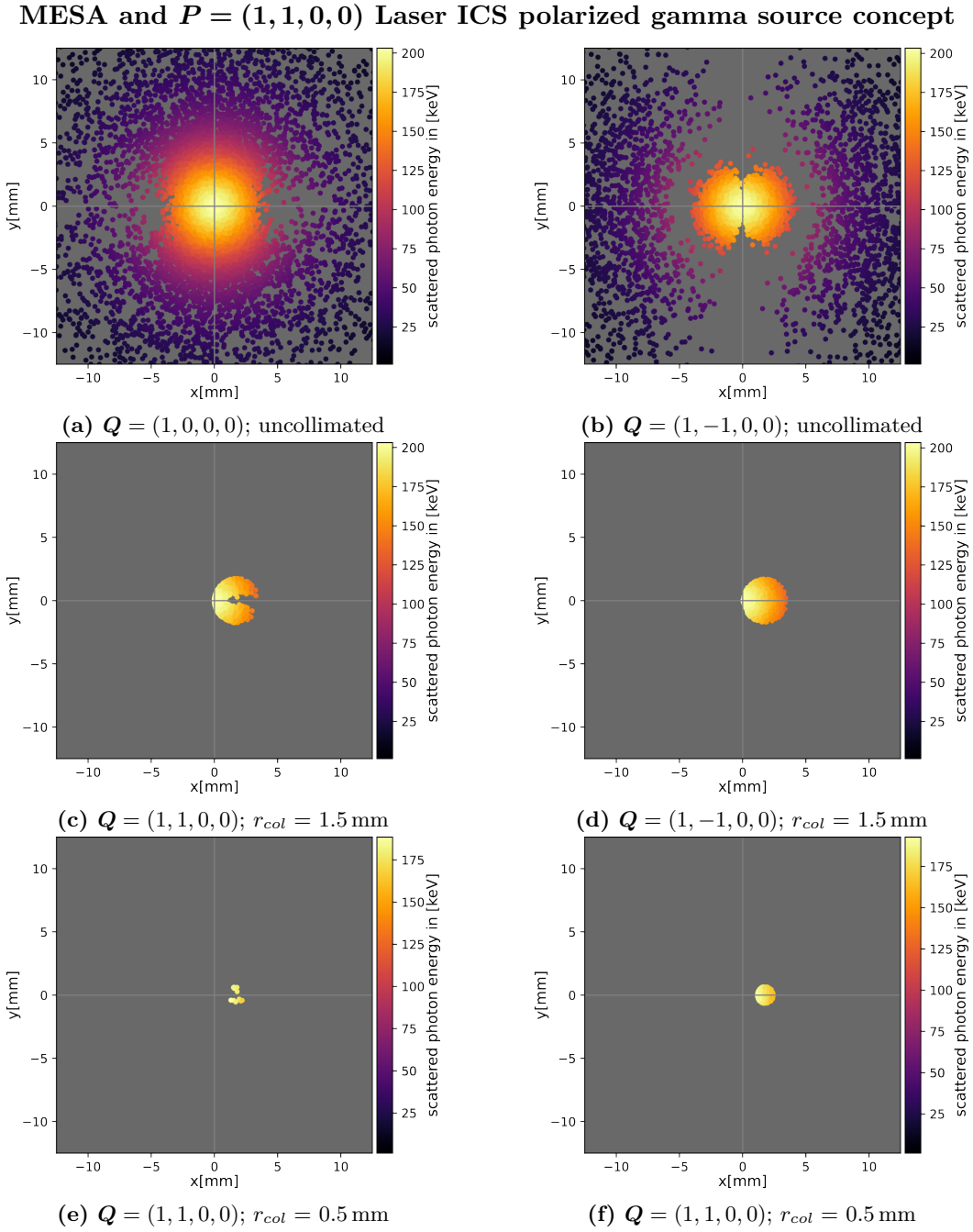

(a) $\boldsymbol{Q} = (1, 0, 0, 0)$; uncollimated

(b) $\boldsymbol{Q} = (1, -1, 0, 0)$; uncollimated

(c) $\boldsymbol{Q} = (1, 1, 0, 0)$; $r_{col} = 1.5\,\text{mm}$

(d) $\boldsymbol{Q} = (1, -1, 0, 0)$; $r_{col} = 1.5\,\text{mm}$

(e) $\boldsymbol{Q} = (1, 1, 0, 0)$; $r_{col} = 0.5\,\text{mm}$

(f) $\boldsymbol{Q} = (1, 1, 0, 0)$; $r_{col} = 0.5\,\text{mm}$

Figure 5.40.: ICS scattering images of MESA with a fully linearly polarized laser using various filters and pinhole collimators. The collimator is virtually placed in $d_{col} = 80\,\text{cm}$ distance to the experiment at a $\Delta x_{col} = 1.5\,\text{mm}$ shift towards the positive x-direction where the linear polarization $\boldsymbol{Q} = (1, -1, 0, 0)$ is dominant among the scattered photons. Calculated for a frontal collision $\theta_{inc} = 180°$. Plots simulated and generated in Comparse using a MESA-ER-IB-42m-nominal (App. tab. A.2) Astra generated electron distribution and Tangor-100-IR-focused (App. tab. A.8) presets. For this plot, W was calculated for $\rho_\theta = 181$ & $\rho_\phi = 360$ scattering angles by way of averaging over $N'_{par} = 17321$ scattering particle pairs chosen by weighted probability $W_{ics,norm}$.

Comparing Comparse Simulation Results

For the specific case of a fully linearly polarized laser beam performing ICS with electrons, several research papers have been published by colleagues that show the above described spatial gamma intensity distribution. Examples include, among others, simulations "Fig. 5" in [62] and "Figure 4." in [63] and experiment measurements such as "FIG. 2." of [64]. The characteristic spatial profile shown in fig. 5.37 can be seen here as well, including the probability minima and compression towards the screen center.
Note, that part of the deviations in how tightly bundled the scattered image is towards the middle can be attributed to differences in electron bunch distribution and emittance. The spatial distribution of photons traced towards a detector screen heavily depends on the origin point in space, where the photon is emitted from. Furthermore, since the probability of scattering direction W is calculated in the electron rest frame, the scattering direction must be Lorentz transformed back into the laboratory frame. This Lorentz transformation is dependent on the momentum direction of the electron. Higher than MESA values for transversal bunch distribution and emittance will further spread and intermix the scattering photon positions on the detector screen, reducing the clarity of the polarization dependent spatial characteristic.

5.4. Potential and Limitation of Physical Collimators

At the position within the MESA beamline we selected as the primary subject of our inverse Compton scattering feasibility studies, the electron beam parameters and chosen laser solutions allowed for successful optimization of the scattered photon spectrum towards higher average energies $\overline{E}'_{ph}$ by simulation the inclusion of a physical collimator. Doing so is not always guaranteed to bear fruit. On the example of a recently published accelerator driven ICS x-ray light source commissioning report, we will discuss the limitations of collimation in ICS experiments.

5.4.1. Compact X-ray Light Source Parameters

The Compact X-Ray Light Source (CXLS), currently in the advanced commissioning phase at the Arizona State University (ASU) in Tempe, USA, was designed to generate X-Rays of $E'_{ph} = 2\,\mathrm{keV}$ to $20\,\mathrm{keV}$ at $\nu_{ph,rep} = 1000\,\mathrm{Hz}$. In [65], the design performance is stated to be $\mathfrak{F}'_{ph,col,99.9\%} = 5 \cdot 10^9$ ph/s and $\mathfrak{F}'_{ph,col,95\%} = 1 \cdot 10^{11}$ ph/s for the scattered photon beam collimated to 0.1% and 5% bandwidth respectively. In the same report, the electron beam parameters are given for both design and measured realization. They are copied from table 2 in [65] and converted into Astra generator input parameters as shown below in tab. 5.11:

ASU CXLS Electron Beam Parameters at ICS Experiment Location

Parameter	Design	Measured
Bunch Charge Q_{el}	200 pC	50 pC
Reference Electron Beam Energy $E_{el,ref}$	33 MeV	33 MeV
Longitudinal Bunch Size σ_z	150 µm	150 µm
Horizontal Bunch Size σ_x	3 µm	8 µm
Vertical Bunch Size σ_y	3 µm	4 µm
Energy Spreadv ΔE_{el}	16.5 keV	16.5 keV
Normalized Horizontal Emittance $\epsilon_{x,n}$	1 π mrad mm	1 π mrad mm
Normalized Vertical Emittance $\epsilon_{y,n}$	1 π mrad mm	1 π mrad mm
Simulation Distribution	"Gauss"	"Gauss"
Simulation Macro Particles	500k	500k
Simulation Macro Factor	624	624

Table 5.11.: Performance parameters used to generate an electron distribution in Astra based on the ASU CXLS design and measured specs published in the commissioning report [65].

ASU CXLS Yb:YAG Laser Parameters at ICS Experiment Location

Parameter	Design	Measured
Wavelength λ	1030 nm	1030 nm
Relative Bandwidth $\frac{\sigma_\lambda}{\lambda}$	1%	0.2%
Bandwidth σ_λ	10.3 nm	2.06 nm
Pulse Length $\sigma_{ph,z}$	500 fs	500 fs
Focal Beam Waist Radius w_0	5 µm	5 µm
Pulse Energy E_{pulse}	200 mJ	100 mJ
Repetition Rate $\nu_{ph,rep}$	1 kHz	1 kHz
Beam Quality Factor m^2	1.2	1.1

Table 5.12.: Performance parameters used to generate a Gaussian Laser Beam Intensity distribution in Comparse based on the ASU CXLS design and measured specs published in the commissioning report [65].

5.4.2. Analysis of potential bandwidth narrowing through collimation

To investigate the limitations of collimation in high transversal focus example, we have simulated ICS using the CXLS design as well as measured parameters presented above in section 5.4.1. Using Astra's generator module, electron distributions were created using the parameters presented in table 5.11. In the case of the ICS collision as designed by the ASU, 133623 scattering electrons and photons were simulated, representing one electron bunch - laser pulse collision. When it came to simulating the ICS collision according to measured parameters, we had to gather the scattering partners of 15 collisions, resulting a comparable data set of 132345 electrons and photons. The root of this lies in the difference in flux that we estimate to be $\mathfrak{F}_{\gamma,\text{design}} \approx 134k$ ph/s if realized exactly to the initial design document and

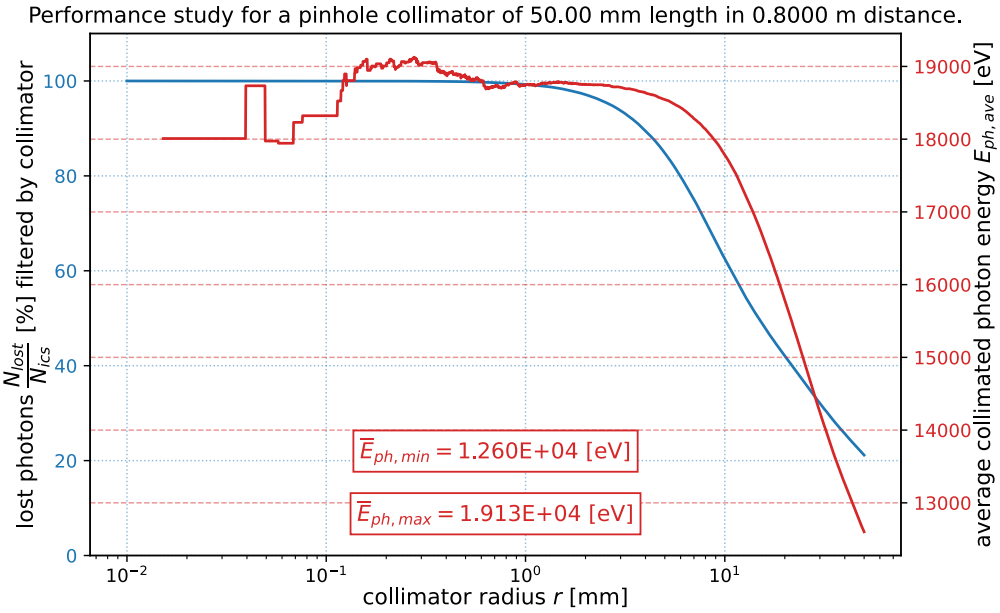

Figure 5.41.: Collimation performance study simulated in Comparse using the ASU CXLS **design** parameters of tables 5.11 and 5.12 taken from [65]. Simulation conducted and plot generated in Comparse v1.0. Electron distribution generated using Astra's "generator" and tab. 5.11 "Design" parameters. Photon distribution simulated using Comparse's "Gauss Beam" model and tab. 5.12 "Design" parameters.

only $\mathfrak{F}_{\gamma,\mathrm{real}} \approx 8.8k$ ph/s when using the measured performance parameters.
Afterwards, the scattering direction was then simulated for both scenarios using directional grid density parameters with an emphasize on scattering angle precision. Each scattered photon momentum was calculated for $\rho_\theta = 1080$ orbital scattering angle θ_{erf} and only $\rho_{phi} = 36$ azimuthal angle ϕ values. When aligning the pinhole collimator opening on the electron momentum axis, ϕ does not meaningfully influence the overall simulation result.
A pinhole collimator was defined as such in a distance of $d_{col} = 80\,\mathrm{cm}$ with a length of $l_{col} = 5\,\mathrm{cm}$. Now, the scattering photons were traced through 5000 versions of this pinhole collimator with the values for opening radius r_{col} sampled with logarithmic scaling from 0.01 mm to 50 mm. Finally, the percentage of photons filtered by the collimator $\mathfrak{N}_{lost}/\mathfrak{N}_{ics}$ and the average energy of the remaining gammas $\overline{E}'_{ph,col}$ were plotted in reference to r_{col}. The resulting graphs are presented in figures 5.41 and 5.42.
At a first glance, when analyzing both graphs, we can see a similar general behaviour. Naturally, with decreasing r_{col}, an increase in $\mathfrak{N}_{lost}/\mathfrak{N}_{ics}$ and $\overline{E}'_{ph,col}$ is observed. At the larger end of the radius scale, both curves are behaving linearly when the radius axis is scaled logarithmically, indicating a rise in collimation effect for per Δr_{col}. This trend turns at around $\mathfrak{N}_{lost}/\mathfrak{N}_{ics} \approx 50\%$ at which point onward

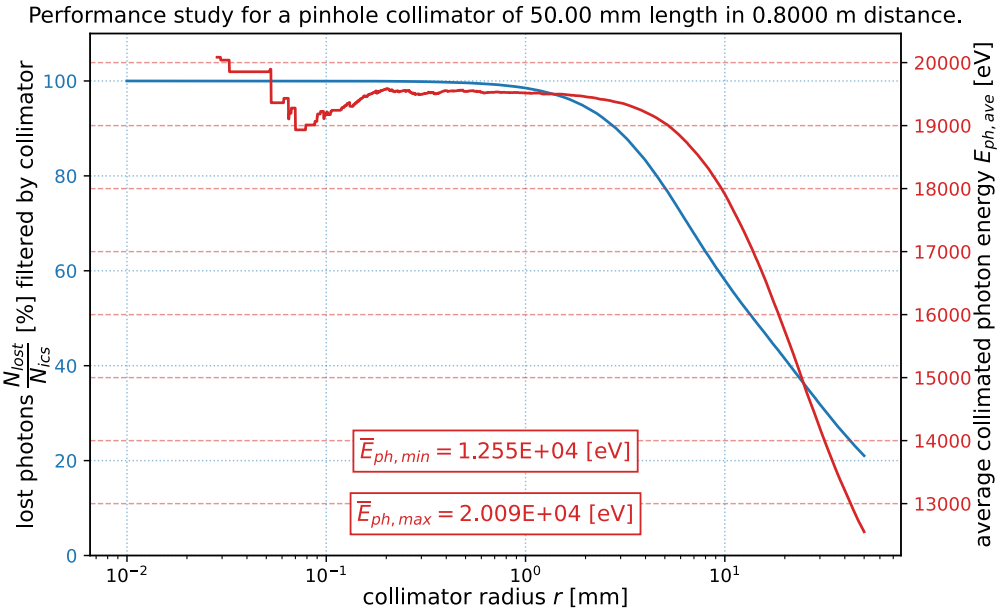

Figure 5.42.: Collimation performance study simulated in Comparse using the **measured** ASU CXLS parameters of tables 5.11 and 5.12 taken from [65]. Simulation conducted and plot generated in Comparse v1.0. Electron distribution generated using Astra's "generator" and tab. 5.11 "Measured" parameters. Photon distribution simulated using Comparse's "Gauss Beam" model and tab. 5.12 "Measured" parameters.

both curves now gradually tend towards a plateau. Differences between the simulations become apparent when investigating the plateau. While the percentage of filtered photons inevitably plateaus at $\mathfrak{N}_{lost}/\mathfrak{N}_{ics} = 100\%$, the average energy of the remaining photons differs between design and measured ICS experiment parameters.

When simulating ICS scattering according to the initial CXLS design, the average scattered energy of our representative data set cannot be collimated beyond $\overline{E}'_{ph,col,max} \approx 18.8\,\mathrm{keV}$. Although figure 5.41 shows energy values above 19 keV, they are only found when filtering more than 99.9% of the gamma radiation and therefore have to be interpreted as numerical noise as a result of a small sample size. This is a notable difference from the simulation based on measured results. The plateau in fig. 5.42 sits considerably higher at around $\overline{E}_{ph,col,max} = 19.5\,\mathrm{keV}$ compared to 18.8 keV despite the fact that both simulations were conducted with identical reference electron and photon energies of $E_{el,rf} = 33\,\mathrm{MeV}$ and $E_{ph,rf} = 1.2\,\mathrm{eV}$ which should result in a maximum scattered photon energy of $E'_{ph,ref,max} = 20.09\,\mathrm{keV}$ under ideal conditions. Even below the plateau, the average energy among the remaining photons is higher per percentage lost to collimation when simulating using measured parameters

5.4.3. Interpretation of the simulation results

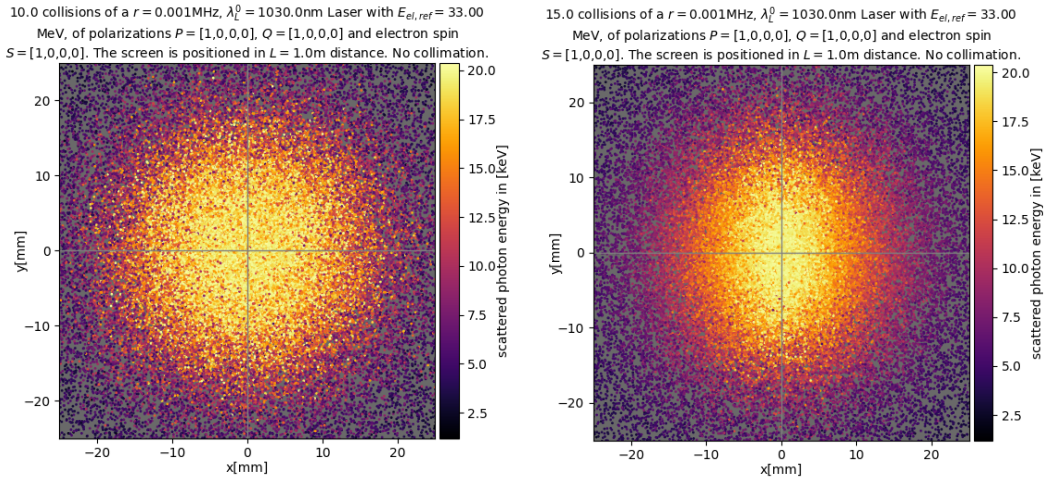

(a) Simulated from design

(b) Simulated from measurements

Figure 5.43.: Simulation of scattering photons produced via ICS at the ASU CXLS [65] traced to a 50 mm edge length square screen positioned in 1 m distance from the ICS interaction point. Scattering images simulated and generated in Comparse v1.0. Electron distribution generated using Astra's "generator" and tab. 5.11 "Design" parameters. Photon distribution simulated using Comparse's "Gauss Beam" model and tab. 5.12 "Design" parameters.

We have discovered, that energy bandwidth improvements via pinhole collimation on the example of the ASU CXLS initial design are limited to below $\overline{E}'_{ph,col,max} \approx 18.8\,\text{keV}$. The reason for that becomes apparent when analyzing the energies of scattered photons collected on a screen. Figure 5.43 shows that the measured electron and laser beam parameters result in a cleaner E'_{ph} - $\theta_{ph,lab}$ dependence. Isolating the higher energy photons colored in yellow from the lower energy purple and red ones appears noticeably easier in fig. 5.43b. In fig. 5.43a, more photons of median and lower energies are found in the inner radii of the photon screen.
The example shows, that while an accelerator driven ICS experiment might generate a higher photon flux when designed with an ambitiously narrow spatial focus, the bandwidth of the resulting gamma radiation might not be able to be improved beyond a certain limit. In the case of the CXLS, the simulation modelled after the measured parameters in which the transversal electron bunch size focus is considerably relaxed compared to the design specs, the ICS generated gamma flux $\mathfrak{F}_\gamma$ is reduced, but in exchange, we now calculate a narrower potential bandwidth to be obtained via pinhole collimation.
The purpose of this example was to illustrate the importance of precise simulations that take into account as many deviations from an idealized setup caused by real laboratory circumstances as possible. Furthermore, similar simulations conducted for MESA as presented in figures such as 5.9, 5.20 and 5.21 show that the ICS ex-

periment configurations proposed in section 5.2 can be expected to provide gammas of tunable energy and energy bandwidth. None of the MESA simulations exhibit a degree of noisy spatial scattered energy distribution comparable to fig. 5.43a and even 5.43b.

5.5. Evaluation of Temporally Static Model Validity

If not explicitly stated otherwise, all simulations for this thesis were conducted without activated temporal dynamics. As we shall recall from section 4.5.4, this means that the laser pulse is assumed to be at maximum power for a time period T_{obs} equal to the pulse length sigma $\sigma_{z,ph}$ and the electron bunch remains static in the laboratory frame for the entire $\sigma_{z,ph}$. It is evident, that this is a simplification of the experiment. Dividing the simulation into time steps, as described in section 4.5.4, will more closely describe the ICS collision when performed experimentally. This however comes at a steep cost in simulation time, as even with optimized order, each time step constitutes another scattering selection simulation of equal length. Thus for instance, dividing the observation time into 20 consecutives steps increases the simulation time by a factor of at least 20.
In this section, we intent to quantify the degree of approximation when simulating a temporally static collision and look for fundamental changes in the behavior of the simulated results.

5.5.1. Parameter Setup

As in previous sections, we will match the location of MESA operated in ERL mode in the Internal Beamline at $E_{el,ref} = 105\,\text{MeV}$ and $Q_{el} = 7.7\,\text{pC}$ (App. tab. A.2) with a $\lambda = 1030\,\text{nm}$ Tangor 100 IR laser pulsed at $E_{pulse} = 50\,\mu\text{J}$ over $\sigma_{z,ph} = 10\,\text{ps}$ (App. tab. A.8). The photon distribution model is "Gauss Beam".
In the collection of scattering partners, $n_{sim} = 10\,000$ collisions were simulated using boost factor $B = 10$. For the temporally dynamic simulation, the number of time steps t_i before and after t_0 was set to 10, resulting in 21 time steps overall. The period of observation T_{obs} was set to $\sigma_{z,ph} \cdot 2.5 = 2.5\,\text{ps}$.
Additionally, for the flux estimation simulation, the number of static runs condition was set to $n_{sim,c}$ =10 000 and the static mean condition to $\Delta\overline{N}_c = 0.0001$ for the static model and to $n_{sim,c}$ =1 000, $\Delta\overline{N}_c = 0.001$ when using temporal dynamics due to the factor 21 increase in simulations per collision corresponding to the number of time steps.

5.5.2. Simulation Results

Starting with the first ICS simulation step, the stochastic decision of scattering particles (sec. 4.5), we begin by gathering the fermion - photon scattering partners resulting from an equivalent of $n_{sim} \cdot B = 100\,000$ collisions corresponding to $T_{ics} = 0.5\,\text{s}$ of real experiment time. Using the static routine, we obtain $N'_{par} = 58\,378$

while activating temporal dynamics gathers the information of 61 951 fermions and photons. This represents an increase of approximately 6.12%. To ascertain if the deviation is a rare statistic exception and not a systematic difference, the simulation is repeated for $n_{sim} \cdot B = 12\,000\,000$ collisions, gathering the data corresponding to 1 s of the ICS experiment. Additionally, a flux estimation simulation is conducted for both static and activated temporal dynamics settings.
The flux estimation routine concluded at $\mathfrak{F}_{\gamma,ts} = 116\,895$ ph/s for the static model and at $\mathfrak{F}_{\gamma,tv} = 123\,706$ ph/s when using temporal dynamics. The difference represents an increase in scattering probability over the static approach of approximately 5.83%.
Unlike the deviation in the absolute number of scattering electrons, a difference in scattering position was expected beforehand. During the rise and fall of the laser pulse, the electron bunch continues moving with close to the speed of light.

$$v_{el} = \beta_{par,lab} \cdot c \approx \sqrt{1 - \frac{1}{\left(\frac{E_{el,ref}}{E_0}\right)^2}} \cdot c \approx 0.99998 \cdot c \tag{5.10}$$

When the electron bunch is in motion with about v_{el} for the entire T_{obs}, it will translate $\Delta s \approx 7.5\,\text{mm}$. About half of this is the maximum possible shift a scattering electron can have from it's t_0 position in the initial reference electron bunch. Naturally, the early and late timesteps, when the electron bunch is furthers away from the t_0 center are the least unlikely timesteps to result in collisions. To visualize the impact of the z position shift, we have plotted the scattering positions z'_{el} to their original z_{el} within the t_0 electron bunch used in the static approach in fig. 5.44. Additionally, the z'_{el} was plotted over particle index $\boldsymbol{i}$ in fig. 5.45 to emphasize the widening of the longitudinal scattering position range.
So far we have shown that the temporally dynamic simulation results in a higher $\mathfrak{F}_\gamma$ and that the origin of ICS scattering is longitudinally extended when not using the static approach. Of main concern for researchers however is the produced gamma spectrum, which we will investigate next. For this, we shall now return to the $N'_{par,100k}$ gathered initial ICS data sets to conduct the scattering simulations.
The relativistic scattering routine was executed over both data sets with $\rho_\theta = \rho_{phi} = 360$ and no polarization. Right away, the resulting average gamma energy $\overline{E}'_{ph}$ was calculated to be similar. While the static model produced $\overline{E}'_{ph,ts} \approx 101.553\,\text{keV}$ average gamma energy, the time variable model resulted in $\overline{E}_{ph,tv} \approx 101.651\,\text{keV}$, a $\overline{E}'_{ph,tv}/\overline{E}'_{ph,ts} \approx 0.01\%$ increase. Considerably less than the flux increase recorded earlier, the higher average scattering energy cannot be attributed to the temporal calculation as it is within the limits of purely stochastic fluctuation.
This interpretation is partially based on the lack of an apparent mathematical cause. Recall that the temporal dynamic model does not include space charge effects. The angle of electron momentum, a key factor of the energy transfer efficiency, does not change over Comparse's time progression. Only a small drift of higher transversal momentum electrons from the bunch center can leave a trace in the incident angle, as electrons found further outside experience a greater curvature of the laser Gauss

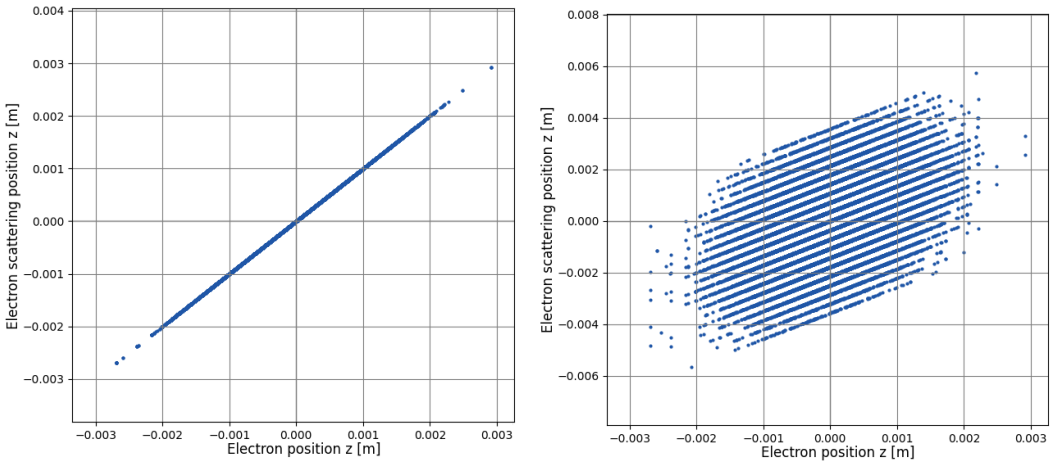

(a) Temporally static **(b)** Temporally dynamic

Figure 5.44.: Longitudinal ICS event position z'_{el} plotted over longitudinal electron position z_{el} within the initial electron bunch at t_0 as generated by Astra in the laboratory frame for both a static and temporally dynamic simulations. As a result of the large data size, one can see scattering events of all 21 timesteps distinctly in fig. 5.44b. Obviously, the horizontal and vertical axis values are identical in fig. 5.44a. This plot is only shown to illustrate the difference. Figures simulated and generated in Comparse using a MESA-ER-IB-42m-nominal (App. tab. A.2) Astra generated electron distribution and Tangor-100-IR-focused (App. tab. A.8) presets.

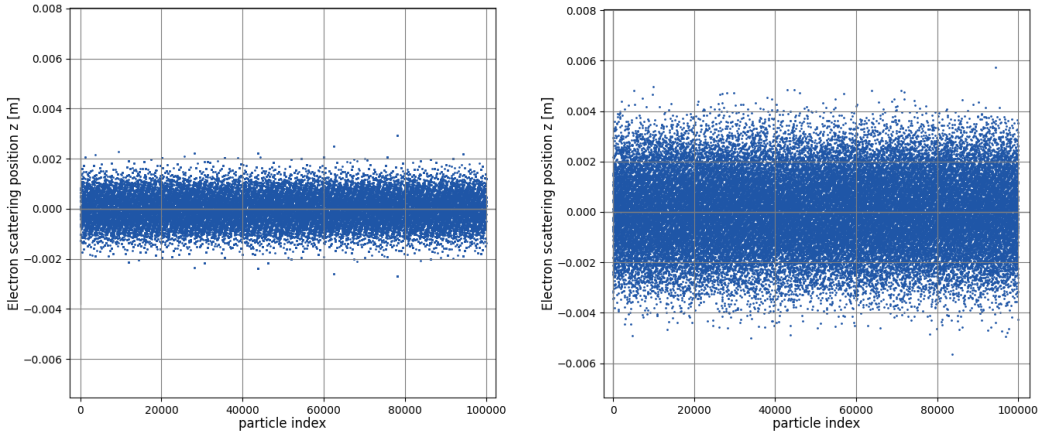

(a) Temporally static **(b)** Temporally dynamic

Figure 5.45.: Longitudinal scattering position z'_{el} plotted to particle index i for both static and temporally dynamic simulation. As both plots have been scale aligned, one can clearly see the greater range of longitudinal scattering positions. Figures simulated and generated in Comparse using a MESA-ER-IB-42m-nominal (App. tab. A.2) Astra generated electron distribution and Tangor-100-IR-focused (App. tab. A.8) presets.

beam model. However, as the temporal shift duration is symmetrical around t_0, the opposite transversal shift in the negative time range t_{neg} is equal to the positive one. Before arriving at the t_0 interaction point, the electron bunch already dissipated in the transversal direction. In Comparse, the reverse calculation would see it compress from t_0 to $t_{-T_{obs}/2}$. These electrons are transversely shifted towards the center of the Gaussian laser beam curvature. Taking this into account, one would expect an equal overall transferred energy or even a reduced one, as a Gaussian bell curvature increases with distance to the center in it's first sigma range. Thus in sum, the average incident angle θ_{inc} would be increased, statistically lowering the scattered photon energy due to a reduced recoil X (eq. 3.24). That instead, we record an increase in gamma energy when using temporal dynamics, implies a stochastic origin of the small deviation.
Lastly, we have investigated the impact on the collimation potential of both simulation routines. For this, the pinhole collimator efficiency study presented in sec. 5.4 was repeated, once for the gathered scattering photons without temporal dynamics and once with. The result is plotted in fig. 4.15. No change in the curve's characteristic is observable. The thinner plotted temporally dynamic curves fit above the wider plotted temporally static one with barely any change in overlap distance along the graph. Setting the collimator to the radius at which the average remaining photon energy is 95% of $E'_{ph,max}$ filters out $\mathfrak{N}_{ph,los,95\%} \approx 68.83\%$ with temporal dynamics and $\mathfrak{N}_{ph,los,95\%} \approx 68.89\%$ without. In both cases, the $\overline{E}'_{ph,95\%}$ radius was calculated to be $r_{col,95\%} = 1.778\,\text{mm}$. Repeated for $\overline{E}'_{ph,99\%}$, the correct collimator radius was again determined to be the same for both modes, now $r_{col,99\%} = 0.671\,\text{mm}$. Here, the percentage of photon lost was $\mathfrak{N}_{ph,los,95\%} \approx 86.33\%$ in the dynamic and 85.60% in the static case.
All results so far are summarized in table 5.13.

	t **Static**	t **Variable**	**Variable/Static**
$\boldsymbol{N'_{par,100k}}$	58 378	61 951	+6.12%
$\boldsymbol{N'_{par,12m}}$	584302	617637	+5.71%
$\boldsymbol{\mathfrak{F}_{\gamma}}$	116 895 ph/s	123 730 ph/s	+5.82%
$\boldsymbol{\overline{E}_{ph}}$	101.553 keV	101.651 keV	+0.01%
$\boldsymbol{\mathfrak{N}_{ph,los,95\%}}$	68.8270%	68.8907%	−0.09%
$\boldsymbol{\mathfrak{N}_{ph,los,99\%}}$	86.5977%	86.3263%	+0.31%

Table 5.13.: Comparison of key simulation results between one static time step of length $\sigma_{z,ph}$ at t_0 and 21 time steps symmetrically around t_0 adding to an overall observation time of T_{obs}. Simulated in Comparse using a MESA-ER-IB-42m-nominal (tab. A.2) Astra generated electron distribution and Tangor-100-IR-focused (tab. A.8) presets.

Collimator radius scan of MESA ER-IB-42m scattering with Tangor100 laser, simulated via "Gauss Beam" with both deactivated and activated temporal dynamics

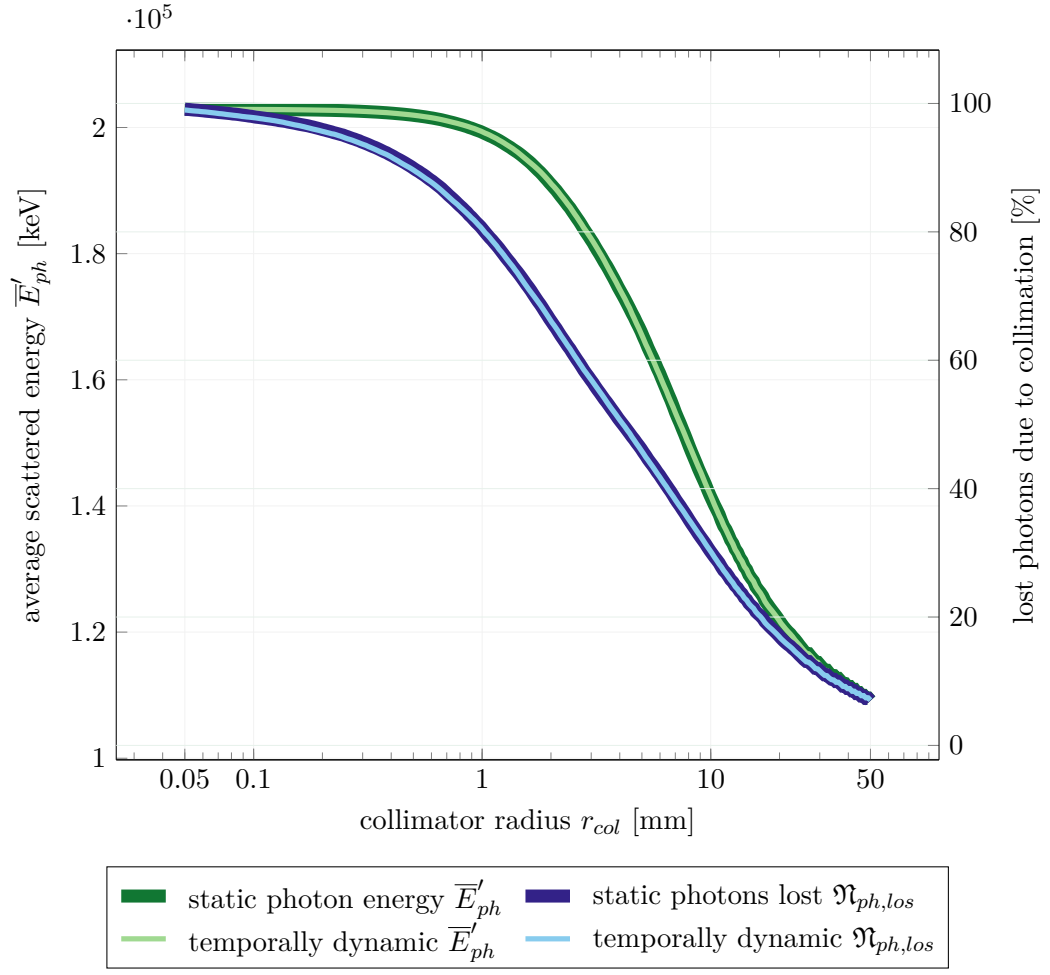

Figure 5.46.: Physical collimation efficiency simulation of MESA ER-IB-42m and a focused Tangor100 IR laser. The collimation series was simulated for a data set of 58378 scattering photons determined without temporal dynamics and a data set of 61951 determined with. Curves plotted thick correspond to the static simulation and curves plotted thin correspond to the dynamic. The virtual pinhole collimator was placed in $d_{col} = 80\,\text{cm}$ distance. It has a length of $l_{col} = 5\,\text{cm}$. In these settings, equivalent to default settings with which the MESA studies were conducted, physical collimation per ray tracing of scattered photons does not appear to be noticeably affected by the choice of temporal dynamics or not. Laser parameters were taken from Tangor-100-IR-focused (app. tab. A.8) while the electron distribution was generated in Astra using the MESA ER-IB-42m (app. tab. A.2) preset. It is the same distribution used in the studies in sec. 5.2.

5.5.3. Interpretation of the Results

Aside from the incident scattering probability, no statistically significant difference between the time steps $\boldsymbol{t}_i$ and the t_0 static simulation model was discovered. The sub % deviations in the energy spectrum and collimation efficiency can be explained by standard statistical fluctuations. Furthermore, we have explained that variables such as average scattered energy collimated to 95% of maximum gamma energy $E'_{ph,max}$, $\mathfrak{N}_{ph,los,95\%}$, are inherently difficult to compare, as the $E'_{ph,max}$ value is taken from the result of the scattering electron and photon pair with the combined highest positive deviation and smallest scattering angle θ. As this is determined by several variables with underlying statistical variation, $E'_{ph,max}$ will be different for every simulation and with it, the average energy collimated to within a defined percentage $E'_{ph,col,x\%}$.
Disregarding the energy related ICS performance parameters leaves us with a significant increase in ICS probability of more than 5%, when activating temporal dynamics. As for the feasibility studies in this thesis, we intended to err on the side of conservative performance prediction, this is acceptable. Optimistic researchers may add 5% to their flux simulation results. We for our part have been emboldened in our confidence in the simulation results presented in the previous sections and in Comparse itself. That the simulations have shown next to no variations when none are expected, speaks to the robustness of the mathematical foundation.

6. Conclusion

With the "Mainz Superconducting Energy Recovering Linear Accelerator" (MESA), the Institute for Nuclear Physics of the Johannes Gutenberg-University Mainz aims to become one of the test-bed facilities employing the novel Energy-Recovery-Linac scheme for foundational research. As of this writing, MESA is planned to provide an environment for precise measurements of the proton charge radius and for experiments shedding light onto topics such as dark matter as well as heavy nuclei parity violation through the weak mixing angle. Beyond that, any machine built with significant investment for experiments of inevitably finite terms can profit from having options for upgrade paths outline in advance.
One such paths might be Inverse Compton Scattering. On a fundamental level, ERLs and ICS are suited for each other, as the accelerator attempts to recover the energy spent on accelerating fermions, while the experiment has a typically very low cross section that causes only a tiny fraction of fermions to transfer their energy in scattering processes with an incoming laser pulse. The goal of this thesis, was to provide a comprehensive and reliable feasibility study for a expansion of MESA with an ICS gamma source. It needed to take into account how real laboratory conditions impact the gamma performance and what changes are caused to the phase space of the electron bunches that MESA aims to recirculate for energy recovery.
Throughout the work for this thesis, MESA was still in the midst of being built. Because of that, we lacked experimental data but in exchanged had a high a level of freedom to envision various implementation scenarios. Given that, it was deemed that the studies should be conducted on a swiftly executable simulation pipeline producing precise results. Therefore, the first part of this work represents a review of the theoretical principles underlying Inverse Compton Scattering. We have summarized the mathematics tracing back many decades. The equations and matrices derived in chapter 3 approach ICS as a relativistic scattering between fermion and photons in the particle view but account for effects of Quantum Electrodynamics and polarization.
Based on this mathematical foundation, a Python program called Comparse was developed. It was written fully vectorized in order to be able to quickly execute mathematical calculations over large data sets as is described in chapter 4. Through this, we were able to investigate a multitude of experiment scenarios. Based on preliminary simulation results and investigations of both MESA beamline simulations and the experiment hall, a few promising locations were identified.
In chapter 5, we have presented studies detailing the expected performance of ICS at the chosen locations. Paired with a Tangor 100 IR or comparable laser, MESA can provide a monochromatic $\overline{E}'_{ph,col,99\%} \approx 200\,\mathrm{keV}$ X-Ray source for medical and

material imaging applications. The realization of this would require relatively little financial and person hour investment.
Using MESA as a driver for a high brightness monochromatic gamma source in the low-MeV range would require significantly more investment and modifications to MESA's beamline layout. However, with $\lambda = 193\,\mathrm{nm}$ industrial Excimer Laser systems, $\overline{E}'_{ph,col,99\%} \approx 1.065\,\mathrm{MeV}$ gammas produced with a flux of $\mathfrak{F}_{\gamma,col,99\%} = 3.29 \cdot 10^8$ ph/s are in reach. This would enable foundational research in the low-energy realm of nuclear photonics. The impact of these experiments on the electron beam was calculated to be significant for affected singular electrons, but in face of the low cross section negligible compared to other sources of losses in energy recovery efficiency when operating MESA in ERL mode. For this reason, we predict that ICS can be used as a non-destructive beam diagnostics tool for electron beam energy and energy spread measurements. This usage scenario in particular can be facilitated by an off-the-shelve $\lambda = 1030\,\mathrm{nm}$ in a small-footprint experiment setup.
More ambitious beam diagnostics applications of ICS include spin polarization coupling. Compton polarimeters can measure the degree of spin polarization of an electron beam through the asymmetry of the Compton spectrum. We have simulated the effect and concluded that the normalized relative spectrum deviation is below $\Delta_{IR}E'_\gamma = 5 \cdot 10^{-6}$ when using a $\lambda_{IR} = 1030\,\mathrm{nm}$ industry laser and $\Delta_{EX}E'_\gamma = 2.5 \cdot 10^{-5}$ for a $\lambda_{EX} = 193\,\mathrm{nm}$ laser. The measurement time necessary for the asymmetry to rise above the background noise, a major challenge in Compton polarimetry, would be significantly longer than at other accelerator facilities employing the concept.

In terms of error estimation, none was calculated for this thesis. The reason for that lies in the sheer number of interdependent and often statistically afflicted variables. Compounding to the issue, is that the initial electron distribution, representing MESA or other accelerators, used in this thesis is sampled from spatial Gaussian distributions. For more precise simulations, actual measurements of the MESA beam line are required, but as MESA is still under construction, for now, that will have to wait. Additionally, we cannot be certain that our simulation models actually do reflect reality. A convincing quantification of the simulation error is only possible in comparison to laboratory measurements or other simulations. Here, the fact that accelerator driven ICS sources are in their early stages, the options are limited.
The S-Dalinac of the TU Darmstadt was intended to serve as a comparison point for our simulations, as part of a GRK 2128 AccelencE co-internship, but didn't start ICS operation throughout the years 2023 and 2024. From other accelerator facilities that already conduct ICS experiments, we have limited access to setup details and influence on the operation but can tentatively confirm publicly released performance parameters.
Another category of comparison point is provided by simulation codes developed by other researchers. However, their finished code will have had similar validation challenges. Furthermore, we have used Comparse to simulate with the inclusion of aspects that are often neglected, such as varying incident angles, Gaussian beam

photon momentum curvature and polarization. Having said that, let it be known that in the cases where results could be compared, Comparse compares favourably. Looking ahead, we still see room for expanded feasibility studies at MESA, a benefit from experimental validation and naturally plenty of potential for additional features and refinement of the simulation code Comparse. Considering ideas projected further, the mathematical routines already built could be used as the foundation for a live polarimetry code. The concept would involve feeding beam measurements during operation to a software that would iteratively simulate polarized scattering in an attempt to have simulated results approach the measurements.
We have thus presented our estimation of the feasibility of an ICS gamma source at MESA and aspire that this work turns out to be the start of a dialog at Mainz regarding an ICS experiment expansion. Even if it is deemed, that the possible performance is not worth the investment of time and resources, this study and the program written for it will have already served it's purpose. Outside of Mainz, we hope that colleagues from other institutions find value in Comparse. It was written with users of different backgrounds and knowledge depths in minds insofar that it requires no programming or deeper familiarity with the mathematical theory of ICS. When Comparse convinces planners of the potential for accelerator driven ICS gamma sources and when it manages to prevent expensive mistakes, all is well and as intended.

A. Appendix

A.1. Mathematical Derivations

A.1.1. Four-Vector Algebra

A.1.1.1. Rest Mass eq.3.54

$$\begin{aligned}
\mathbf{p}'^2 &= \mathbf{p}^2 + 2\mathbf{p}\cdot\mathbf{k} - 2\mathbf{p}\cdot\mathbf{k}' + \mathbf{k}^2 - 2\mathbf{k}\cdot\mathbf{k}' + \mathbf{k}'^2 \\
\mathbf{p}'^2 &= \mathbf{p}^2 + 2\mathbf{p}\cdot\mathbf{k} - 2\mathbf{p}\cdot\mathbf{k}' + (\mathbf{k}-\mathbf{k}')^2 && |3.12 \\
\mathbf{p}'^2 &= \mathbf{p}^2 + 2\mathbf{p}\cdot\mathbf{k} - 2\mathbf{p}\cdot\mathbf{k}' - 2\mathbf{k}\cdot\mathbf{k}' && \left|-\mathbf{p}'^2\right. \\
0 &= \left(\mathbf{p}^2 - \mathbf{p}'^2\right) + 2\mathbf{p}\cdot\mathbf{k} - 2\mathbf{p}\cdot\mathbf{k}' - 2\mathbf{k}\cdot\mathbf{k}' && \left|\mathbf{p}^2 = E_0^2 = \mathbf{p}'^2\right. \\
0 &= \mathbf{p}\cdot\mathbf{k} - \mathbf{p}\cdot\mathbf{k}' - \mathbf{k}\cdot\mathbf{k}'
\end{aligned} \tag{A.1}$$

A.1.1.2. Mandelstam Invariant Inequality *su* in eq.3.2.1.1

The invariant equations

$$\begin{aligned}
s &= E_0^2 + 2\mathbf{pk} && |\text{eq.3.10} \\
u &= E_0^2 - 2\mathbf{pk}' && |\text{eq.3.12}
\end{aligned}$$

simplify in the frame in which the fermion is at rest ($\mathbf{p} = (E_0, 0, 0, 0)$ to

$$s = E_0^2 + 2E_0 ku \qquad\qquad = E_0^2 - 2E_0 k'$$

Thus follows for us:

$$\begin{aligned}
us &= \left(E_0^2 + 2E_0 k\right)\cdot\left(E_0^2 - 2E_0 k'\right) \\
&= \left(E_0^4 + 2E_0^3 k - 2E_0^3 k' - 4E_0^2 kk'\right) \\
&= E_0^4 + 2E_0^3\left(k - k'\right) - 4E_0^2 kk' && |\text{eq.3.58} \\
&= E_0^4 + 2E_0^2 kk'\left(1 - \cos\theta_{erf}\right) - 4E_0^2 kk' \\
&= E_0^4 + 2E_0^2 kk'\left(\left(1 - \cos\theta_{erf}\right)2\right)
\end{aligned} \tag{A.2}$$

Consider the boundary conditions $k \geq 0$, $k' \geq 0$ and $1 \geq \cos\theta_{erf} \geq -1$. From the latter follows

$$2 \geq 1 - \cos\theta \geq 0$$

and thus

$$0 \geq (1 - \cos\theta_{erf}) - 2 \geq -2$$

which ensures that the summand added to E_0^4 in eq. A.2 is always negative.

$$us = E_0^4 + x \quad \text{where} \quad x \leq 0$$
$$\Rightarrow us \leq E_0^4 \quad \text{q.e.d}$$

A.1.2. Stokes Vector Algebra

A.1.2.1. Unpolarized ICS cross section eq.3.80 calculated as the sum of two linear polarization filter checks

$$\boldsymbol{W}_{D(1,1,0,0)} = \frac{1}{2}(1,1,0,0)\mathbf{T}\begin{pmatrix}1\\0\\0\\0\end{pmatrix}$$
$$= \frac{1}{4}r_e^2\left(\frac{k_0'}{k_0}\right)^2\left[\left(1+\cos^2\theta + (k_0-k_0')(1-\cos\theta)\right) - \sin^2\theta\right] \tag{A.3}$$

$$\boldsymbol{W}_{D(1,-1,0,0)} = \frac{1}{2}(1,-1,0,0)\mathbf{T}\begin{pmatrix}1\\0\\0\\0\end{pmatrix}$$
$$= \frac{1}{4}r_e^2\left(\frac{k_0'}{k_0}\right)^2\left[\left(1+\cos^2\theta + (k_0-k_0')(1-\cos\theta)\right) + \sin^2\theta\right] \tag{A.4}$$

$$\boldsymbol{W}_{D(1,1,0,0)} + \boldsymbol{W}_{D(1,-1,0,0)} = \frac{1}{4}r_e^2\left(\frac{k_0'}{k_0}\right)^2\left(1+\cos^2\theta + (k_0-k_0')(1-\cos\theta)\right) \tag{A.5}$$

Equation A.5 mirrors eq.3.79.

A.2. MESA Electron Beam Configurations

A.2.1. ERL Mode Positions

A.2.1.1. MESA ER-Mode in Internal Beam Line

MESA-ER-IB-42m Beamline

Beamline Parameter	Symbol	Value
Bunch Charge	Q_{el}	7.7 pC
Beam Current	I_{el}	10 mA
Bunch Repetition Rate	$\nu_{el,rep}$	1.3 GHz

Table A.1.: Performance parameters of the MESA Internal Beamline in ERL mode as currently under construction (Summer 2024).

MESA-ER-IB-42m-nominal

Astra Parameter	Abbreviation	Value
Reference Electron Beam Energy	$E_{el,ref}$	105 MeV
Bunch Charge	Q_{el}	7.7 pC
Longitudinal Bunch Size	σ_z	640 µm
Transversal Bunch Size x	σ_x	169 µm
Transversal Bunch Size y	σ_y	73 µm
Energy Spread	σE_{kin}	10.5 eV
Normalized Transversal Emittance x	ϵ_x	0.3
Normalized Transversal Emittance y	ϵ_y	0.3
Simulation Distribution	Dist x/y/z	'gauss'
Simulation Macro Particles	IPart	200k
Simulation Macro Factor	$\mathfrak{M}_e$	240

Table A.2.: Performance parameters used to generate an electron distribution in Astra representing MESA in ERL mode in the Internal Beamline at 42.19 m as currently under construction (Summer 2024).

MESA-ER-IB-42m-high-emittance

Astra Parameter	Abbreviation	Value
Reference Electron Beam Energy	$E_{el,ref}$	105 MeV
Bunch Charge	Q_{el}	7.7 pC
Longitudinal Bunch Size	σ_z	640 µm
Transversal Bunch Size x	σ_x	169 µm
Transversal Bunch Size y	σ_y	73 µm
Energy Spread	σE_{kin}	10.5 eV
Normalized Transversal Emittance x	ϵ_x	1
Normalized Transversal Emittance y	ϵ_y	1
Simulation Distribution	Dist x/y/z	'gauss'
Simulation Macro Particles	IPart	200k
Simulation Macro Factor	$\mathfrak{M}_e$	240

Table A.3.: Performance parameters used to generate an electron distribution in Astra representing MESA in ERL mode in the Internal Beamline at 42.19 m, theoretical high emittance version for collimation studies.

MESA-ER-IB-42m 1nC

Astra Parameter	Abbreviation	Value
Reference Electron Beam Energy	$E_{el,ref}$	105 MeV
Bunch Charge	Q_b	1 nC
Longitudinal Bunch Size	σ_z	640 µm
Transversal Bunch Size x	σ_x	169 µm
Transversal Bunch Size y	σ_y	73 µm
Energy Spread	σE_{kin}	10.5 eV
Normalized Transversal Emittance x	ϵ_x	0.3
Normalized Transversal Emittance y	ϵ_y	0.3
Simulation Distribution	Dist x/y/z	'gauss'
Simulation Macro Particles	IPart	200k
Simulation Macro Factor	$\mathfrak{M}_e$	240

Table A.4.: Performance parameters used to generate an electron distribution in Astra representing MESA in ERL mode in the Internal Beamline at 42.19 m, theoretical high bunch charge version for flux limit studies.

MESA-EB-50m

Astra Parameter	Abbreviation	Value
Reference Electron Beam Energy	$E_{el,ref}$	155 MeV
Bunch Charge	Q_b	0.77 pC
Longitudinal Bunch Size	σ_z	640 µm
Transversal Bunch Size x	σ_x	116 µm
Transversal Bunch Size y	σ_y	86 µm
Energy Spread	σE_{kin}	15.5 eV
Normalized Transversal Emittance x	ϵ_x	0.3
Normalized Transversal Emittance y	ϵ_y	0.3
Simulation Distribution	Dist x/y/z	'gauss'
Simulation Macro Particles	IPart	100k
Simulation Macro Factor	$\mathfrak{M}_e$	48

Table A.5.: Performance parameters used to generate an electron distribution in Astra representing MESA in External Beam mode in the External Beamline at ≈50 m as currently under construction (Summer 2024).

MESA-T5-16m

Astra Parameter	Abbreviation	Value
Reference Electron Beam Energy	$E_{el,ref}$	130 MeV
Bunch Charge	Q_b	0.77 pC
Longitudinal Bunch Size	σ_z	640 µm
Transversal Bunch Size x	σ_x	564 µm
Transversal Bunch Size y	σ_y	93 µm
Energy Spread	σE_{kin}	13 eV
Normalized Transversal Emittance x	ϵ_x	0.3
Normalized Transversal Emittance y	ϵ_y	0.3
Simulation Distribution	Dist x/y/z	'gauss'
Simulation Macro Particles	IPart	100k
Simulation Macro Factor	$\mathfrak{M}_e$	48

Table A.6.: Performance parameters used to generate an electron distribution in Astra representing MESA in External Beam mode in the Turn 5 recirculation arc at ≈16 m as currently under construction (Summer 2024).

A.3. Lasers and Photon Sources for ICS

A.3.1. Yb:YAG Lasers

Name	$\sigma\lambda_\nu$ [nm]	E_{pulse} [µJ]	$r_{f,\nu}$ [Hz]	$\overline{P}$ [W]	$\sigma_{x/y}$ [mm]	m^2
Tangor 100 IR	< 3	500	$200 \cdot 10^3$	100	3.35	< 1.3

Table A.7.: Overview of commercially available λ_ν =1030 nm Yb:YAG lasers.

Tangor-100-IR-focused

Initial Photon Beam Parameters			
1030.0	=	1.03E+03	wavelength [nm]
1.2037300818757308	=	1.20E+00	particle energy [eV]
0.001	=	1.00E-03	relative bandwidth
1.0300000000000002	=	1.03E+00	bandwidth [nm]
1e-11	=	1.00E-11	pulselength [s]
5e-05	=	5.00E-05	focal beam waist radius [m]
0.0005	=	5.00E-04	pulse energy [J]
200000.0	=	2.00E+05	repetition rate [Hz]
1.3	=	1.30E+00	m^2

Table A.8.: Tangor 100 with applied focus optics preset used for Simulations in Comparse.

Tangor-100-IR-SMILE-focused

Initial Photon Beam Parameters			
1030.0	=	1.03E+03	wavelength [nm]
1.2037300818757308	=	1.20E+00	particle energy [eV]
0.0010000000000000002	=	1.00E-03	relative bandwidth
1.0300000000000005	=	1.03E+00	bandwidth [nm]
1e-11	=	1.00E-11	pulselength [s]
5e-05	=	5.00E-05	focal beam waist radius [m]
0.004	=	4.00E-03	pulse energy [J]
200000.0	=	2.00E+05	repetition rate [Hz]
1.3	=	1.30E+00	m^2

Table A.9.: Tangor 100 with 8-fold SMILE laser pulse amplification and applied focus optics preset used for Simulations in Comparse.

A.3.2. Excimer Lithography Lasers

Name	ΔE [%]	max	E_{pulse} [mJ]	r [Hz]	max	$\overline{P}$ [W]	$\sigma_{x/y}$ [mm]	m^2
Atlex-1000-L	< 2	10	-	1000	8	-	6x4	31
EX50IN	< 2	35	-	750	-	15	9x4	40
EX10IN	< 1	20	5-20	1000	-	10	8x3-4	35
GT80A	-	-	10	6750	90	60	-	-
IndyStar	< 2	8	4	2000	-	8	5.5x2.3	26
Leap 60	≤ 2	400	350	150	60	-	32x13	262
IPEX-848	< 1	230	150	200	-	30	12x26	155
MLI-1000L	2	-	6	1000	-	6	6x3	27
OptoSystems	< 2	20	-	4000	80	-	14x2.5	76

Table A.10.: Overview of commercially available $\lambda_\nu = 193\,\text{nm}$ excimer lasers.

EX10IN-Excimer-focused

Initial Photon Beam Parameters			
193.00000000000003	=	1.93E+02	wavelength [nm]
6.424051732290169	=	6.42E+00	particle energy [eV]
0.001	=	1.00E-03	relative bandwidth
0.193	=	1.93E-01	bandwidth [nm]
1.5e-08	=	1.50E-08	pulselength [s]
5e-05	=	5.00E-05	focal beam waist radius [m]
0.02	=	2.00E-02	pulse energy [J]
1000.0	=	1.00E+03	repetition rate [Hz]
35.0	=	3.50E+01	m^2

Table A.11.: EX10IN excimer laser with applied focus optics preset used for Simulations in Comparse.

EX10IN-Excimer-focused-SMILE

Initial Photon Beam Parameters			
193.00000000000009	=	1.93E+02	wavelength [nm]
6.424051732290168	=	6.42E+00	particle energy [eV]
0.0009999999999999996	=	1.00E-03	relative bandwidth
0.193	=	1.93E-01	bandwidth [nm]
1.5e-08	=	1.50E-08	pulselength [s]
5e-05	=	5.00E-05	focal beam waist radius [m]
0.16	=	1.60E-01	pulse energy [J]
1000.0	=	1.00E+03	repetition rate [Hz]
35.0	=	3.50E+01	m^2

Table A.12.: EX10IN excimer laser with applied focus optics preset used for Simulations in Comparse.

A.3.3. Hypothetical Photon Sources for Visualization Purposes

hypthetical-10nm-photon

Initial Photon Beam Parameters			
0.01	=	1.24E+06	wavelength [nm]
123984.19843320028	=	1.24E+05	particle energy [eV]
0.001	=	1.00E-03	relative bandwidth
1e-05	=	1.00E-05	bandwidth [nm]
1e-11	=	1.00E-11	pulselength [s]
5e-05	=	5.00E-05	focal beam waist radius [m]
0.0005	=	5.00E-04	pulse energy [J]
200000.0	=	2.00E+05	repetition rate [Hz]
1.3	=	1.30E+00	m^2

Table A.13.: Hypothetical 10nm photon preset used for spin - circular polarization coupling visualization purposes.

A.4. Comparse User Manual

In this section, a logical step by step path through a standard Comparse usage scenario will be outlined. Each step is presented in necessary order of execution. Note, that detailed background informations to each step are found in the following sections of this chapter, following the same order.

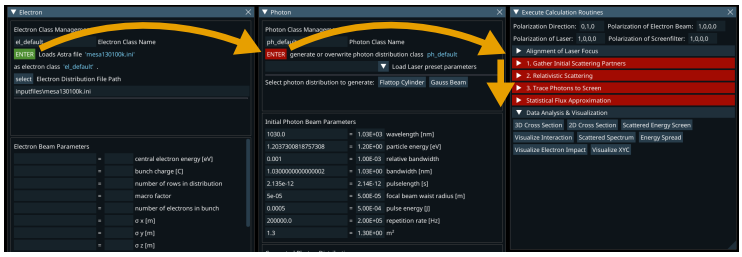

Figure A.1.: General logic direction in the user interface of Comparse. First an electron class and distribution needs to be created, then a matching photon one until finally, the user can perform the 3-step ICS simulation routine.

A.4.1. Import or Generation of an Electron Distribution

When starting Comparse, the "Enter" button found in the "Electron" window on the left side of the Comparse viewport is highlighted in green, while the "Photon" window "Enter" button and several "Execute Calculation Routines" collapsible headers are highlighted in red. Comparse works by matching a photon to an electron position. Hence, as a first step, an electron distribution is required.

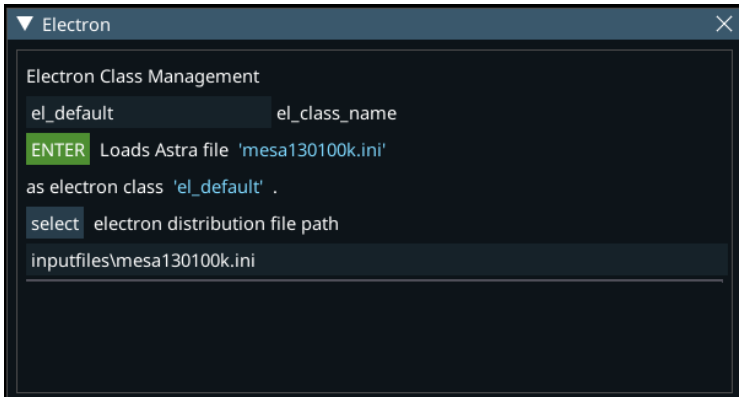

Figure A.2.: Highlighted "Electron" "Enter" button on Comparse start.

Figure A.3.: Electron distribution generation dialog "Electron Generator".

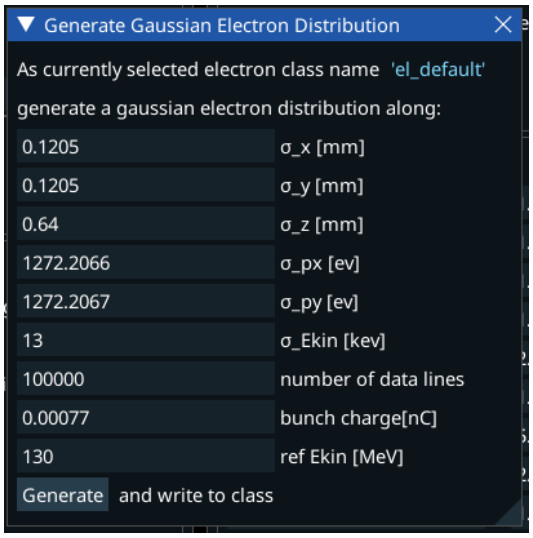

This can be either imported from an Astra format electron distribution file ending in .ini (subsec.4.2.1), generated via Comparse module "Electron Generator" found under the "Electron Gen" register (subsec.4.2.2) or by loading a previously created Comparse class per Comparse's "Load" dialog. When loading an .ini input file by pressing the "Electron" "Enter" button, Comparse will attempt to fill all "Electron" window fields with the data derived and calculated from the Astra format input file specified in the "Electron Distribution File Path" while at the same time writing the parameters and values into a Comparse electron class named by the text written in the input text field labelled "Electron Class Name". If an electron class already exists under that name, it will be overwritten. If not, a new button will be created and labelled with the electron class name. When pressed, this button will reload the class and fill all fields in the "Electron" window with the according electron class values. This way, one can work with several electron distributions in a single session and quickly switch between them. Once an electron class has been created, the "Photon" window "Enter" button changes color from red to green. This indicates, that a photon class can be created for the selected electron class. Values listed in the "Electron Beam Parameters" table are calculated from the selected electron distribution and cannot be changed afterwards.

A.4.2. Creation of a Matching Photon Class

Upon pressing the "Photon" "Enter" button, a new photon class will be created under the name entered in the "Photon Class Name" input field. A button connected to the newly created class will appear similarly to the electron class buttons. Now, the user can select one of currently two photon distribution models: "Flattop Cylinder" and "Gauss Beam". Photon classes work in inverse to electron classes in Comparse. Before creating a new photon class, the "Initial Photon Beam Parameters" text fields are already filled out, as photon beam parameters are not calculated from a pre-existing photon distribution, but instead are the necessary basis for the creation of one. According to the initial photon beam parameters and selected photon distribution type, photon four vectors prior to collision and a photon density value are calculated for every electron distribution position data entry. See section 4.3 for further details on how photon distribution data is created and used in the Comparse backend.
Users can change the initial photon beam parameters at will or load values from a number of presets selectable from the "Load Laser Preset Parameters" combo menu located below the "Photon" "Enter" button. Once any initial photon parameter value is changed, users need to press the now yellow highlighted "Photon" "Enter" button again to confirm the changes as a new class, when also changing the "Photon Class Name" input field, or overriding the old class when leaving said field the same. Afterwards, once again a photon distribution model needs to be chosen and generated.

Once a complete combination of pre-scattering electron and photon data exists,

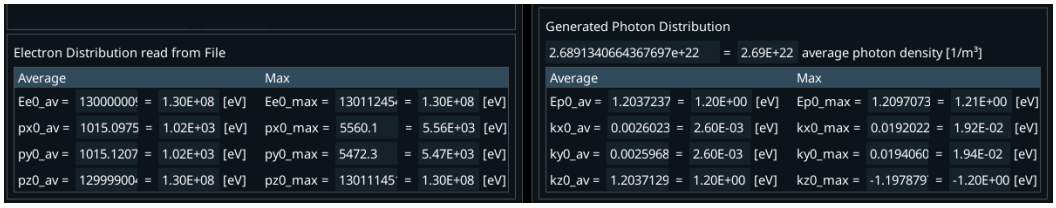

Figure A.4.: Parameter fields of electron and photon distribution pre-scattering event. Values in these fields indicate the existence of four-vector and photon density data required for the calculation of the Compton scattering probability with recoil, the first step of the three step ICS simulation.

users can proceed to to the three step ICS simulation. This is the case, when the "Electron Distribution read from File" and "Generated Photon Distribution" sub-window fields are all filled in (fig.A.4).

A.4.3. Optional: Defining Simulation Geometry and Polarization

Before proceeding with the first step of the ICS simulation, users can define the initial polarization of electron beam, Laser and of a polarization filter in front of the photo detector screen as well as the the alignment of the Laser in regards to

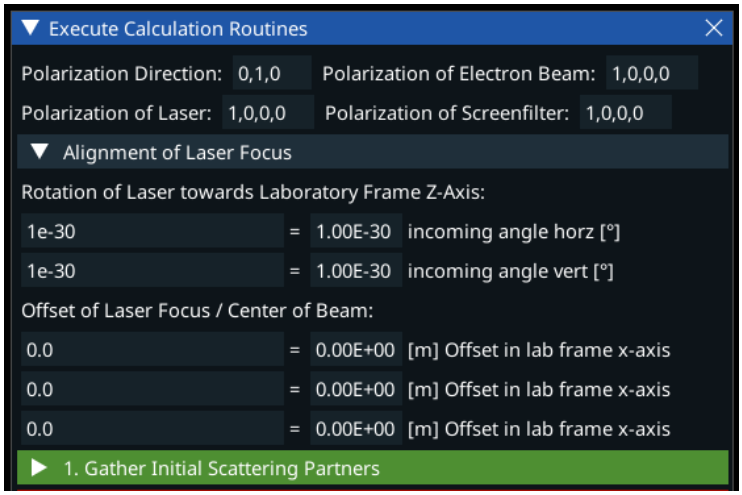

Figure A.5.: Optional inclusion of polarization effects, collision angles and offset are entered into the first input fields found in the "Execute Calculation Routines" window of Comparse, above step "1. Gather Initial Scattering Partners". Polarization information is written in Stokes four-vectors normalized to intensity "1".

scattering angle and 3D offset (fig.A.5. By default, the input fields are set to a head-on collision on-axis without polarization effects. Despite being located outside of the "Photon" window, some of these inputs are parameters required to generate a photon distribution and as such changing them requires users to reset the photon class. Users are notified of this with the same yellow highlight on the "Photon" "Enter" button that appears when changing "Initial Photon Parameter" fields. See sec.3.2.2 for a detailed explanation of the Stokes four-vector formalism in which the polarization information is written. With both electron and photon distribution in place, users can proceed with the main 3-step ICS simulation routine or utilize Comparse's "Statistical Flux Approximation" module to determine the number of scattering photons that can be expected.

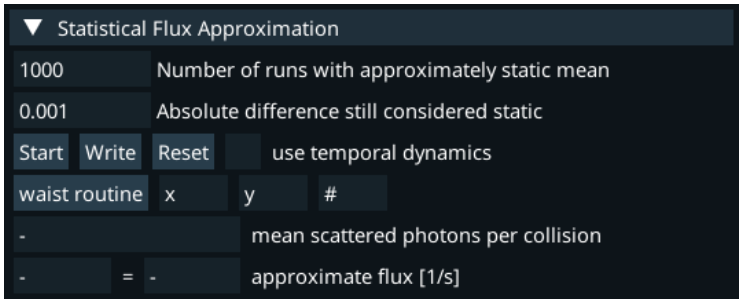

Figure A.6.: Comparse menu section for the estimation of the statistical flux and average number of scatter photons per collision.

A.4.4. Gathering of Initial Scattering Partners

For the purposes of flexibility, the Comparse ICS calculation routine is split up in three parts, starting with the gathering of the initial scattering data. In this step, the stochastic selection of scattering electrons formula presented in section 4.5.1 that implements cross section equation 3.74 is implemented. When executed once, a collision of one electron bunch and one laser pulse is simulated for the purpose of determining which electrons lead to a scattering event. A list of array indices is returned, that points to the specific positions and respective momenta. This reduces the likely large data set of initial electrons and photons to a fraction of it's original size.

When opening the collapsible header menu item named "1. Gather Initial Scattering Partners", the user is presented a number of choices and settings (fig.A.7):

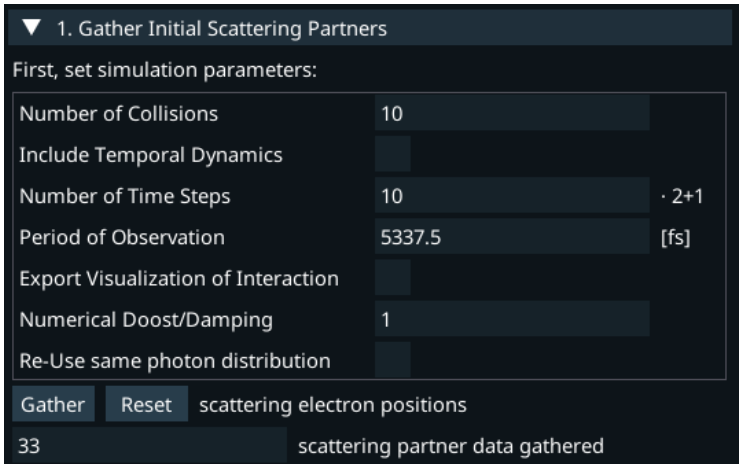

Figure A.7.: Comparse menu section for the scattering partner gathering step of the ICS calculation routine.

- **"Number of Collisions"** input field
  - sets how many collision calculations are performed in a row after the user presses "Gather"
- **"Include Temporal Dynamics"** checkbox
  - activates time step based collision simulation
  - for further details, see sec.4.5.4
- **"Number of Time Steps"** input field
  - defines the number of time steps used when time step based simulation is activated
  - the value entered in the text field sets the number of time steps generated before and after time step $t = 0$

- **"Period of observation"** input field
  - sets the overall time period to be divided into time steps in fs
- **"Export Visualization of Interaction"** checkbox
  - exports a .png image file per time step to the local "outputfiles/tseries" folder found in the same directory as comparse_main
  - the image files are named "t_series_x.png" with "x" automatically being replaced with a consecutive number starting with 1
  - images show the spatial electron distribution in y and z dimension as a Matplotlib scatter plot with photon density as the color dimension and highlighted electron scattering positions, if any exist
- **"Numerical Boost/Damping"** input field
  - defines the numerical boost or damping factor included in the scattering probability simulation
  - default value "1" means that the average scattering electrons per collision calculation should approximate a realistic scenario
  - values in the range $0 < x < 1$ lower the expected scattering positions per collision, while values $x > 1$ increase the probability
  - the change to the scattering probability in the simulation is removed from statistical values calculated via Comparse such as flux or average scattering events per collision
- **"Re-Use Same Photon Distribution"** checkbox
  - if left unchecked, Comparse generates a new photon distribution per collision, including a randomization of the incoming photon direction, wavelength and wave number according to set initial photon beam parameters when using "Gauss Beam" photon distribution model
  - when activated, generates the photon four-vector distribution just once, slightly speeding up the scattering partner gathering process

With each press of the "Gather" button, the simulation is repeated, adding more scattering positions and photon four-vectors to the internal data arrays. The number of collected collision partners is displayed in the input field labeled "Scattering Partner Data Gathered". When pressing the "Reset" button or when generating a new photon or electron class, the collected data gets deleted. To proceed to the next step, the relativistic scattering of electron and photon, the user is required to have collected a nonzero amount of electron - photon pairs, meaning their momentum and polarization four-vectors.

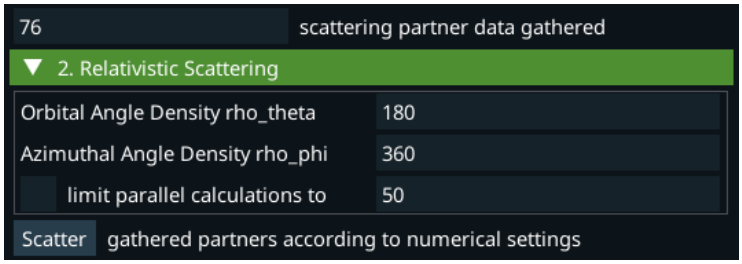

Figure A.8.: Comparse menu section for the relativistic scattering step of the ICS calculation routine.

A.4.5. Relativistic Scattering of Gathered Electrons and Photons

With all requisite photon and electron data gathered, the user can initiate Comparse's core function: The relativistic angle, recoil and polarization dependent Inverse Compton Scattering of photons and electrons. This step is configured and initiated in the collapsible header labelled "2. Relativistic Scattering" that should be highlighted green upon completion of the previous step, sec.A.4.4. When unfolding the header, three options and a "Scatter" button can be seen. Regarding the settings, there is:

- **"Orbital Angle Density $\rho\_\theta[1/\pi]$"** input field
- **"Azimuthal Angle Density $\rho\_\phi[1/2\pi]$"** input field
- **"limit parallel calculations to"** checkbox & input field

When pressing the "Scatter" button, Comparse calculates the direction of scattering for all electron - photon pairs. It does so, by creating a grid over a number of orbital angles θ and azimuthal angles ϕ, then calculating a likelihood value for each direction combination and finally deciding on a single angle combination per scattering event via likelihood weighted random selection. This means, that the number of angle data points, the angle density mentioned in the menu, decides how detailed the resulting scattering image can be. Low angle densities lead to a coarse sampling of the in reality continuous value spectrum, while high angle densities significantly increase the computation load.
To illustrate this relation, let's assume that the user gathered 500 photon and electron partners in the previous step. If angle density $\rho_\theta = 360$ and $\rho_\phi = 720$, a grid of 0.5° sized angles, then Comparse performs it's most complicated series of calculations $360 \cdot 720 \cdot 500 \approx 130$ million times at once. On computers with relatively small working memory, this conservative example can be too taxing on the system. For this reason, users can either limit the angular precision in orbital or azimuthal inclination by lowering their respective density ρ_θ and ρ_ϕ or check "limit parallel

calculations to x". If the latter is activated, Comparse will divide the gathered scattering partner data into arrays of the size entered in the input field and perform the scattering direction decision calculation for each subset in a loop. The last set is smaller than selected, if the total data size is not a multitude of the parallelisation limit. The progress of this looped execution is shown in the input field that previously held the parallel calculation limit entered by the user. It is written in the format of "Finished x collisions i/G", where x is the selected parallelisation limit, i is the current subset being calculated and G is the amount of all subsets of the initially gathered data.
After a scattering direction has been chosen and the relativistic scattering event calculated for each electron - photon pair, the "Electron -" and "Photon Distribution after Collision" data fields in the electron and photon window will be filled with the calculated data. We now gained complete information about the state of the scattering particles immediately after collision: Their polarization and four-vector after scattering. In a real experiment, the exact moment in space and time immediately after collision cannot be observed without disrupting the experiment. For this reason, the scattered photons or gamma radiation is measured by a detector placed outside of the electron beam path. To match the simulation with measurements, the user needs to trace the scattered photons through space, which is the third and final step of the 3-step ICS simulation in Comparse.

A.4.6. Tracing of Photon to a Screen

In this final step of the 3-step ICS simulation routine, only the scattering positions $(x_{e,sc}, y_{e,sc}, z_{e,sc})$ and photon post-scattering four momenta $\vec{k}_{4,ph,sc,lab}$. From the latter, we can derive the 3D unit vector $\hat{k}_{ph,sc,lab}$ and use it in combination with the scattering position to trace the path of the outgoing photon. Path-Tracing mathematics are used in the background to determine the photon position on an arbitrarily positioned screen and whether or not a specific particle is collimated. In the collapsible UI section for the tracing of photons, the users is presented with a number of experiment set-up, data field and a button labelled "Trace". At the top, a cylindrical collimator can be activated and defined in 3D space alongside the photon detector screen with the menu items seen in fig.A.9 and listed below:

- **"Insert Collimator [...]"** checkbox activating or deactivating collimation
- **"c1= *x,y,z* [m,m,m]"** input field requiring 3 coordinates (x,y,z)
- **"c2= *x,y,z* [m,m,m]"** input field requiring 3 coordinates (x,y,z)
- **"r= *r* [m]"** input field requiring 1 radius value
- **"[*x,y,z*] [m,m,m] Screen Center Position P_screen"** input field requiring 3 coordinates (x,y,z)
- **"[*x,y,z*] [m,m,m] Screen Normal n_screen"** input field requiring 3 coordinates (x,y,z)

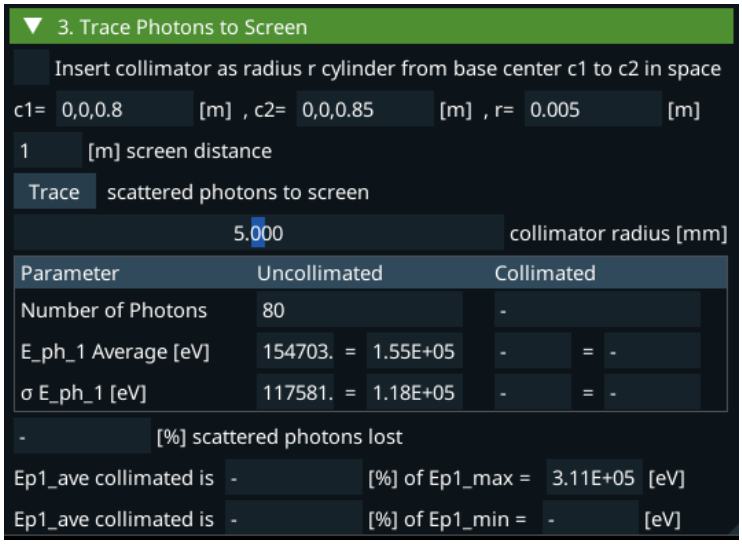

Figure A.9.: Comparse menu section for Comparse's path tracing of scattered photons function.

A cylinder can be unequivocally defined by two face center points and a radius. The line l between center points c_1 and c_2 represents the cylinder axis and can be calculated for arbitrary coordinates via vector algebra: The absolute of the vector $\vec{v}_{cyl}$ pointing from c_1 to c_2 is the cylinder length $|\vec{v}_{cyl}| = l$, it's direction the cylinder orientation, the coordinate value of c_1 and c_2 define the cylinder's position in space in relation to the origin. A cylinder's description is complete with radius value r. The cylinder defined in that manner represents an empty space that photons can pass through. Photons found outside of the cylinder's radius r in the space between the two center points c_1 and c_2 are considered collimated. See section 4.7.3 for more details on the definition of a cylinder and the tracing of photons through it.
The photon detector screen's position and orientation in space is defined in a similar manner to the collimator cylinder's face, with a screen center position P_{screen} and a normal vector target point n_{screen} that defines the orientation. It is not used as a second plane center point. That way, the simple case of a cylinder being positioned in 1 m distance electron downstream of the scattering center point, laboratory frame coordinate $P_0 = (0, 0, 0)$ [m,m,m] and positioned head-on to the electron momentum would be defined by $P_{screen} = [0, 0, 1]$ and $n_{screen} = [0, 0, u]$, whereas u can be any value $u > 1$, for instance "2": $P_{screen} = [0, 0, 1]$ & $n_{screen} = [0, 0, 2]$, the default values of Comparse. Once data is entered and activated, the "Trace" button starts the Comparse routine for the tracing of photons. This creates new data arrays containing the scattered photon position on the screen plane, the vectors to the screen, the number of collimated photons and two new data index arrays internally named `posz_index` and `coll_index`:

- `posz_index` array of integers

  - points to the scattered photons that move towards the screen
  - the name is derived from "positive z", although it works for a screen positioned in any direction, even in negative longitudinal z

- `coll_index` array of integers
  - points to the scattered photons that move towards the screen and trace through the defined collimator without collision
  - if any collimation occurs, this index array will be shorter than `posz_index`

Both can be applied to all scattered photon related arrays in data analysis purposes. Some of the traced uncollimated and collimated gamma parameters are displayed in the data output fields in the lower half of the Trace Photon to Screen menu section.
The trace method that is executed upon pressing of the "Trace" button is also executed every time the "Collimator Radius" labelled slider UI element found below is moved, with all data output fields being refreshed. On well performing hardware, this allows for instant user optimization of the collimator radius according according to personal collimation targets. However, for large scattered photon data sets and on slow hardware, this potentially high frequency of trace method execution orders might be too taxing on the system and complete with delays.
Below the slider in the "Trace Photons to Screen" UI section fig.A.9, only non interactive data output fields exist. First, a table listing the "Number of Photons", the average scattered photon energy in eV $\overline{E}_{ph,sc}$ ("E_ph_1 Average") and the standard deviation of the scattered photon Energy $\sigma E_{ph,sc}$ in eV ("σE_ph_1") for both cases with and without collimation traced to the photon detector screen is presented. Below the percentage of scattered photons lost due to collimation is displayed. Lastly, there are two lines with each two output fields:

- **"Ep1_ave collimated is** [*output field 1*] **[%] of Ep1_max = [*output field 2*] [eV]"**
  - *output field 1* contains the relative value of the average Energy of the scattered and collimated photons $\overline{E}_{ph,sc,coll}$ in relation to the maximum scattered and uncollimated photon Energy $E_{ph,sc,max}$ displayed in *output field 2*
  - *output field 1* = $\overline{E}_{ph,sc,coll}/E_{ph,sc,max}$ [%]
  - *output field 2* = $E_{ph,sc,max}$ [eV]

- **"Ep1_ave collimated is** [*output field 3*] **[%] of Ep1_min = [*output field 4*] [eV]"**
  - *output field 1* contains the relative value of the average Energy of the scattered and collimated photons $\overline{E}_{ph,sc,coll}$ in relation to the minimum scattered and collimated photon Energy $E_{ph,sc,col,min}$ displayed in *output field 2*

  - *output field 1* = $\overline{E}_{ph,sc,coll}/E_{ph,sc,min}$ [%]
  - *output field 2* = $E_{ph,sc,min}$ [eV]

As the energy spectrum of ICS generated gamma radiation is characteristic for it's sharp drop at the Compton Peak with ideally energies only found below the highest intensity point (see fig. 5.18 for an example of this), the application and interpretation of standard distribution variance is problematic. For this reason, Comparse displays how close the average collimated gamma energy $\overline{E}_{ph,sc,coll}$ is to the highest possible value in the total set of scattered photons and how close $\overline{E}_{ph,sc,coll}$ is to the lowest photon energy still detected on the screen after collimation $E_{ph,sc,col,min}$. These three energy data points can be interpreted by the user as a measure of bandwidth quality in the scattered radiation.

A.5. Comparse Files

- **compton_main**.py,
  - contains most of the UI methods
  - opens the UI when run
  - a brief overview is given in sec. 4.1.1
  - a detailed user manual is given in sec. A.4
- **logger**.py,
  - functions and UI for Comparse logger
  - logs start and completion of major user initiated tasks such as calculations or save and load operations
- **theme_class**.py,
  - contains functions related to the UI themes in Comparse
- **fermion_class**.py,
  - creates and processes the fermion bunch properties within a `Fermion` class instance
  - several instances of this class can be created and used during runtime
- **laser_class**.py,
  - creates and processes the laser beam properties within a `Laserbeam` class instance
  - several instances of this class can be created and used during runtime
- **neutral_class**.py,
  - `Neutral` class management functions

  - for UI variables unrelated to photons and fermions

- **constants**.py,
  - look up file from which physical constants used in all files are imported from to ensure changes to units or physical constant values apply everywhere at once
  - defines default values of UI input fields. Users can enter their own unique most common simulation starting values to save time on repeated simulations
  - could be modified, if necessary

- **figsfile**.py,
  - contains all graphical data analysis functions
  - based predominantly on "Matplotlib" Python library [28]

- **outputs**.py,
  - functions related to data export
  - enables writing class variables to files of different formats: simple CSV, Astra format TSV and custom Comparse formats.

- **unpol**.py,
  - functions for the application of physical calculations with no relation to polarization effects
  - mostly single step equations that are part of the mathematical "toolbox"

- **polvec**.py,
  - functions for the application of polarization vector based physical equations
  - mostly single step equations that are part of the mathematical "toolbox"

- **time_calc**.py,
  - functions related to time dependent calculations
  - mostly single step equations that are part of the mathematical "toolbox"

- **unit_vector_angles**.py,
  - contains collected functions for the application of vector and angle related algebra
  - mostly single step equations that are part of the mathematical "toolbox"

- **routines**.py,
  - contains functions for complicated multi step calculation routines of all kinds

  - encodes the mathematical principles described in chapter 3

- **theme_class**.py,
  - contains functions related to the UI themes in Comparse

- **xyc_support**.py,
  - contains additional methods for the logic behind the "display_xyc" module

A.6. Comparse Data Export

A.6.1. Class File

Class files can be used in the fermion and photon save and load functions as well as in the combined "Quick Save" and "Quick Load" modules. When pressing the "Quick Save" button found in the "Quick S/L" window header menu, the currently active fermion and photon class is exported to the "quick_save" folder found in the root location of Comparse using the python standard module "pickle" [66]. The file extensions are ".elc" for `Fermion` and ".phc" for the `Laserbeam`. While the `Neutral` modified during run time is also saved as a ".ntc" file, as of Comparse v0.8.5-Beta, there is no way to load it back into the program. Clicking the "Quick Load" button only loads the "last_el_class.elc" and "last_ph_class.phc" created previously via "Quick Save". Specific location and filenames can be selected when saving or loading a class file using the save and load fermion or photon functionality functionality described earlier.
Upon loading a class files using any of the two methods, the user interface will reset to the state of the Comparse program at the time of saving. This enables users to easily pause and come back to their work. As class files are interpreted in python code, loading corrupt or manipulated files poses a certain risk when allowing the Comparse executable or python version to read and write on your local hard drive. Users should only load class files of known and trustworthy origin.

A.6.2. Comma Separated Value File

When it comes to raw data export as a text file, Comparse's version of a comma separated value (csv) file is the most straight forward one available in Comparse. Users can chose to save a fermion or photon distribution as a csv file with the extension ".csv" in the "Save" menu. It displays the values of the parameters of a particle distribution in columns separated by commas. The first row of the file is the header row, all following rows each contain a particle's parameters.
These are, in the case of a fermion distribution: "`x-pos [m],y-pos [m],z-pos [m], macro factor [1/q_e],E`*"type" "i"* `[eV],p`*"i"*`_x [eV],p`*"i"*`_y [eV],p`*"i"*`_z [eV]`". Fermion csv files thus contain 3 columns for the macro particle's position in

the laboratory frame space, the macro factor, and finally the 4 columns containing the relativistic four momentum values. For Fermion distributions, either the unscattered, scattered or combined unscattered and scattered macro particles of the ICS collision simulation can be selected for export. In the four-momentum columns, index "i" is replaced with "0", in case of unscattered fermions, "1" for scattered and is removed when exporting combined scattered and unscattered fermion distributions. Additionally *"type"* is replaced with `el` and `pr` for electrons and protons respectively.
In a similar manner, the photon distribution .csv header row reads "`x-pos [m],y-pos [m],z-pos [m],rho [ph/m^3],Eph`*"i"* `[eV],k`*"i"*`_x [eV],k`*"i"*`_y [eV],k`*"i"*`_z [eV]`". Instead of the macro factor, photon distribution csv files contain a column filled with the photon density value experienced by the fermion macro particle found at the position given by the first 3 columns. The unit of the photon density is photons per $1\,\mathrm{m}^3$ space volume. In the case of photons, only either the scattered or unscattered distribution can be exported.

A.6.3. Astra Format File

In the "Save Fermion" menu, users can also choose to export scattered, unscattered and combined fermion distributions as Astra format files with the extension ".ini". These are structured and formatted exactly as "`High_res = True`" flagged Astra generated particle distributions. See section 4.2.1 for a discussion of the logic and mechanics underlining the creation of particle distributions in Astra. When choosing to export either the unscattered or combined unscattered and scattered particles of the currently active fermion distribution, the $p_{total}/p_{z,ref}$ value saved upon creation or import of the initial fermion distribution is used as the Astra reference row value. However, when only writing the scattered particles to file, the mean longitudinal momentum of the fermions after scattering p'_z is calculated and used for p_{total}. As of Comparse v1.0, there is no option to export photon distributions in Astra format.

A.6.4. Flux List & Table Files

When unfolding the "Statistical Flux Estimation" menu header found inside of the "Execute Calculation Routines" window, users find buttons labeled "Start", "Reset" and "Write". These refer to the statistical flux Estimation routine described in subsec. 4.5.2. Initiated by pressing "Start", once completed, Comparse will display the results in the UI. Internally, for each run, a set of data related to the simulation saved. This set contains the initial parameters and results of the calculation. Starting a new run will generate a new set. They are saved internally in the neutral class until the users clicks "Reset", which deletes all previously accumulated sets. Pressing "Write", creates two files in the "outputfiles" folder: One .txt file named "fluxseries_X_Y" and one .csv file file named "fluxtable_X_Y" whereas "X" is replaced by the fermion class name and "Y" is replaced by the

laser class name. In fluxseries files, the simulation data is written as a line of text legible by humans for each run, whereas fluxtable files are written in csv format to enable facilitate straightfoward access by data analysis tools such as Excel, Origin, Tikz or other tools of the user's choosing. The fluxtable header row contains the columns "`el_class, ph_class, distribution, laser_w_r_m, avg_ph_density_1/m^3,avg_coll_ph, rep_rate_1/s, flux_ph/s, runs, criterium, num_exposed_el, percent_exposed, sig_x, sig_y, sig_z`". An example of a line found in fluxseries files is "`ElectronC:'er42m10mA'+ PhC:'Tangor100' @'Gauss Beam'with beam waist = 5e-05[m] avg photon density = 3.053429613668997e+22[ph/m**3] -> avg coll.:0.5626780626780626[ph], @ rr = 200000.0 [1/s] -> F = 112535.61253561253 [ph/s] Accuracy:1000runs@ <= 0.001 with 36206 electrons exposed (36.205999999999996 percent) damping:1.0`". In both cases, one row represents one run of the flux Estimation routine. The automatic creation and internal bookkeeping of summary data sets helps when users initiate parameter scans, for example over laser focus spot size $\sigma_{ph,x/y}$, to optimize the gamma flux of ICS experiments. Fluxtables generated in Comparse are used as input files in the Tikz plots found in subsec. 5.1.1 and 5.1.2.

A.6.5. Spectrum CSV File

Motivated by feedback of colleagues, a "Save .csv" button has been added to Comparse's "Display Scattered Spectrum" data analysis module. When activated, a 2 columns and N_{bins} rows csv file named "spectrum_X_Y.csv" is exported to the local "outputfiles" folder. As usual, "X" and "Y" are replaced by the name of the currently active fermion and photon class. The two columns are "Gamma Energy [eV]" and "Gamma Intensity". As mentioned above, the exported file follows the binning settings defined in Comparse.

A.6.6. Matplotlib Plots in Comparse

Comparse features 9 visualization tools generating plots using the Matplotlib Python module [28]. All implementations except one work by opening a window running the interactive Matplotlib user interface. The sole exception is the visualization of the interaction between fermion distribution and the laser beam. While the "Visualize Interaction" Comparse function found in the "Data Analysis & and Visualization" menu allows users to open a Matplotlib UI as usual, the "Export Visualization of Interaction" checkbox found within the "Gather Initial Scattering Partners" forgoes this step and directly writes image files to the outputfiles folder. When also activating the "Include Temporal Dynamics" checkbox, one plot is saved as an image file of the "png" extension per timestep in the outputfiles subfolder "outputfiles/tseries" as part of a series.
Aside from this implementation, the default Matplotlib usage in Comparse is via a Matplotlib UI window that opens upon pressing of a Comparse button. Inside of this interactive window, users can adjust the plot size, ratio, whitespace and zoom

level. A "Save the figure" button symbolized by a floppy diskette allows users to save the plot in it's current state as an image file. Of the filetypes available in Matplotlib, the standalone executable version of Comparse v1.0 supports: ".eps", ".jpg", ".pdf", ".png", ".ps", ".raw", ".svg", ".tif", ".webp".
All figures created using Matplotlib in this thesis were generated in Comparse using methods accessible through the Comparse user interface without custom modification.

A.7. Collected Polarized Inverse Compton Scattering Examples

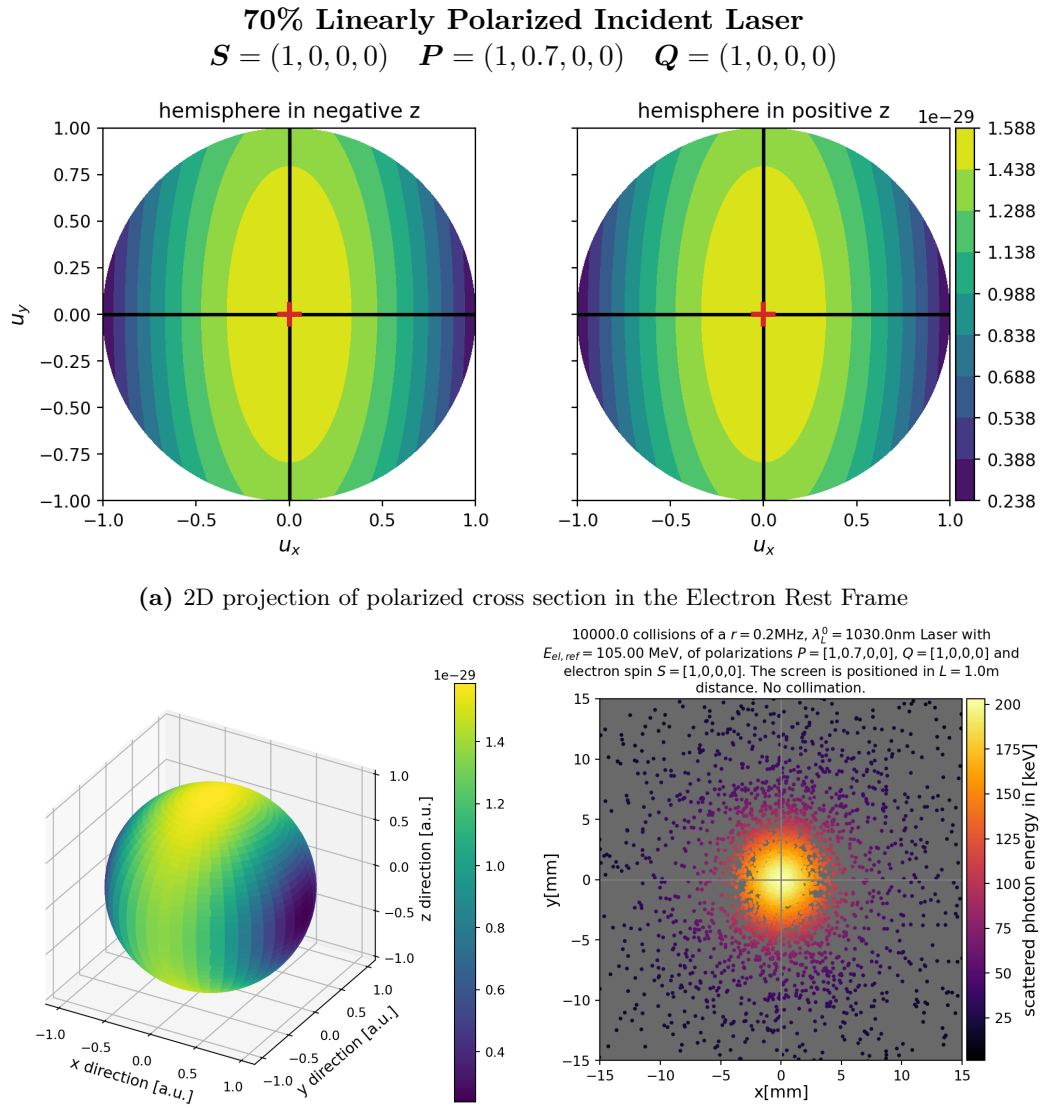

(a) 2D projection of polarized cross section in the Electron Rest Frame

(b) 3D polarized ICS cross section (ERF)

(c) ICS photons projected on a screen (LAB)

Figure A.10.: Spatial characteristics of ICS emitted photons under the inclusion of polarization effects. Directional scattering probability W in the ERF and emitted photons of ICS between unpolarized electrons and $\boldsymbol{P} = (1, 0.7, 0, 0)$ polarized incident photons detected by a $\boldsymbol{Q} = (1, 0, 0, 0)$ polarization filter. Calculated for a frontal collision $\theta_{inc} = 180°$. Plots simulated and generated in Comparse using a MESA-ER-IB-42m-nominal (App. tab. A.2) Astra generated electron distribution and Tangor-100-IR-focused (App. tab. A.8) presets. For this plot, W was calculated for $\rho_\theta = 361$ & $\rho_\phi = 720$ scattering angles by way of averaging over $N'_{par} = 5891$ scattering particle pairs chosen by weighted probability $W_{ics,norm}$.

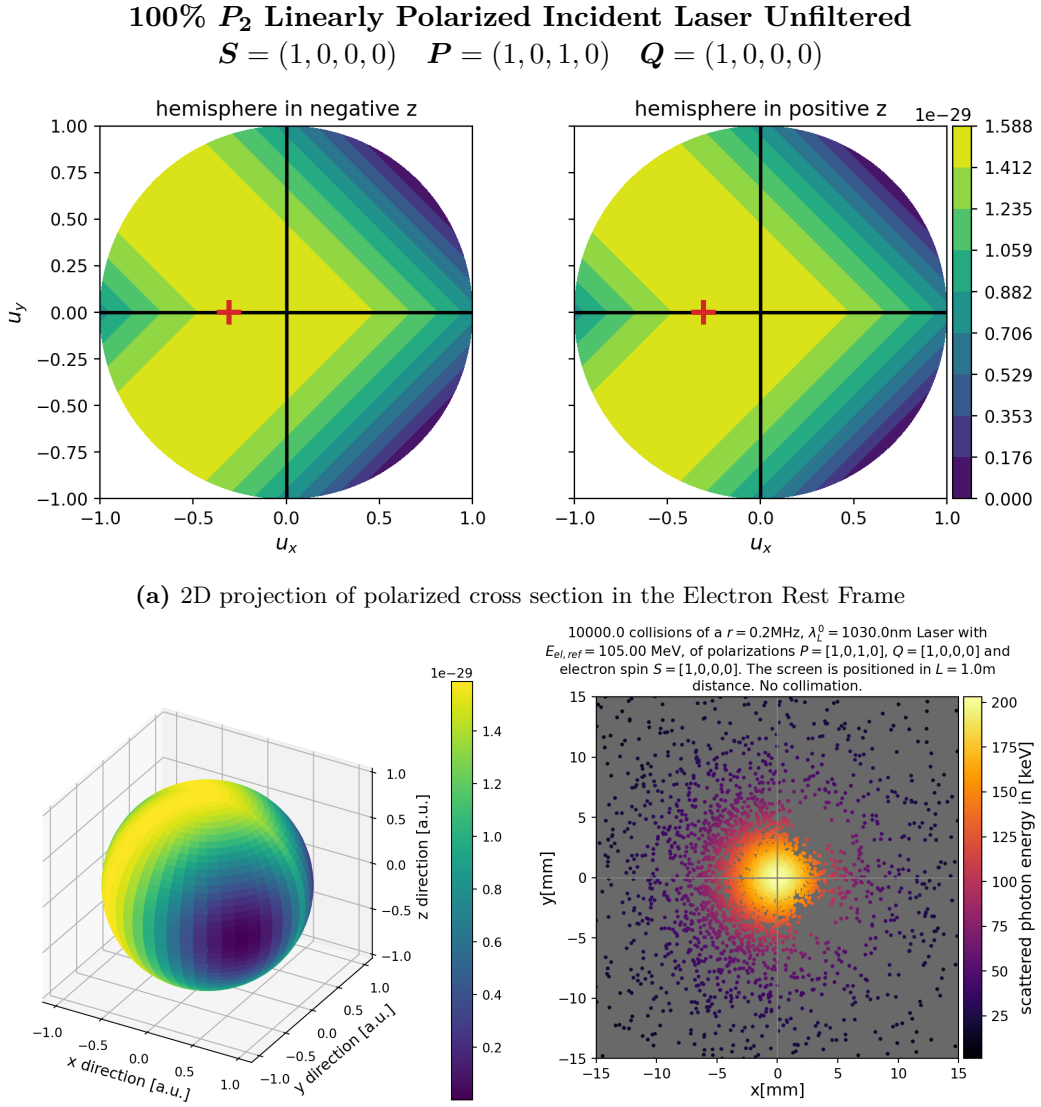

(a) 2D projection of polarized cross section in the Electron Rest Frame

(b) 3D polarized ICS cross section (ERF)

(c) ICS photons projected on a screen (LAB)

Figure A.11.: Spatial characteristics of ICS emitted photons under the inclusion of polarization effects. Directional scattering probability W in the ERF and emitted photons of ICS between unpolarized electrons and $\boldsymbol{P} = (1,0,1,0)$ polarized incident photons detected by a $\boldsymbol{Q} = (1,0,0,0)$ polarization filter. Calculated for a frontal collision $\theta_{inc} = 180°$. Plots simulated and generated in Comparse using a MESA-ER-IB-42m-nominal (App. tab. A.2) Astra generated electron distribution and Tangor-100-IR-focused (App. tab. A.8) presets. For this plot, W was calculated for $\rho_\theta = 361$ & $\rho_\phi = 720$ scattering angles by way of averaging over $N'_{par} = 5891$ scattering particle pairs chosen by weighted probability $W_{ics,norm}$.

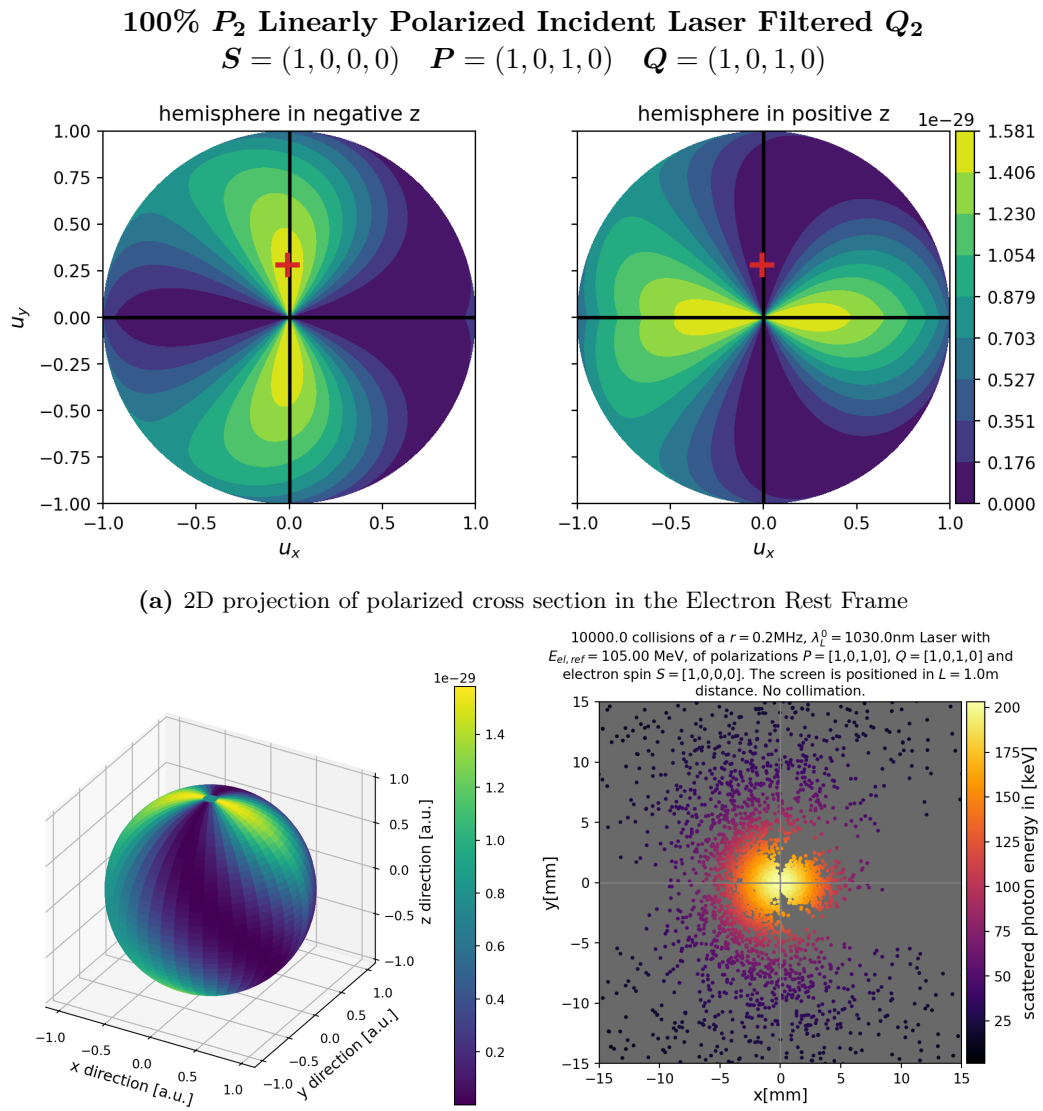

(a) 2D projection of polarized cross section in the Electron Rest Frame

(b) 3D polarized ICS cross section (ERF)

(c) ICS photons projected on a screen (LAB)

Figure A.12.: Spatial characteristics of ICS emitted photons under the inclusion of polarization effects. Directional scattering probability W in the ERF and emitted photons of ICS between unpolarized electrons and $\boldsymbol{P} = (1,0,1,0)$ polarized incident photons detected by a $\boldsymbol{Q} = (1,0,1,0)$ polarization filter. Calculated for a frontal collision $\theta_{inc} = 180°$. Plots simulated and generated in Comparse using a MESA-ER-IB-42m-nominal (App. tab. A.2) Astra generated electron distribution and Tangor-100-IR-focused (App. tab. A.8) presets. For this plot, W was calculated for $\rho_\theta = 361$ & $\rho_\phi = 720$ scattering angles by way of averaging over $N'_{par} = 5891$ scattering particle pairs chosen by weighted probability $W_{ics,norm}$.

100% P_2 Linearly Polarized Incident Laser Inversely Filtered Q_2

$\boldsymbol{S} = (1, 0, 0, 0) \quad \boldsymbol{P} = (1, 0, 1, 0) \quad \boldsymbol{Q} = (1, 0, -1, 0)$

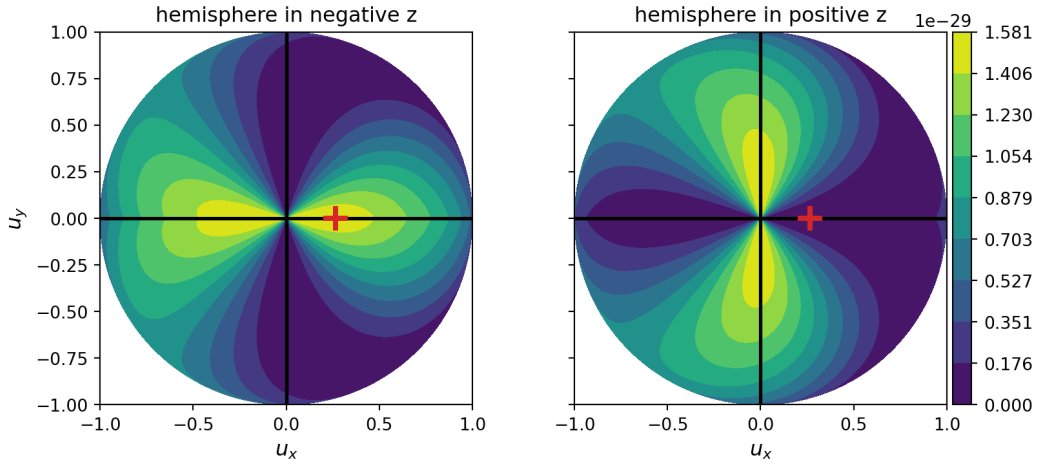

(a) 2D projection of polarized cross section in the Electron Rest Frame

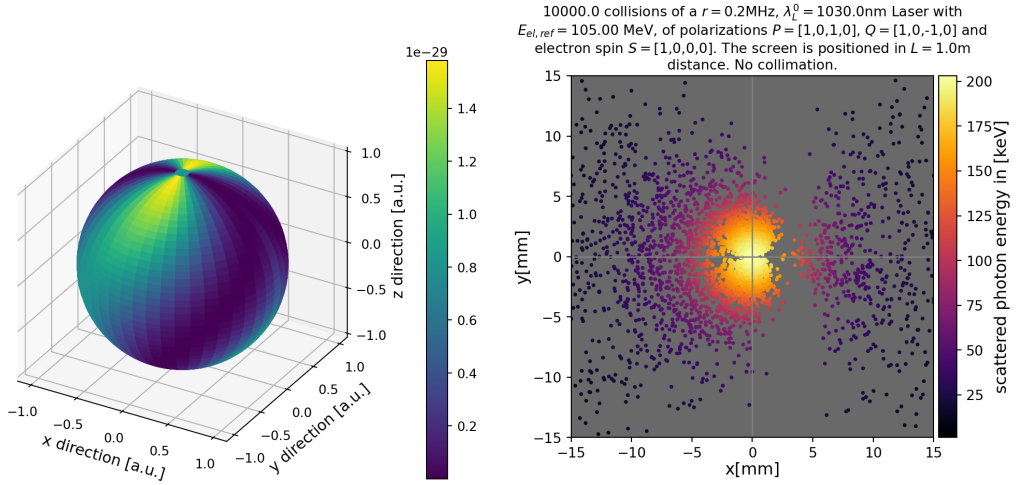

(b) 3D polarized ICS cross section (ERF) **(c)** ICS photons projected on a screen (LAB)

Figure A.13.: Spatial characteristics of ICS emitted photons under the inclusion of polarization effects. Directional scattering probability W in the ERF and emitted photons of ICS between unpolarized electrons and $\boldsymbol{P} = (1, 0, 1, 0)$ polarized incident photons detected by a $\boldsymbol{Q} = (1, 0, -1, 0)$ polarization filter. Calculated for a frontal collision $\theta_{inc} = 180°$. Plots simulated and generated in Comparse using a MESA-ER-IB-42m-nominal (App. tab. A.2) Astra generated electron distribution and Tangor-100-IR-focused (App. tab. A.8) presets. For this plot, W was calculated for $\rho_\theta = 361$ & $\rho_\phi = 720$ scattering angles by way of averaging over $N'_{par} = 5891$ scattering particle pairs chosen by weighted probability $W_{ics,norm}$.

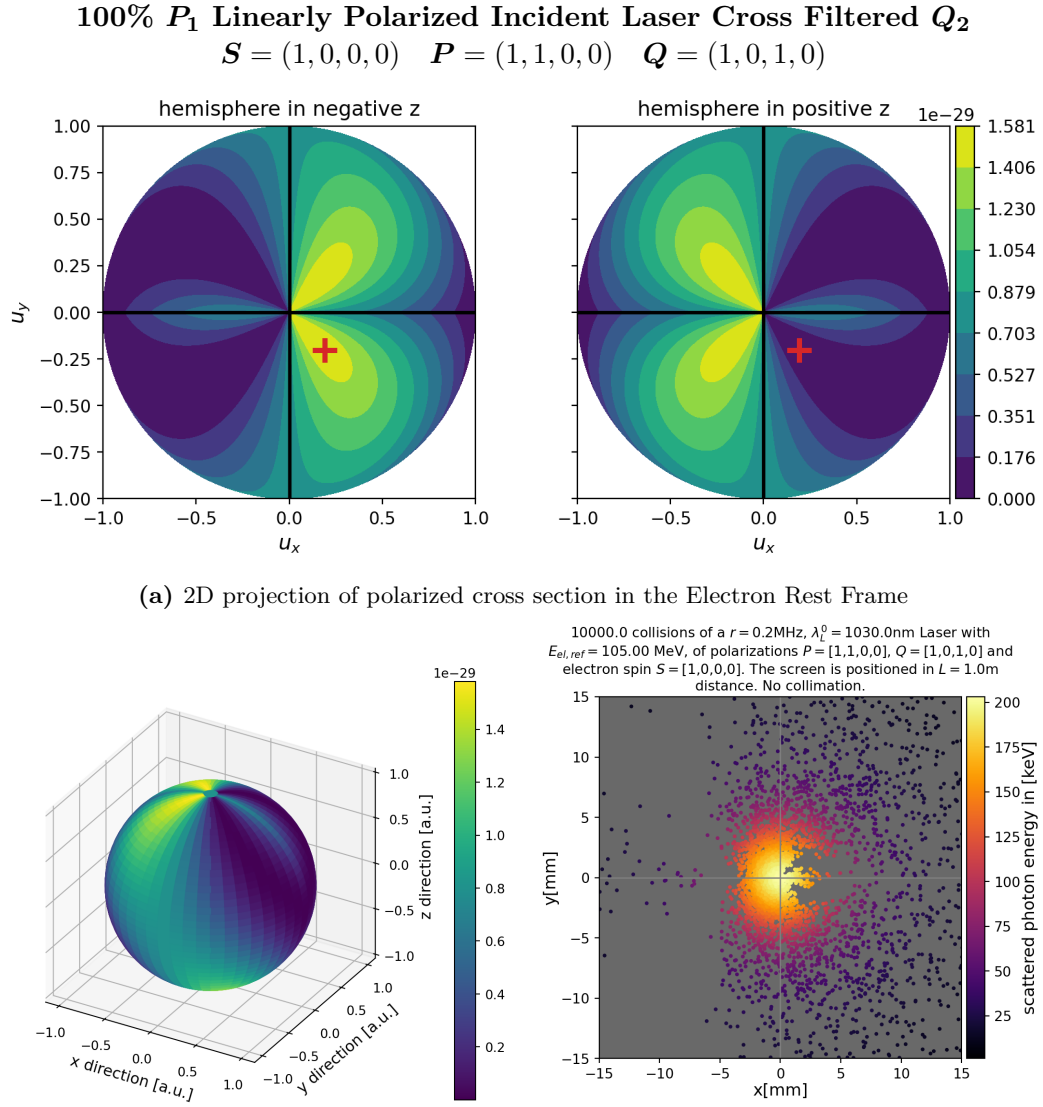

(a) 2D projection of polarized cross section in the Electron Rest Frame

(b) 3D polarized ICS cross section (ERF)

(c) ICS photons projected on a screen (LAB)

Figure A.14.: Spatial characteristics of ICS emitted photons under the inclusion of polarization effects. Directional scattering probability W in the ERF and emitted photons of ICS between unpolarized electrons and $\boldsymbol{P} = (1,1,0,0)$ polarized incident photons detected by a $\boldsymbol{Q} = (1,0,1,0)$ polarization filter. Calculated for a frontal collision $\theta_{inc} = 180°$. Plots simulated and generated in Comparse using a MESA-ER-IB-42m-nominal (App. tab. A.2) Astra generated electron distribution and Tangor-100-IR-focused (App. tab. A.8) presets. For this plot, W was calculated for $\rho_\theta = 361$ & $\rho_\phi = 720$ scattering angles by way of averaging over $N'_{par} = 5891$ scattering particle pairs chosen by weighted probability $W_{ics,norm}$.

"Ferengi Cruiser"

$\boldsymbol{S} = (1, 0, 0, 0) \quad \boldsymbol{P} = (1, 0.707, 0.707, 0) \quad \boldsymbol{Q} = (1, 0, 1, 0)$

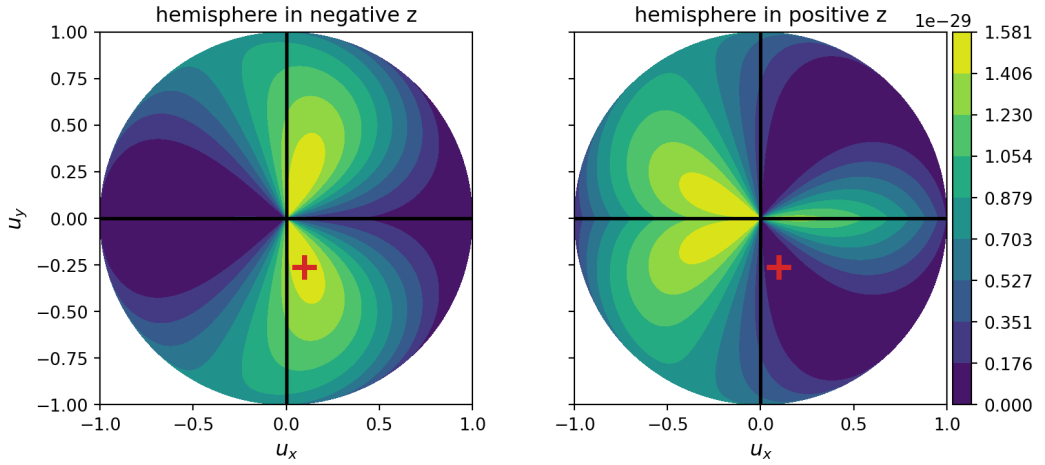

(a) 2D projection of polarized cross section in the Electron Rest Frame

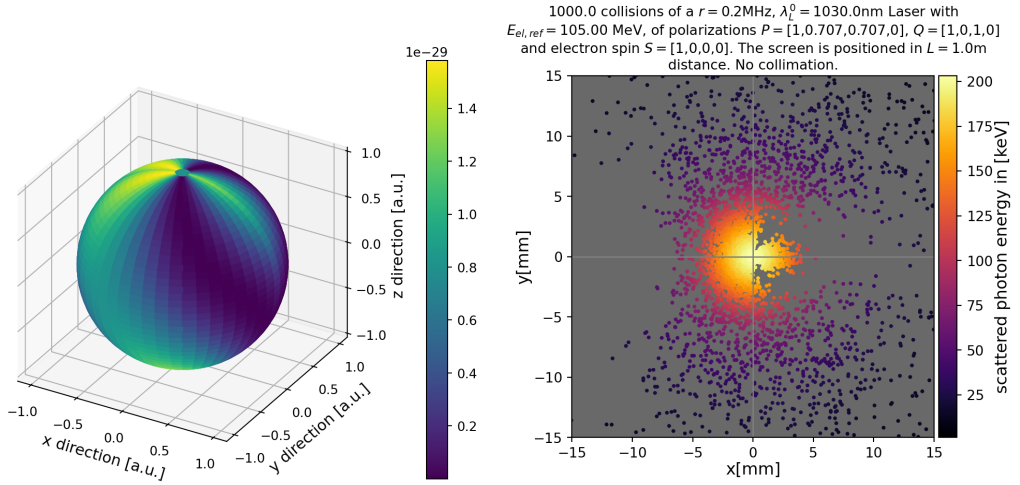

(b) 3D polarized ICS cross section (ERF) **(c)** ICS photons projected on a screen (LAB)

Figure A.15.: Spatial characteristics of ICS emitted photons under the inclusion of polarization effects. Directional scattering probability W in the ERF and emitted photons of ICS between unpolarized electrons and $\boldsymbol{P} = (1, 0.707, 0.707, 0)$ polarized incident photons detected by a $\boldsymbol{Q} = (1, 0, 1, 0)$ polarization filter. Calculated for a frontal collision $\theta_{inc} = 180°$. Plots simulated and generated in Comparse using a MESA-ER-IB-42m-nominal (App. tab. A.2) Astra generated electron distribution and Tangor-100-IR-focused (App. tab. A.8) presets. For this plot, W was calculated for $\rho_\theta = 361$ & $\rho_\phi = 720$ scattering angles by way of averaging over $N'_{par} = 5891$ scattering particle pairs chosen by weighted probability $W_{ics,norm}$.

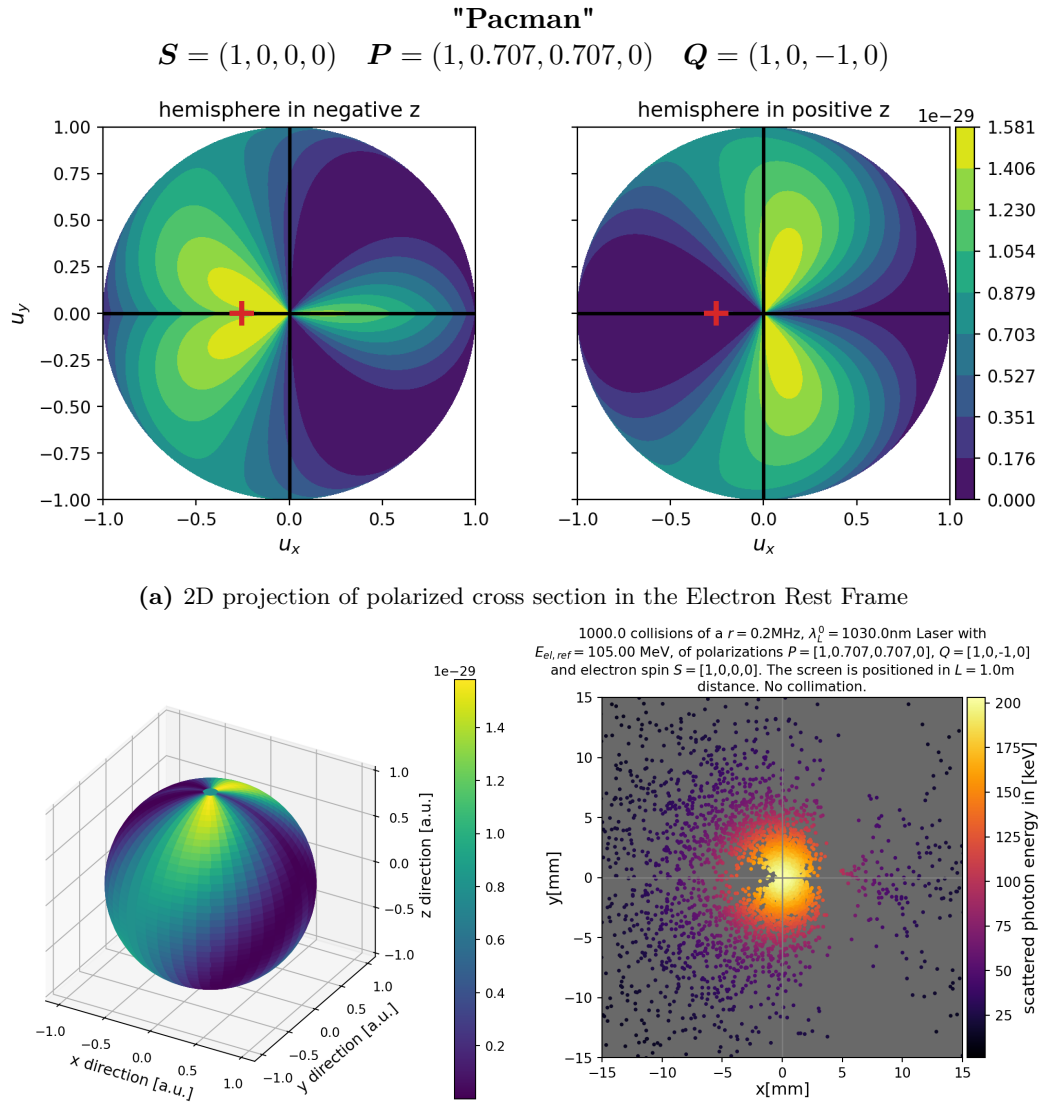

(a) 2D projection of polarized cross section in the Electron Rest Frame

(b) 3D polarized ICS cross section (ERF)

(c) ICS photons projected on a screen (LAB)

Figure A.16.: Spatial characteristics of ICS emitted photons under the inclusion of polarization effects. Directional scattering probability W in the ERF and emitted photons of ICS between unpolarized electrons and $\boldsymbol{P} = (1, 0.707, 0.707, 0)$ polarized incident photons detected by a $\boldsymbol{Q} = (1, 0, -1, 0)$ polarization filter. Calculated for a frontal collision $\theta_{inc} = 180°$. Plots simulated and generated in Comparse using a MESA-ER-IB-42m-nominal (App. tab. A.2) Astra generated electron distribution and Tangor-100-IR-focused (App. tab. A.8) presets. For this plot, W was calculated for $\rho_\theta = 361$ & $\rho_\phi = 720$ scattering angles by way of averaging over $N'_{par} = 5891$ scattering particle pairs chosen by weighted probability $W_{ics,norm}$.

A.8. Example Time Series Visualization

Complete example time series of ICS interaction over 21 time steps. Scattering events of 100 collisions corresponding to the current timestep are highlighted in bright green, while previously recorded scattering positions are highlighted in a darker green. Figure 4.13b shows how approximating fermion distribution trajectories can lead to scattering positions in longitudinal positions that temporally static simulations would not allow for. Simulated and generated in Comparse with activated temporal dynamics using a MESA-ER-IB-42m-nominal (Appendix tab. A.2) Astra generated electron distribution and Tangor-100-IR-focused (Appendix tab. A.8) presets.

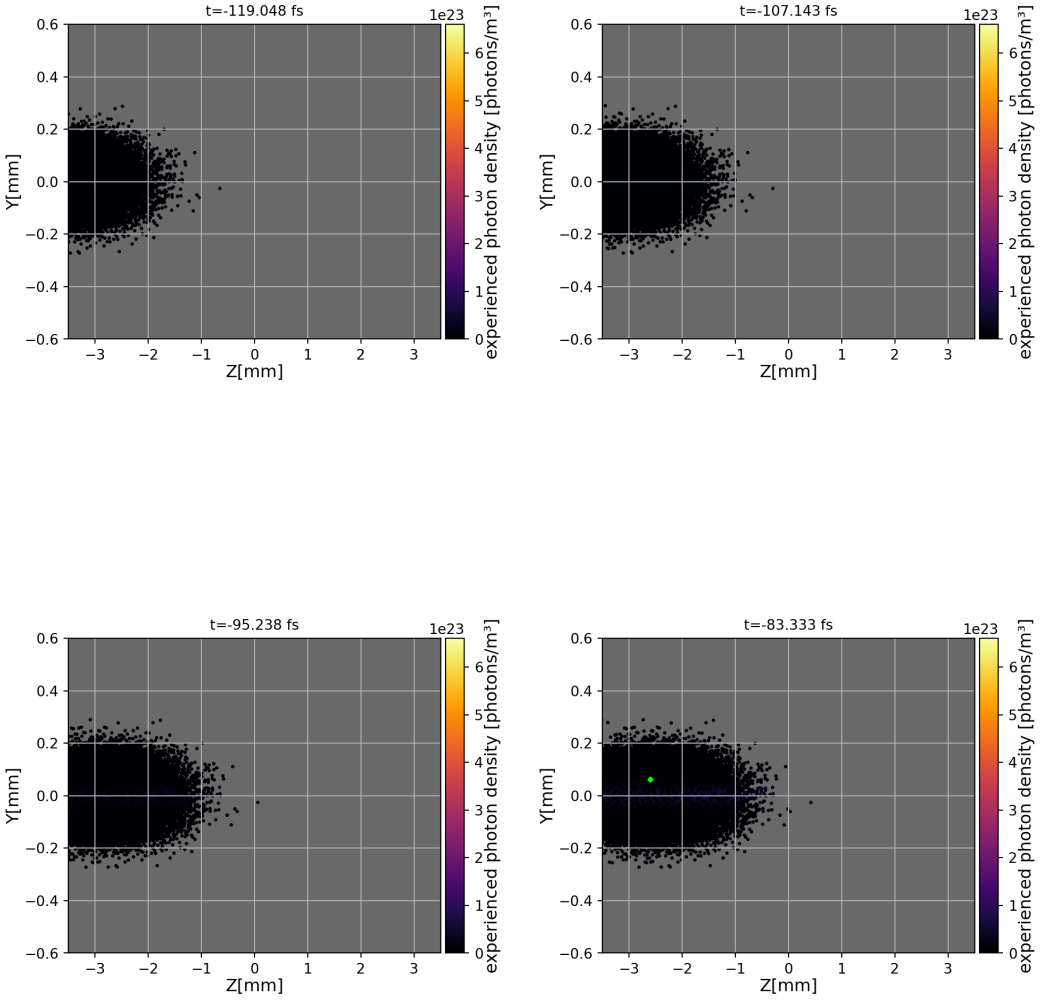

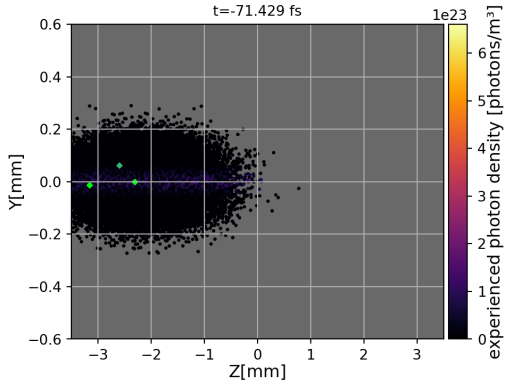
t=-71.429 fs
1e23
Y[mm]
Z[mm]
experienced photon density [photons/m³]

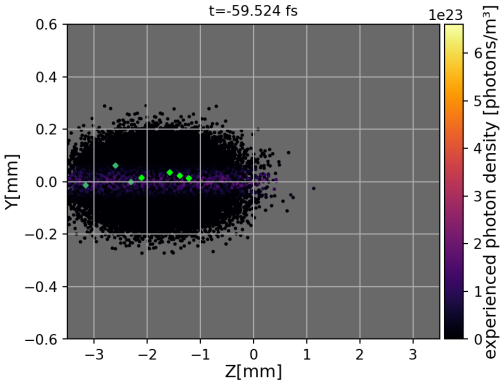
t=-59.524 fs
1e23
Y[mm]
Z[mm]
experienced photon density [photons/m³]

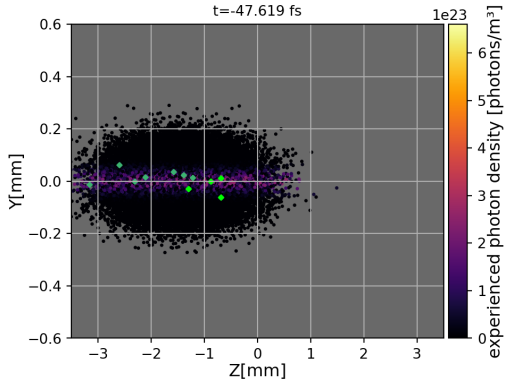
t=-47.619 fs
1e23
Y[mm]
Z[mm]
experienced photon density [photons/m³]

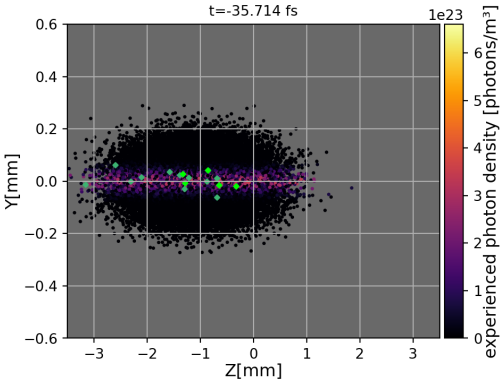
t=-35.714 fs
1e23
Y[mm]
Z[mm]
experienced photon density [photons/m³]

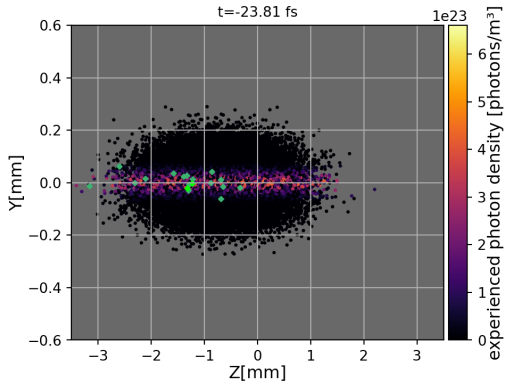
t=-23.81 fs
1e23
Y[mm]
Z[mm]
experienced photon density [photons/m³]

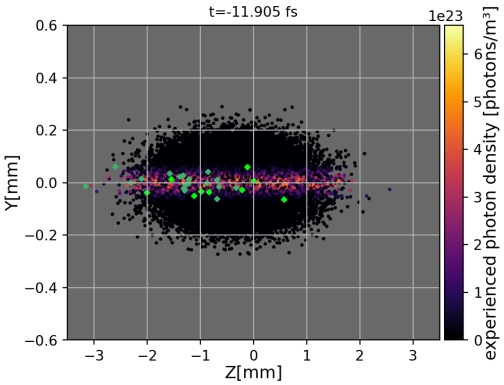
t=-11.905 fs
1e23
Y[mm]
Z[mm]
experienced photon density [photons/m³]

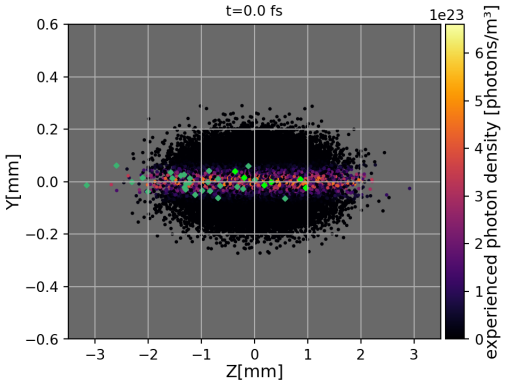
t=0.0 fs
1e23
Y[mm]
Z[mm]
experienced photon density [photons/m³]

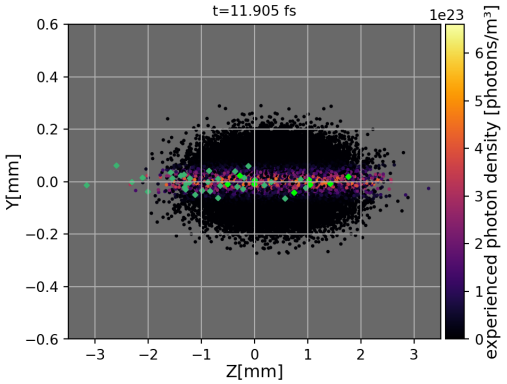
t=11.905 fs
1e23
Y[mm]
Z[mm]
experienced photon density [photons/m³]

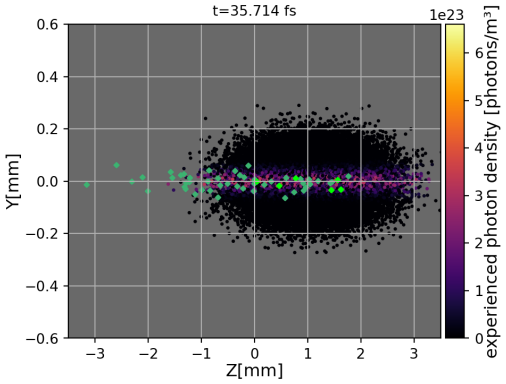
t=35.714 fs
1e23
Y[mm]
Z[mm]
experienced photon density [photons/m³]

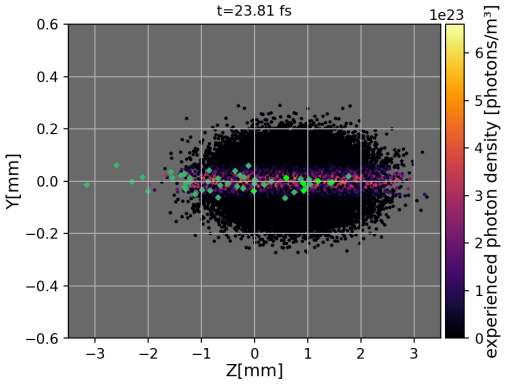
t=23.81 fs
1e23
Y[mm]
Z[mm]
experienced photon density [photons/m³]

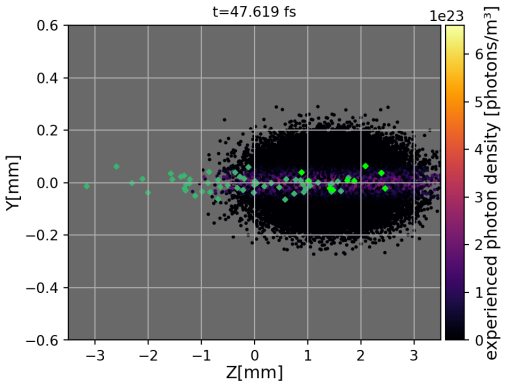
t=47.619 fs
1e23
Y[mm]
Z[mm]
experienced photon density [photons/m³]

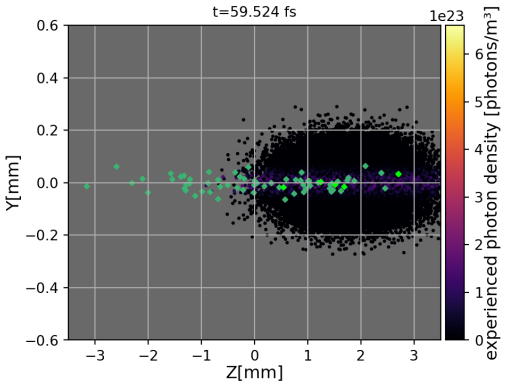
t=59.524 fs
1e23
Y[mm]
Z[mm]
experienced photon density [photons/m³]

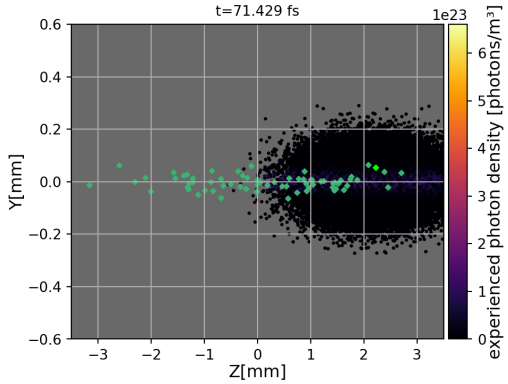
t=71.429 fs
1e23
Y[mm]
Z[mm]
experienced photon density [photons/m³]

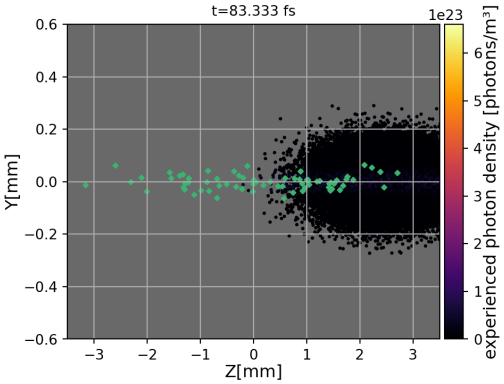
t=83.333 fs
1e23
Y[mm]
Z[mm]
experienced photon density [photons/m³]

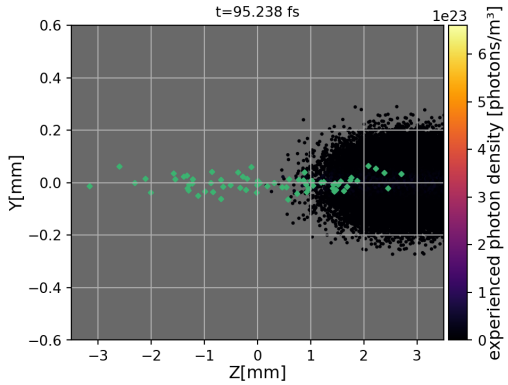
t=95.238 fs
1e23
Y[mm]
Z[mm]
experienced photon density [photons/m³]

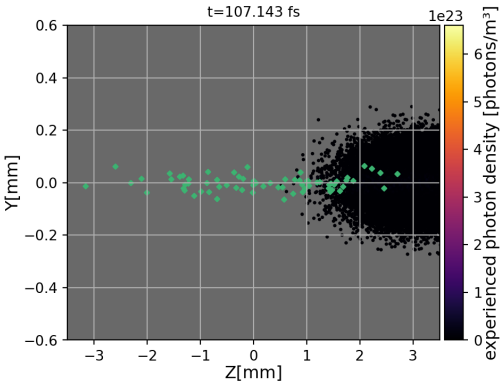
t=107.143 fs
1e23
Y[mm]
Z[mm]
experienced photon density [photons/m³]

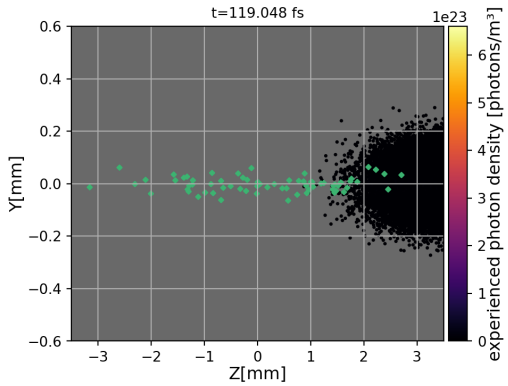
t=119.048 fs
1e23
Y[mm]
Z[mm]
experienced photon density [photons/m³]

Bibliography

[1] D. Meschede, *Gerthsen Physik*, 23rd ed. Berlin: Springer, 2005.

[2] NIST, national Institute of Standards and Technology. [Online]. Available: https://pml.nist.gov/cuu/Constants/

[3] D. Simon, "Gesamtkonzept für den MESA-Teilchenbeschleuniger unter besonderer Berücksichtigung von Strahloptik und Kryogenik," Ph.D. dissertation, Mainz U., 2021.

[4] M. Dehn *et al.*, "The MAMI-C Accelerator: 25 Years of Operation and Strategies for the Next Decade," in *Proc. of International Particle Accelerator Conference (IPAC'17), Copenhagen, Denmark, 14-19 May, 2017*, ser. International Particle Accelerator Conference, no. 8. Geneva, Switzerland: JACoW, May 2017, paper TUPIK054, pp. 1816–1818, https://doi.org/10.18429/JACoW-IPAC2017-TUPIK054. [Online]. Available: http://jacow.org/ipac2017/papers/tupik054.pdf

[5] S. Schlimme, K. Aulenbacher, S. Baunack, N. Berger, A. Denig, L. Doria, A. Khoukaz, F. Maas, H. Merkel, C. Sfienti, and M. Thiel, "The mesa physics program," 2024. [Online]. Available: https://arxiv.org/abs/2402.01027

[6] S. Friederich, K. Aulenbacher, and C. Matejcek, "Status of the Polarized Source and Beam Preparation System at MESA," in *12th International Particle Accelerator Conference* , 8 2021.

[7] R. G. Heine, "Testing of the Milliampere Booster Prototype Cavity," in *Proc. IPAC'21*. JACoW Publishing, Geneva, Switzerland, 2021, paper WEPAB041, pp. 2693–2696. [Online]. Available: https://jacow.org/ipac2021/papers/WEPAB041.pdf

[8] P. Achenbach and M. Christmann, "Application of accelerator beam dumps for dark matter searches," *Nuclear Science and Engineering*, vol. 198, no. 1, pp. 1–6, 2024.

[9] C. L. R. Heine and F. Fichtner, "The mesa high power 1.3 ghz cw solid state power amplifier systems," in *Proc. IPAC'24*, ser. IPAC'24 - 15th International Particle Accelerator Conference, no. 15. JACoW Publishing, Geneva, Switzerland, 05 2024, paper TUPR27, pp. 1482–1485. [Online]. Available: https://indico.jacow.org/event/63/contributions/3949

[10] A. H. Compton, "A quantum theory of the scattering of x-rays by light elements," *Phys. Rev.*, vol. 21, pp. 483–502, May 1923. [Online]. Available: https://link.aps.org/doi/10.1103/PhysRev.21.483

[11] J. Thomson, "Xxxiv. on momentum in the electric field," *The London, Edinburgh, and Dublin Philosophical Magazine and Journal of Science*, vol. 8, no. 45, pp. 331–356, 1904. [Online]. Available: https://doi.org/10.1080/14786440409463203

[12] L. D. Landau and E. M. Lifschitz, *The Classical Theory of Fields*, ser. Course of Theoretical Physics. Oxford: Pergamon Press, 1975, vol. Volume 2.

[13] V. B. Berestetskii, E. M. Lifshitz, and L. P. Pitaevskii, *QUANTUM ELECTRODYNAMICS*, ser. Course of Theoretical Physics. Oxford: Pergamon Press, 1982, vol. 4.

[14] K. Wille, *The physics of particle accelerators : an introduction; Repr.* Oxford [u.a.]: Oxford Univ. Press, 2009, includes bibliographical references and index; English. [Online]. Available: https://reserves.ub.rwth-aachen.de/record/131066

[15] C. Curatolo, I. Drebot, V. Petrillo, and L. Serafini, "Analytical description of photon beam phase spaces in inverse compton scattering sources," *Phys. Rev. Accel. Beams*, vol. 20, p. 080701, Aug 2017. [Online]. Available: https://link.aps.org/doi/10.1103/PhysRevAccelBeams.20.080701

[16] W. H. McMaster, "Polarization and the Stokes Parameters," *American Journal of Physics*, vol. 22, no. 6, pp. 351–362, 09 1954. [Online]. Available: https://doi.org/10.1119/1.1933744

[17] ——, "Matrix representation of polarization," *Rev. Mod. Phys.*, vol. 33, pp. 8–28, Jan 1961. [Online]. Available: https://link.aps.org/doi/10.1103/RevModPhys.33.8

[18] W. Heitler, *The quantum theory of radiation*, ser. International Series of Monographs on Physics. Oxford: Oxford University Press, 1936, vol. 5.

[19] J. A. Wheeler, "On the mathematical description of light nuclei by the method of resonating group structure," *Phys. Rev.*, vol. 52, pp. 1107–1122, Dec 1937. [Online]. Available: https://link.aps.org/doi/10.1103/PhysRev.52.1107

[20] W. Heisenberg, "Die "beobachtbaren Größen" in der Theorie der Elementarteilchen," *Zeitschrift fur Physik*, vol. 120, no. 7-10, pp. 513–538, Jul 1943.

[21] P. A. M. Dirac, "The Quantum Theory of the Electron," *Proceedings of the Royal Society of London Series A*, vol. 117, no. 778, pp. 610–624, Feb 1928.

[22] W. Heisenberg, "Development of concepts in the history of quantum theory," in *The physicist's conception of nature*, J. Mehra, Ed. Reidel, 1973, pp. 264–275.

[23] G. G. Stokes, "On the Composition and Resolution of Streams of Polarized Light from different Sources," *Transactions of the Cambridge Philosophical Society*, vol. 9, p. 399, Jan. 1851.

[24] W. A. Shurcliff, *Polarized Light - Production and Use*. Cambridge, MA and London, England: Harvard University Press, 1962. [Online]. Available: https://doi.org/10.4159/harvard.9780674424135

[25] A. Wightman, "Note on polarization effects in compton scattering," *Phys. Rev.*, vol. 74, pp. 1813–1817, Dec 1948. [Online]. Available: https://link.aps.org/doi/10.1103/PhysRev.74.1813

[26] U. Fano, "Remarks on the classical and quantum-mechanical treatment of partial polarization∗," *J. Opt. Soc. Am.*, vol. 39, no. 10, pp. 859–863, Oct 1949. [Online]. Available: https://opg.optica.org/abstract.cfm?URI=josa-39-10-859

[27] J. Hoffstadt, "Dearpygui," https://github.com/hoffstadt/DearPyGui, 2024.

[28] J. D. Hunter, "Matplotlib: A 2d graphics environment," *Computing in Science & Engineering*, vol. 9, no. 3, pp. 90–95, 2007.

[29] C. R. Harris, K. J. Millman, S. J. van der Walt, R. Gommers, P. Virtanen, D. Cournapeau, E. Wieser, J. Taylor, S. Berg, N. J. Smith, R. Kern, M. Picus, S. Hoyer, M. H. van Kerkwijk, M. Brett, A. Haldane, J. F. del Río, M. Wiebe, P. Peterson, P. Gérard-Marchant, K. Sheppard, T. Reddy, W. Weckesser, H. Abbasi, C. Gohlke, and T. E. Oliphant, "Array programming with NumPy," *Nature*, vol. 585, no. 7825, pp. 357–362, Sep. 2020. [Online]. Available: https://doi.org/10.1038/s41586-020-2649-2

[30] K. Floettmann, *ASTRA - A Space Charge Tracking Algorithm*, Hamburg, Germany, 2017.

[31] L. J. Kedward, B. Aradi, O. Čertík, M. Curcic, S. Ehlert, P. Engel, R. Goswami, M. Hirsch, A. Lozada-Blanco, V. Magnin, A. Markus, E. Pagone, I. Pribec, B. Richardson, H. Snyder, J. Urban, and J. Vandenplas, "The state of fortran," *Computing in Science & Engineering*, vol. 24, no. 2, pp. 63–72, 2022.

[32] A. Adelmann, P. Calvo, M. Frey, A. Gsell, U. Locans, C. Metzger-Kraus, N. Neveu, C. Rogers, S. Russell, S. Sheehy, J. Snuverink, and D. Winklehner, "OPAL a Versatile Tool for Charged Particle Accelerator Simulations," *arXiv e-prints*, p. arXiv:1905.06654, May 2019.

[33] A. Papoulis and S. U. Pillai, *Probability, Random Variables, and Stochastic Processes*, 4th ed. Boston: McGraw Hill, 2002. [Online]. Available: http://www.worldcat.org/search?qt=worldcat_org_all&q=0071226613

[34] "Cvi melles griot historic technical guide," 2012. [Online]. Available: https://www.idex-hs.com/resources/resources-detail/cvi-melles-griot-technical-guide

[35] A. Einstein, "Die Grundlage der allgemeinen Relativitätstheorie," *Annalen der Physik*, vol. 354, no. 7, pp. 769–822, Jan. 1916.

[36] S. van der Walt, S. C. Colbert, and G. Varoquaux, "The numpy array: A structure for efficient numerical computation," *Computing in Science & Engineering*, vol. 13, no. 2, pp. 22–30, 2011.

[37] J.-C. Diels and W. Rudolph, *Ultrashort Laser Pulse Phenomena Fundamentals, Techniques, and Applications an a Femtosecond Time Scale Second Edition.* Elsevier, 2006.

[38] C. L. Lorey, "Comparse," https://gitlab.rlp.net/clorey/thomson-scattering-phd, 2024.

[39] K. H. Steffens, "Konzeption und optimierung eines 100kev injektionssystems zur erzeugung eines longitudinal polarisierten elektronenstrahls an mami," Ph.D. dissertation, 1993.

[40] H. Grote, F. Iselin, E. Keil, and J. Niederer, "The mad program," in *Proceedings of the 1989 IEEE Particle Accelerator Conference, . 'Accelerator Science and Technology*, vol. 2, 1989, pp. 1292–1294.

[41] "Mad - methodical accelerator design," current homepage and repository of the software. [Online]. Available: https://madx.web.cern.ch

[42] T. "Persson, H. Burkhardt, R. De Maria, L. Deniau, E. Høydalsvik, A. Latina, P. Skowroński, R. Tomás García, and L. van Riesen-Haupt, "Mad-x for future accelerators," vol. IPAC2022, 2022, pp. 1858–1861.

[43] D. Simon, "Unpublished mad-x mesa beamline simulations," 2020, internally conducted by Daniel Simon at KPH Mainz, MESA working group.

[44] W. Herr and B. Muratori, "Concept of luminosity," 2006. [Online]. Available: https://cds.cern.ch/record/941318

[45] M. G. Meier, "Entwicklung und aufbau der laser-getriebenen compton-rückstreuquelle cobra für strahldiagnose am s-dalinac," Ph.D. dissertation, Technische Universität Darmstadt, Darmstadt, August 2024. [Online]. Available: http://tuprints.ulb.tu-darmstadt.de/27694/

[46] E. Eggl, M. Dierolf, K. Achterhold, C. Jud, B. Günther, E. Braig, B. Gleich, and F. Pfeiffer, "The Munich Compact Light Source: initial performance measures," *Journal of Synchrotron Radiation*, vol. 23, no. 5, pp. 1137–1142, Sep 2016. [Online]. Available: https://doi.org/10.1107/S160057751600967X

[47] A. Chaleil, V. Le Flanchec, A. Binet, J. P. Nègre, J. F. Devaux, V. Jacob, M. Millerioux, A. Bayle, P. Balleyguier, and R. Prazeres, "Inverse Compton scattering X-ray source yield optimization with a laser path folding system inserted in a pre-existent RF linac," *Nuclear Instruments and Methods in Physics Research A*, vol. 840, pp. 113–120, Dec. 2016.

[48] A. Pires, "Optimization of ELSA electron beam transport for its inverse Compton scattering X-ray source," May 2024. [Online]. Available: https://indico.jacow.org/event/63/contributions/3467/

[49] D. Basting and G. Marowsky, *Excimer Laser Technology*, 01 2005, vol. 364.

[50] *Excimer lasers -Industrial Version*, 2005. [Online]. Available: https://www.gmp.ch/htmlarea/pdf/IN.pdf

[51] K. Abrahamyan, J. Bähr, I. Bohnet, S. Choroba, K. Flöttmann, H.-J. Grabosch, M. Hartrott, R. Ischebeck, O. Krebs, Z. Li, D. Lipka, A. Oppelt, V. Peplov, B. Petrosyan, M. Pohl, J. Rossbach, S. Simrock, F. Stephan, T. Thon, R. Wenndorff, and M. Winde, "Rf commissioning of the photo injector test facility at desy zeuthen," in *Free Electron Lasers 2002*, K.-J. Kim, S. Milton, and E. Gluskin, Eds. Amsterdam: Elsevier, 2003, pp. II–45–II–46. [Online]. Available: https://www.sciencedirect.com/science/article/pii/B9780444514172501541

[52] B. Faatz, M. Braune, O. Hensler, K. Honkavaara, R. Kammering, M. Kuhlmann, E. Ploenjes, J. Roensch-Schulenburg, E. Schneidmiller, S. Schreiber, K. Tiedtke, M. Tischer, R. Treusch, M. Vogt, W. Wurth, M. Yurkov, and J. Zemella, "The flash facility: Advanced options for flash2 and future perspectives," *Applied Sciences*, vol. 7, no. 11, 2017. [Online]. Available: https://www.mdpi.com/2076-3417/7/11/1114

[53] Y. Sakai, M. Babzien, M. Fedurin, K. Kusche, O. Williams, A. Fukasawa, B. Naranjo, A. Murokh, R. Agustsson, A. Simmonds, P. Jacob, G. Stenby, R. Malone, M. Polyanskiy, I. Pogorelsky, M. Palmer, and J. Rosenzweig, "Hard x-ray inverse compton scattering at photon energy of 87.5 kev," *Scientific Reports*, vol. 14, 08 2024.

[54] J. Schuemann, R. Berbeco, D. B. Chithrani, S. H. Cho, R. Kumar, S. J. McMahon, S. Sridhar, and S. Krishnan, "Roadmap to clinical use of gold nanoparticles for radiation sensitization," *International Journal of Radiation Oncology*Biology*Physics*, vol. 94, no. 1, pp. 189–205, 2016. [Online]. Available: https://www.sciencedirect.com/science/article/pii/S0360301615265315

[55] K. Dupraz, M. Alkadi, M. Alves, L. Amoudry, D. Auguste, J.-L. Babigeon, M. Baltazar, A. Benoit, J. Bonis, J. Bonenfant, C. Bruni, K. Cassou, J.-N. Cayla, T. Chabaud, I. Chaikovska, S. Chance, V. Chaumat, R. Chiche,

A. Cobessi, P. Cornebise, O. Dalifard, N. Delerue, R. Dorkel, D. Douillet, J.-P. Dugal, N. El Kamchi, M. El Khaldi, E. Ergenlik, P. Favier, M. Fernandez, A. Gamelin, J.-F. Garaut, L. Garolfi, P. Gauron, F. Gauthier, A. Gonnin, D. Grasset, E. Guerard, H. Guler, J. Haissinski, E. Herry, G. Iaquaniello, M. Jacquet, E. Jules, V. Kubytskyi, M. Langlet, T. Le Barillec, J.-F. Ledu, D. Leguidec, B. Leluan, P. Lepercq, F. Letellier-Cohen, R. Marie, J.-C. Marrucho, A. Martens, C. Mageur, G. Mercadier, B. Mercier, E. Mistretta, H. Monard, A. Moutardier, O. Neveu, D. Nutarelli, M. Omeich, Y. Peinaud, Y. Petrilli, M. Pichet, E. Plaige, C. Prévost, P. Rudnicky, V. Soskov, M. Taurigna-Quéré, S. Trochet, C. Vallerand, O. Vitez, F. Wicek, S. Wurth, F. Zomer, P. Alexandre, R. Ben El Fekih, P. Berteaud, F. Bouvet, R. Cuoq, A. Diaz, Y. Dietrich, M. Diop, D. Pedeau, E. Dupuy, F. Marteau, F. Bouvet, A. Gamelin, D. Helder, N. Hubert, J. Veteran, M. Labat, A. Lestrade, A. Letrésor, R. Lopes, A. Loulergue, M. Louvet, M. Louvet, P. Marchand, M. El Ajjouri, D. Muller, A. Nadji, L. Nadolski, R. Nagaoka, S. Petit, J.-P. Pollina, F. Ribeiro, M. Ros, J. Salvia, S. Bobault, M. Sebdaoui, R. Sreedharan, Y. Bouanai, J.-L. Hazemann, J.-L. Hodeau, E. Roy, P. Jeantet, J. Lacipière, P. Robert, J.-M. Horodynski, H. Bzyl, C. Chapelle, M. Biagini, P. Walter, A. Bravin, W. Del Net, E. Lahéra, O. Proux, H. Elleaume, and E. Cormier, "The thomx ics source," *Physics Open*, vol. 5, p. 100051, 2020. [Online]. Available: https://www.sciencedirect.com/science/article/pii/S2666032620300387

[56] D. Savran, "Experimental results on the pygmy dipole resonance," *EPJ Web of Conferences*, vol. 66, no. 02094, 2014.

[57] E. G. Lanza, L. Pellegri, A. Vitturi, and M. V. Andrés, "Pygmy dipole resonances: open problems," *J. Phys. Conf. Ser.*, vol. 2586, no. 1, p. 012084, 2023.

[58] G. Toth, *Glimpses of Algebra and Geometry*. New York, NY: Springer New York, 2002. [Online]. Available: https://doi.org/10.1007/0-387-22455-6_7

[59] J. Diefenbach, "Aufbau einer elektronischen Stabilisierung für das A4-Compton-Polarimeter," Master's thesis, JGU Mainz, 2003.

[60] Y. Imai, "Messung und optimierung der lichtpolarisation des a4-compton-rückstreupolarimeters," Ph.D. dissertation, Mainz, 2019.

[61] E. D. Monte, S. Fabiani, and M. Pearce, "Compton polarimetry," 2023. [Online]. Available: https://arxiv.org/abs/2301.09934

[62] C. Sun and Y. K. Wu, "Theoretical and simulation studies of characteristics of a compton light source," *Physical Review Special Topics - Accelerators and Beams*, vol. 14, no. 4, Apr. 2011. [Online]. Available: http://dx.doi.org/10.1103/PhysRevSTAB.14.044701

[63] H. Krawczynski, "The polarization properties of inverse compton emission and implications for blazar observations with the gems x-ray polarimeter," *The Astrophysical Journal*, vol. 744, no. 1, p. 30, dec 2011. [Online]. Available: https://dx.doi.org/10.1088/0004-637X/744/1/30

[64] W. J. Brown, S. G. Anderson, C. P. J. Barty, S. M. Betts, R. Booth, J. K. Crane, R. R. Cross, D. N. Fittinghoff, D. J. Gibson, F. V. Hartemann, E. P. Hartouni, J. Kuba, G. P. Le Sage, D. R. Slaughter, A. M. Tremaine, A. J. Wootton, P. T. Springer, and J. B. Rosenzweig, "Experimental characterization of an ultrafast thomson scattering x-ray source with three-dimensional time and frequency-domain analysis," *Phys. Rev. ST Accel. Beams*, vol. 7, p. 060702, Jun 2004. [Online]. Available: https://link.aps.org/doi/10.1103/PhysRevSTAB.7.060702

[65] W. G. et al., "Results from cxls commissioning," in *Proc. IPAC'24*, ser. IPAC'24 - 15th International Particle Accelerator Conference, no. 15. JACoW Publishing, Geneva, Switzerland, 05 2024, paper TUCN3, pp. 981–984. [Online]. Available: https://indico.jacow.org/event/63/contributions/3222

[66] G. Van Rossum, *The Python Library Reference, release 3.8.2.* Python Software Foundation, 2020.

Diese Arbeit wurde durch Mittel der DFG im Zuge des GRK 2128 „AccelencE“ unterstützt.

Versicherung

für das Gesuch um Zulassung zur Promotion am Fachbereich 08

Hiermit versichere ich gemäß § 12 Abs. 3e der Promotionsordnung des Fachbereichs 08, Physik, Mathematik und Informatik der Johannes Gutenberg-Universität Mainz vom 02.12.2013:

a) Ich habe die jetzt als Dissertation vorgelegte Arbeit selbständig verfasst. Es wurden ausschließlich die angegebenen Quellen und Hilfsmittel verwendet. Von der Ordnung zur Sicherung guter wissenschaftlicher Praxis in Forschung und Lehre und vom Verfahren zum Umgang mit wissenschaftlichem Fehlverhalten habe ich Kenntnis genommen.

b) Ich habe oder hatte die jetzt als Dissertation ~~vorgelegte Arbeit nicht schon als Prüfungs~~arbeit für ~~eine andere Prüfung~~ eingereicht ***)**

~~Ich hatte die jetzt als Dissertation vorgelegte Arbeit als Prüfungsarbeit für folgende Prüfung~~ eingereicht: ***)**

_____

(Bezeichnung der Prüfung)

_____

(Bezeichnung und Ort der Prüfungsstelle)

c) ~~Ich hatte weder die jetzt als Dissertation vorgelegte Arbeit noch Teile davon an einer anderen~~ Stelle als Dissertation eingereicht ***)**

Ich hatte die folgende Abhandlung mit anstehendem Ergebnis als Dissertation eingereicht ***)**

_____

(Titel der Abhandlung)

_____

(Fakultät bzw. Fachbereich und Hochschule)

_____

(Ergebnis bzw. Beurteilung)

19.12.24
(Datum)

Ch. Lorey
(Unterschrift)

) Nichtzutreffendes bitte streichen

18.03.2014/mm